ESTIMATION OF SOUNDING UNCERTAINTY FROM MEASURMENTS OF WATER MASS VARIABILITY

JONATHAN DANIEL BEAUDOIN

January 2010

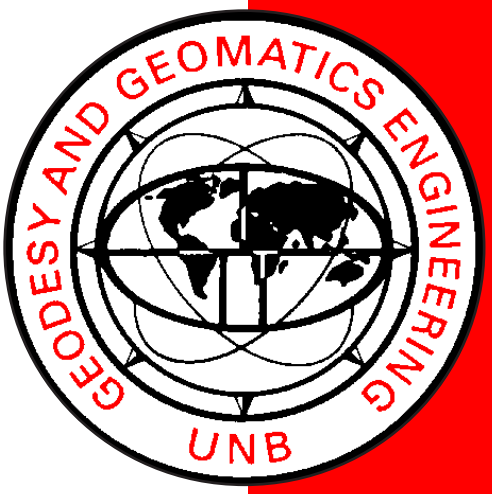

TECHNICAL REPORT
NO. 271

ESTIMATION OF SOUNDING UNCERTAINTY FROM MEASUREMENTS OF WATER MASS VARIABILITY

Jonathan Daniel Beaudoin

Department of Geodesy and Geomatics Engineering
University of New Brunswick
P.O. Box 4400
Fredericton, N.B.
Canada
E3B 5A3

January, 2010

PREFACE

This technical report is a reproduction of a dissertation submitted in partial fulfillment of the requirements for the degree of Doctor of Philosophy in the Department of Geodesy and Geomatics Engineering, January 2010. The research was supervised by Dr. John Hughes Clarke, and funding was provided by the ArcticNet Network of Centres of Excellence of Canada.

As with any copyrighted material, permission to reprint or quote extensively from this report must be received from the author. The citation to this work should appear as follows:

Beaudoin, Jonathan (2010). *Estimation of Sounding Uncertainty from Measurements of Water Mass Variability*. Ph.D. dissertation, Department of Geodesy and Geomatics Engineering, Technical Report No. 271, University of New Brunswick, Fredericton, New Brunswick, Canada, 232 pp.

ABSTRACT

Analysis techniques are proposed that allow for estimation of potential sounding uncertainty due to water mass variability based solely on high temporal and/or spatial resolution observations of either sound speed or oceanographic measurements of temperature and salinity. The techniques do not require sounding data, thus analyses can be tailored to match any survey system; this allows for pre-analysis campaigns to optimize survey instrumentation, sound speed profiling locations/rates and survey line spacing such that a desired sounding accuracy can be maintained. In addition to this, the output of the methods can provide a higher fidelity estimation of sounding uncertainty due to water mass variability as compared to existing uncertainty models in common use.

The analysis techniques are used to assess an extensive oceanographic data set collected in the Canadian Arctic Archipelago (CAA) in an effort to provide water mass sampling guidelines for current and future seabed mapping efforts in the CAA. In particular, the problem of mapping while in transit is investigated with oceanographic climatological grids of temperature and salinity being examined as a potential source of sound speed information when underway sampling of the water column is not possible.

ACKNOWLEDGEMENTS

Many hands and minds have helped me along the way and I must give thanks to all those who provided me with guidance, constructive criticism, data, advice, etc. Firstly I would like to thank my supervisory committee for their guidance, specifically I would like to thank my supervisor Dr. John Hughes Clarke for his unwavering enthusiasm for all things related to ocean mapping. Dr. David Wells provided useful and insightful comments and critiques during all stages of my work that provided me with a sense of focus and direction.

Many people have provided high resolution Moving Vessel Profiler data sets against which I could test my analysis methods. Though the data sets they acquired on my behalf may not appear in this dissertation, the various data sets were instrumental in the development and testing of the analysis methods described herein. I would like to thank Mike Lamplugh, Jonathan Griffin, Russ Parrott and Jason Bartlett for collecting MVP data on my behalf with the CCGS Matthew, CCGS Creed and CSL Merlin. Thanks to my co-workers and fellow students Steve Brucker, Doug Cartwright, Ian Church, Auke van der Werf and Reenu Toodesh who collected many MVP data sets with the CSL Heron. Additional extensive MVP data sets were provided by Diederick van der Plas and Simon Bicknese.

Fruitful discussions led to many ideas and developments that I must acknowledge. I thank Gretchen Imahori, James Hiebert and Brian Calder for their input and energies in a collaborative case study using the analysis tools. I thank Yves Gratton, Connie Lovejoy

and Susan Haigh for their patience with my musings about physical oceanographic processes in the Canadian Arctic Archipelago.

I would like to thank the sponsors of the Ocean Mapping Group and the ArcticNet Canadian Network of Centres of Excellence for financially supporting this research. Of the former, Rijkswaterstaat was instrumental in organizing an intensive MVP field trial that provided a case study data set that proved ideal for showcasing the fruits of this research. In addition to funding this work, the ArcticNet Network provided the *raison d'être* and the data set for the case study undertaken in this dissertation.

Many friends and family members cheered me on along the way and I thank you all for your support. Lastly, and most importantly, I would like to thank my wife and daughter for their patience and understanding as I methodically made my way through the field work, research and writing involved with this effort. It is to the two of you that this work is dedicated.

TABLE OF CONTENTS

Page

LIST OF FIGURES

Page

LIST OF TABLES

Page

LIST OF ACRONYMS

ABW	Arctic Bottom Water
ADCP	Acoustic Doppler Current Profiler
AO	Arctic Oscillation
APL	Applied Physics Laboratory
ARDB	Arctic Runoff Database
ASW	Arctic Surface Water
AVHRR	Advanced Very High Resolution Radiometer
AW	Arctic Water
BIO	Bedford Institute of Oceanography
CAA	Canadian Arctic Archipelago
CCGS	Canadian Coast Guard Ship
CHS	Canadian Hydrographic Service
CSL	Canadian Survey Launch
CTD	Conductivity-Temperature-Depth
CUBE	Combined Uncertainty Bathymetry Estimator
DTM	Digital Terrain Model
GDEM	Generalized Digital Environmental Model
GPS	Global Positioning System
GRDC	Global Runoff Data Centre
GSDW	Greenland Sea Deep Water
IFREMER	French Research Institute for Exploitation of the Sea
IHO	International Hydrographic Organization
IMU	Inertial measurement unit
ISO	International Organization for Standardization
JPOTS	Joint Panel on Oceanographic Tables and Standards
MBT	Mechanical Bathythermograph
MEDS	Marine Environmental Data Service
MOODS	Master Oceanographic Observation Data Set

MVP	Moving Vessel Profiler
NADW	North Atlantic Deep Water
NAO	North Atlantic Oscillation
NAVOCEANO	Naval Oceanographic Office (US Navy)
NCE	Network of Centres of Excellence of Canada
NOAA	National Oceanic and Atmospheric Administration (US)
NODC	National Oceanographic Data Centre (US)
NPL	National Physical Laboratory (UK)
NWP	Northwest Passage
OMG	Ocean Mapping Group
RWS	Rijkswaterstaat
SBES	Single Beam Echosounder
SSP	Sound Speed Profile
TPU	Total Propagated Uncertainty
TWTT	Two-Way Travel Time
UA	Uncertainty Analysis
UNESCO	United Nations Educational, Scientific and Cultural Organization
VA	Variability Analysis
w.d.	water depth
WGC	West Greenland Current
WOA	World Ocean Atlas
WOA01	World Ocean Atlas of 2001
WOA98	World Ocean Atlas of 1998
WOD	World Ocean Database
WOD01	World Ocean Database of 2001
WOD05	World Ocean Database of 2005
XBT	Expendable Bathythermograph
XCTD	Expendable Conductivity Temperature Depth

1 INTRODUCTION

1.1 Assessment of Sounding Uncertainty Due to Refraction

Multibeam echosounders (MBES) collect oblique soundings, allowing for a remarkable increase in coverage compared to traditional downward looking single beam echosounders (SBES). The gain in coverage comes at a cost: the speed of sound varies with depth and can cause the oblique sounding ray paths to refract, introducing significant and systematic biases in soundings. This is readily corrected by measuring the sound speed variation with depth and using this additional information to model the acoustic ray path using acoustic ray tracing techniques (Medwin and Clay, 1997). Since the speed of sound in water is determined primarily by temperature and salinity, any significant spatio-temporal variations of these two quantities can significantly change the sound speed structure and can lead to sounding biases if an unrepresentative sound speed profile is used for refraction correction. The hydrographic surveyor must then take care to sample often enough to capture the important changes in the water mass such that refraction type biases are avoided.

Although it is possible to monitor changing water column conditions while mapping, it is often beneficial to understand the potential impact of water mass variability at the survey design stage such that appropriate measures can be taken before the survey, e.g. decreasing the planned survey line spacing, or investing in underway sound speed sampling instrumentation. Though *data* is sometimes available for this type of pre-

analysis, it has been difficult to extract meaningful *information* regarding the impact of water column variability on sounding uncertainty, mainly due to a lack of standardized and widely accepted analysis techniques.

A numerical simulation method is proposed which can be used to assess the impact of water column variability on sounding uncertainty. The simulation requires only sound speed profiles as input and works by mimicking the ray tracing portion of the MBES depth reduction procedure. The simulator can be configured to match the sounding geometry of any MBES system and can also investigate the entire potential sounding space, i.e. from sounder to seafloor and across the entire angular sector. The proposed methods can (a) quantify the impact of observed variability in terms of sounding uncertainty and (b) analyze sounding uncertainties associated with various refraction correction solutions, e.g. use of oceanographic databases in lieu of in-situ measurement of sound speed.

1.2 Case Study

In 2003, the decommissioned Canadian Coast Guard icebreaker Sir John Franklin was brought back into service as a multidisciplinary science platform for research in the Canadian Arctic Archipelago (CAA). Renamed the CCGS Amundsen, the ship was outfitted with a variety of acoustic and supporting survey instruments to make her capable of seabed mapping. The 98-meter vessel is equipped with a 30 kHz Kongsberg-Simrad EM300 MBES (Kongsberg, 2002), which is a shallow to mid-ocean depth system (nominally 10m - 5000m). The Amundsen plays an integral role in the ArcticNet

program, a Network of Centres of Excellence of Canada (NCE) that studies the impact of climate change in the coastal Canadian Arctic (Fortier and Leblanc, 2003). The ArcticNet NCE proposal lists one of its many goals as building *"a precise bathymetry for the Northwest Passage and other areas of the Canadian Arctic, using the state-of-the-art EM300 multi-beam echo-sounder"*. What is particularly unique about the ArcticNet mapping initiative is that the vast majority of it is to be done while in transit, slowly building up coverage with each additional year's passage (Figure 1-1).

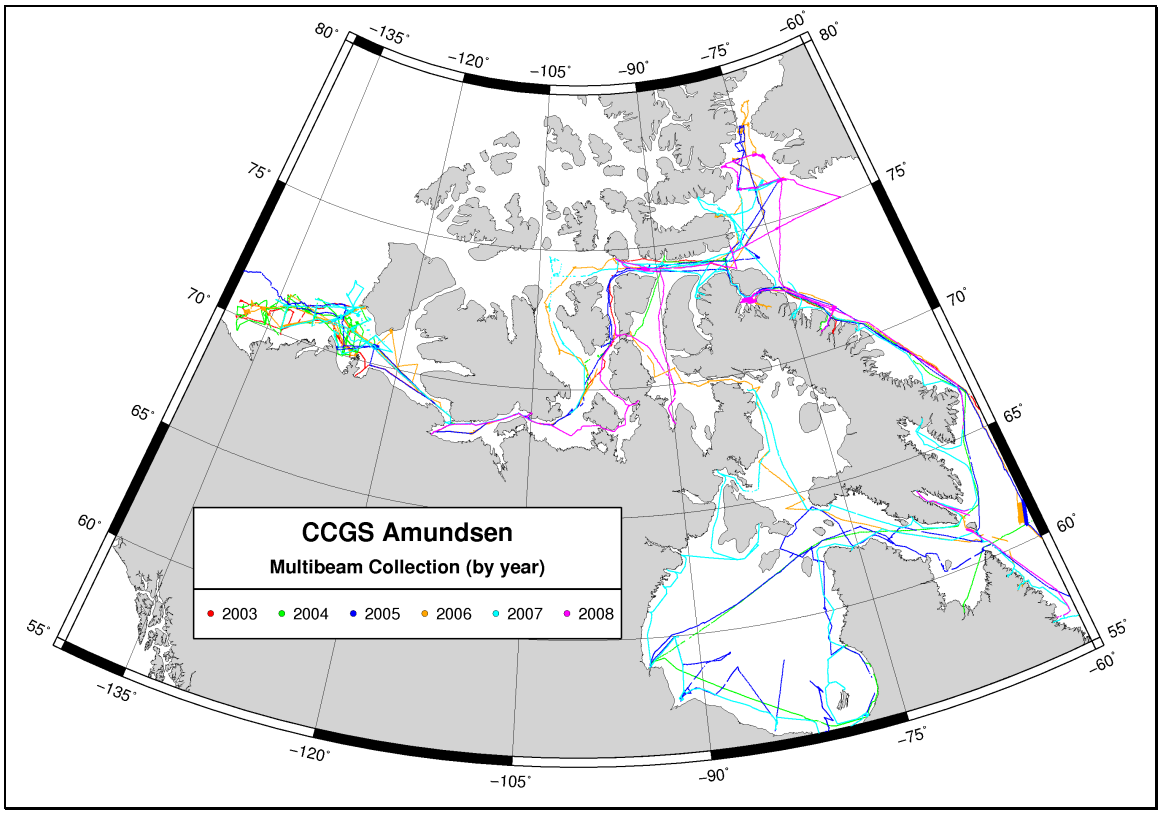

Figure 1-1. Ship track of the CCGS Amundsen, 2003-2008.

The NCE proposal uses the term "precise bathymetry", which implies that due care must be taken to ensure that all soundings are as accurate as possible. Sources of error in multibeam echosounding have been previously examined in great detail (Hare et al., 1995); for the sake of brevity, a full discussion is left to Chapter 2. Onboard the

Amundsen, uncertainties in orientation and position of the vessel are dealt with through use of precise instrumentation: an Applanix POS/MV 320 inertial measurement unit (IMU) (Applanix Corporation, 2004) for orientation, heave, heading and differentially corrected horizontal positioning (corrections provided by a CNAV GPS receiver from C&C Technologies, (C&C Technologies, 2004)). Previous work has addressed the challenges of vertical control in the CAA (Hughes Clarke et al., 2005; Beaudoin et al., 2008). Surface sound speed errors were a problem in 2003 and 2008, but have since been dealt with in post-processing (Beaudoin and Hughes Clarke, 2004).

The remaining and most worrisome source of uncertainty onboard the Amundsen is refraction due to a limited ability to sample the water column while underway. Dedicated site surveys enjoy the benefit of adequate sound speed profile sampling, however, this is not the case for soundings collected while in transit. Although the Amundsen is equipped with underway sound speed profiling instrumentation (Moving Vessel Profiler (MVP) 300 (Furlong et al., 1997)), it is not always feasible to deploy the instrument while underway due to logistical constraints imposed by ice cover. This operating procedure is not likely to change over the duration of the ArcticNet project, thus the problem will only grow if left unattended.

Given the limited ability to systematically sample the water column while underway, it is imperative to investigate the use of other sources of sound speed information instead of limiting the post-processing to the few sound speed profiles collected during transit. Since the speed of sound in water is a function of pressure, temperature and salinity, three dimensional gridded oceanographic climatologies of

average temperature and salinity values may be used to calculate an average sound speed profile. Three such climatologies are examined in this case study:

a. ¼° World Ocean Atlas 2001 (WOA01), (Boyer et al., 2005)

b. Generalized Digital Environmental Model, Variable resolution (GDEM-V 3.0), (US Naval Oceanographic Office, 2002)

c. Kliem and Greenberg climatology of the CAA (Kliem and Greenberg, 2003)

Alhough climatologies provide a potential solution, it is unclear whether or not they would be suitable for several reasons:

1. Climatologies provide spatially and temporally smoothed depictions of average conditions. Sounding accuracy may suffer when (and where) significant natural deviations from average conditions occur due to high spatio-temporal variability of the water column.
2. The climatologies are time invariant and assume no interannual variations though some studies suggest significant yearly variations in volume, freshwater and heat fluxes in some areas of the CAA (Prinsenberg and Hamilton, 2005).
3. For some times of year and/or geographic areas, the underlying source data used in the construction of the climatologies is spatially and temporally sparse, potentially leading to interpolation artifacts in the temperature and salinity grids. The three climatologies examined herein are constructed from very similar data sets and likely share biases due to sparse data.

For these reasons, the climatologies must be assessed in terms of sounding uncertainty. The first concern listed above is addressed in this work by testing climatological averages against a large data set of in-situ observations which capture a subset of the range of possible oceanographic conditions. Turning to the second and third points listed above, three climatologies are assessed in order to help distinguish between cases of interpolation error and long term temporal variability (inter-annual and decadal). By having multiple assessments, it becomes easier to determine when and where a particular climatology might suffer from interpolation error in the case where significant discrepancies arise between the performances of the three climatologies. The analysis methods described earlier provide the means to perform all of these assessments in a simple and efficient manner compared to existing techniques.

The goal of the case study is thus to assess the various climatologies in terms of sounding uncertainty and to identify the conditions under which the climatological grids of temperature and salinity might fail to provide a reasonable alternative to in-situ measurement of sound speed, i.e. when and where are the uncertainties involved with the use of a climatology unacceptable, and perhaps more importantly, why?

1.3 Contributions to the discipline

The major contribution to the discipline is a generalized method to estimate sounding uncertainty when using alternate sources of sound speed for sounding reduction. The case study uses these methods to systematically evaluate the performance of sound speed profiles derived from climatological profiles of mean temperature and

salinity. Though the case study is limited in geographic scope to the CAA, the climatologies examined herein could be used elsewhere in the world and for other MBES systems.

The analysis methods developed for this case study have been purposely generalized to allow for sophisticated analyses regarding refraction based uncertainty for MBES. Several uses are foreseen:

1. Mission Planning: The methods could be used by project managers to plan sound speed profile collection schemes for surveys based on a set of historical profiles in the area or from data gathered during a pre-analysis of a survey area. Objective decisions regarding survey design (e.g. effective angular sector, survey line spacing, water column sampling strategies) can be based on quantitative information, using only a reasonable sample of sound speed profiles and a required accuracy specification (Beaudoin et al., 2009).

2. Acquisition: The analysis techniques can be incorporated into high rate profiling systems (Beaudoin, 2008) where analysis output could inform users of the discrepancy between profiles as they are collected in real-time and help the hydrographer to optimize the profile sampling rate in order to maintain a desired sounding accuracy while minimizing the wear of supporting hardware (e.g. winches, cables, etc) and limiting the risk of grounding or fouling of the instrumentation. Field trials took place in 2008 (Beaudoin, 2009) with many of the suggested analysis methods and visualizations of uncertainty being incorporated into ODIM Brooke Ocean acquisition software (Peyton et al., 2009).

3. Improvement of uncertainty models: Existing uncertainty models (e.g. Hare, 1995) do not address the impact of spatio-temporal sound speed variability on sounding uncertainty and limit themselves to a treatment of the uncertainty in the sound speed measurement itself. The techniques developed in this work could be used to improve and/or augment the fidelity of current uncertainty models.

4. Training: Uncertainties due to refraction can be counter-intuitive and difficult to grasp for the novice hydrographer. By allowing users to experiment with alternate sound speed profiles and immediately observe the effects, the analysis tools could prove a useful training aid that helps develop a better understanding of the nature of refraction based uncertainties.

1.4 Document Organization

Chapter 2 introduces some of the required background concepts that are critical to this work, namely properties of sound in seawater and multibeam echosounding. This is followed by an overview of previous work from other researchers with a critique of their methods in terms of their applicability to this work. An overview of the physical oceanography of the CAA and a review of the climatologies examined in this work are included as appendices for reference to the reader. A context map, which labels all locations referenced in the case study, is included as a final appendix.

Fundamentals of the proposed analysis techniques are discussed in Chapter 3, followed by examination of the climatologies in Chapter 4. Conclusions and recommendations are presented in Chapter 5.

2 MULTIBEAM ECHOSOUNDING

2.1 Review of multibeam echosounding principles

MBES have been in use in the scientific community since the 1970s (Lurton, 2002), though the original patent was filed in the early 1960s (Lustig et al., 1964). A MBES differs from the traditional single beam echosounder in that it gathers multiple soundings across the ship's track simultaneously. Multiple beams are formed orthogonal to the vessel track in a fan-like configuration, allowing for a corridor to be fully sounded through the forward propagation of the vessel.

MBES typically employ separate transmit and receive arrays. The arrays are linear and highly directive to give narrow mainlobe beamwidths. The transmitter is usually aligned in the fore-aft direction such that its projected footprint on the seafloor is a long strip orthogonal to the vessel track. The receive array is oriented at 90° to the transmitter (i.e. athwart ship) such that the main lobe of the receive sensitivity pattern intersects the corridor insonified by the transmitter, producing a small footprint. Multiple receive beams are formed simultaneously in multiple directions, allowing the system to isolate sounding footprints across the transmit footprint (Lurton, 2002).

Whereas MBES transmitter arrays are typically flat line arrays, there are three common configurations used in practice for receiver arrays: (1) flat linear array, (2) twin linear arrays aligned in a v-configuration, and (3) arcuate arrays. Each configuration has benefits and drawbacks; these are summarized in the table below (Lurton, 2002).

Table 2-1. Receiver array configurations.

Array Configuration	Benefit	Drawback
Single line array	Easily manufactured to high precision; simple installation (flush mounting)	Beam forming/steering is complex; Requires surface sound speed measurement for electronic beam steering; beam widths grow with steering angle
Twin line array, v-configuration	Less sensitive to surface sound speed error compared to a single line array; can achieve larger angular sector than a single receive array; growth of beam width with steering angle is not as drastic as with single line array	Requires surface sound speed measurement for electronic beam steering; beam widths grow with steering angle; difficult to perform installation calibration (patch test)
Arc array	Does not requires surface sound speed measurement as no (or very little) beam steering is required; beam widths are independent of steering angle; beam forming is very simple	Requires precise machining of array; installation may be more difficult; requires longer array (must cover an angle at least as large as the angular sector)

The characteristic most relevant to this work is the sensitivity to surface sound speed uncertainty, this is discussed in the next section.

2.2 Refraction of sound through water

Knowledge of the speed of sound in water is fundamental to echosounding and it must be measured whenever the propagation characteristics of the water column change significantly, especially with MBES. The variation in sound speed not only changes the scaling of time measurements into range measurements, but it also causes refraction of

the acoustic ray path. The refracted ray path can be estimated by measuring the vertical variation in sound speed and modeling the ocean as a series of horizontal layers of either constant sound speed or constant gradient in sound speed. Snell's Law allows for an estimation of the ray path through each layer (Medwin and Clay, 1997):

$$\frac{\sin\theta_0}{c_0} = \frac{\sin\theta_1}{c_1} = \frac{\sin\theta_z}{c_z} = k \tag{2.1}$$

Given an initial launch angle, two-way travel time and a sound speed profile, one can arrive at an estimation of an acoustic ray's horizontal and vertical distance traveled by tracing the path of the ray through the water column and using Snell's law at each new layer to determine the refracted angle, as depicted in Figure 3-1.

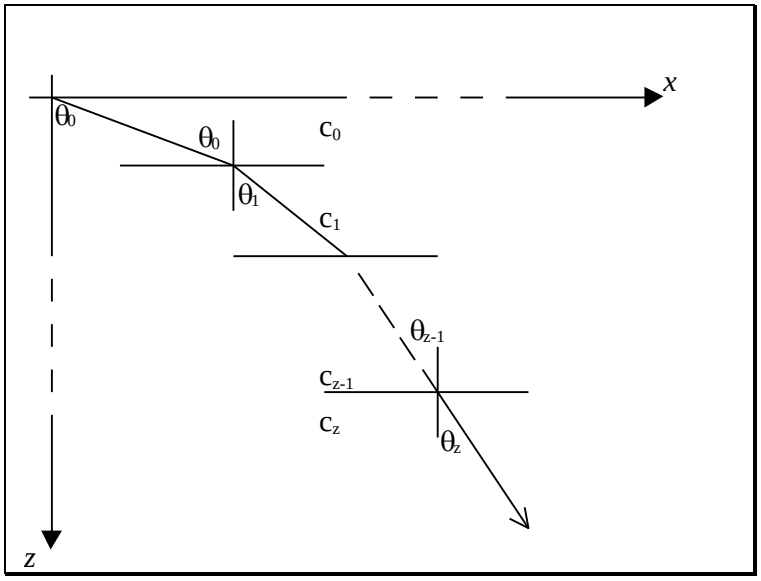

Figure 2-1. Ray tracing geometry, after (Medwin and Clay, 1997), p. 85.

2.2.1 Constant velocity model

Given an initial incidence angle, θ_0, and sound speed, c_0, at the initial depth, the ray parameter is computed as:

$$k = \frac{\sin\theta_0}{c_0} \tag{2.2}$$

The ray parameter allows for the calculation of the sine of the incidence angle at any layer in the sound speed profile:

$$\sin\theta_n = kc_n \tag{2.3}$$

The cosine and tangent of the same angle can be computed as well, these quantities being useful in the calculation of radial distance and travel time:

$$\cos\theta_n = \sqrt{1-(kc_n)^2} \tag{2.4}$$

$$\tan\theta_n = \frac{kc_n}{\sqrt{1-(kc_n)^2}} \tag{2.5}$$

The horizontal distance traveled by the ray and the accrued travel time is computed through the following summations (Medwin and Clay, 1997):

$$x_N = \sum_{n=0}^{N-1}(z_{n+1}-z_n)\tan\theta_n \tag{2.6}$$

$$t_N = \sum_{n=0}^{N-1}\frac{z_{n+1}-z_n}{c_n\cos\theta_n} \tag{2.7}$$

In practice, the distance and time sums are computed until the summation of travel times exceeds the one-way travel-time. Since it is unlikely that the one-way travel-time is exhausted exactly at a layer boundary, a linear interpolation must be performed in the last layer in order to remove the amount of overshoot in both depth and horizontal distance. It should also be noted that the constant velocity model requires that interfaces between layers occurs at the midpoint depth between measurements and not at the depth associated with each sound speed sample in the profile, i.e. each measurement is taken to represent speed of sound of a layer that extends half way to the depth of the previous

measurement and half way to the depth of the next measurement. Thus for n measurements of sound speed, n layers are created in which the speed of sound is constant for each layer.

2.2.2 Constant gradient model

A constant gradient model can be used in lieu of the constant speed method. In this case, the sound speed is assumed to vary linearly between samples, thus the gradient in sound speed is constant in the layer:

$$g_n = \frac{c_n - c_{n-1}}{z_n - z_{n-1}} \tag{2.8}$$

In a constant gradient medium, rays refract along circular paths with the radius of curvature being inversely proportional to the sound speed gradient (Lurton, 2002):

$$R_{cn} = \frac{c_{n-1}}{g_n \cos\beta_{n-1}} \tag{2.9}$$

where R is the radius of curvature, c is the sound speed, and β is the entry angle of the ray relative to the horizontal. The depth, radial distance traveled and travel time consumed within a layer are given by (Lurton, 2002):

$$r - r_{n-1} = R_{cn}(\sin\beta - \sin\beta_{n-1}) \tag{2.10}$$

$$z - z_{n-1} = R_{cn}(\cos\beta - \cos\beta_{n-1}) \tag{2.11}$$

$$t_n = \left| \frac{1}{g_n} \ln\left(\frac{c_{n-1}}{c} \left| \frac{1+\cos\beta_{n-1}}{1+\cos\beta} \right| \right) \right| \tag{2.12}$$

The angle β is a depression angle is related to the incidence angle θ by:

$$\beta = \frac{\pi}{2} - \theta \tag{2.13}$$

Snell's Law is used to compute the deviation between entry and exit angles for a given layer of constant gradient sound speed:

$$\frac{\cos \beta_n}{c_n} = \frac{\cos \beta_{n-1}}{c_{n-1}} = k \tag{2.14}$$

As with the case of the constant velocity model, the equations are applied layer by layer until the travel time is exhausted. In the final layer, an iterative procedure is followed to determine the endpoint of the ray trace. The constant gradient model provides a more accurate depiction of reality though the constant velocity model outlined earlier provides sufficient accuracy when ranges are less than a few hundred meters (Medwin and Clay, 1997).

2.2.3 Sensitivity of sound speed to temperature and salinity uncertainty

Understanding the relationship between sound speed, temperature and salinity is essential to being able to assess what constitutes a significant change in temperature and salinity in terms of their effect on sound speed. It is thus useful to examine sound speed equations to understand how numerically sensitive sound speed is to changes in the controlling parameters. The UNESCO equation (NPL, 2000), which is generally favoured for the calculation of sound speed, is quite complex with many coefficients, therefore the Mackenzie equation is used for this purpose:

$$\begin{aligned} c = F(d,s,t) = {} & 1448.96 + 4.591t - 5.304 \cdot 10^{-2} t^2 + 2.374 \cdot 10^{-4} t^3 + 1.340(s-35) \\ & + 1.630 \cdot 10^{-2} d + 1.675 \cdot 10^{-7} d^2 - 1.025 \cdot 10^{-2} t(s-35) - 7.139 \cdot 10^{-13} t d^3 \end{aligned} \tag{2.15}$$

Where

c = sound speed in meters per second

t = temperature in degrees Celsius

s = salinity in parts per thousand

d = depth in meters

Note that the depth dependency in the above equation accounts for the influence of pressure on the speed of sound (the UNESCO equation is a function of temperature, salinity and pressure). Standard uncertainty propagation techniques can be used to investigate the propagation of uncertainties in temperature, salinity and depth to uncertainty in sound speed through the following (ISO, 1995):

$$\sigma_c^2 = \left(\frac{\partial F}{\partial d}\right)^2 \cdot \sigma_d^2 + \left(\frac{\partial F}{\partial s}\right)^2 \cdot \sigma_s^2 + \left(\frac{\partial F}{\partial t}\right)^2 \cdot \sigma_t^2 \tag{2.16}$$

Evaluating partial derivatives of the model equation yields:

$$\frac{\partial F}{\partial d} = 1.630 \cdot 10^{-2} + 3.35 \cdot 10^{-7} d - 2.147 \cdot 10^{-12} t d^2 \tag{2.17}$$

$$\frac{\partial F}{\partial s} = 1.340 - 1.025 \cdot 10^{-2} t \tag{2.18}$$

$$\frac{\partial F}{\partial t} = 4.591 - 1.608 \cdot 10^{-1} t + 7.122 \cdot 10^{-4} t^2 - 1.025 \cdot 10^{-2} (s - 35) - 7.139 \cdot 10^{-13} d^3 \tag{2.19}$$

The above equations simplify dramatically if temperature is assumed to be zero, which very closely approximates reality in the case of the Arctic Ocean:

$$\frac{\partial F}{\partial d} \approx 1.630 \cdot 10^{-2} + 3.35 \cdot 10^{-7} d \tag{2.20}$$

$$\frac{\partial F}{\partial s} \approx 1.340 \tag{2.21}$$

$$\frac{\partial F}{\partial t} \approx 4.591 - 1.025 \cdot 10^{-2}(s-35) - 7.139 \cdot 10^{-13} d^3 \tag{2.22}$$

The equations can be further simplified by removing the depth dependant terms as they are negligible over the range of depths in the Arctic Ocean (contributing values in the third decimal place at most). A final simplification would be to assume an average salinity of 33 ppt throughout the water column based on T-S diagrams in Tomczak and Godfrey (2002):

$$\frac{\partial F}{\partial d} \approx 1.630 \cdot 10^{-2} \tag{2.23}$$

$$\frac{\partial F}{\partial s} \approx 1.340 \tag{2.24}$$

$$\frac{\partial F}{\partial t} \approx 4.796 \tag{2.25}$$

Thus the final expression for the variance in sound speed is approximately:

$$\sigma_c^2 = \left(1.630 \cdot 10^{-2}\right)^2 \cdot \sigma_d^2 + \left(1.340\right)^2 \cdot \sigma_s^2 + \left(4.796\right)^2 \cdot \sigma_t^2 \tag{2.26}$$

Examining the values in solitude yields approximate rates of change of sound speed with changes in input values, for example, a change of 1°C gives 4.8 m/s change in sound speed. Similarly, changing salinity by 1 ppt offsets the resulting sound speed by 1.3 m/s. Depth has a smaller effect with only 0.016 m/s for every meter of change in depth. It is clear that changes in temperature are the predominant factor influencing changes in sound speed, and salinity variations are nearly negligible in the open ocean throughout most of the world. Indeed, this is the fundamental assumption made by those that use expendable bathythermographs as these instruments only measure the temperature. Salinity variations are non-negligible in the CAA due to the presence of ice, thus the use of

temperature profiling instruments provides an incomplete depiction of the sound speed structure in the water column.

2.3 Uncertainty propagation and sounding accuracy

Sounding reduction involves computing a geographically referenced depth measurement from several measurements made by the MBES and other supporting systems (e.g. sound speed probes, position and orientation sensors, etc.) (Beaudoin et al., 2004). Every measurement that is made in support of a multibeam sounding is subject to uncertainty. Standard uncertainty propagation techniques allow for the estimate of the total propagated uncertainty (TPU) in the final sounding solution, based on the uncertainties of the associated measurements. This type of analysis allows for the assignment of a TPU value to a sounding, which can be useful in semi-automated data validation methods such as the Combined Uncertainty Bathymetry Estimator (CUBE) algorithm (Calder, 2003).

Numerous studies have been conducted with the aim of characterizing and quantifying sources of uncertainties in multibeam echosounders. An early paper investigated a random uncertainty model for Bathymetric Swath Survey System (BS^3), a 21-beam system with a 55° angular sector (Angelari, 1978). The dominant sources of uncertainty at the time, as identified by the author, were roll, sound speed, bottom detection and random noise. Specifically, the accuracy of the vessel's roll sensor was estimated at 1°, the sound speed measurement uncertainty was estimated at 1-2%. The limitations of amplitude bottom detections at larger incidence angles was a source of

positive bias in range estimates away from nadir with random noise providing an occasional negative bias in the form of false detections prior to the return of the pulse. Given such large sources of uncertainty in the supporting measurements, the accuracy achievable with the entire mapping system was reckoned at several percentages of water depth, far greater than is presently acceptable in current hydrographic practices. It should be noted that no mention of ray bending is made in the paper.

Sensor accuracies have improved since then and recent uncertainty analyses now address sources of uncertainty that were previously considered negligible in light of the dominating effects of roll, sound speed and bottom detection. Hare et al (1995) provide a thorough review of general sources of uncertainty, specifically focusing on the instrumentation suite of Canadian Hydrographic Service survey vessels though their treatment is general enough in nature to be applied (with care) to any multibeam echosounder. The next section discusses the influences of sound speed uncertainties on sounding accuracy, of which some of the material is drawn from Hare et al (1995) and Hare (2001) with occasional references to the source papers referenced by Hare.

2.4 Influences of sound speed error in multibeam echosounding

There are two reasons why the sound speed used in sounding reduction may be in error: (1) the sensor may have systematic or random error, (2) a sampling error may occur where the water mass is undersampled, either spatially or temporally in which case the profile used for ray tracing is not representative of actual conditions at the time of the

sounding. The case of a sensor bias is to introduce a bias in range and angle for a ray path through a layer (Hare, 2001):

$$\Delta r = \frac{r\Delta c}{c} \tag{2.27}$$

where r is the range in meters, c is the sound speed in meters/second. Angular uncertainty is calculated as (Hare, 2001):

$$\Delta\theta = \frac{\tan(\theta - \beta - R)\Delta c}{c} \tag{2.28}$$

where θ is the beam pointing angle relative to the vertical, β is the installation roll angle of the transducer assembly and R is the vessel roll. These effects would be cumulative while ray tracing through the water column and the same behaviour would be observed whether direct or indirect measurements of sound speed are made, i.e. a biased temperature or salinity measurement would lead to biased sound speed estimation.

Examining the case of sampling error, sound speed uncertainty has different effects depending on where it occurs in the water column, either at the transducer depth or elsewhere in the water column. Further complicating this, the net effect of surface sound speed uncertainty is heavily dependant on transducer array geometry and can occasionally cancel out in certain cases. These distinct cases are examined in the next few sections.

2.4.1 Errors in sound speed profiles

The effects of uncertainties in sound speed measurements have been examined within a single layer and throughout the water column (Ambrose and Geneva, 1995).

Uncertainties occurring within a single layer introduce a deviation in the incidence angle and a modified transit time through the layer. Upon entry to the next layer (with a correct sound speed), the preservation of Snell's constant will ensure that the ray path returns to the correct incident angle. Thus the uncertainty incurred from the incorrect layer is a slight horizontal shift of the pierce point into the layer of correct sound speed. The travel-time uncertainty results in an overshoot (or undershoot) in the last layer of travel, resulting in a depth uncertainty. They also note that the effect of sound speed error in a single layer grows with (1) incidence angle, and (2) thickness of the layer with incorrect sound speed. In the case of errors throughout the water column, the cumulative effect of the errors tends to cancel out as long as the errors are equally distributed about the true mean value of the sound speed (Ambrose and Geneva, 1995; Hare, 2001).

If sound speed uncertainties are consistently biased from layer to layer, the result is a "frown" or "smile" shaped seafloor profile in which the outermost soundings exhibit the largest amount of depth and horizontal uncertainty (in wide angular sector systems) and the nadir soundings exhibit only a depth uncertainty, typically much smaller than that associated with the outermost beam. At a beam angle of ~45°, the depth uncertainty experiences a minima but only in the case where the surface sound speed error between the incorrect and the true sound speed profile is small or zero. This has been used by other authors to develop methods of correcting for refraction effects through the addition of a forward looking sounder to the suite of instruments onboard a MBES mapping platform (Cousins and Miller, 2000; Cousins and Miller, 2002).

If sound speed changes occur throughout the water column while the surface sound speed remains correct, it has been shown that the depth and horizontal

uncertainties are directly proportional to the relative area difference between the correct and incorrect sound speed profiles (Geng and Zielinski, 1998; Geng and Zielinski, 1999).

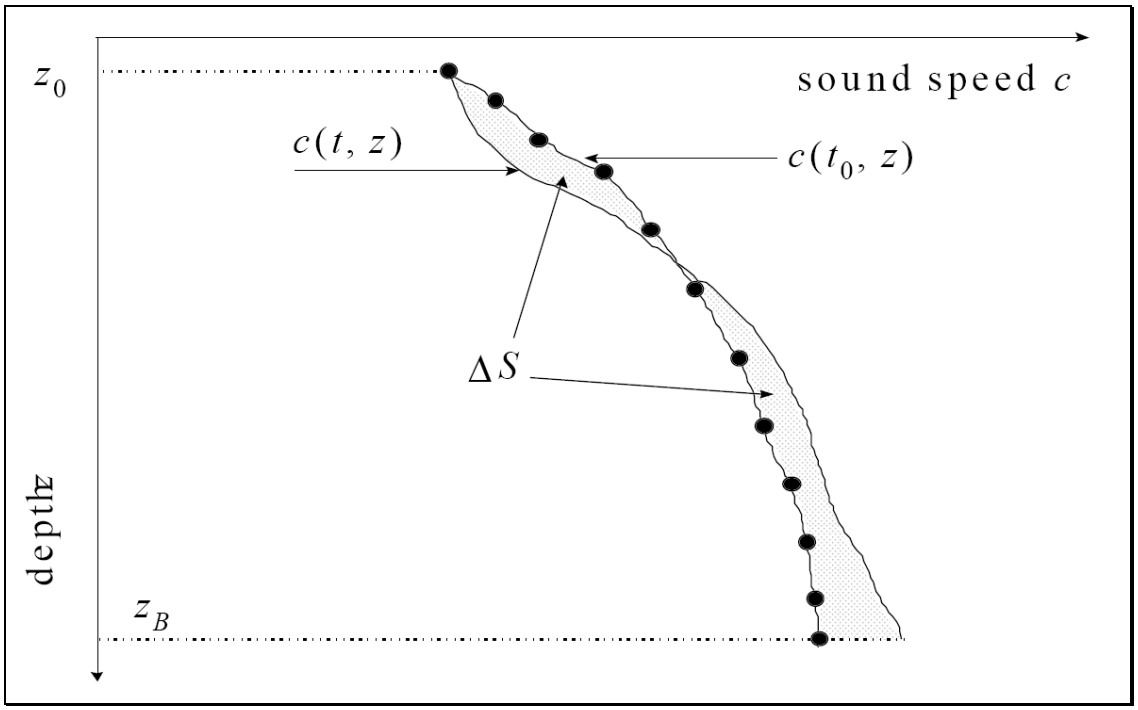

Figure 2-2. Area difference between two sound speed profiles. After (Geng and Zielinski, 1998), p. 3.

The area difference between two profiles is given by:

$$\Delta S = \int dS = \int_{z_0}^{z_B} [c(t_0, z) - c(t, z)] dz \tag{2.29}$$

where z_0 and z_B are the depths corresponding to the transducer draft and bottom, respectively. It should be noted that the area calculation preserves the sign such that the integral may very well result in an area difference of zero. The relative area difference is computed as:

$$\varepsilon_s = \frac{\Delta S}{\int_{z_0}^{z_B} c(t_0, z) dz} = \frac{\Delta S}{S} \tag{2.30}$$

This idea provides, perhaps, the most intuitive explanation of how sound speed profile uncertainties affect sounding uncertainty: large discrepancies between profiles result in large area differences, which result in large uncertainties. If the area difference is near zero (as is nearly the case for depth Z_B in Figure 2-2), then little uncertainty results since the second profile, on average, is very close to the first profile.

2.4.2 Uncertainties in surface sound speed

An uncertainty in the surface sound speed measurement not only leads to a bias in angle estimation in the surface layer, but it also contaminates the remainder of the ray tracing procedure if the surface sound speed measurement is used for the estimation of Snell's constant. The resulting sounding uncertainty will grow with depth during the ray trace since Snell's constant will be incorrect in each layer and will force the ray to diverge from the true ray path (Ambrose and Geneva, 1995). As will be shown, this has different effects depending on the transducer array geometry and installation on the vessel.

2.4.2.1 Arcuate arrays

Arc arrays typically do not require measurement of sound speed at the array face as each subset of the arc is oriented in the desired direction, though some arc arrays perform small amounts of steering beyond the physical limits of the array in order to acquire soundings across a wider sector than physically permitted by the designed sector of the arc, e.g. EM1002 (Kongsberg, 2001). If conditions change after the collection of a

sound speed profile such that the surface speed in the profile no longer depicts actual conditions, an uncertainty is introduced into the ray tracing process through an incorrect estimation of Snell's constant. As Snell's constant is no longer correct, the ray takes a divergent path relative to the true ray path even though most of the sound speed profile may still be correct. In this case, the resulting uncertainty in depth and radial distance grows with depth (refer to Figure 2-3).

2.4.2.2 Linear arrays

Measurement of sound speed at the transducer face is recommended for arrays that perform electronic beam steering as these arrays require knowledge of the signal wavelength at the array face to estimate the correct signal shifts to apply to achieve the desired steering angle. For a level, two element array, the phase shift required for beam formation is (Dinn et al., 1995):

$$\phi = \frac{2\pi f d}{c} \sin \alpha \tag{2.31}$$

where f is the frequency of the system in Hertz, d is the inter-element spacing in meters, c is the sound speed in m/s and α is the desired steering angle.

The surface sound speed can be extracted from a sound speed profile or measured continuously by a velocimeter or temperature probe placed near the transducer face (or in a sea chest supplied with a constant flow of surface water). Faced with an outdated sound speed profile (and using the profile as a source of surface sound speed), a levelly installed line array does not experience the same growth of uncertainty with depth as is seen with an arc array. Use of the incorrect surface sound speed from the outdated sound

speed profile and the desired steering angle gives an incorrect phase shift for the second element in the array:

$$\phi_i = \frac{2\pi f d}{c_a} \sin \alpha_d \tag{2.32}$$

The incorrect phase shift ϕ_i and the correct (but unknown) sound speed c_c, are related to the steering angle that is actually achieved α_a (which differs from the desired angle, α_d) by

$$\phi_i = \frac{2\pi f d}{c_c} \sin \alpha_a \tag{2.33}$$

The two equations are combined and reduced:

$$\frac{2\pi f d}{c_a} \sin \alpha_d = \frac{2\pi f d}{c_c} \sin \alpha_a \tag{2.34}$$

$$\frac{\sin \alpha_d}{c_a} = \frac{\sin \alpha_a}{c_c} \tag{2.35}$$

This demonstrates that the same ray parameter would be calculated in either case, i.e. using the desired steering angle and the assumed sound speed would give the same ray parameter as using the achieved steering angle and correct sound speed. As the ray parameter is correct, the computed ray path would be similar to the actual ray path for portions of the water column which match the observed sound speed profile. Uncertainties would, of course, be introduced in portions of the water column where there is a mismatch, e.g. at the surface (Dinn et al., 1995). This same logic applies in the scenario where the surface sound speed is measured accurately (and is used for the ray parameter calculation) and the surface portion of the sound speed profile used for ray bending is incorrect. Since Snell's constant is correct, the ray path diverges from reality

only in layers where a discrepancy exists. In layers where the sound speed profile matches actual conditions, the calculated ray path is parallel to the actual ray path, but offset horizontally, as shown in Figure 2-3. This has important ramifications for the use of climatologically derived sound speed profiles, as will be shown later in this work.

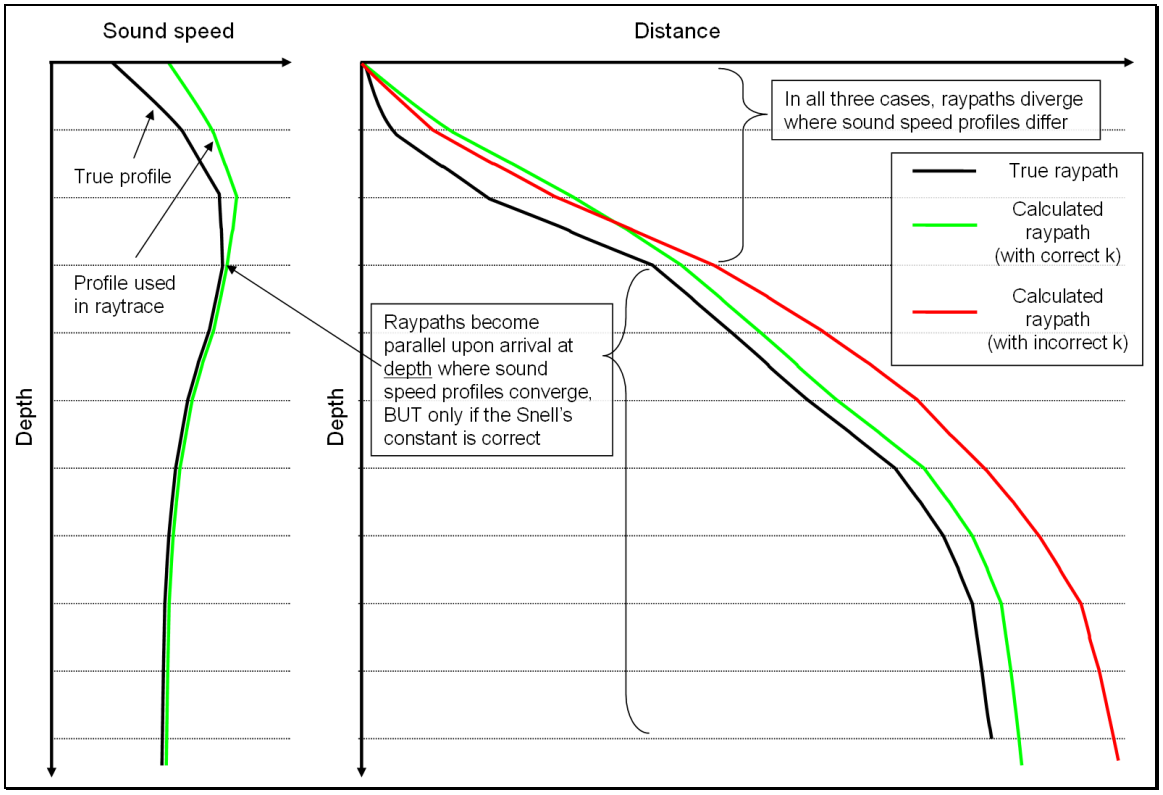

Figure 2-3. Effect of Snell's constant on ray trace recovery. The ray path with the correct ray parameter (due to measurement of surface sound speed) is shown in green whereas the red ray path shows the effect of an incorrect ray parameter. Linear arrays typically require the measurement of surface sound speed and arcuate arrays do not. Thus, the effect of surface variability on the speed of sound has a dampened effect with linear arrays but not with arcuate arrays.

Depth uncertainties due to imperfect knowledge of surface sound speed grow proportionally to steering angle (though non-linearly), thus the largest uncertainty is encountered in the most steered beams of a steered linear array whereas the accuracy of

beams close to the array bore site suffers little. The Amundsen's EM300 is installed nearly level. As such, the major issues occur at angles away from nadir.

2.4.2.3 Tilted linear arrays

The derivation above assumed of course that the transducer mounting angle and vessel roll were zero, i.e. the beam steering angle is equivalent to the incidence angle used in the initial layer of the ray trace. In the event that either of these assumptions is false, the ray parameter is no longer preserved; this results in non-linear tilting of the swath that grows with the amount of angular departure from the level and with steering angle (Dinn et al., 1995; Hughes Clarke, 2003).

As the magnitude of the depth uncertainty grows with departure from level conditions, larger uncertainties occur with (1) large roll events, and (2) large installation angles. Uncertainties due to imperfect surface sound speed are most easily observed during large vessel roll events since they introduce a variable non-linear tilting of the swath that correlates with receiver roll (Hughes Clarke, 2003). When a vessel experiences large roll events, artifacts due to surface sound speed uncertainties will manifest themselves as a downward curl in the outer beams of one side of the swath and an opposite effect (upward curl) on the side of the swath that only appears with roll events. The special case of a permanently tilted array can be thought of as a permanent roll event; thus the entire swath would take on a permanent non-linear tilt, this would additionally be modulated by the vessel roll (Hughes Clarke, 2003). The Amundsen's EM300 installation produces a signature artifact in the face of surface sound speed uncertainties since the receiver array is mounted approximately 6° from level. In order to

maintain a symmetric receiver sector, for example +/-60°, the transceiver must steer the outer beams on the starboard side 66° whereas the port beams need only be steered to 54°. As such, uncertainties in surface sound speed generate a distinctive non-linear tilt to the swaths where the starboard outer beams suffer larger depth uncertainty than the port outer beams due to the larger amounts of electronic steering applied (Beaudoin et al., 2004).

It should be noted that the above type of uncertainty occurs only in the case where the surface sound speed used for the calculation of the ray parameter is incorrect, i.e. the second scenario depicted in the section above does not suffer these types of artifacts as the surface sound speed and steering angle are both correct. This is true for both flat, tilted and arcuate arrays.

2.5 Use of oceanographic databases in MBES processing

Climatologies are typically not used by agencies responsible for nautical charting, such as the United States National Oceanic and Atmospheric Administration (NOAA) or the Canadian Hydrographic Service (CHS). Such agencies are dedicated to the task of performing high precision surveys; as such they tend to perform small regional surveys with adequate time and resources dedicated to the collection of sufficient sound speed profiles to meet the required accuracy of the survey. In the case of a multidisciplinary scientific mission (or while in transit), mapping accuracy requirements are potentially not as stringent and historical databases of profiles (or grids of temperature and salinity resampled from such profiles) may suffice for providing information about the water

column. MB System is an example of MBES processing software that uses ocean climatologies for sound speed profile estimation (Caress and Chayes, 2005). MB System uses the 1982 Climatological Atlas of the World Ocean (Levitus, 1982) to produce sound speed profiles for a desired location, with a profile generated on the basis of the yearly mean in a user specified 1º by 1º cell. According to documentation, there is no allowance for quality control, thus the onus lies on the user to evaluate the applicability of the profile(s) provided by the Levitus database. Cruise reports from the R/V Maurice Ewing suggest frequent use of the Levitus lookup abilities of MB Systems software (e.g. McNutt and Caress (1996). The French Research Institute for Exploitation of the Sea (IFREMER) have the capability to extract sound speed profiles from the Levitus oceanographic database, though it is unclear whether any validation is undertaken (Bourillet et al., 1996).

Another typical use of oceanographic databases (be they sets of historic profiles or gridded climatologies) is for sound speed profile extension. In this situation, observed sound speed profiles are not deep enough to ensure coverage of the range of depths encountered during a survey or transit and the profile must be extended beyond the maximum sampling depth. Simrad real-time acquisition and processing systems automatically extend all input profiles to a depth of 12,000 m through a default profile or through user-provided profile that is hopefully representative of the conditions in the work area. The user profiles are extended using the gradient between the last valid values until a depth of 500 m is reach, at which point the system profile is used (Pedersen, pers. comm.). Personal communications with two CHS employees indicate that the CHS practice is to collect a profile in the deepest part of the survey area, thus minimizing the

amount of profile extension required by the logging and processing software (Bartlett, pers. comm.; Cartwright, pers. comm.). The U.S. Office of Coast Survey (part of NOAA), uses an internal software program to extend observed profiles to the required depths based on user input, historical profiles or the "most probable slope" (NOAA Office of Coast Survey, 2001). The latter method extrapolates the sound speed profile by first calculating the gradient between the deepest sound speed measurement in the file and all other measurements (yielding a set of *n-1* gradients for *n* sound speed measurements in the cast). The mode of the set of *n-1* gradients is then used to extrapolate the sound speed profile beyond the deepest observation (Huff, pers. comm.).

From the post-processing point of view, the ray tracing algorithm used by MB Systems extends all profiles based on the last value in the sound speed profile, essentially holding the last observed sound speed to a depth of 12,000 metres (Caress and Chayes, 2005). Again, the onus lies with the user to ensure that this model of profile extension is reasonably correct. Theoretically, the user could use the MB System Levitus lookup functions (which extends profiles to a depth of 12,000 metres based on the deepest values available in the Levitus database). The user could then use the Levitus profile to extend an observed profile to a required depth, though it is unclear whether this option is implemented in software at all or if the user must perform the extension manually.

2.6 Existing methods for analyzing refraction based uncertainty

Though the instruments and algorithms to measure sound speed and correct for ray bending effects have been in use for quite some time, there is no universally agreed

upon method to assess sounding uncertainties due to sound speed variability. How then, can the various climatologies be tested against a control dataset? One option would be to simply compare an observed CTD profile to a profile derived from a climatology and use the RMS of the discrepancies between the two casts as a first step towards objectively quantifying the impact on sounding accuracy. This approach, however, would not lead directly to an estimate of the effect of sound speed profile uncertainties on the accuracy of soundings as discrepancies in sound speed profiles have cumulative and non-intuitive effects on depth and positioning error (Dinn et al., 1995).

Work done in the late 1990s demonstrated that the sounding discrepancy observed when ray tracing with two different sound speed profiles is almost entirely proportional to the area between the sound speed profiles as long as the surface sound speed is common between the two profiles (Geng and Zielinski, 1998; Geng and Zielinski, 1999). This base principal is applied by the authors to provide equivalent yet simplified sound speed profiles which have the potential to dramatically speed up ray tracing algorithms through a reduction of the number of layers in the acoustic model of the ocean. The notion that uncertainty is proportional to the area between the sound speed profiles could be used in this work. However, it is not general enough for cases where sound speed profiles exhibit large discrepancies at the surface.

Other researchers have successfully validated oceanographic models and databases for MBES sound speed correction in an experiment off the island of Kauai, in the Pacific Ocean (Calder et al., 2004). Summarizing their work, a series of local oceanographic models were used to provide salinity and temperature profiles for survey work in water depths ranging from 30 to 900 metres. The survey work was performed

with two multibeam systems: (1) a Kongsberg Simrad EM120, and (2) a Reson SeaBat 8111-ER. CTD and Expendable Bathy Thermograph (XBT) casts were collected in real-time and served as "truth" against which the model output would be tested. Digital terrain models (DTM) were produced from the actual and modeled sound speed profiles, with the two DTMs agreeing within +/- 0.5% of water depth in most cases.

Their work differs in several aspects from the research problem presented herein. Firstly, in terms of sheer scale, Calder's work area was only 100 square kilometers, whereas the entire CAA must be dealt with in this work (which spans approximately 1,500 kilometers in the east-west direction and 750 kilometers in the north-south direction). Secondly, the oceanography is vastly different in their region, with temperature variations throughout the water column being the dominant source of sound speed change (horizontal gradients of salinity and temperature are small (Lewis et al., 2001)). The sound speed structure in the CAA is heavily influenced by the presence of pack ice, which modulates sound speed through changes in salinity (albeit to a lesser degree than temperature); this effect typically has strong vertical and horizontal gradients associated with it. Finally, another major difference is the complexity and sophistication of the oceanographic models available for the area. For example, the oceanographic models used by Calder incorporate surface and internal waves and have much higher spatio-temporal resolution than anything that would be available in the CAA (Lewis, 1997; Lewis et al., 2001).

As is common when performing error analyses with MBES, Calder's evaluation was based on differencing of DTMs derived from the different processing schemes. In Calder's case, two DTMs were generated, the first using sounding data ray traced with

the CTD and expendable bathy thermograph (XBT) profiles collected during the survey, the second using sounding data ray traced with sound speed profiles generated from the oceanographic models. With the first DTM serving as a reference surface, the discrepancy between the two DTMs served as an indicator of the validity of using the oceanographic model for ray tracing purposes.

Calder's approach cannot be followed directly in the CAA due to insufficient CTD control data. The Kauai experiment saw the collection of sufficient CTD/XBT casts to adequately model the oceanographic environment for the entire work area (profiles were spaced, at most, a few kilometers apart). As such, the DTM generated using sounder data ray traced with the observed profiles can be confidently used as a control surface against which alternative processing schemes may be tested. This is not possible in the case of the ArcticNet EM300 dataset since the motivation for this research is that there are insufficient profiles to post-process the soundings. If the area of operations was significantly smaller, it may be plausible to design a similar experiment; however, this is not realistic given the size of the ArcticNet research domain and the limited amount of resources (ship-time) that could be dedicated to such an onerous task.

Another approach that is occasionally taken when evaluating different post-processing schemes is to avoid gridding altogether and simply monitor the difference in sounding depth and position after the application of different processing methods, e.g. (Hughes Clarke et al., 2000)). The main advantage of this technique over DTM differencing is that it preserves the relationship between beam angle and error. This allows for straightforward monitoring of error behaviour as a function of depression angle, this being important in the investigation of uncertainties related to sound speed

post-processing schemes. Another advantage is that it is insensitive to survey line spacing, i.e. a DTM produced with very close survey line spacing might lead one to falsely conclude that sound speed effects are negligible. Though this method is applicable to the ArcticNet dataset, it is still awkward as it would involve a large overhead in terms of data management. For example, the closest survey line (in time and space) would need to be located for each CTD station. This is not always possible in conditions of heavy ice-cover: some CTD stations have no corresponding sounding data at all. In other cases, the CTDs are collected several hours (or even days) before or after any multibeam sounding data are acquired.

The techniques used by Calder and Hughes Clarke have several drawbacks. Firstly, they require the use of sounding data; thus one must sample the seafloor in order to learn about the sea. Secondly, as the methods require soundings, the findings from such analyses are only applicable to the sounding geometry with which the seafloor was mapped and it is difficult to extrapolate from the findings to ascertain how other sounding geometries might react to the same oceanographic conditions. For example, one cannot make any quantitative statements about how findings might vary with different angular sectors, drafts, use of a sound speed probe or survey line spacing. Thirdly, post-processing of sounding data is required, which can involve significant operator interaction and time, thus these techniques are not well suited to timely evaluations of water mass variability.

In this work, a numerical simulation method is proposed which can be used to assess the impact of water column variability on sounding uncertainty without any requirement for soundings, i.e. sound speed casts are the sole required input. Previous

researchers have used simulation to address refraction based uncertainty (Imahori and Hiebert, 2008). Their approach is not suited to this work for several reasons:

1. The underlying assumption that surface variability is correlated with variability at depth is only true in a very limited set of oceanographic conditions.
2. The method does not address the difference in ray tracing behaviour in the presence of aiding surface sound speed measurements. In this work it is necessary to model the unique ray tracing behaviour of MBES systems where *"transducer depth sound speed is used as the initial entry in the sound speed profile used in the ray tracing calculations"* (Kongsberg, 2006).
3. The method is limited to the maximum sampling depth of the casts even though sounding uncertainty due to refraction can vary dramatically throughout the water column. The analyses in this work would thus be limited to the range of depths where sound speed profiles are collected, but would give no indication of how observed variability might affect shallower regions (assuming, of course, that similar variability regimes would exist in these regions).

3 METHODOLOGY

3.1 Fundamentals

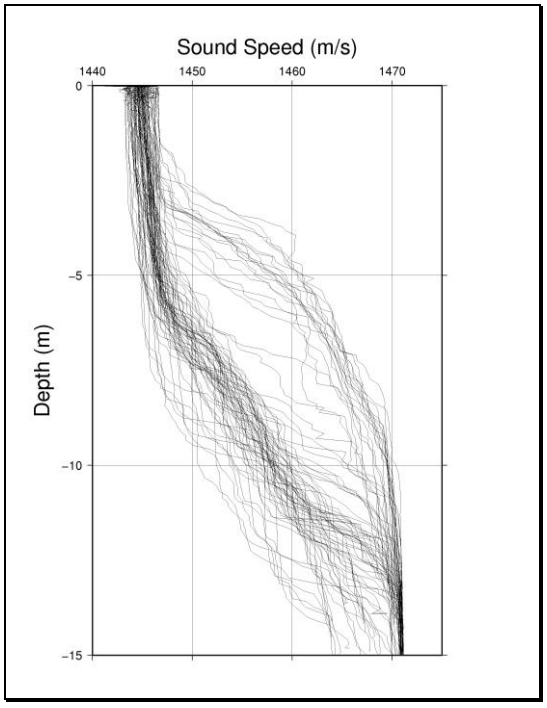

Figure 3-1. Sound speed profiles collected over a 2.5 hour interval in the Rotterdam Waterway (Netherlands) with a Moving Vessel Profiler (MVP) (Beaudoin et al., 2009).

The ray trace simulator is based upon monitoring the progression of two or more acoustic ray paths, all sharing a common initial depression angle and each ray path being associated with a particular sound speed profile in a set of sound speed profiles, e.g. Figure 3-1. Variable parameters include draft, angular sector, range performance envelope (which can constrain the angular sector with depth), and the use of a surface sound speed probe measurement to augment the ray tracing algorithm (though surface sound speed probe data are not required). Section 3.5 discusses in detail the case of simulating the inclusion of a surface sound speed measurement.

In the numerical simulation, a constant velocity acoustic ray tracing algorithm (Medwin and Clay, 1997) is used to explore how differing measurements of the sound speed structure, e.g. the two sound speed profiles shown in Figure 3-2, can alter the ray

path, and ultimately, the divergence of the set of ray traced solutions for a given two-way travel-time (TWTT) and depression angle, as shown in Figure 3-3. By systematically modifying the depression angle and TWTT, the entire potential sounding space is explored to populate a depth and distance indexed table of sounding depth and horizontal discrepancies, as shown in Figure 3-4. In this figure, the sounder would be situated at the apex of the triangular wedge on the upper left. The wedge shaped look-up table represents half of the angular sector covered by the mapping system and uncertainty is assumed to be symmetric about the vertical axis. These look-up tables, first described in (Hughes Clarke, 1994), are referred to as uncertainty wedges throughout the remainder of this work.

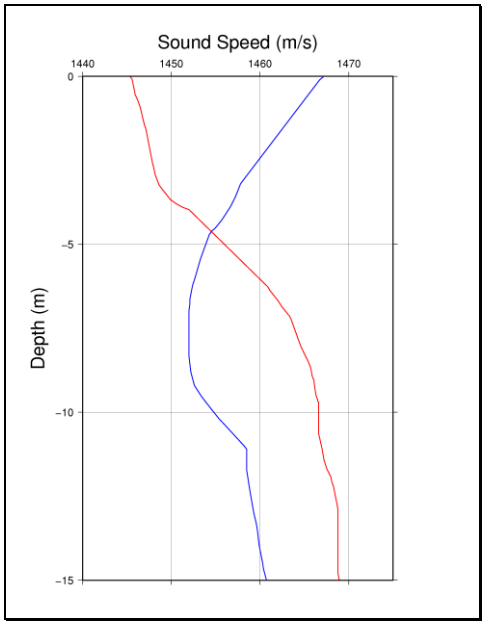

Figure 3-2. Two sample sound speed profiles.

The entire potential sounding space is investigated for two reasons. Firstly, the seafloor is not always flat and it is sometimes necessary to estimate the effect of refraction based uncertainties for depths shoaller than the nominal seafloor depth, especially as the refraction bias can vary dramatically with depth. An extreme example is the mast of a shipwreck that is above the depth of variability (or vice versa). Secondly, it is important to understand at what depth the divergence in ray paths occurs for identification of the most troublesome sources of variability, e.g. when trying to ascertain if surface variability causes more uncertainty than mid-water variability.

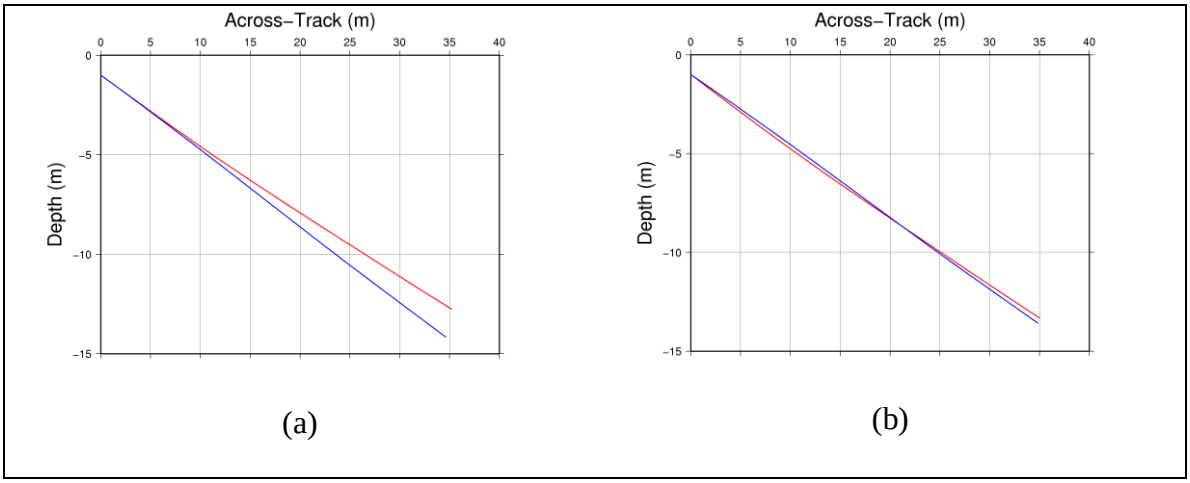

Figure 3-3. Ray trace solutions associated with sound speed casts (see Figure 3-2). Simulated draft is 1.0 m, depression angle is 20° and TWTT is 0.051 s. The ray traces in Panel A demonstrate how variations in the water column cause divergence in the ray paths. Panel B demonstrates how using a common surface sound speed has the potential to mitigate the effects of surface variability in some cases.

3.1.1 Variability Analysis

The ray trace simulator can be used to track the dispersion of ray paths associated with a set of several sound speed profiles representing a sample of the population of possible water column conditions in a given area. A Variability Analysis (VA) allows for the construction of a variability wedge, or a v-wedge, which quantifies the potential uncertainty associated with water mass variability. In essence, it quantifies the expected variance of soundings based on a sample of typical water mass variability; this allows the surveyor to assess whether water mass variability will have a significant impact on sounding accuracy and to react accordingly.

Figure 3-5 demonstrates the principle behind the estimation of the potential horizontal and depth uncertainty for a single location in the potential sounding space. The uncertainty associated with observed water mass variability is estimated as the standard deviation computed from the terminal points of a set of ray traced solutions where each

ray is traced using one of the candidate sound speed profiles. The vertical and horizontal standard deviations of the set are scaled to the 95% confidence level (ISO, 1995) as required by most hydrographic survey order specifications. Expanding the analysis to all points in the sounding space, one can construct a v-wedge. Figure 3-6 shows a v-wedge constructed for the set of sound speed casts from Figure 3-1 with a simulated sector of 150°, draft of 0.3 m and a surface sound speed probe. In this case, the variability of the water column can have a pronounced effect on sounding accuracy and a surveyor working in these conditions should take care to adequately measure the water column.

Variability Analysis provides the hydrographic surveyor with a statistical tool that assesses water mass spatio-temporal variability in terms that matter to the surveyor: sounding uncertainty. As with any statistical tool, the results strongly depend on an adequate and representative sampling of the population. Furthermore, the results only quantify the uncertainty associated with the water mass that was measured; one must still understand the underlying causes of variability in order to assess whether the nature of the variability is likely to remain the same over space and time.

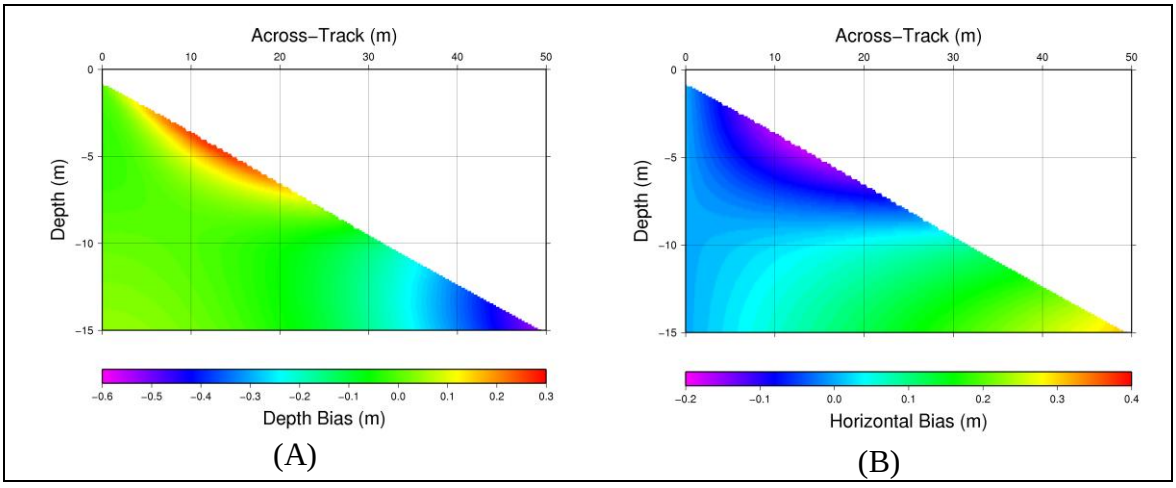

Figure 3-4. Depth (A) and horizontal (B) discrepancies associated resulting from investigation over entire potential sounding space. Simulated draft is 1.0 m and angular sector is 150° (see casts of Figure 3-2).

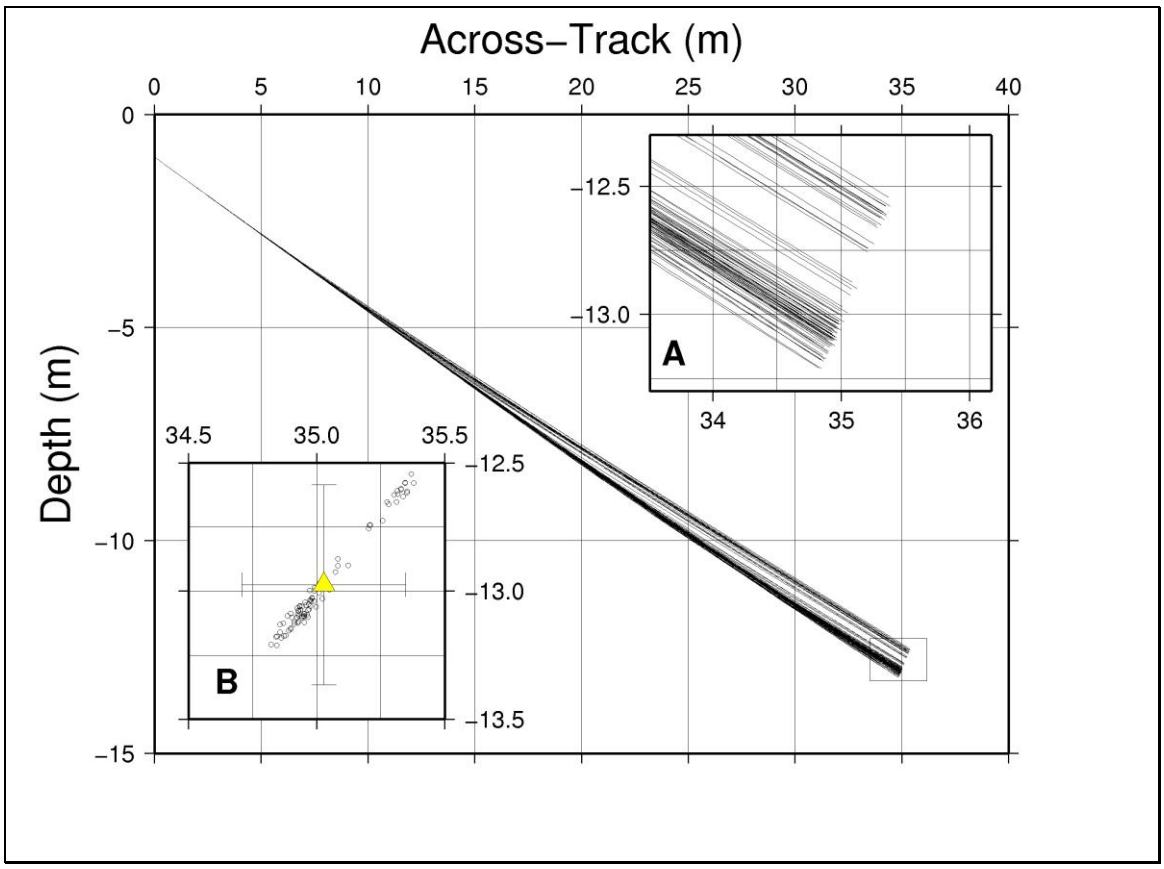

Figure 3-5. Ray paths calculated for the 82 sound speed profiles (see Figure 3-1). Simulated parameters include a draft of 1.0 m, a depression angle of 20°, a TWTT of 0.051 s and a common surface sound speed of 1445 m s^{-1}. The inset panel (A) on the upper right corresponds to the rectangular box drawn near the termini of the ray paths shown in the main panel. The lower left panel (B) shows the ends of the ray paths only and demonstrates how the final ray traced solutions disperse depending on which sound speed profile is used for ray tracing. The mean depth and position are indicated by the yellow triangle, the error bars indicate the 95% confidence level. Note that the main panel and upper right panel share the same distorted aspect ratio whereas the aspect ratio of the lower left panel is correct.

3.1.2 Uncertainty Analysis

An Uncertainty Analysis (UA) consists of comparing two ray paths only, allowing for a quantitative answer to the following question: "What sounding bias would result if sound speed profile B was used in the place of sound speed profile A?", where profile A represents known conditions and profile B represents an alternate model whose fitness is to be tested by a comparison to A. As the comparison of two casts quantifies the

sounding bias that would be introduced if one cast had been used in the place of the other, the resulting uncertainty wedge is named a bias wedge, or a b-wedge. An example is shown in Figure 3-7, alongside the two sound speed casts that were compared.

By comparing many pairs of casts, a set of b-wedges can be generated; these can then be averaged to provide a mean bias wedge along with a standard deviation wedge, these being calculated on a node-by-node basis for each node position in the look-up table based on the b-wedge values at the same look-up position. The resulting mean and standard deviation wedge (scaled to the 95% confidence level) are respectively referred to as an m-wedge and s-wedge in this text.

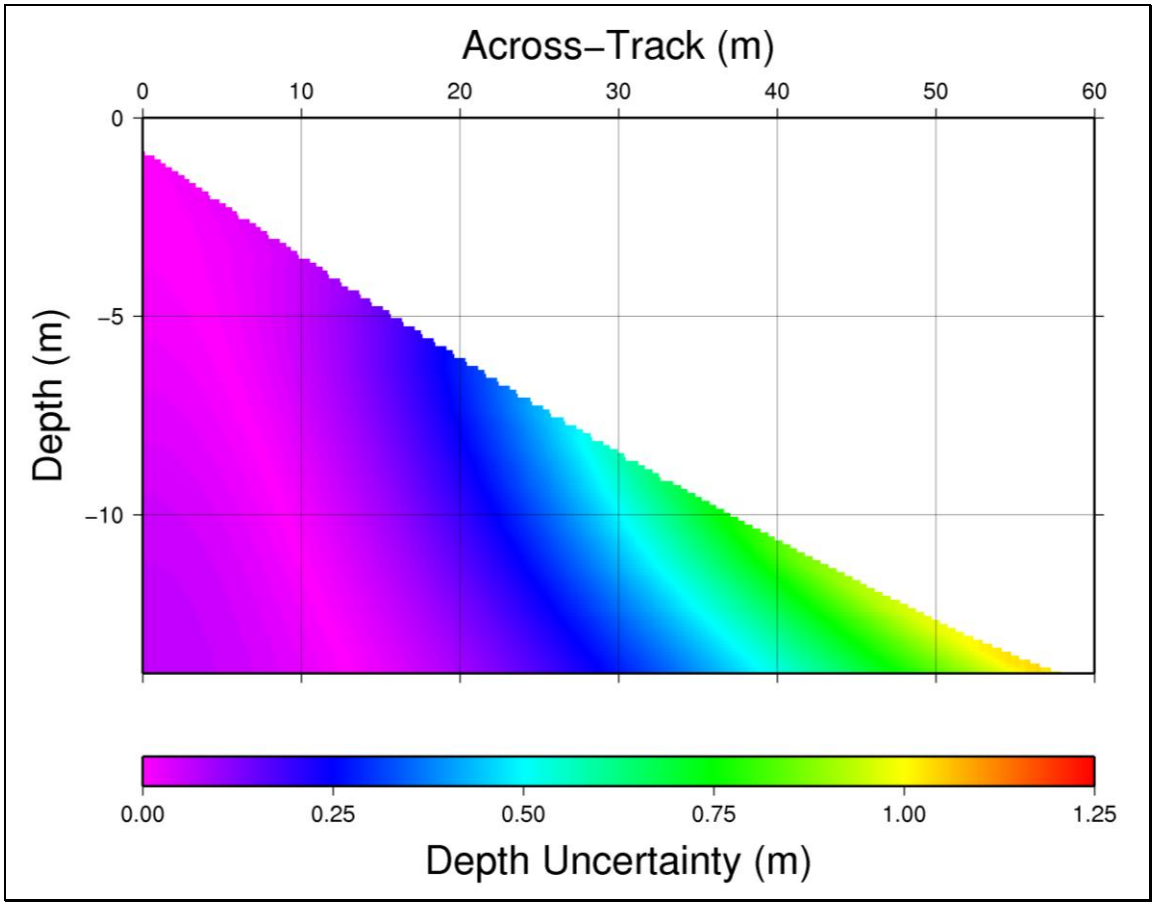

Figure 3-6. A Variability Wedge generated from a set of sound speed casts (see Figure 3-1). Uncertainty is scaled to the 95% confidence level.

Whereas a VA quantifies potential uncertainty associated with water mass variability, a UA allows for experimentation with alternate solutions for sound speed and is based on the comparison of the alternate solution to a reference, or truth, measurement. For example, having a set of CTD casts (the truth), one can assess, on a cast-by-cast basis, the loss of accuracy that might occur if only temperature was measured using an XBT. In this case, the experiment would consist of constructing candidate sound speed casts from the CTD casts in which the sound speed is computed with a constant salinity. A set of b-wedges is generated by comparing each candidate cast against its reference cast; the results are tallied in an m-wedge and an s-wedge. The m-wedge would capture the mean bias that would result from the simulated situation, e.g. on average, ignoring the salinity would introduce a small positive bias to the outermost beam. The effect of variability in salinity is captured by the s-wedge, which depicts the dispersion of bias about the mean. As with VA, the results of the experiment strongly depend on an adequate and representative reference data set.

3.1.3 Calculation Procedures

Descriptions of the VA and UA algorithms are provided to document the approach taken during calculation of the various uncertainty wedge formats in tables 3-1 and 3-2 below.

Table 3-1. Summary of VA algorithm.

Step 1. Based on a set of n sound speed profiles (ssp), build a time-angle look-up table for the mean ray path and standard deviation about the mean ray path for a series of depression angles that extend over half the angular sector in 1° increments. Each ray path extends from the sounder to the maximum sampling depth of the ssp associated with the ray path.

For each depression angle (δ)
   For each ssp
      1. Compute the ray path from the sounder depth (draft) to the maximum sampling depth of the ssp by tracking the cumulative two-way travel time (t) at each layer in the ssp using a constant velocity ray tracing algorithm. This gives a ray path: $y(\delta,t)$, $z(\delta,t)$. Note that the time interval between samples is variable due to the varying sound speed in each layer.
      2. Resample the ray path from the previous step to a fixed time sampling interval, this gives a resampled ray path: $y_r(\delta,t)$, $z_r(\delta,t)$.
   End

   For each two-way travel time, t
      Compute mean depth and horizontal position and standard deviation using $y_r(\delta,t)$, $z_r(\delta,t)$ from each ssp in the set of ssps, this gives:
      a. The mean resampled ray path: $\mu_{yr}(\delta,t)$, $\mu_{yr}(\delta,t)$
      b. The resampled standard deviation about the mean ray path: $\sigma_{yr}(\delta,t)$, $\sigma_{zr}(\delta,t)$
   End

End

Step 2. Map the standard deviations $\sigma_{yr}(\delta,t)$, $\sigma_{zr}(\delta,t)$ from the time-angle (t,δ) look-up table from step 1 into a distance-depth (y,z) look-up table.

For each depth, z
    For each depression angle, δ
      1. Interpolate the horizontal distance (y) between the two solutions bounding depth z in the resampled mean ray path ($\mu_{yr}(\delta,t)$, $\mu_{yr}(\delta,t+1)$), this gives the y value of the ray at depth z: $y(\delta)$
      2. Interpolate the standard deviation between the two solutions bounding depth z in the resampled standard deviation ray path ($\sigma_{yr}(\delta,t)$, $\sigma_{zr}(\delta,t+1)$), this gives the standard deviation for position $y(\delta)$,z: $\sigma_y(y,z)$, $\sigma_z(y,z)$
    End

    Resample the set y, $\sigma_y(y,z)$, $\sigma_z(y,z)$ to a constant interval in the y-direction: y_r, $\sigma_{yr}(y,z)$, $\sigma_{zr}(y,z)$. Scale the standard deviations to the 95% confidence level.
End

Table 3-2. Summary of UA algorithm.

Step 1. Based on a set of n control sound speed profiles (ssp) and n candidate sound speed profiles to be tested, build a time-angle look-up table for each control ssp and its corresponding candidate ssp for a series of depression angles that extend over half the angular sector in 1° increments. Each ray path extends from the sounder to the minimum of the control ssp sampling depth and the candidate ssp sampling depth. The look-up tables are then differenced to compute the bias that is associated with use of the candidate ssp in place of the control ssp.

For each control/candidate ssp pair
  For each depression angle (δ)
    1. Compute the ray path from the sounder depth (draft) to the maximum sampling depth of the control ssp by tracking the cumulative two-way travel time (t) at each layer in the control ssp using a constant velocity ray tracing algorithm. This gives a ray path: $y_{cont}(\delta,t)$, $z_{cont}(\delta,t)$. Note that the time interval between samples is variable due to the varying sound speed in each layer.
    2. Resample the ray path from the previous step to a fixed time sampling interval, this gives a resampled ray path: $y_{cont\text{-}r}(\delta,t)$, $z_{cont\text{-}r}(\delta,t)$.
    3. Repeat above two steps for the candidate ssp, giving resampled candidate ray path: $y_{cand\text{-}r}(\delta,t)$, $z_{cand\text{-}r}(\delta,t)$
    4. Compute the difference in y,z between the control and candidate ray path, this gives a resampled bias ray path: $\Delta y_r(\delta,t)$, $\Delta z_r(\delta,t)$
  End
End

Step 2. The resampled time-angle control ssp look-up table ($y_{cont\text{-}r}(\delta,t)$, $z_{cont\text{-}r}(\delta,t)$) and resampled bias look-up tables ($\Delta y_r(\delta,t)$, $\Delta z_r(\delta,t)$) for each control/candidate pair are mapped onto distance-depth (y,z) look-up tables giving a bias-wedge, or b-wedge, for each control candidate pair.

For each control/candidate pair
  For each depth, z
    For each depression angle, δ
      1. Interpolate the horizontal distance (y) between the two solutions bounding depth z in the resampled control ssp ray path ($y_{cont\text{-}r}(\delta,t)$, $z_{cont\text{-}r}(\delta,t)$), this gives the y value of the ray at depth z: $y(\delta)$
      2. Interpolate the bias between the two solutions bounding depth z in the resampled bias ray path ($\Delta y_r(\delta,t)$, $\Delta z_r(\delta,t)$), this gives the bias for position $y(\delta)$,z: $\Delta_y(y,z)$, $\Delta_z(y,z)$
    End

    Resample the set y, $\Delta_y(y,z)$, $\Delta_z(y,z)$ to a constant interval in the y-direction: y_r, $\Delta_{yr}(y,z)$, $\Delta_{zr}(y,z)$
  End
End

Step 3. Compute the mean bias and standard deviation about the mean bias for the set of n b-wedges resulting from steps 1 and 2. This gives distance-depth look-up tables of mean bias (m-wedge) and standard

```
deviation about the mean bias (s-wedge).

For each depth, z
  For each distance, y
      1. For the set of biases at location y,z (Δyr(y,z), Δzr(y,z)),
         calculate the mean bias (μΔy(y,z), μΔz(y,z)) and standard
         deviation (σΔy(y,z), σΔz(y,z)).  Scale the standard deviations
         to the 95% confidence level.
  End
End
```

A list of the various uncertainty wedge types is given below along with a brief description of what they are meant to represent.

- v-wedge (variability wedge): measure of the potential uncertainty associated with the spatio-temporal variability of the water column (scaled to the 95% confidence level).
- b-wedge (bias wedge): measure of the bias had an alternative cast been used in place of an observed cast.
- m-wedge (mean bias wedge): arithmetic mean of several b-wedges, represents the average bias associated with the sound speed sampling/calculation regime that is being tested.
- s-wedge (sigma wedge): standard deviation (scaled to the 95% confidence level) associated with a set of b-wedges, represents the dispersion about the average bias captured by the m-wedge.

Tables 3-1 and 3-2 and the list above all note that the standard deviations in v-wedges and s-wedges are scaled to the 95% confidence level. This is done to ensure ease of use when comparing analysis results with common survey accuracy specifications, which typically require uncertainties to be expressed at the 95% confidence level. All v-

wedges and s-wedges presented in this work have been scaled to the 95% confidence level.

It should be noted that horizontal uncertainties can be computed in the same manner for all uncertainty wedge formats. Depth accuracies, however, are typically much more stringent than horizontal accuracy requirements in most survey accuracy specifications. For example, IHO Order 1A/B and Order 2 allow for 5% and 10% w.d. horizontal uncertainty, respectively, both of which are roughly 4x the allowable vertical uncertainty for each order (IHO, 2008).

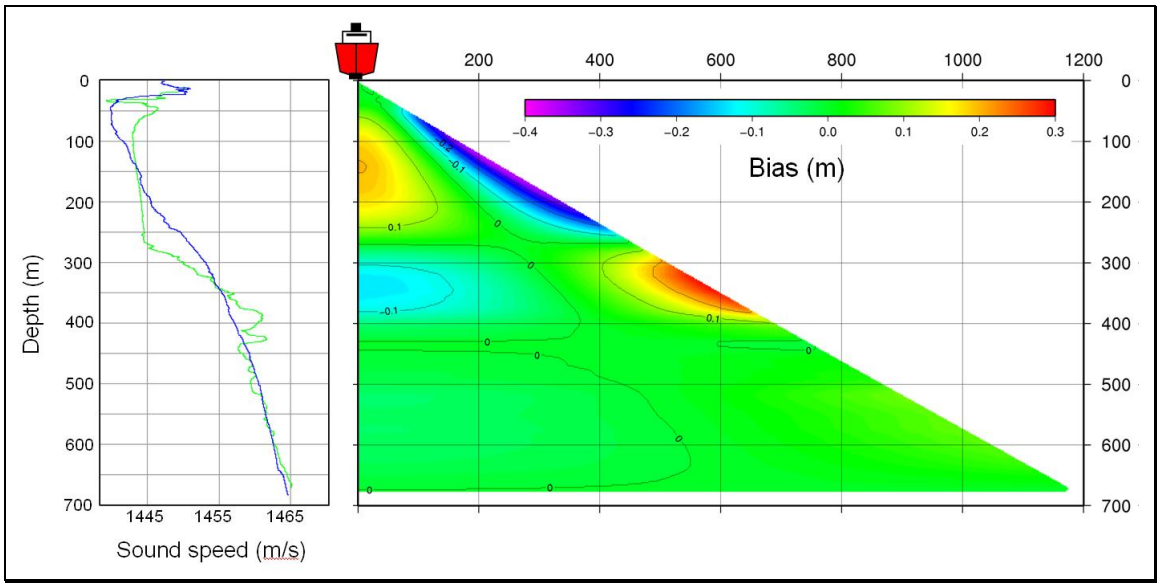

Figure 3-7. Sounding depth bias presented as an uncertainty wedge.

3.2 Alternate Representations

Though uncertainty wedges are a convenient representation format for visualization and look-up of uncertainty, they are not well suited for inter-comparison. In this case,

distilled versions of the content in any of the wedge representations allows for a more useful examination and analysis of uncertainty. The evolution of uncertainty over any given ray over the depth range of investigation (see Figure 3-8) is useful when investigating the impact of variability at different points in the water column.

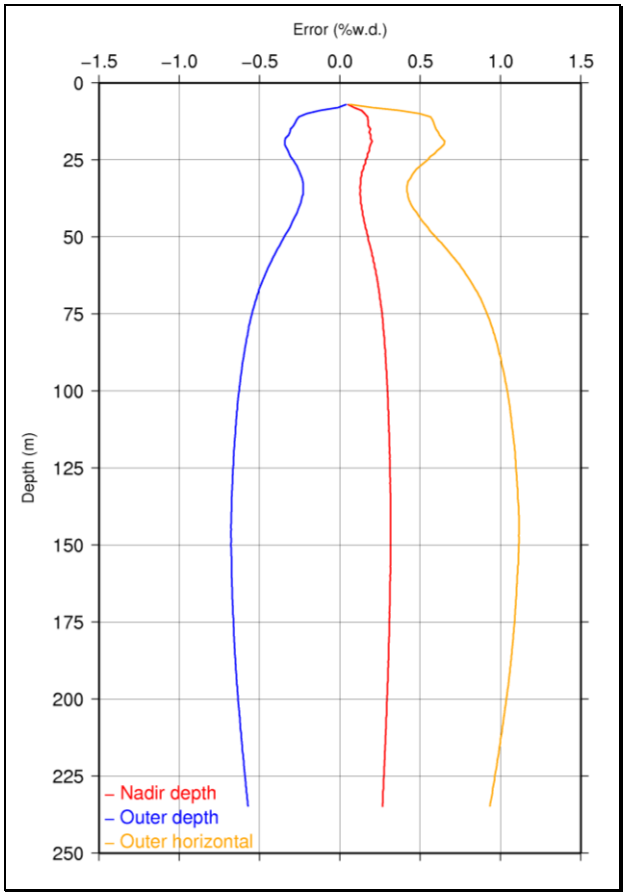

Figure 3-8. Sample of bias as a function of depth for the nadir and outermost beam in a swath.

An alternate distillation that is useful for survey design is a horizontal section at a selected depth in an uncertainty wedge. An example of this is shown in Figure 3-10, in which uncertainty sections from 5 v-wedges show how the variability in oceanographic conditions depicted in Figure 3-9 have more impact than others. These two representation formats are referred to as uncertainty profiles (Figure 3.8) and uncertainty sections (Figure 3.10), respectively.

Spatio-temporal analyses sometimes require distillation of the wedge formats to a single scalar value. In this case, the uncertainty involved with the outermost beam at the maximum investigation depth is chosen as the most significant candidate as it experiences the largest uncertainty across the swath at the maximum depth of investigation due to the large incidence angle. This proves particularly useful in

investigating b-wedges where it can be difficult to examine several hundred b-wedges for comparative purposes; in this case the details that are masked in the compilation of m-wedges and s-wedges can be examined as a spatial and/or temporal series.

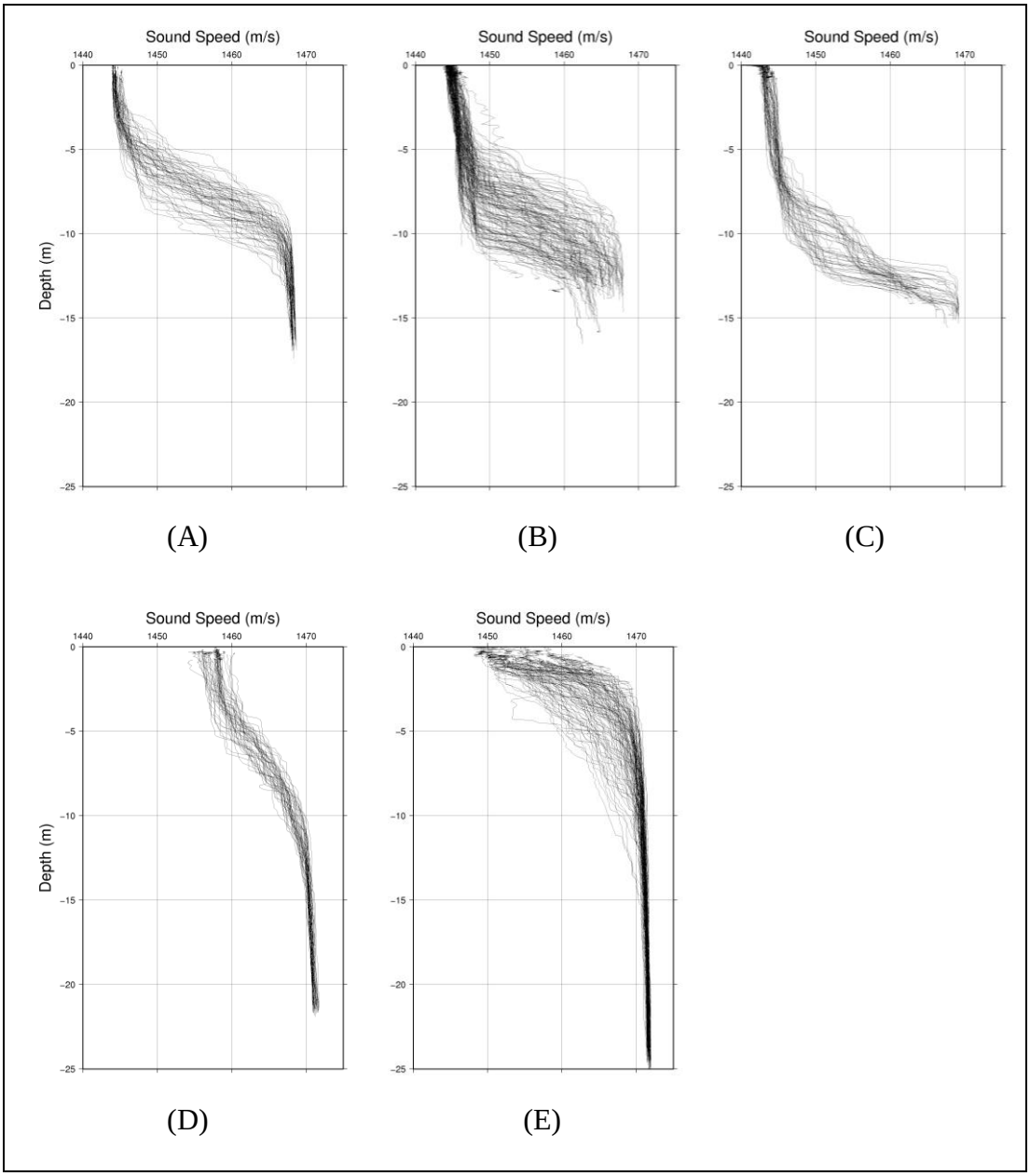

Figure 3-9. Sound speed profiles acquired in 5 locations of the Rotterdam Waterway in the Netherlands. The casts were acquired over a 1.5-2.5 hour period at each location (on different days) with a Moving Vessel Profiler 30 (MVP30) (Beaudoin et al., 2009).

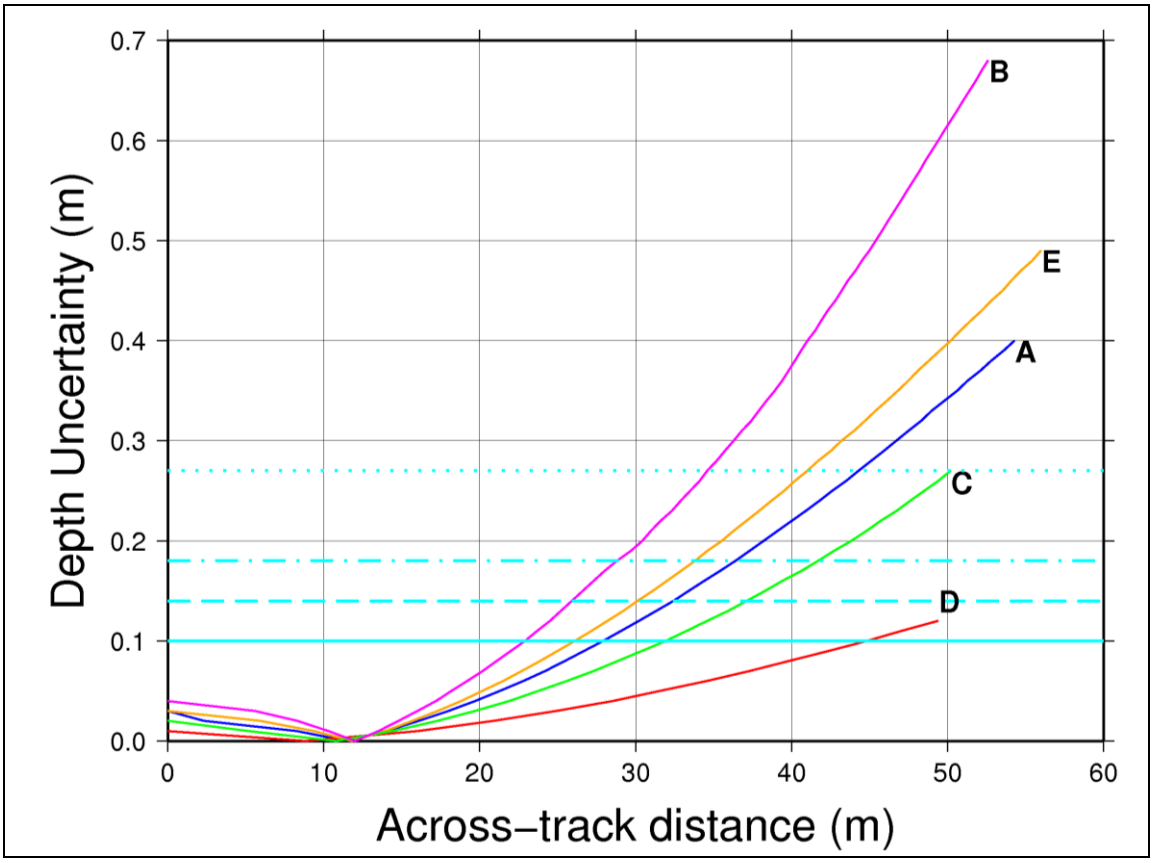

Figure 3-10. Uncertainty sections at a depth of 13 m through variability wedges compiled for Rotterdam Waterway sound speed casts (see Figure 3-9). From bottom to top, cyan horizontal lines represent 0.75% water depth, and allowable vertical uncertainties for Rijkswaterstaat (RWS) Survey Order A, RWS Survey Order B and IHO Special Order, respectively (Beaudoin et al., 2009).

3.3 Surface Sound Speed

A surface sound speed probe is often required to ensure correct electronic beam steering angles with linear transducer arrays. It is also often used to augment the sound speed profile during ray tracing by (1) using the measured surface value as "the initial entry in the sound speed profile used in the ray tracing calculations" (Kongsberg, 2006) or (2) calculating Snell's constant, or the ray parameter, with the observed surface value

prior to ray tracing (Beaudoin et al., 2004). The incorporation of the surface sound speed measurement has a significant effect on the behaviour of a ray tracing algorithm (Cartwright and Hughes Clarke, 2002). In some cases it allows for a graceful recovery from surface layer variability as long as the deeper portion of the water mass is relatively invariant. Regardless of this potential gain, the inclusion of the surface sound speed as an additional measurement fundamentally changes the behaviour of a ray tracing algorithm, thus its effect on ray tracing should be included in uncertainty estimates.

For UA, the use of a surface sound speed probe is mimicked by retrieving the sound speed at the transducer depth from the reference profile and using this to compute the ray parameter for the candidate cast ray trace without modifying the candidate cast. One must take care, however, to only perform this additional step if acquisition and/or post-processing software can accommodate the surface sound speed as an additional aiding measurement during sounding reduction, specifically the ray tracing portion of the procedure. For example, consider the case where a pre-analysis of the impact of surface sound speed variability indicates that a surface sound speed probe would be beneficial. The user should verify that the software used to reduce the soundings (either in real-time or in post-processing) is able to include the surface sound speed measurements during ray tracing, otherwise, the benefit of the additional information is not realized.

VA, on the other hand, is based upon examining the divergence of several ray paths, with each ray path being associated with one sound speed profile of the set. For a given travel time, depression angle and surface sound speed, the bundle of rays will land at some location in the potential sounding space. The dispersion, or scatter, of the solutions about the mean position in the potential sounding space serves as an indicator of

the sensitivity to water column variability. Given many potential values for a surface sound speed value, which should be chosen as the "common" surface sound speed? The following exercise demonstrates that the actual value of the common surface sound speed is irrelevant. Consider a ray trace with a depression angle of 20° (incidence angle of 70°) and surface sound speed of 1445 ms^{-1}. The ray parameter used in the ray trace is calculated as:

$$k_1 = \sin(70°)/1445 \tag{3.1}$$

As the ray parameter is a function of depression angle and sound speed, there exists other angle/sound speed pairs that would yield the same ray parameter. For example, consider a surface sound speed of 1440 ms^{-1}. Snell's law is applied to determine which angle would give the same ray parameter:

$$\begin{aligned} &k_2 = \sin(\theta)/1440 = k_1 \\ &\theta = \arcsin(1440\sin(70°)/1445) \approx 69.462° \\ &\therefore \psi = 90° - \theta \approx 20.538° \end{aligned} \tag{3.2}$$

where ψ is the depression angle.

If one were to perform an acoustic ray trace with a common sound speed profile and differing surface sound speed/depression angle pairs, the rays would share the exact same ray path, despite having different depression angles and different surface sound speeds. In essence, it is possible to arrive at the same location in the potential sounding space through a different launch angle and surface sound speed combination.

If the above exercise is true for one ray, then it is true for all rays in a bundle of rays being investigated in a VA. One can arrive at the mean location by investigating a given depression angle and surface sound speed from one of the casts, or by using a different depression angle and a different surface sound speed, chosen from a different

cast in the set. As all of the rays in the bundle will all arrive at their same respective positions in either case, then their relative positions with respect to their mean position will remain the same. It follows that the dispersion of the solutions about the mean location would also remain the same regardless of how the bundle of rays arrived at the mean location. In other words, any one of the casts can be chosen as a measurement of truth and the VA would eventually, through some combination of surface sound speed and depression angle, arrive at the same mean location and calculate the same dispersion of the ray traced solutions. So, an arbitrary surface sound speed value could be chosen, and with a systematic sweep across the angular sector every node in the potential sounding space will be visited with the dispersion being calculated in the same manner had another surface sound speed been chosen.

Note that the exact matching of ray traced solutions depends heavily on how the ray trace algorithm uses the additional surface sound speed measurement to augment the sound speed profile. The following procedure is used in this work: (1) the surface sound speed and depression angle are used to define the ray parameter, and (2) the ray is immediately refracted at the beginning of the ray trace as if an infinitesimally thin layer of water exists at the transducer face in which the speed of sound is the measured surface sound speed. Deviation from this methodology will result in small discrepancies in the equality of the ray solutions when one modifies the surface speed or depression angle as has been done in this exercise.

3.4 Challenges

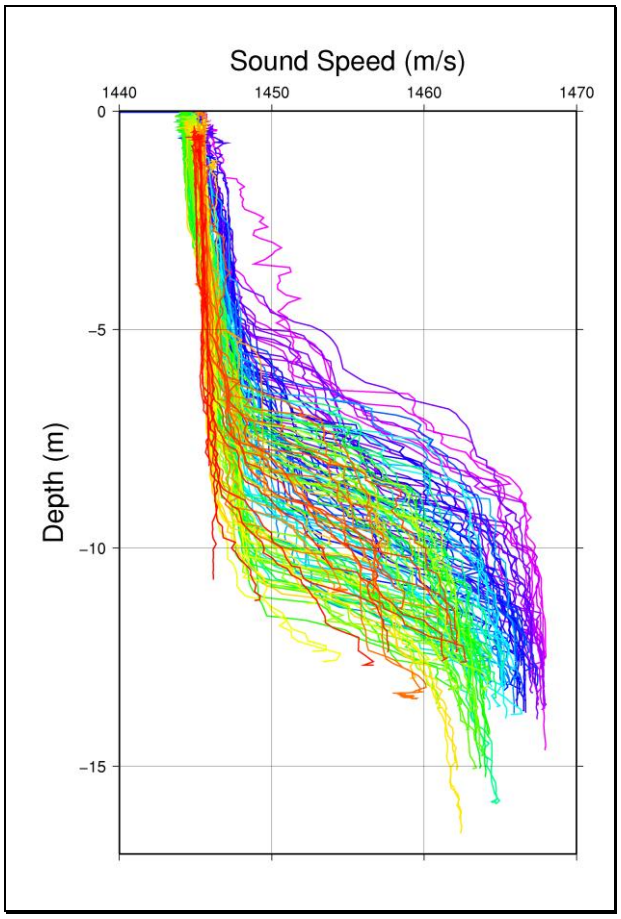

Figure 3-11. 148 sound speed profiles collected over a 2.5 hour period by a MVP30 in the Rotterdam Waterway in March 2009 (Beaudoin et al., 2009).

A major challenge in performing these types of analyses is dealing with sets of casts and b-wedges that extend to different depths. The root of this problem is one that is common in hydrographic surveying ray tracing applications: how should a ray tracing algorithm estimate the remainder of the ray path beyond the depth of the last sample in a sound speed cast? Some software packages force the user to extend the cast to the required depth while others hold the last observed sound speed to the required ray tracing depth. As a false extension of a cast could bias the analyses herein, it was decided to halt ray tracing beyond the terminal depth of each cast. Thus, the ray paths from shallower casts do not contribute at greater depths and the sample mean and standard deviation calculated in the analyses lock on to the potentially much tighter distribution of the deeper casts in any given analysis. Unfortunately, this has the effect of introducing discontinuities in the various uncertainty wedge representations. In some cases, the discontinuities are easily remedied by extending all casts to the same depth. In

other cases it is unclear how casts should be extended; Figure 3-11 provides an example where water column variability at depth can complicate sound speed profile extension, a sound speed plot of the first 30 casts of the set shows the variation in maximum sampling depth within the set in Figure 3-12. A v-wedge for the entire set of casts is shown in Figure 3-13.

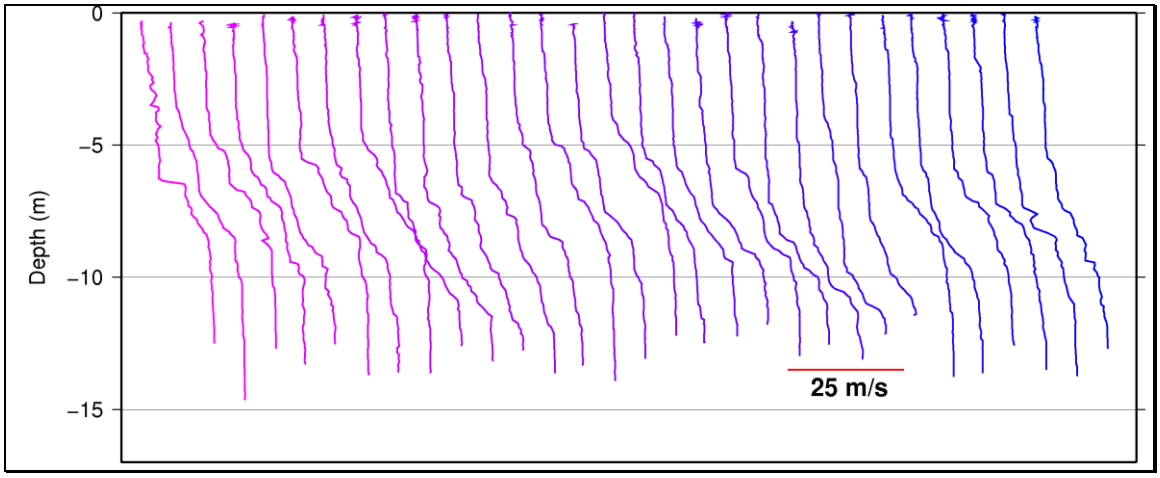

Figure 3-12. Waterfall plot of first 30 sound speed casts (see Figure 3-11).

If the casts are of similar depth, the uncertainties at the last depth prior to the first discontinuity can be held constant or be extended with a constant gradient for the remainder of the ray path depth investigation, as shown in Figure 3-14. In this case, extending a single uncertainty profile is much more straightforward (and as such, perhaps more robust) than extending several sound speed profiles. Figures 3-15 and 3-16 demonstrate the constant value and constant gradient extension methods applied to a v-wedge constructed for the casts of Figure 3-11.

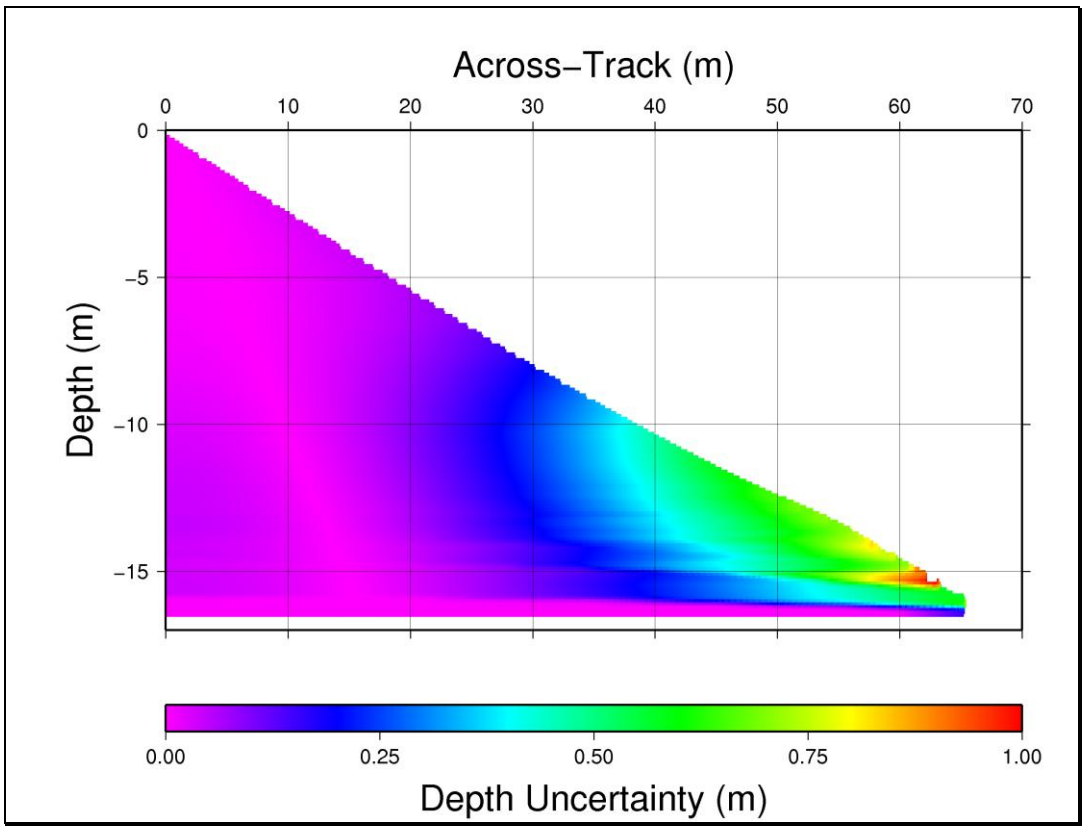

Figure 3-13. V-wedge for 148 sound speed casts (see Figure 3-11). Note discontinuities due to the decreasing number of ray paths that contribute to the sample standard deviation with depth.

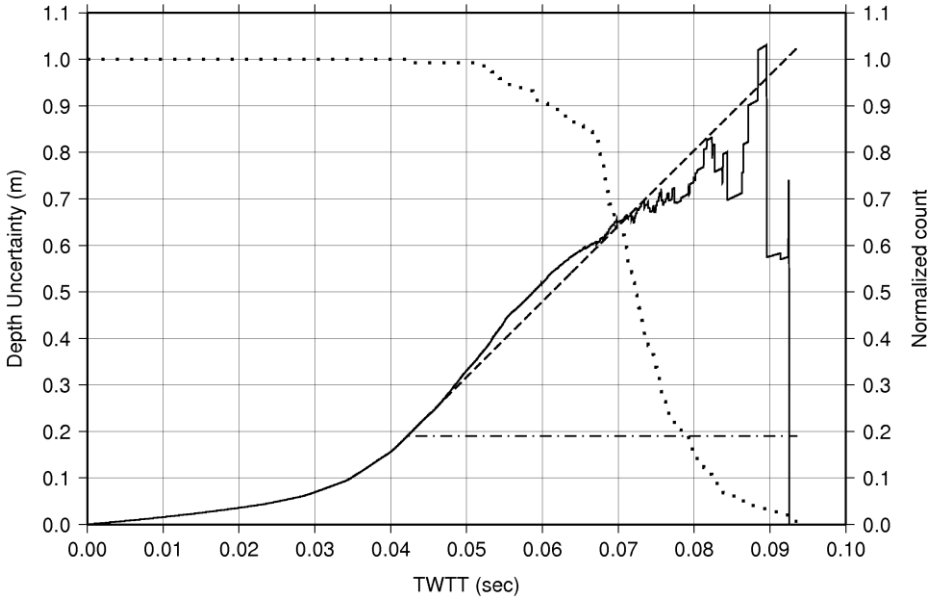

Figure 3-14. VA derived depth uncertainty at 75° incidence for 148 sound speed casts (see Figure 3-11). The raw uncertainty is shown in solid black, with a constant value (dashed-dotted) and constant gradient (dashed) extension applied after the number of contributing rays begins to drop. Normalized count of the contributing rays is shown as the dotted line (n = 148).

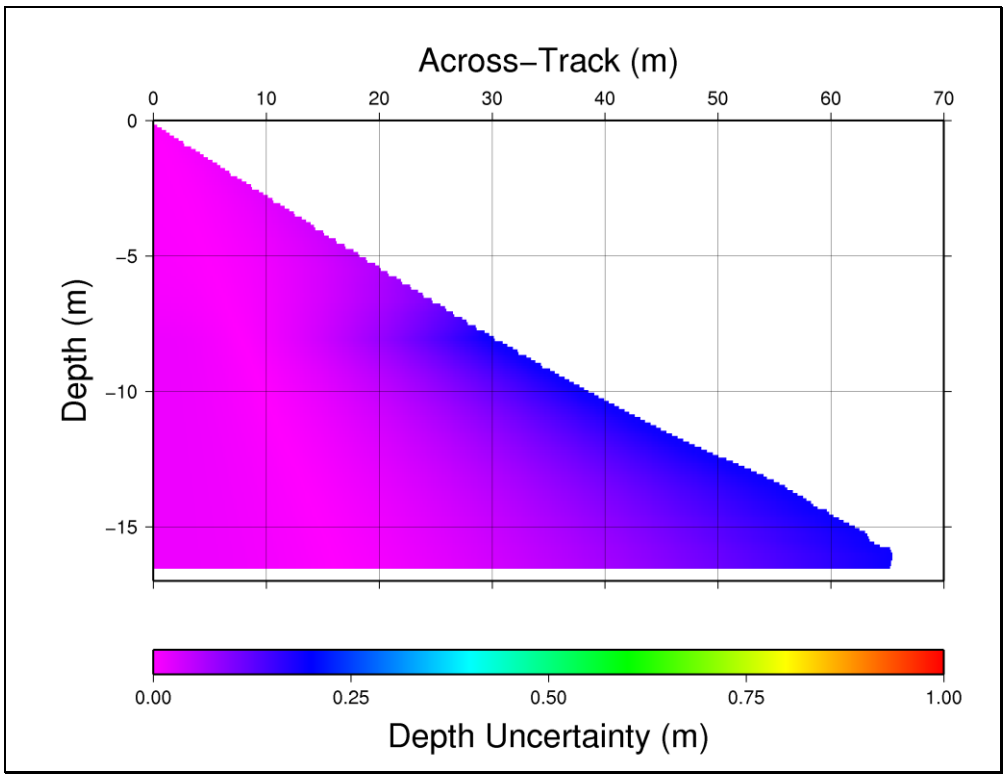

Figure 3-15. V-wedge with constant value extension of standard deviation beyond a depth of approximately 8 m (cf. Figure 3-13).

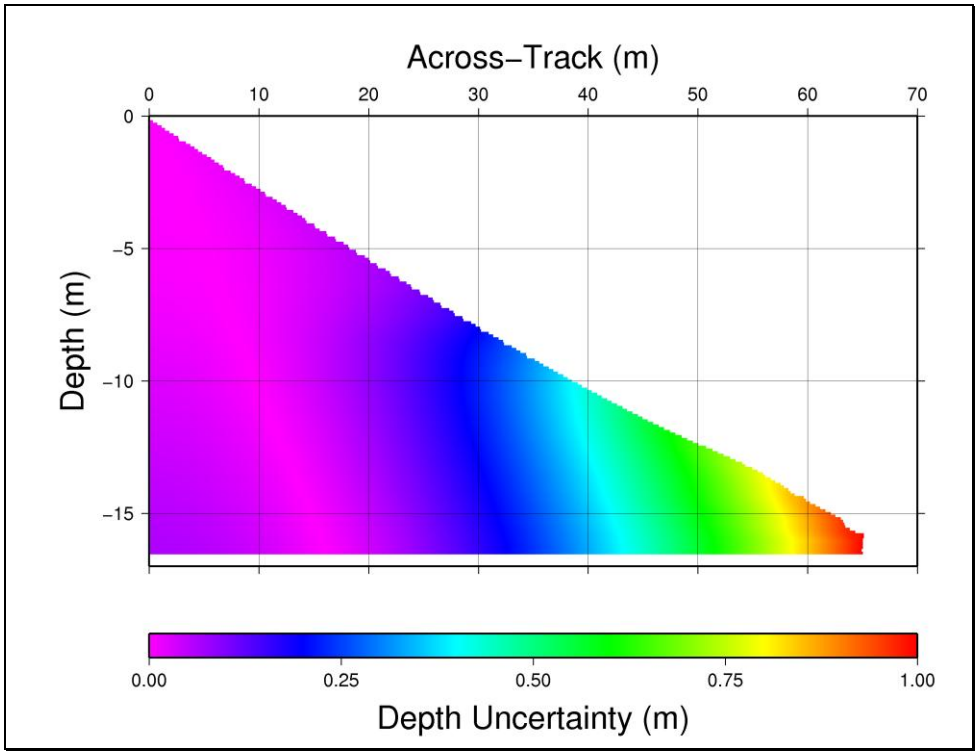

Figure 3-16. V-wedge with constant gradient extension of standard deviation beyond a depth of approximately 8 m (cf. Figure 3-13).

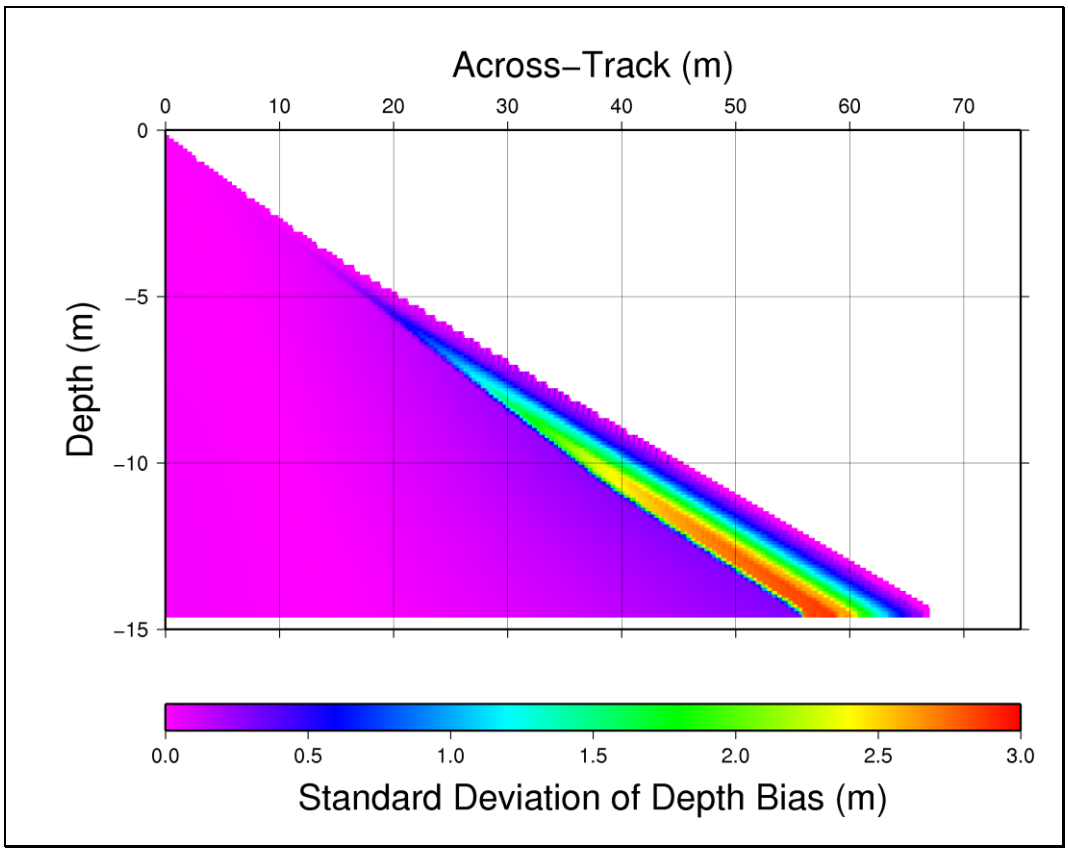

Figure 3-17. S-wedge compiled from 113 b-wedges, note outer edge discontinuities associated with varying sizes of the b-wedges.

A similar effect can occur with the compilation of m-wedges and s-wedges at the outer most edge of the wedge. As each b-wedge can potentially have a different reference sound speed profile, the outermost ray path can take dramatically different paths depending on the nature of the water column conditions in each reference profile. For example, one b-wedge may have an upward refracting reference sound speed profile whereas another b-wedge may have one that is downward refracting. The upward refracting b-wedge will extend further in horizontal distance than the that of the downward refracting reference cast; when it comes time to compile the b-wedges (again, on a node-by-node basis), there will exist nodes at the outer edges that have not been examined in some of the b-wedge comparisons, and the sample mean and standard

deviation may experience sharp discontinuities as the sample size decreases. Figure 3-17 shows an s-wedge compiled from 113 b-wedges resulting from a sequential comparison of 114 MVP30 casts collected along a 11.5 km section of the Rotterdam Waterway in March of 2009 (Beaudoin et al., 2009).

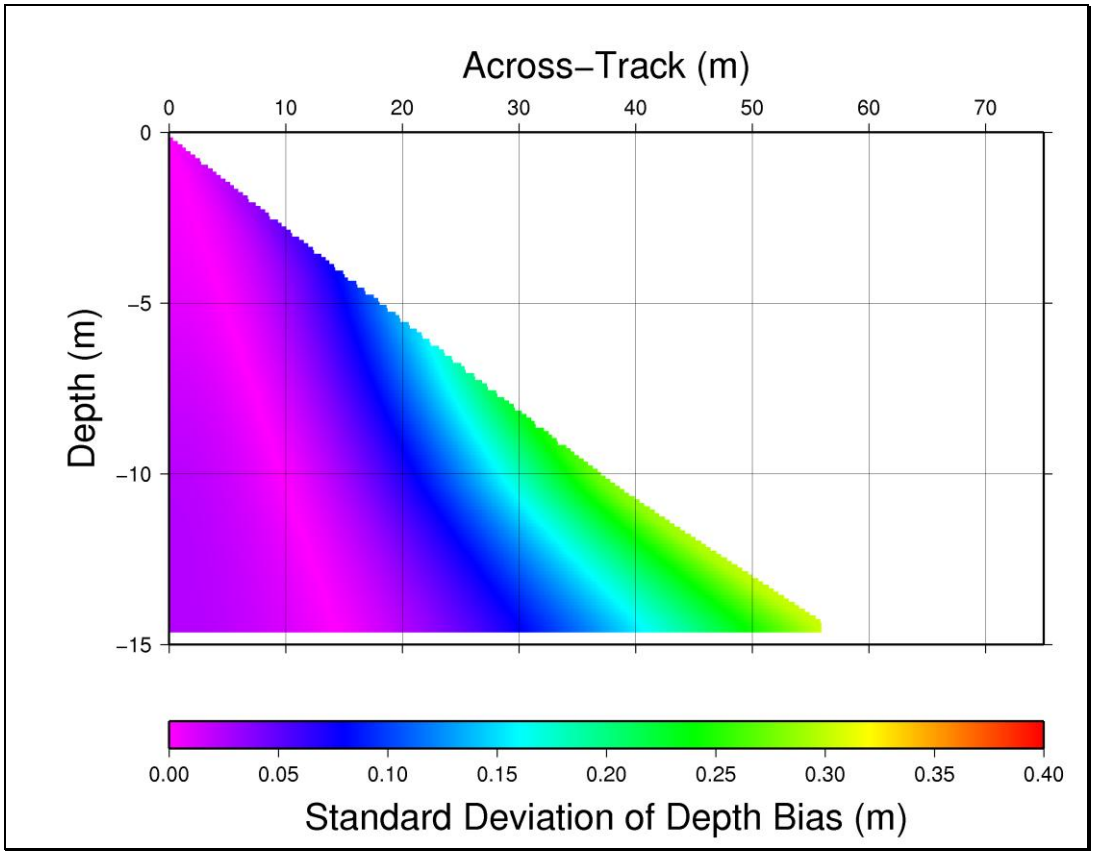

Figure 3-18. S-wedge of Figure 3-16, trimmed at outer edges (cf. Figure 3-17, note the different colour scale).

One solution to this problem is to limit the compilation of b-wedges to the nodes which have been examined by all b-wedges, as shown in Figure 3-18. This potentially reduces the desired angular sector of examination; however, this is preferable to having discontinuities that are unrepresentative of the uncertainty that would be achieved had all ray paths examined all nodes. Artificially increasing the angular sector of investigation during the compilation of the b-wedges can be done to compensate for the "trimming"

performed on the s-wedge (and m-wedge). This brings the investigated sector much closer in size to that which is desired, as is shown in Figure 3-19.

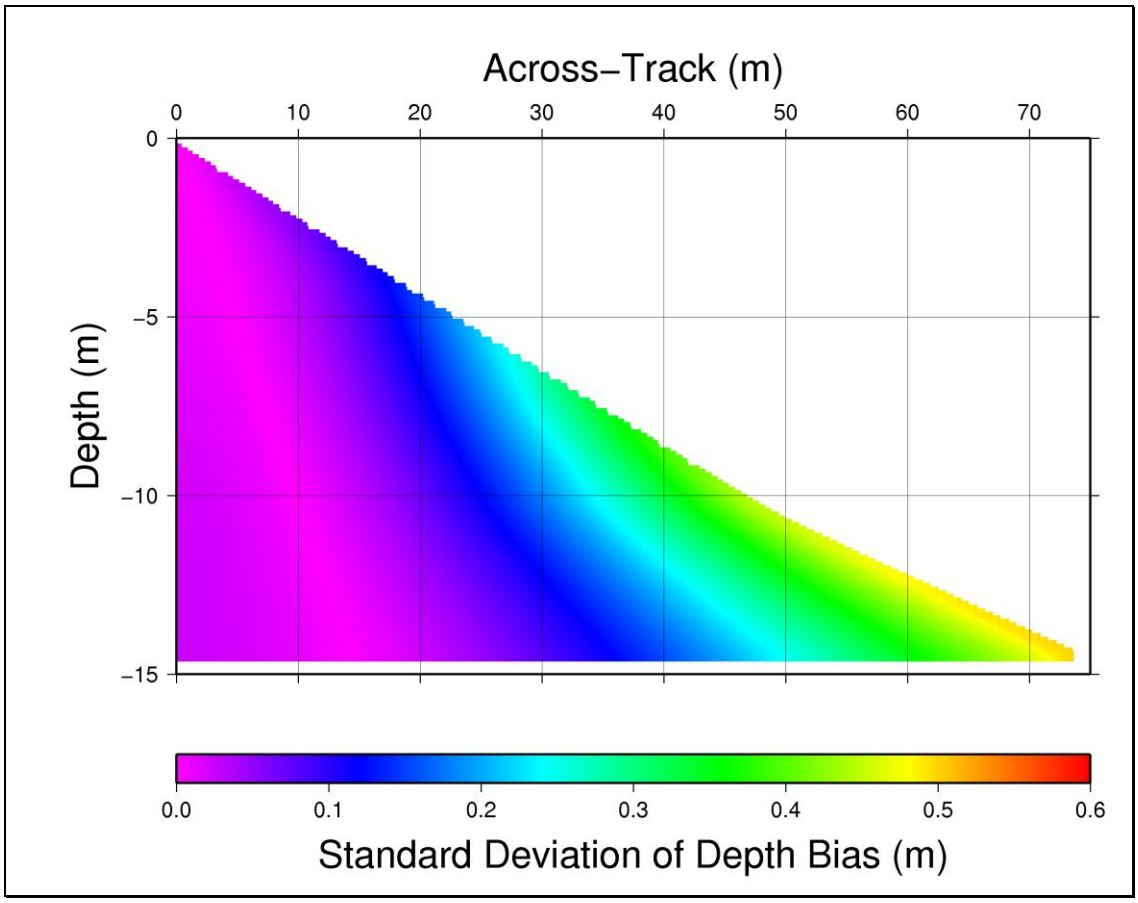

Figure 3-19. Trimmed s-wedge compiled from artificially increased b-wedges, (compare with figures 3-17 and 3-18).

4 CASE STUDY

4.1 Introduction

As discussed in the introductory chapter, this case study involves assessing the sounding uncertainty associated with the use of oceanographic climatologies for refraction correction of soundings acquired by MBES, specifically in the area of operations of the CCGS Amundsen in the CAA. Such an approach is fully expected to introduce uncertainty in the sounding reduction process as a static climatology is not meant to reproduce the wide range of oceanographic conditions that can occur in any given area, it is only meant to represent mean conditions over a well defined time period. The previous chapter outlined analysis methods which can be used to assess the impact of such an approach on sounding uncertainty. All that is required is a reference data set against which the climatologies in question can be compared. An ideal reference data set would provide synoptic measurements of temperature and salinity across the spatial domain of interest over the entire vertical extent of the water column. Furthermore, the spatial domain would be sampled at a sufficient rate to capture oceanographic processes of interest; it would also be sampled for a sufficiently long period of time to capture all possible conditions. Of course, such an ideal data set does not exist, nor is it practical to collect. Instead, a series of non-synoptic observations is proposed as the reference data set; in this case, it consists of several hundred high-resolution vertical CTD profiles which are widely spaced in space and time over the domain of the case study.

Table 4-1. Amundsen CTD casts.

Year	June	July	Aug.	Sept.	Oct.	Nov.	Total
2004	14	38	18	0	0	0	70
2005	0	0	48	40	0	0	88
2006	0	0	0	61	52	0	113
2007	0	0	0	4	74	21	99
2008	0	0	0	45	0	0	45
2009	0	22	46	-	-	-	68
Total	14	60	112	150	126	21	483

Though the Amundsen rarely samples the water column while in transit, a substantial number of CTD casts have been collected at the various scientific sampling stations throughout the CAA over the 2004-2009 field seasons (refer to Table 4-1 and Figure 4-1). Extending over six field seasons and much of the CAA, the 483 CTD casts provide an extensive control data set. The underlying assumption is that the Amundsen has sampled most of the natural range of variability in most locations, i.e. a significant number of excursions from average conditions have been observed over the course of six field seasons. This assumption is difficult to prove since one must have complete knowledge of the range of possible conditions for all locations. Instead, it is assumed that the natural variability is a stationary process and that a spatial series of measurements over a region will have the same statistical properties as a time series at a single location. The analysis is thus done on a regional basis with the measurements scattered throughout each region contributing to a regional uncertainty estimate for each climatology. The confidence in the uncertainty estimate grows, of course, with the number of contributing

observations. Evaluations of climatological means for months with many observations are thus likely to be more robust than those with few, especially those which were only sampled in a single field season (e.g. June and November).

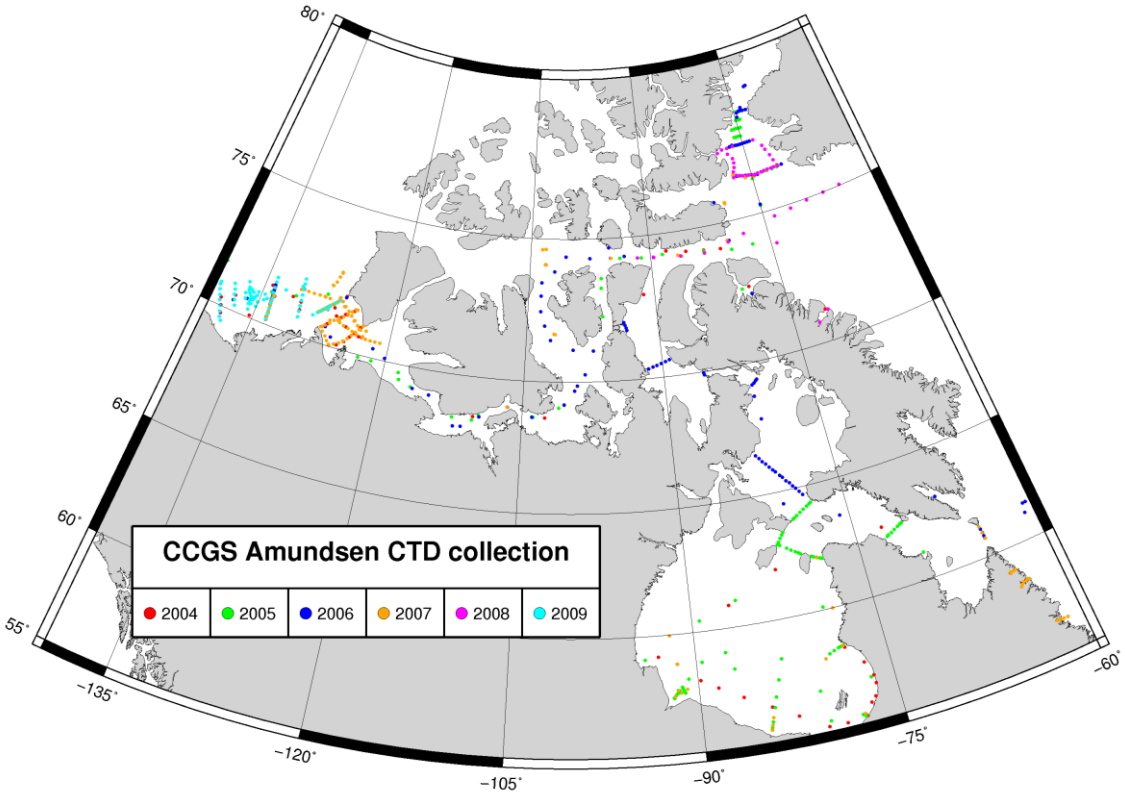

Figure 4-1. ArcticNet CTD sampling stations.

The WOD is another potential source of reference data, however it is also the major source of observations used to construct all three climatologies. Since an important part of this case study is to assess each climatology's predictive skill at forecasting current mean conditions, it is important that an independent reference data set be used. This is especially important in this case, as interpolation biases are expected in some regions and in some months due to the paucity of data in the CAA. Though the

WOD is not used directly to assess the climatologies, it does provide useful contextual information. Appendix B discusses WOD and the spatio-temporal distribution of observations available for the CAA.

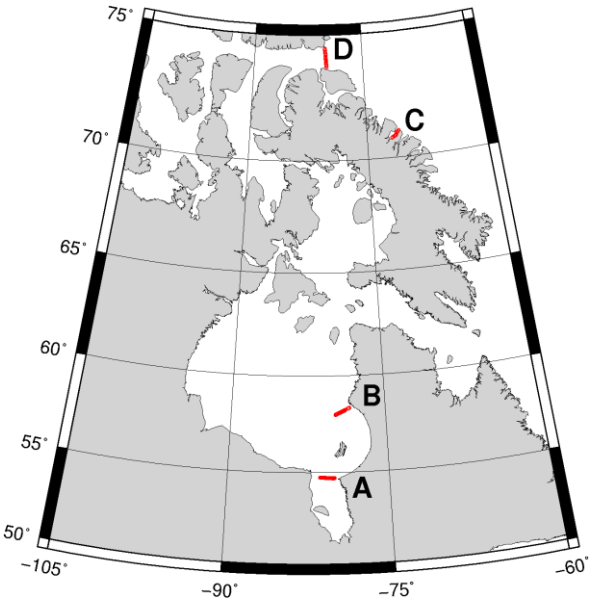

Figure 4-2. MVP transects acquired by the CCGS Amundsen.

A third data set that is of use to this case study is a collection of MVP300 transects acquired by the Amundsen during the 2007 and 2008 field seasons in Hudson Bay and the eastern CAA, respectively. The transects, shown in Figure 4-2, consist of a series of MVP casts collected at high spatial resolution over a short period of time, typically a few hours. These provide high resolution snapshots of spatio-temporal variability that the CTD casts cannot match. Though the Hudson Bay transects fall outside of the area of interest to this study, they nonetheless provide a useful study of shallow water spatial variability (the other transects are collected in deep water) that aids in the interpretation of the results derived from the CTDs. This is especially important as the CTD sampling locations are often biased to deeper depths and climatology performances in shallow water must be inferred from deep water investigations.

The remainder of this chapter consists of a brief discussion of the pre-processing required for the various data sets, followed by a detailed examination of potential

uncertainty using the MVP transects. The geographic scope of coverage is then expanded through an examination of the CTD dataset on a regional basis. Note that a regional map indicating the locations named throughout this case study is provided in Appendix C.

4.2 Pre-processing

MVP casts were collected for 4 transects by the CCGS Amundsen in Hudson Bay and the eastern CAA during the 2006 and 2008 field seasons (see Figure 4-2). The MVP towfish was instrumented with a sound speed probe as well as a CTD sensor, which yields insight into the oceanographic causes of sound speed variability. Data from the CTD sensor are favoured for this reason in this work, and sound speed is calculated from these measurements using the UNESCO equation (Fofonoff and Millard, 1983). Note that all calculations of sound speed in this work use the UNESCO equation, thus no further reference to the method of sound speed calculation will be made.

CTD casts acquired by the Amundsen's CTD/rosette team were provided as binary files shortly after acquisition, at which point they were exported into a text file that included the cast date, time and position as well as the pressure, depth, temperature, and salinity (downcast and upcast). During export to text format, sound speed was calculated from the observed pressure, temperature and salinity and was also included in the exported file. The text files were converted into OMG sound speed profile format (version 2), preserving only the downcast portion of each profile. Profiles were then visually inspected for quality assurance and to identify and remove outlier measurements from further processing. ArcticNet oceanographic stations occasionally collect multiple

casts; in these cases, the deepest cast of the set is retained and the remaining casts are removed from the data set so as not to bias the evaluations with redundant observations of very similar conditions (though these redundant casts do provide opportunities to investigate the temporal evolution of sounding bias and are occasionally used for this reason).

Turning to the climatologies, initial pre-processing steps include converting the potential temperatures (i.e. the temperature a parcel of water would have if brought adiabatically to the surface) of the Kliem and Greenberg climatology to in-situ temperatures by iteratively inverting the UNESCO equation for potential temperature (Fofonoff and Millard, 1983). Climatological temperature and salinity profiles were then generated using a nearest neighbour approach for each of the CTD profile locations. This was followed by computation of the sound speed from depth, temperature and salinity for all three climatologies.

Temporal interpolation was not performed between the monthly climatological grids for the WOA01 or GDEM profiles to ensure that the monthly climatologies could be examined separately as it was suspected that some of the monthly grids were biased due to sparse input data (refer to Appendix B for an extensive discussion of the three climatologies investigated in this work). The WOA01 and GDEM profiles were vertically extended using the nearest neighbour method until a standard depth level is reached at which no neighbour can be found within a search radius of 10 grid cells (each grid cell spans ¼° latitude and ¼° longitude, thus the search area is not circular and is longer in the latitudinal direction). In the event that an observed cast position fell outside the domain of the WOA01 or GDEM climatologies (e.g. due to coarse shoreline

resolution of the models), the observed cast and all derivative files were removed from the data set. Likewise, if any climatological cast consisted of only a surface value (e.g. due to coarse depth resolution of the climatology), the observed cast and its derivatives were also removed. Additionally, CTD casts that were collected outside the bounds of the study area were removed from further analysis, most notably the casts in Hudson Bay and the Labrador Sea. For all ray trace analyses, a constant velocity sound speed model is used in which the sound speed for each layer is calculated from temperature and salinities, whether they are derived from measurements or from climatological means.

4.3 MVP300 Transects

The four transects acquired by the Amundsen are separated significantly in time and space; thus they provide only interesting snapshots of how the variability of the water column can vary and very little can be extrapolated from any analyses thereof. Nonetheless, these snapshots provide useful information in this analysis as they provide high resolution measurements of water column spatio-temporal variability. This type of information can help interpret results from analyses based on the CTD data set which is spaced much more evenly throughout the domain but suffers from a lack of spatial and temporal resolution. The case study begins by examining these 4 transects in terms of their variability through a VA, followed by a UA to ascertain how the WOA01 climatology would impact sounding accuracy had it been used instead of the MVP measurements. For the sake of brevity, the MVP analysis is limited to the WOA01

climatology. The WOA01 climatology was chosen in this case over the other two as it is already heavily used in ArcticNet post-processing (Beaudoin et al., 2008).

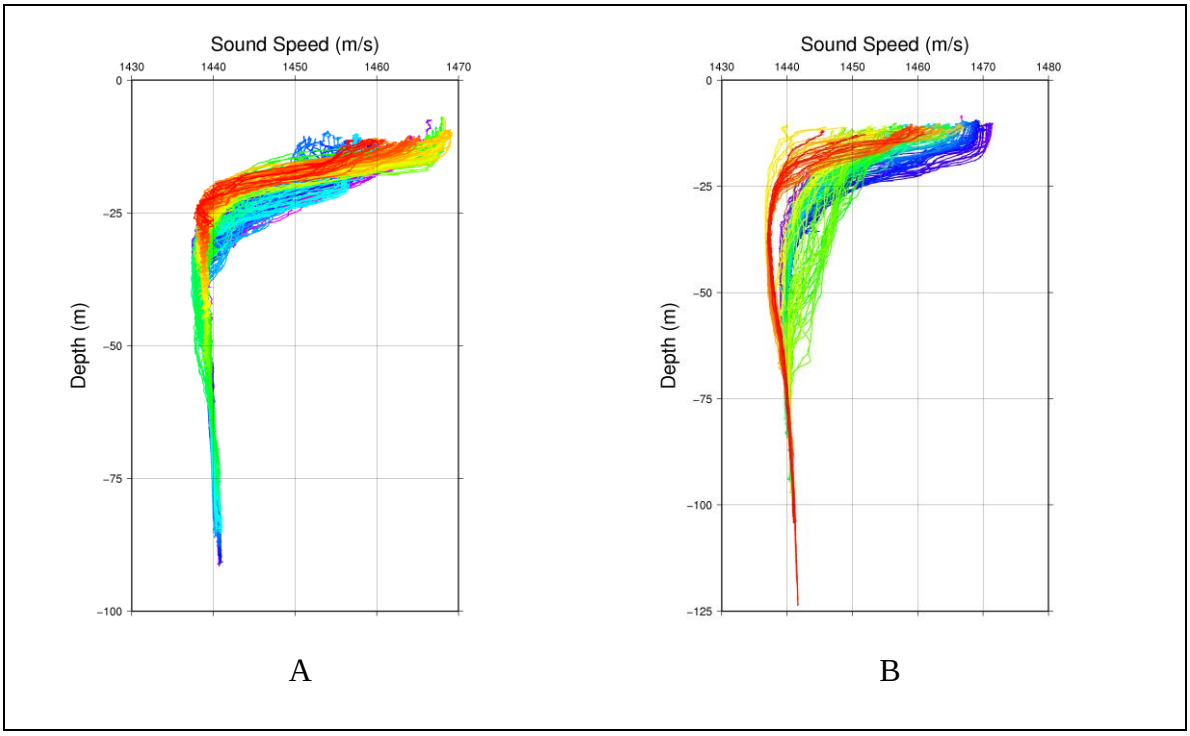

Figure 4-3. Sound speed casts from transects A and B. Colour coding of casts varies with time (see Figure 4-6).

4.3.1 Transects A and B

Sound speed casts from transects A and B are plotted in Figure 4-3, letter labeling of the panels corresponds to labeled locations in Figure 4-2. Transects A and B, collected on August 11th and 6th 2007, respectively, were both approximately 90 km in length with water depths ranging from 25 m to 125 m. Both locations were characterized by a warm and brackish surface layer (2-8°C, 25-29 psu), extending to a depth of 40 m for transect A and 65 m for transect B with the surface layer of transect B being cooler and saltier than that of A (see figures 4-4 and 4-5). Deep water at both locations had similar temperature

and salinity values, -1.25°C and 32.4 psu, respectively. Referring to the plots of Figure 4-6, the casts of transect A varied primarily in the depth of the thermocline with the thermocline depth oscillating between 20 m and 30 m over the length of the transect with a gradual rising toward the western end of the transect. Observations from transect B differed markedly with more pronounced thermocline depth oscillations, with occasional near complete erosions of the thermocline consistent with intense upper water column mixing (most notably in the central portion of the western sector).

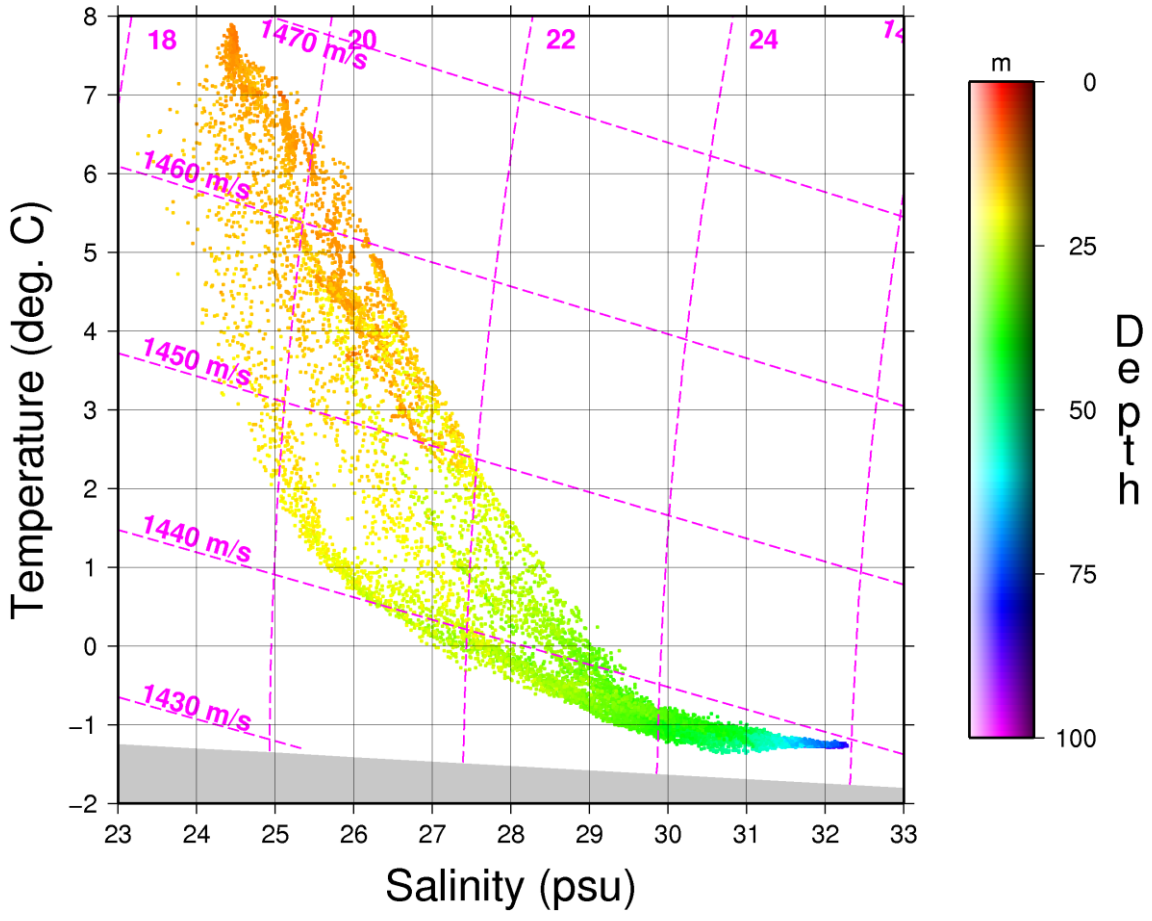

Figure 4-4. T-S diagram for transect A. Sigma-density and sound speed contours are overlaid for reference (dashed magenta lines). Both of these are computed at the sea surface and do not reflect the change in either parameter due to increasing pressure with depth.

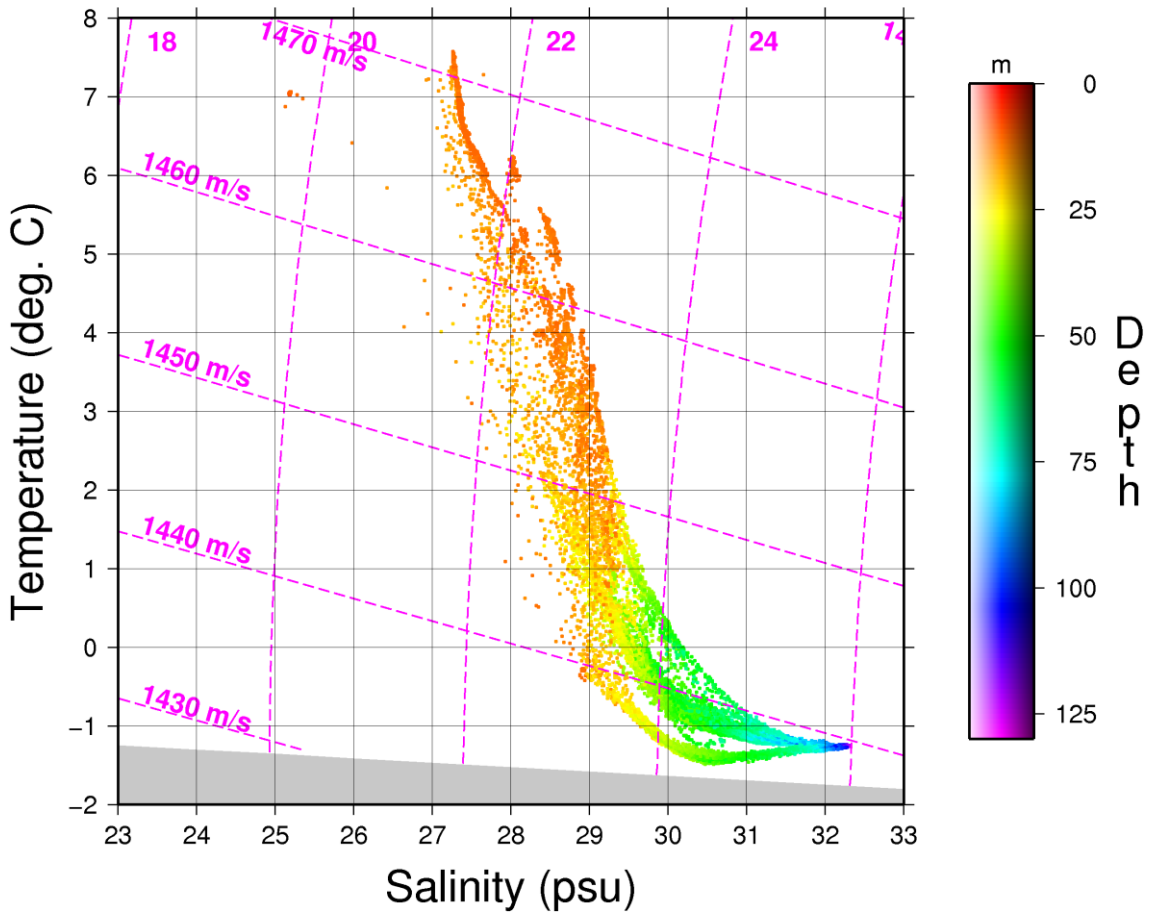

Figure 4-5. T-S diagram for transect B.

A VA was performed to quantify the impact that the differing conditions would have on sounding uncertainty; analysis parameters were set to match the sounding geometry of the Amundsen's MBES (120° angular sector, draft of 6.7 m and a surface sound speed probe). The Amundsen's 1°x2° EM300 yields a footprint which is, at best, approximately 1.7% x 3.5% of the water depth (w.d.); the horizontal component of refraction based uncertainties in this analysis (and all remaining analyses) are smaller than the resolution abilities of the EM300 system, thus the VA and UA examinations in

this case study are limited to the vertical dimension only (however, analyses for MBES with higher angular resolution and more stringent horizontal accuracy requirements should include the calculation of horizontal uncertainties). Finally, it should be noted that the VA and UA methods undertaken throughout the remainder of this work are done without any extension of the uncertainty profiles (cf. Section 3.6); thus many of the uncertainty estimates suffer from discontinuities beyond the depth at which the number of contributing sound speed profiles begins to decrease from the total number in each examination.

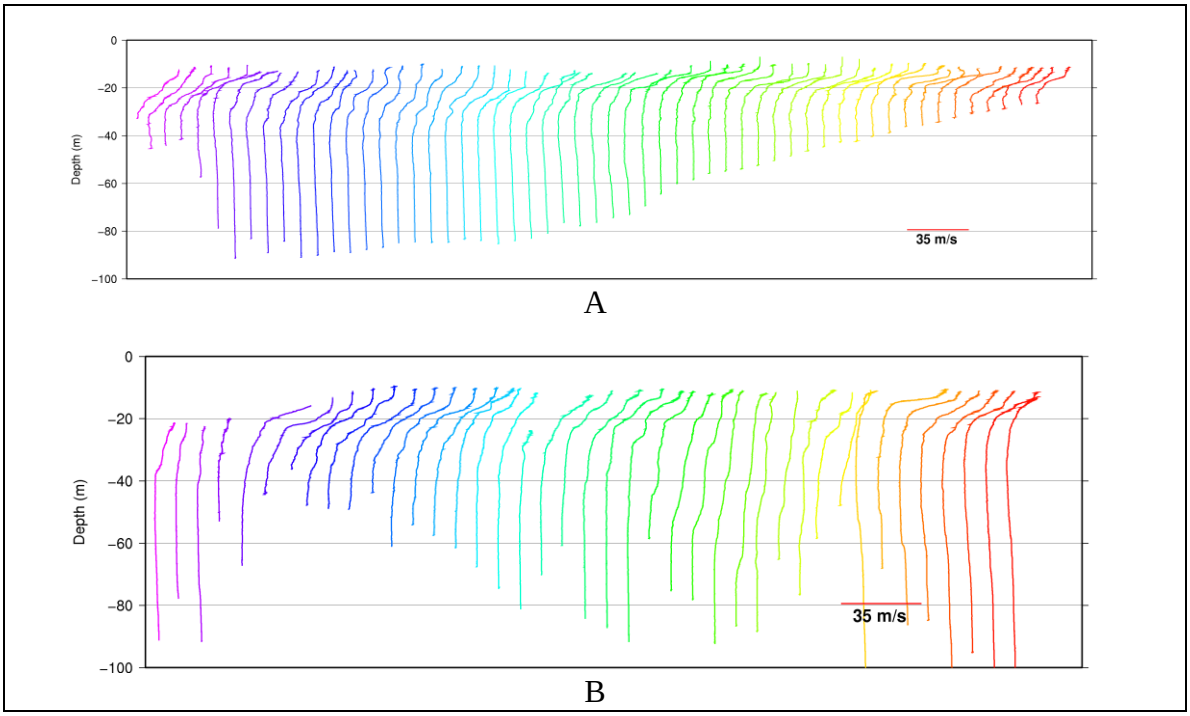

Figure 4-6. Plots of successive sound speed casts for transects A and B, with time on the x-axis. The right side of each plot corresponds to the western end of each transect (look direction is from the north). Colour coding of casts corresponds to that of Figure 4-3, note that the number of casts plotted was thinned by a factor of 5 as compared to Figure 4-3.

V-wedges for transects A and B are shown in Figure 4-7, with an uncertainty section at a depth of 75 m shown in Figure 4-8. The variability encountered over transect B has roughly three times the impact of that observed along transect A with a maximum

uncertainty of +/- 0.35 m in the outermost section of the Amundsen's angular sector at a depth of 75 m. For context, IHO Special Order, Order 1A/B and Order 2 surveys would allow vertical uncertainties of 0.61 m, 1.10 m and 1.99 m at this depth, respectively. Though the observed variability is interesting, it is hardly significant from a hydrographic surveyor's point of view if the only aim is to meet any of the IHO survey orders in 75 m of water.

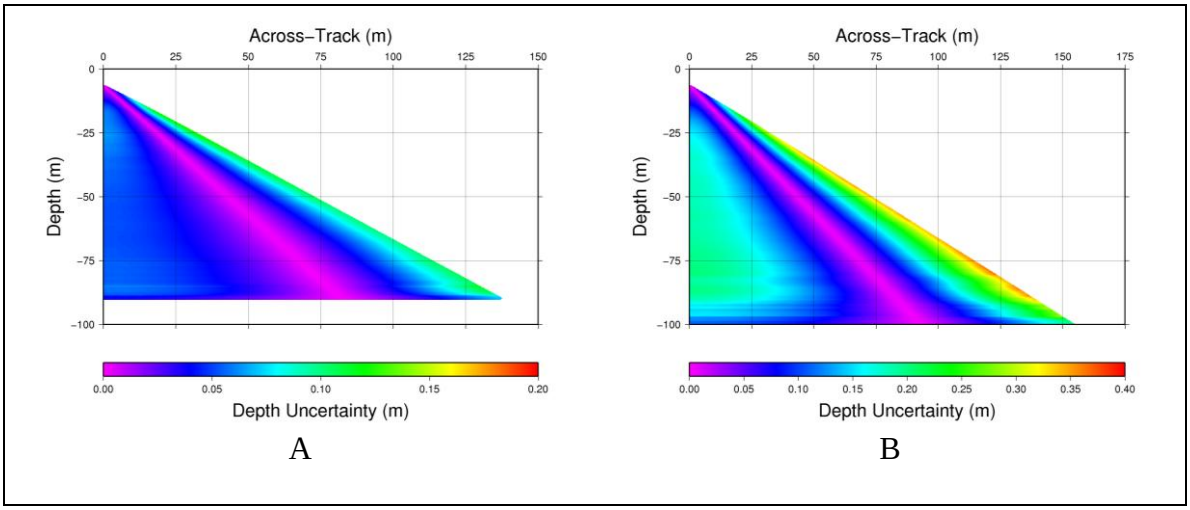

Figure 4-7. V-wedges for transects A and B.

It is useful to examine the v-wedges with uncertainty expressed in percentage of water depth, as in Figure 4-9, where it is clear that though the variability is of little concern at 75 m depth, this is not the case for shallower depths. The spatial variability observed over transect B suggests that it would be imprudent to plan long survey lines in shallow water under these types of conditions, unless underway sound speed profiling instrumentation is available. The VA also suggests that there may be cause for concern when using a climatology for sounding reduction while in transit through the shallow coastal waters of Hudson Bay. Figure 4-10 shows the WOA01 casts based on the position and date of the MVP casts from transects A and B. In the case of transect A, the

MVP measurements are slightly cooler (~0.5° C) and fresher (~0.5 psu) than the WOA01 means and the measured sound speed is slower than that predicted by WOA01 over most of the lower portions of the water column. Transect B was also cooler than the WOA01 mean (~0.7° C) with little difference in salinity over the water column, thus measured sound speed was also slower than the WOA01 prediction.

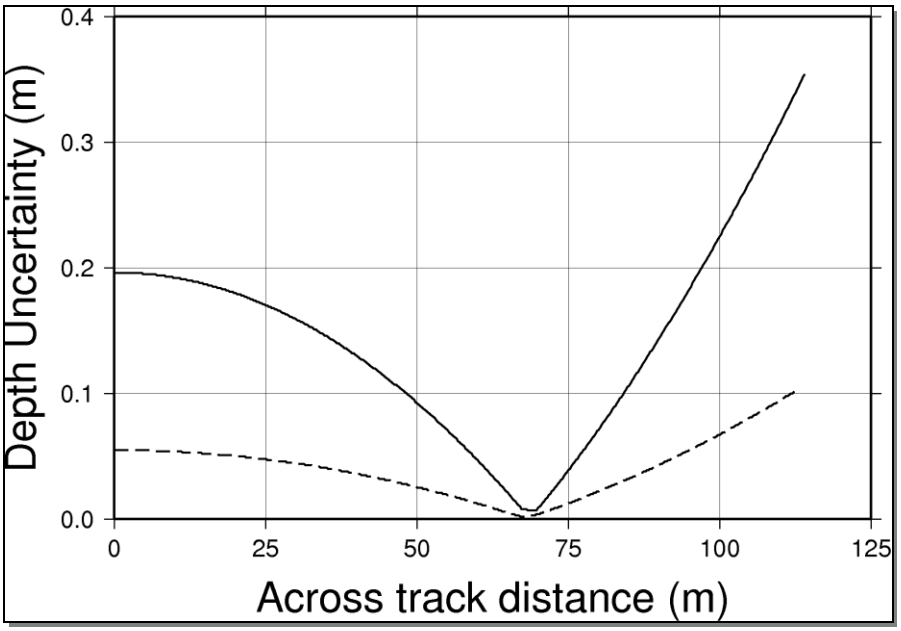

Figure 4-8. Uncertainty sections at 75 m depth for transect A (dashed) and B (solid).

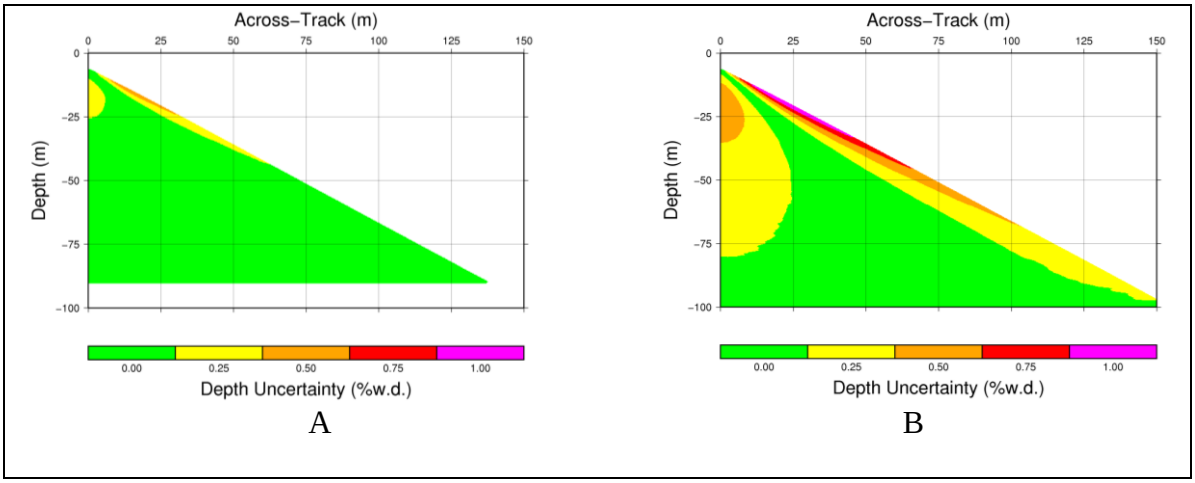

Figure 4-9. V-wedges for transects A and B, expressed in percentage water depth.

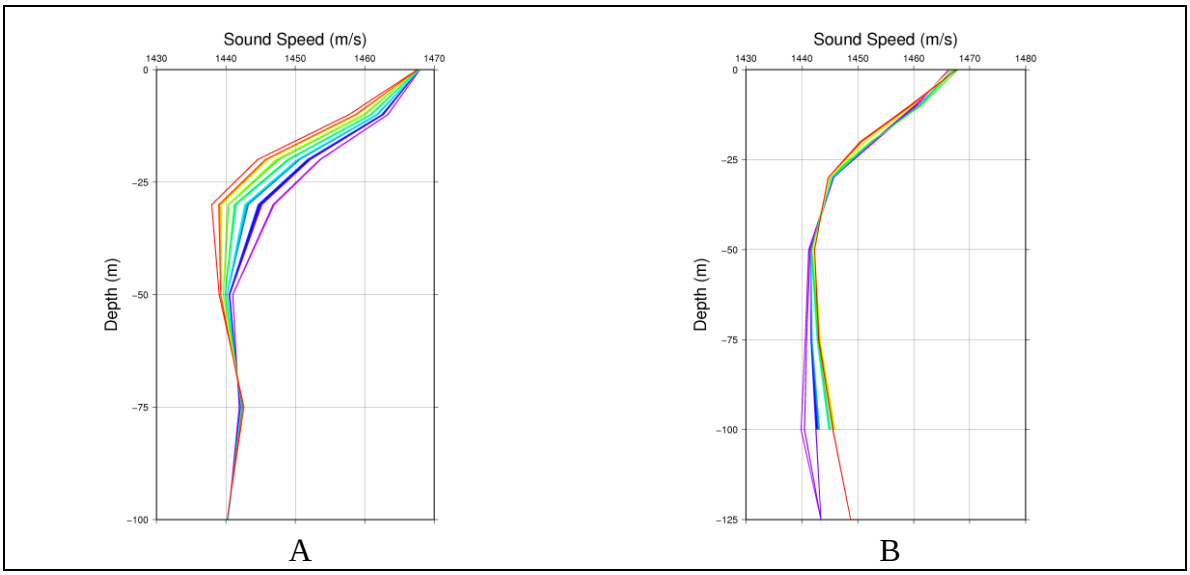

Figure 4-10. WOA01 casts for transects A and B.

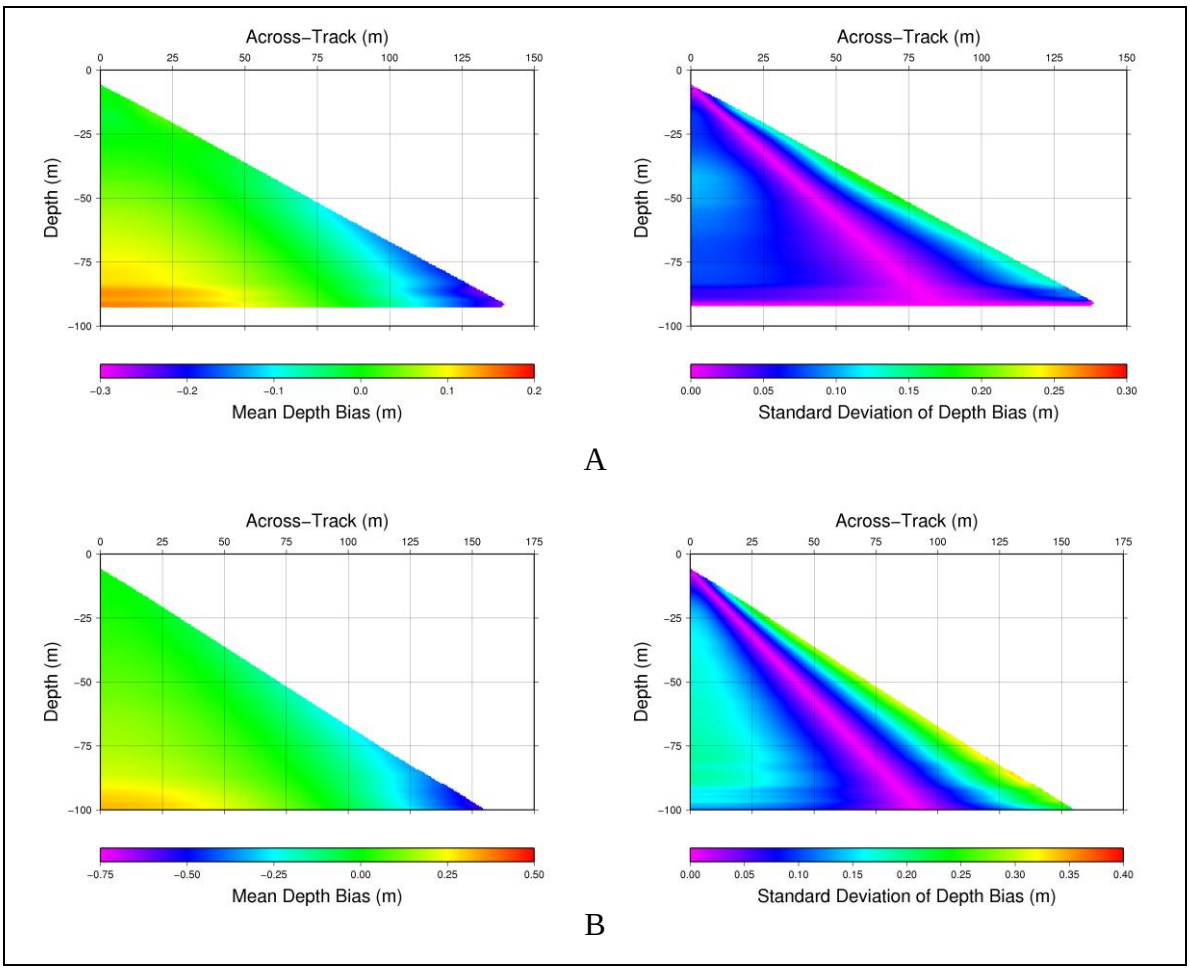

Figure 4-11. UA results for comparison of WOA01 to transects A and B.

UA can be used to summarize the sounding uncertainty associated with using WOA01 by calculating b-wedges and tabulating them into an m-wedge and an s-wedge. These are shown for both transects in Figure 4-11; for comparison purposes, the bias and standard deviation of the outermost beam is plotted as an uncertainty profile for both transects in Figure 4-12 and an uncertainty section at a depth of 75 m is plotted in Figure 4-13. In both transects, using the WOA01 would have resulted in an appreciable sounding bias as the average conditions depicted by WOA01 differed from the average conditions during acquisition of the two transects; as the bias persists over the water column, the sounding bias increases with depth as shown in Figure 4-12. This is not to say that WOA01 is incorrect, or biased (though it very well could be). Instead, this simply captures the effect that observed conditions were slightly cooler than average conditions. Referring to Figure 4-13, the net result on soundings is a slight, but persistent, "smile" artifact with this effect being more pronounced over transect B than A.

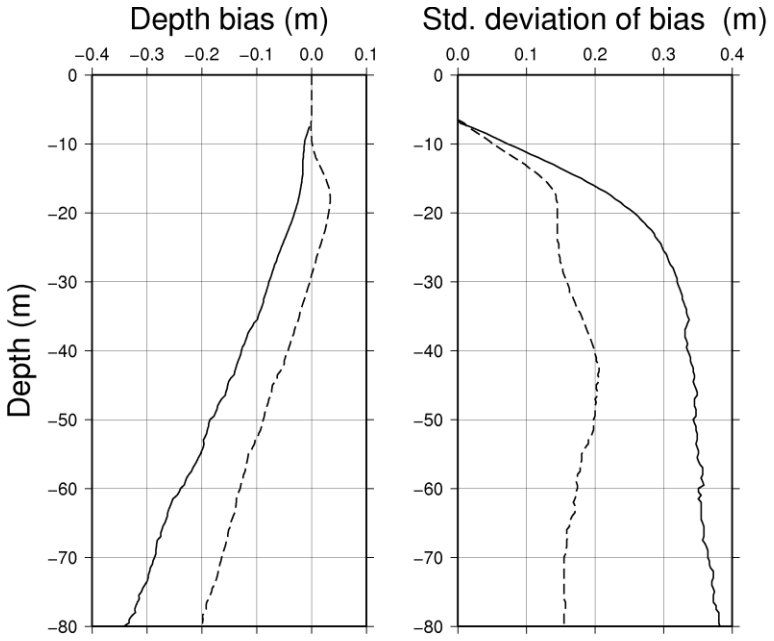

Figure 4-12. Uncertainty profiles associated with use of WOA01 for transect A (dashed) and B (solid).

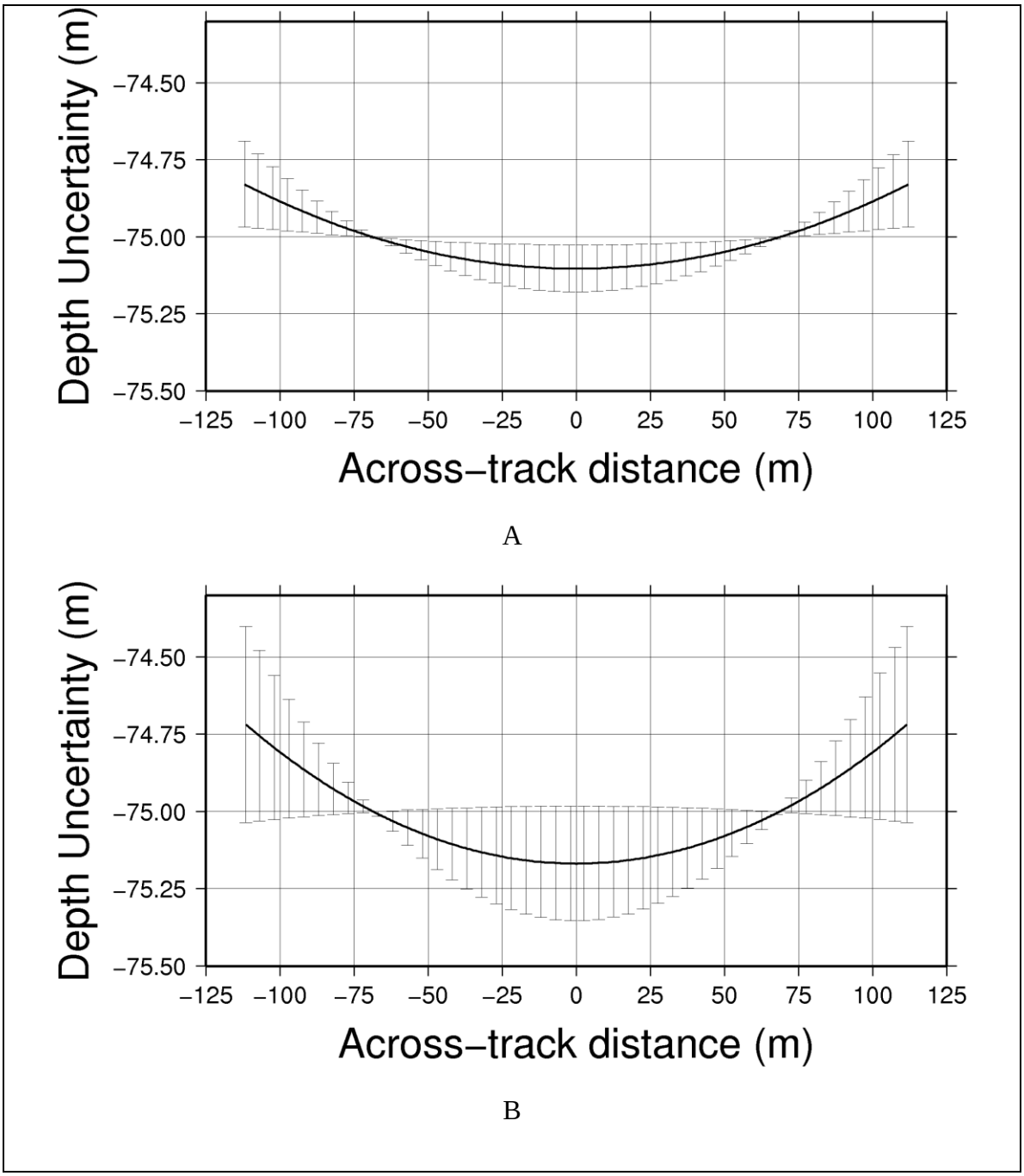

Figure 4-13. WOA01 uncertainty sections for transects A and B at a depth of 75 m. The mean "smile" bias, as derived from the m-wedge, is plotted as the solid line, with uncertainty about the mean coming from the s-wedge.

The s-wedge, on the other hand, captures the inability of a heavily smoothed climatology to represent fine scale spatio-temporal water mass variability. The

uncertainty profiles of Figure 4-12 show that sounding uncertainty increases rapidly in the upper 20-30 m with growth tapering off once past the depth of the thermocline. Thus, there are two effects: the mean bias in temperature and salinity and the spatio-temporal variability of these. The first causes the overall "smile" artifact whereas the second alters the magnitude of the artifact, in some cases exacerbating it, and in others, completely cancelling it out.

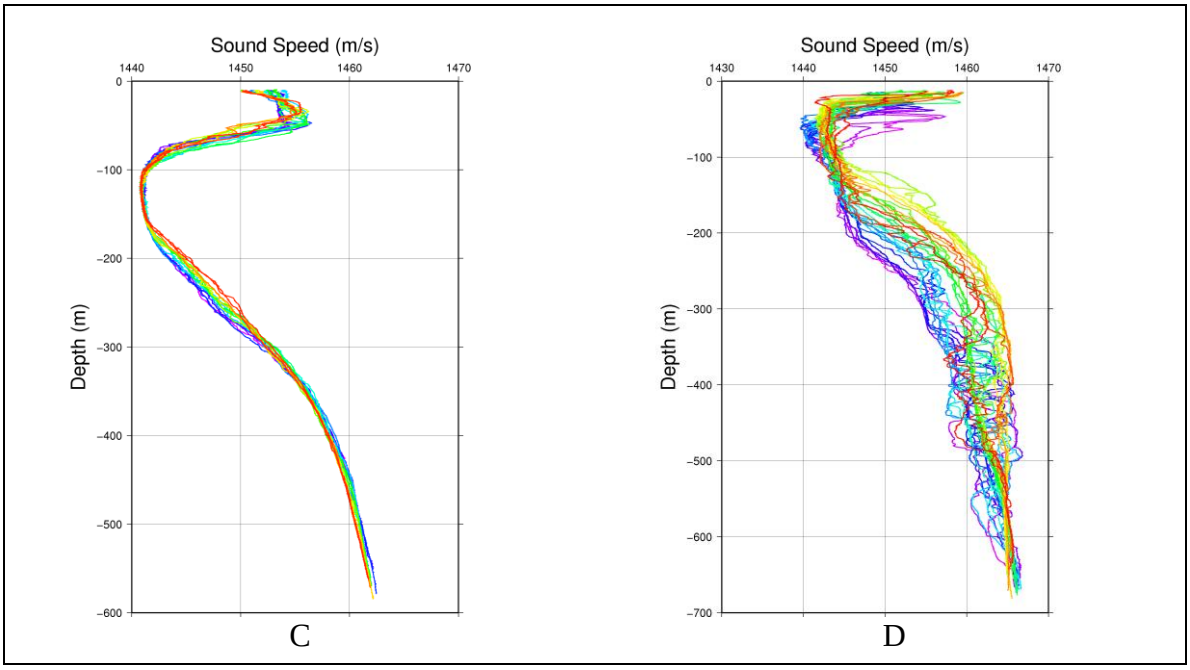

Figure 4-14. Sound speed casts from transects C and D.

4.3.2 Transects C and D

Transects C and D were collected in 2008 on September 24th and 9th, respectively. Transect C was acquired in Clark and Gibbs fjord on Baffin Island with sampling depths reaching nearly 600 m over the 50 km transect into the fjord. Transect D, approximately 80 km in length, was collected across the mouth of Lancaster Sound with sampling

depths ranging from 600 m to 675 m in water depths that reached just over 800 m in some locations. Sound speed casts from both locations are plotted in Figure 4-14 with transect D exhibiting pronounced variability over the entire water column relative to transect C in the fjord. Figures 4-15, 4-16, 4-18 and 4-19 show sound speed plots and T-S diagrams for both transects. Referring to the T-S diagrams, both water masses were consistent with typical summer conditions in the CAA: a brackish and warm surface layer sits on top of near freezing and slightly saltier water. This layer, in turn, sits on top of a warm and salty deep water mass of Atlantic origin. Variability along transect C consisted of a steady change in the nature of the upper 50 m due to temperature variations along the transect (see Figure 4-15). Referring back to Figure 4-14, oscillations of 15-20 m were observed on the upper thermocline between the warm surface water and mid-water cold water (extending from 50 m to 100 m depth). The lower thermocline, extending from 150 m to 450 m, steadily rose by approximately 40 m while transiting from the mouth to the head of the fjord (easily observed in the sound speed plots of Figure 4-14).

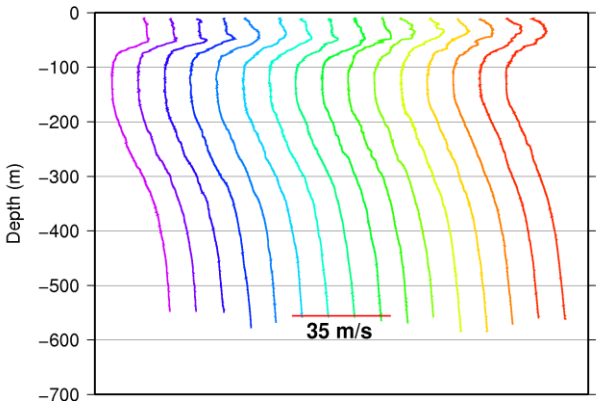

Figure 4-15. Plot of successive sound speed profiles from transect C. Look direction is from the north, with the head of the fjord on the right side of the plot.

Transect D is characterized by much more variability with water column structure varying dramatically in the upper 50 m and with complex temperature structure at depth for most of the casts. Of particular note is the rising of the lower thermocline from north to south. This is consistent with separation of inbound and outbound flow in the wide

channel with Arctic Ocean surface outflow through the CAA being bound to the southern coast with a deep counter flow of Atlantic Water on the along the northern coast (Leblond, 1980). Note the mass of deep warm water at the northern end in the temperature section of Figure 4-17. A lens of warm water was observed at similar depths in the southern half of the transect, with the lens deforming significantly in depth (500 m to 350 m) over a distance of 25 km. The source of this deep water variability is explored later in Section 4.4.1. The discussion at this point is limited to the effects of such variability on sounding accuracy.

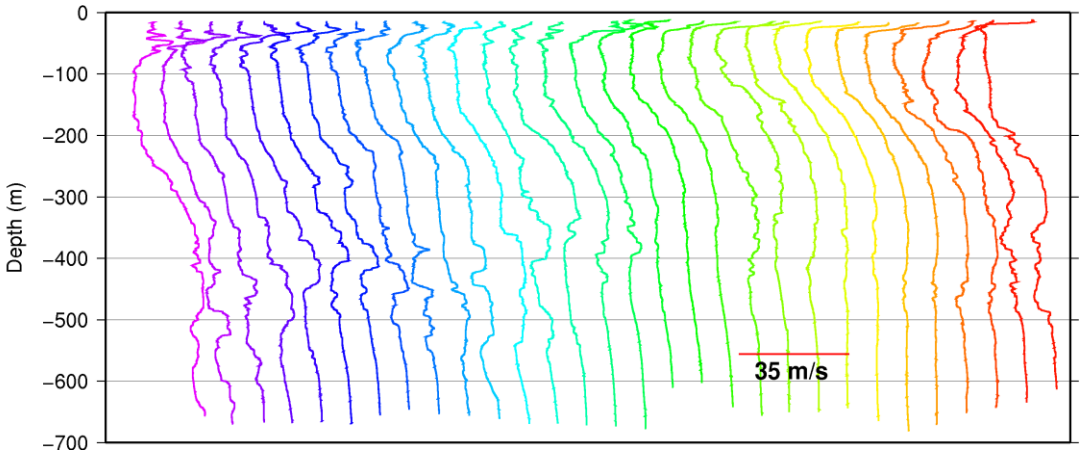

Figure 4-16. Plot of successive sound speed profiles from transect D across Lancaster Sound. Look direction is from the east with the northern end of the transect on the right side.

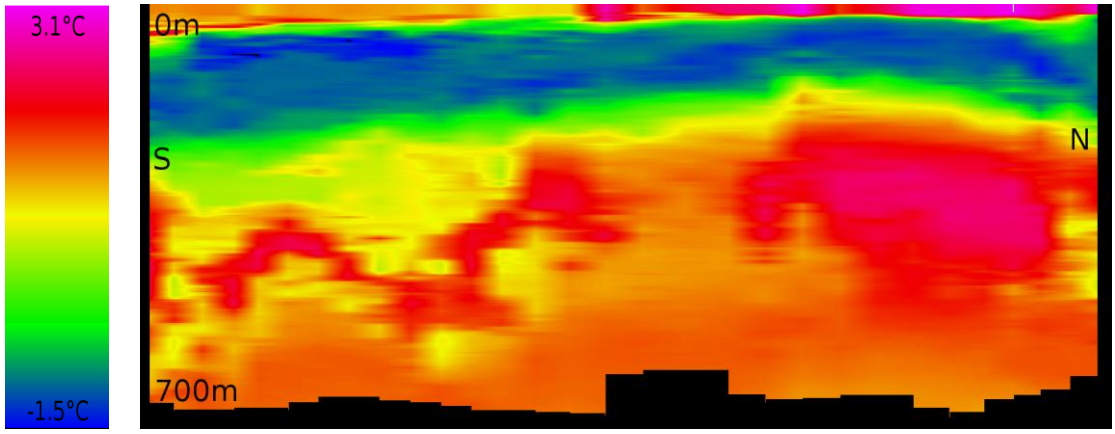

Figure 4-17. Temperature section of transect D. Note the deep warm lens in the south and the larger warm plug of warm water on the northern end of the transect.

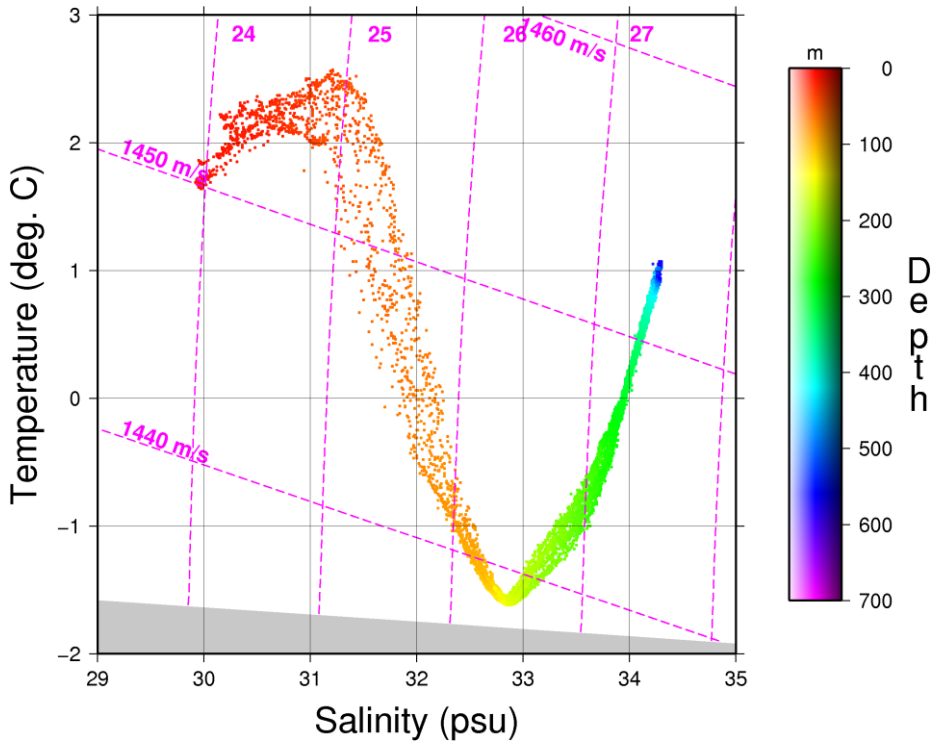

Figure 4-18. T-S diagram of casts for transect C.

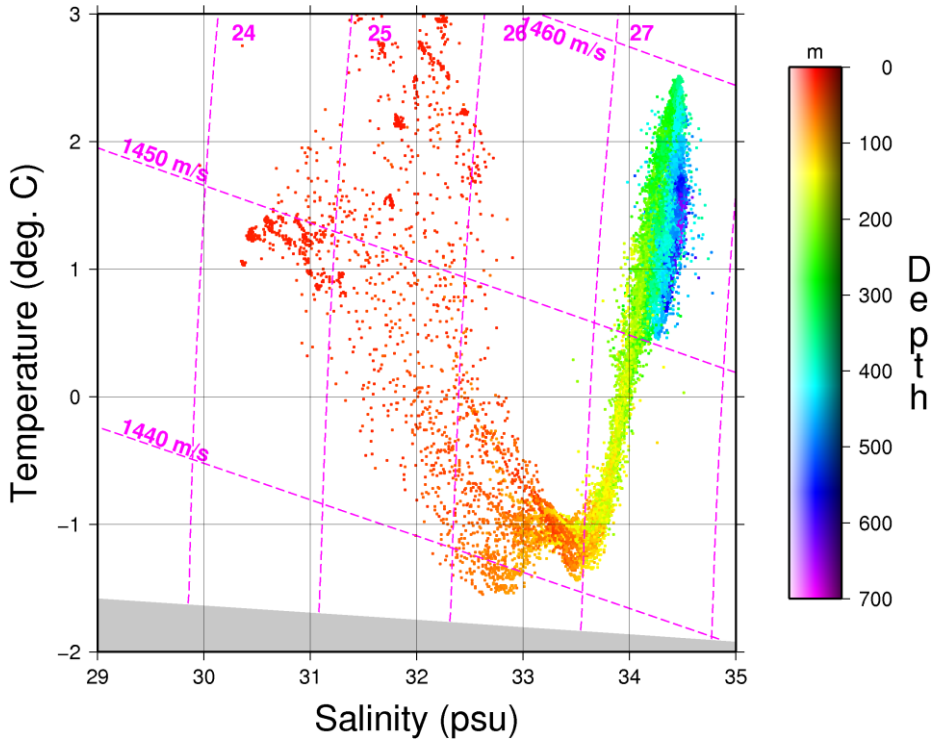

Figure 4-19. T-S diagram of casts from transect D.

A VA was performed on both transects, the result v-wedges are shown in Figure 4-20. Not surprisingly, the variability over transect D has approximately an order of magnitude more impact on sounding accuracy relative to that of transect C.

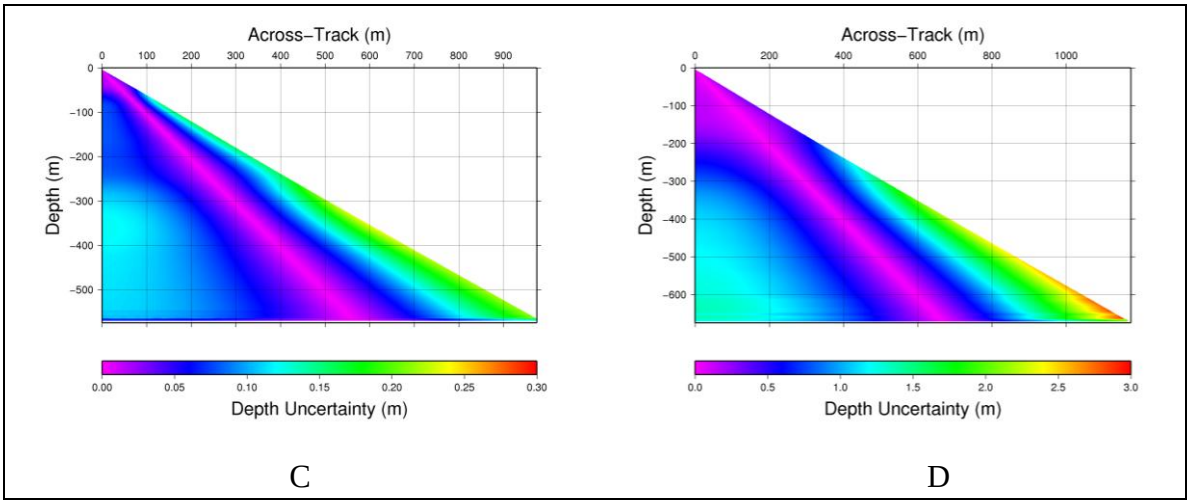

Figure 4-20. V-wedges for transects C and D.

It is informative to examine the depth evolution of the uncertainty for both these transects as they differ from the previous two transects in maximum sampling depth and in variation of variability over the depth of the casts. Figure 4-21 shows plots of the depth uncertainty associated with the outermost edge of the v-wedges of Figure 4-20, the lower panel plots the same profiles but focuses on the upper 400 m and changes the aspect ratio to highlight the variations in uncertainty with depth. Examining transect C first, the impact of the aforementioned types of variability can be quantified: surface variability from 0 to 50 m introduces ~0.05 m of sounding uncertainty; the upper thermocline variability introduces an additional ~0.10 m of uncertainty with another ~0.10 m of uncertainty deriving from the variability associated with the lower thermocline.

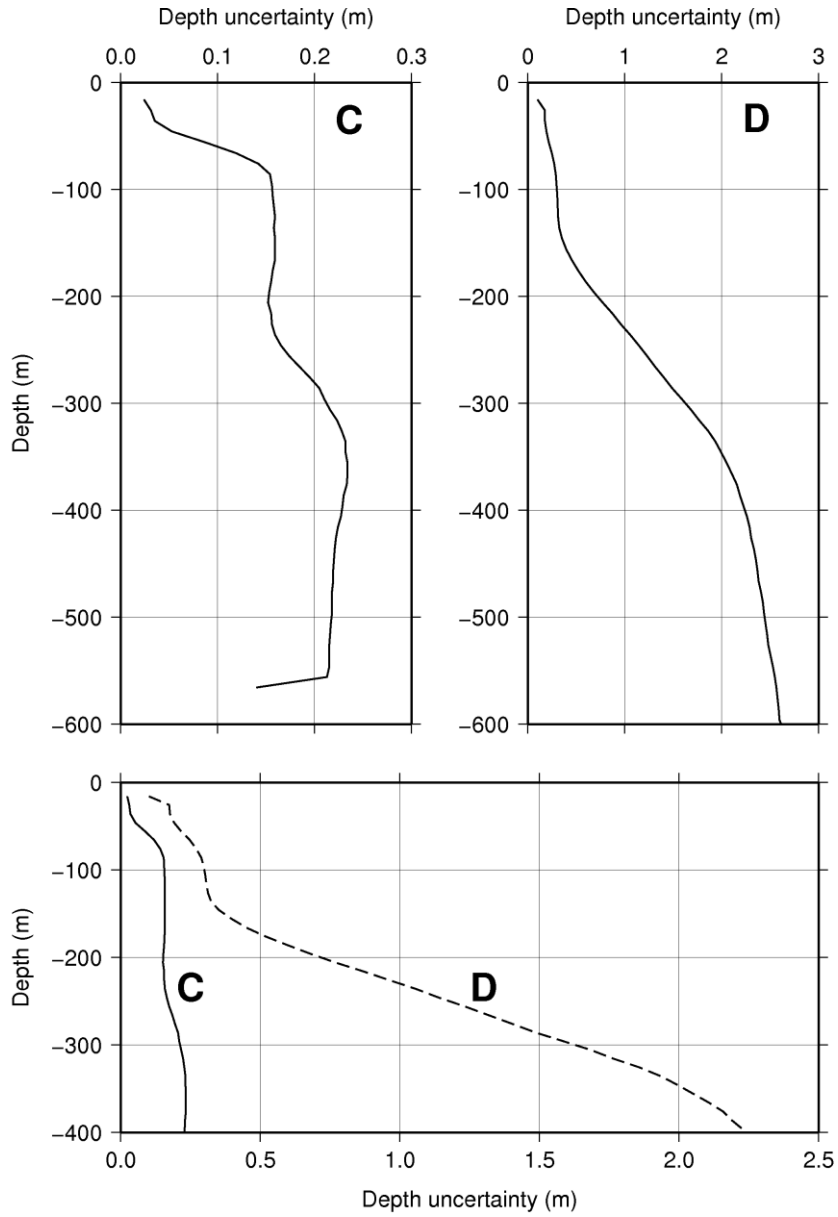

Figure 4-21. Uncertainty profiles for transects C and D. The upper panels have differing x-axis scales whereas the bottom panel plots both curves at the same scale. Note that the kink in the lower portion of the uncertainty profile for transect C is due to the drop in number of observations contributing to the variance estimate near the terminal depth of the casts.

Turning to transect D, the incremental increases in uncertainty due to surface and upper thermocline variability are small in comparison with the pronounced variability at depth, thus the same two profiles are plotted again in the lower panel of Figure 4-21 with the aspect ratio optimized to show the detail in the upper portion of the uncertainty profiles. Variability in the upper 50 m accounts for ~0.2 m of sounding uncertainty, twice that

observed in transect C. An additional ~0.15 m is introduced travelling from 50 to 100 m depth. As expected, the largest portion of the uncertainty is due to the significant variability below ~110 m, adding ~2.3 m of uncertainty and accounting for approximately 90% of the total observed uncertainty at 600 m depth (~2.6 m, or 0.4% w.d.).

Recall that these transects were acquired with an MVP300, which allows for sampling up to 300 m depth while travelling at 12 Kts. The fjord could have been surveyed at 12 Kts with little impact to sounding accuracy as the variability below 300 m is largely inconsequential and a single deep cast would have sufficed to extend all other casts to the necessary depth for ray tracing. This is not the case for the transect across Lancaster Sound. The most important variability was at great depth, which could only be sampled by the MVP300 with a significant reduction in vessel speed (this particular transect was sampled at ~ 6 Kts and took ~7 hours to complete). It is important to note that water depths reach up to 800 m across this section of Lancaster Sound AND that the uncertainty continues to grow with depth, suggesting that even deeper sampling might be required (refer to the upper right panel of Figure 4-21).

Interestingly, the vessel doubled back on transect D and collected a single CTD cast 4 hours after the same location had been sampled by the MVP (cast 21 of 30), roughly one quarter of the distance from the northern end of the transect. The CTD/MVP casts from the same location are plotted in the left panel of Figure 4-22. For comparison, the same MVP cast (21) is plotted in the right panel along with the preceding and following MVP casts (casts 20 and 22, which were collected 16 minutes before and after cast 21, with a spacing of 3.1 km between each cast).

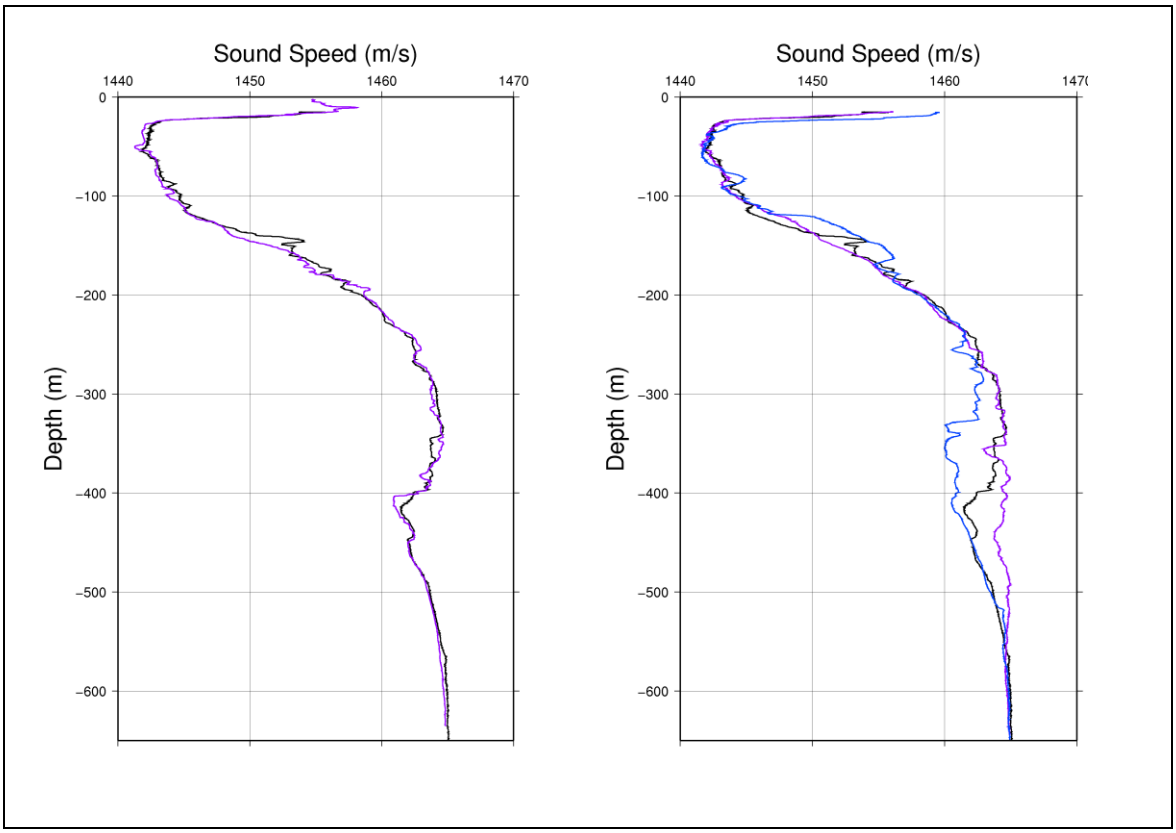

Figure 4-22. Sound speed profiles from co-located CTD and MVP cast 21 (left) compared to MVP collected in sequence along the transect (casts 20-22, right). MVP cast 21 is plotted in black in both panels.

These casts provide an opportunity to assess spatio-temporal decorrelation of the water mass in terms of sounding accuracy through the use of UA by calculation of b-wedges with MVP cast 21 being the reference cast to which all others are compared. The b-wedge derived from comparing the co-located CTD cast and MVP cast 21 yields an outer beam depth bias of 0.11 m at a depth of 600 m. Comparing all remaining MVP casts to MVP cast 21 gives a set of 29 b-wedges, for which the outer beam depth bias from a depth of 600 m is plotted in Figure 4-23. The time separation of 4 hours between MVP cast 21 and the CTD cast has negligible effect (0.11 m, or 0.02% w.d.) compared to the increase of bias with distance across the Sound, which increases at a rate of approximately 0.5 m/10 km or 0.08%w.d./10km. This suggests that the variability is

primarily spatial in nature in the across-channel direction, and that temporal variability has a small effect in comparison.

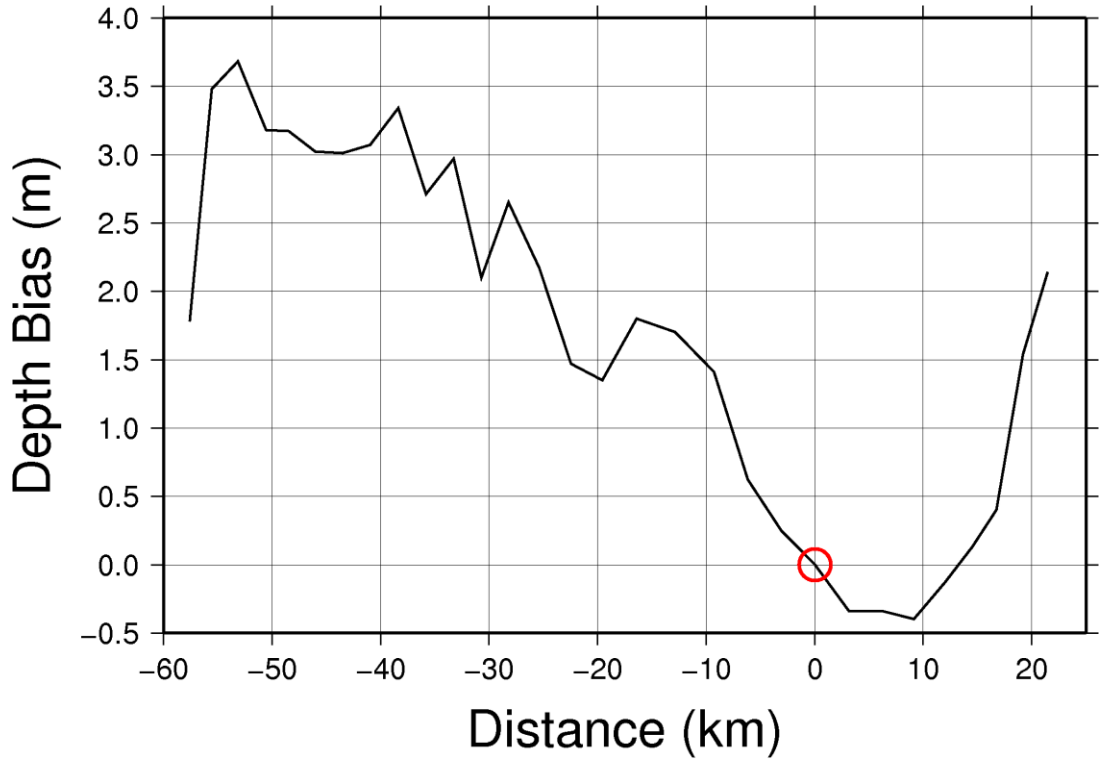

Figure 4-23. Outer beam (60° incidence angle) depth bias at 600 m depth resulting from UA of all MVP casts relative to MVP cast 21. Distance is measured relative to the location of MVP cast 21 (marked with a red circle), with south being on the left and north on the right.

CTD casts from ArcticNet stations with multiple casts along the main axis of Lancaster Sound lend support to this idea. Figure 4-24 shows the temporal evolution of outer beam depth bias for 6 stations with multiple casts, with depth bias expressed as a percentage of water depth due to the station depths varying between 200 – 800 m. Stations were occupied throughout August to October over the years 2005 to 2008. All stations with more than 2 casts exhibit a growth of bias with time though there are insufficient data in terms of temporal resolution and record length to draw any conclusions from the entire set. At the very least, all 6 stations support the notion that temporal variability is largely insignificant, especially when compared to the required

accuracy of common non-critical keel depth survey orders, e.g. IHO Order 1 requires 1.3% w.d. accuracy in the vertical.

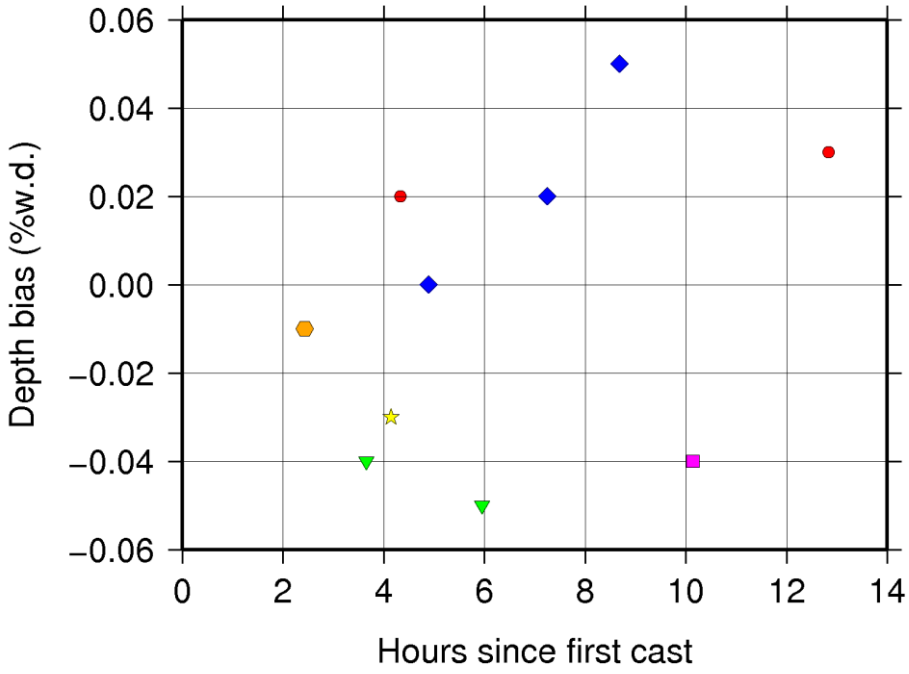

Figure 4-24. Water column temporal stability for 6 multi-cast stations in Lancaster Sound. Stations are distinguished by the coloured symbols with time referenced to the acquisition time of the first cast collected upon arrival at each station.

Simulated sound speed casts from WOA01 were generated for each of the casts of the two transects. The WOA01 casts from both transects predict little spatial variability; a cast from each transect is shown in Figure 4-25 along with the first and last MVP cast from each transect for context. This is not surprising for transect C as the fjord is not well represented in the WOA01 due to the coarse resolution, thus the nearest neighbouring grid node at the mouth of the fjord was the sole contributor for the entire transect (furthermore, no observations exist for the fjord in the WOD). Transect D only spans four WOA01 grid nodes (60 NM) and the climatology retains very little horizontal resolution due to the degree of smoothing that is applied during construction (refer to

Appendix B for details on the construction of WOA01). Examining casts from transect C, WOA01 predicts a much shallower upper thermocline and much deeper lower thermocline and the observed sound speed structure is much "faster" on the whole than mean conditions, resulting in a "frown" type artifact from the use of WOA01. Turning to transect D, WOA01 predicts a much less stratified sound speed structure due to the upper layer being ~0.5°C warmer and the lower layer being cooler by 1.0 – 1.5°C than the WOA01 average. On the whole, the observed sound speeds are faster than WOA01 predicts, when averaged over the water column.

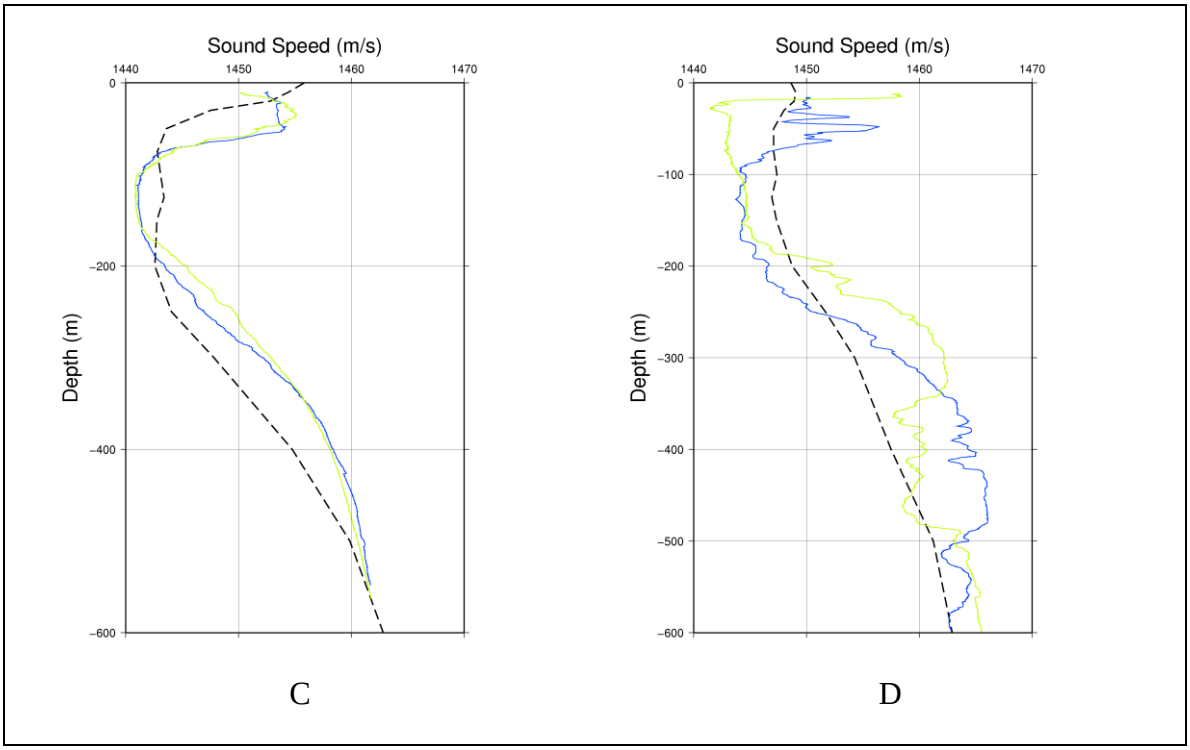

Figure 4-25. WOA01 casts for transect C and D. The first and last MVP casts from each transect are plotted for context in blue and green, respectively. The WOA01 cast for each transect is plotted as the dashed black line.

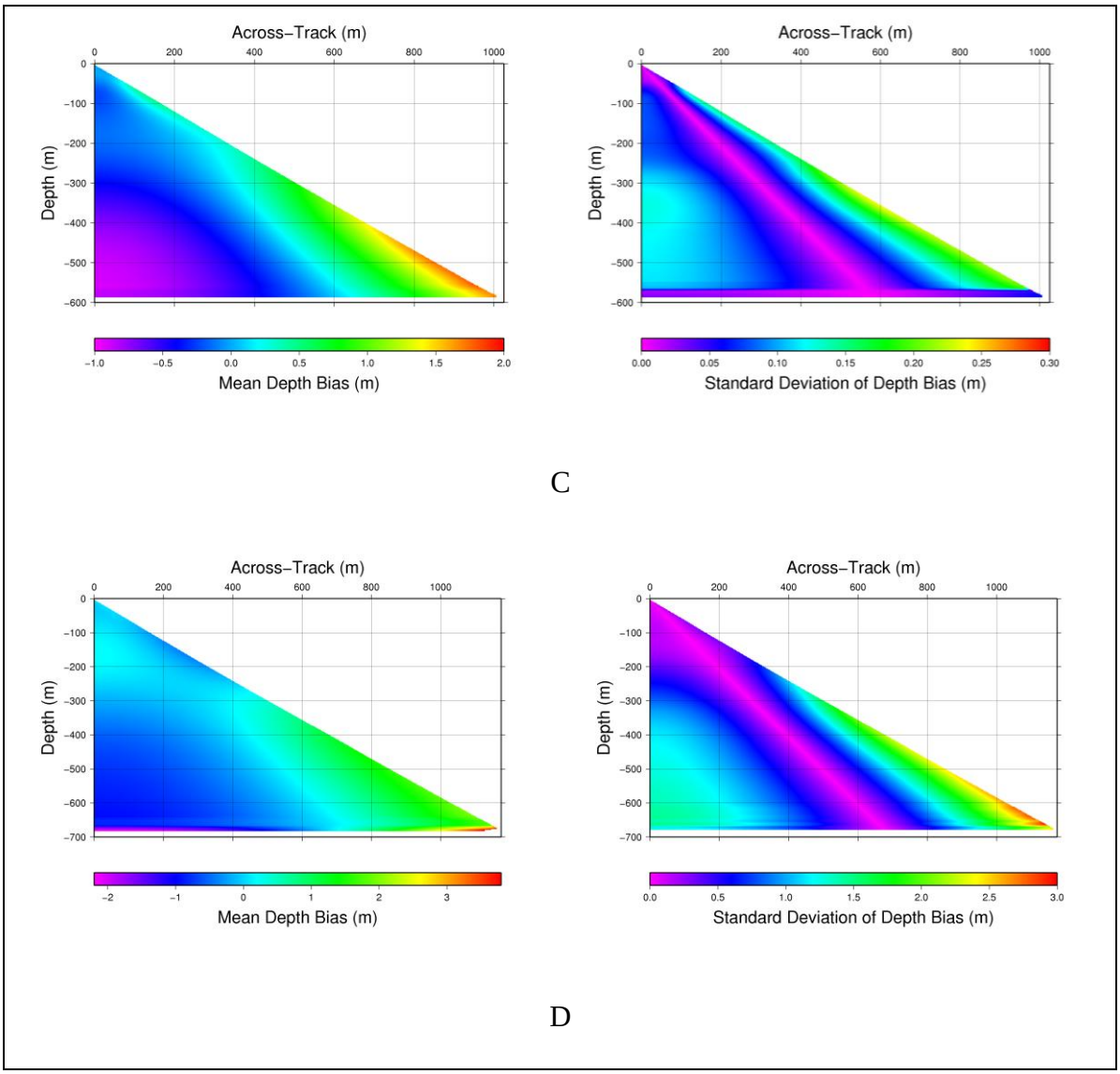

Figure 4-26. WOA01 m-wedges and s-wedges for transects C and D.

A UA was performed to assess the WOA01 casts following the method used in Hudson Bay with a set of b-wedges being generated for each MVP/WOA01 comparison. M-wedges and s-wedges were compiled for both transects and are shown in Figure 4-26 with uncertainty sections at 600 m depth shown in Figure 4-27. Using an unvarying depiction of the water column across these transects would result in soundings that suffer from the full effect of variability; the s-wedges therefore closely approximate the v-wedges shown earlier. In addition to this, the WOA01 casts are a poor predictor of the

mean conditions found over each transect, as captured by the m-wedges. Thus, not only would soundings suffer the full effect of the variability, but they would also be heavily biased. This is best observed in the uncertainty sections of Figure 4-27. Transect C would suffer slightly more bias than transect D, however, variability would play a much stronger role over transect D. Though both transects would suffer a systematic "frown" artifact, there are occasions when WOA01 casts would result in very little bias along transect D. Figure 4-28 demonstrates how the WOA01 bias is minimal at the beginning of the transect and increases with distance from the southern end; even though conditions differ markedly from the WOA01 at the southern end (the upper water is cooler than average and the lower water is warmer than average), the net effect nearly cancels out over the course of the ray trace, resulting in very little bias for some casts.

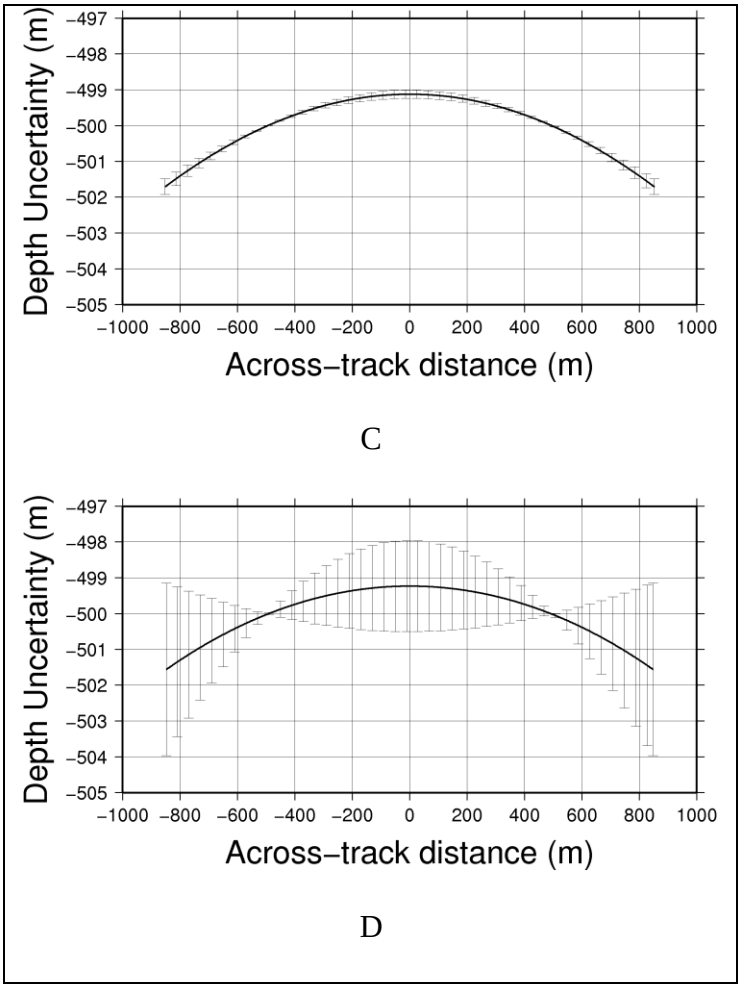

Figure 4-27. Mean WOA01 bias at a depth of 500 m for transects C and D.

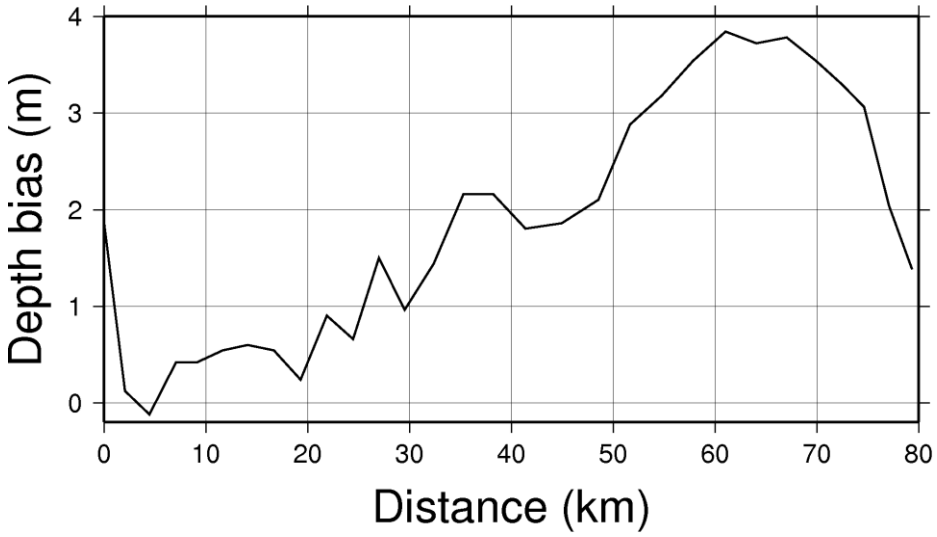

Figure 4-28. Evolution of outer beam depth bias associated with WOA01 over transect D. Distance is referenced to the southern end of the transect.

4.3.3 Discussion

The investigation of the high resolution MVP transects indicated that there is potential for significant spatio-temporal variability in some areas; conversely, there are cases where variability is nearly negligible. The findings also suggest that temporal variability of deep water masses is small and that spatial variability has much more impact. With low tidal and residual currents throughout most of the CAA (Kliem and Greenberg, 2003; Forrester, 1983), it is expected that this would hold true for deep water locations throughout the CAA. Thus, for site surveys over small areas, sampling at a high rate with the MVP is not likely required in deep water. Mapping while in transit or over larger areas, however, would benefit from the use of the MVP when passing through regions characterized by high spatial variability. It would be imprudent to extrapolate the VA findings from these few transects investigated herein to the entire CAA and it is

expected that the CTD data set, with its greater geographic coverage, will give some indication of which areas exhibit high spatial variability.

Shallower water masses will likely exhibit more small scale spatio-temporal variability due to the increased influence of tidal mixing in shallow water. Transect B in Hudson Bay provides a good example as the observed spatial variability (mixed vs. stratified) is likely due to the effect of tidal flow reacting to topographic and bathymetric constrictions, e.g. the ridges, shoals, and islands that are common in the eastern sector of Hudson Bay.

The MVP data also allowed for estimation of the potential uncertainty impact associated with the use of a climatology for sounding reduction. It is clear from transects B and C that a time-invariant and spatially smoothed climatology cannot reproduce fine scale spatio-temporal variability and that any soundings reduced will suffer the full effects of spatio-temporal variability. Figure 4-29 provides a dramatic example of the sea surface temperature in the Gulf Stream, an area where loss of resolution might be especially problematic. In addition to the effect of the local variability is the effect of overall bias, be it due to a biased climatology or from natural deviations from mean conditions. A good example of this effect is transect C in Clark and Gibbs Fjord. Fjords are often quiescent from an oceanographic standpoint but can have markedly different temperature and salinity characteristics at depth compared to deep water offshore if a sill is found at the mouth of the fjord. Climatologies with coarse resolution and sparse measurements cannot typically capture nor preserve these isolated and potentially unique conditions and thus will likely present a biased solution. Working in an environment

with little spatio-temporal variability does not shield the soundings from the effects of a biased climatology.

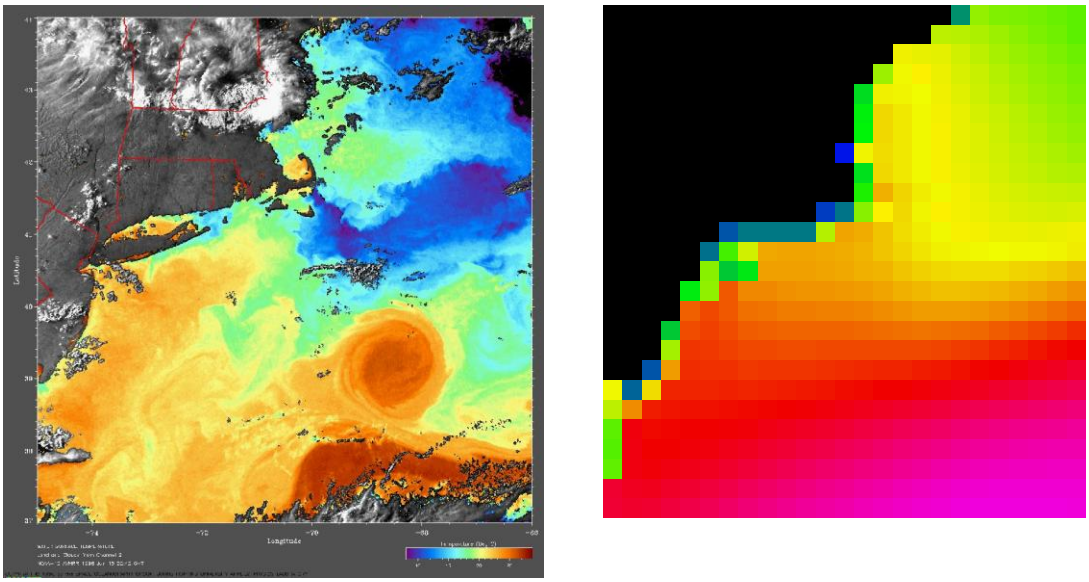

Figure 4-29. Comparison of spatial resolution of satellite based sea surface temperature of the Gulf Stream to that of 15'x15' WOA01 temperature grid. Both images cover an area of approximately 400 NM x 400 NM. Satellite data are from NOAA AVHRR, the image was produced by the Ocean Remote Sensing Group at John Hopkins University (APL, 2009).

In general, MVP sections of high spatial resolution have the potential to allow for discrimination between the effects of bias and variability; it can be said with some degree of certainty that "the water mass as a whole differs significantly from mean conditions" and/or "there is significant variability in the water mass". For all four transects, however, it is unclear whether the observed potential sounding bias is a result from a normal departure of conditions from the mean (e.g. "the water is fresher and colder than average because the ice melted late this year"), or if the WOA01 suffers from interpolation error (which is a plausible explanation given the small number of oceanographic observations in the CAA) or is biased towards a time period where mean conditions differed

significantly from mean conditions encountered at the time of the MVP transects. There is insufficient long term temporal and spatial coverage in the MVP data set to allow for a distinction between these two cases. The CTD casts, if examined in isolation, cannot help. An isolated cast has no context and there is nothing to indicate if discrepancy between a CTD and climatology cast is due to an isolated case of high variability (e.g. "this water is different than the water all around it") or if the cast is representative of local conditions and those conditions deviate from the predicted mean (e.g. "most of the water mass is warmer than usual"). In the next section, multiple isolated examinations over space and time are examined to provide more insight into both the natural range of variability and potential biases in the climatologies investigated in this work.

4.4 Oceanographic CTD Stations

As oceanographic conditions vary spatially over the archipelago, they are best investigated on a regional basis. This section reviews the CTD data collected by the CCGS Amundsen throughout the CAA, beginning in the North Water polynya between Greenland and Ellesmere Island in the east and continuing westward to the Mackenzie Shelf in the Beaufort Sea. T-S diagrams are presented for each region along with a v-wedge to describe the impact of variability on sounding accuracy; this is followed by a UA investigation of the various climatologies. Recall that CTD casts were collected over the span of several years, typically from August to October in each year. This is in marked contrast to the MVP transects, in which a VA captured the spatio-temporal

variability as measured over the span of a few hours. In these situations, a VA explores inter annual variability as most locations were sampled over several years.

4.4.1 Eastern CAA

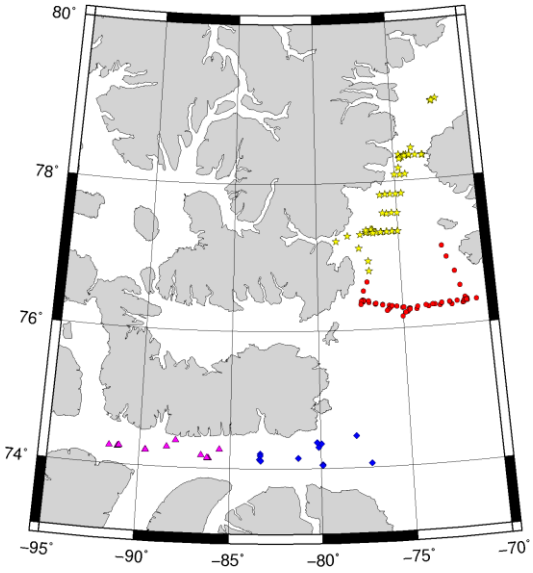

Figure 4-30. CTD locations in eastern CAA. Stations in the North Water are grouped into northern and southern casts (yellow stars and red circles). Stations in Lancaster Sound are grouped into eastern and western casts (blue diamonds and magenta triangles).

Casts acquired in the eastern CAA casts exhibited distinct spatial patterns of high and low variability and were grouped into sets based on the observed variability. Figure 4-30 plots the positions of all casts, colour coded by variability grouping. Plots of sound speed profiles for each region are shown in Figure 4-31. Figures 4-32 through 4-35 provide T-S plots of these four regions, alongside with v-wedges that quantify the potential sounding uncertainty. The southern North Water region and the eastern Lancaster Sound region exhibit high expected uncertainty mostly due to variability below depths of 200 m whereas the other two regions are benign in comparison, suffering mostly from surface variability though some deep variability was observed in the western Lancaster Sound region.

The southern casts of the North Water and the eastern casts of Lancaster Sound were distinguished by pronounced deep variability related to temperature variations of the same nature observed in MVP transect D. This variability is explained by the fact that the southern region of the North Water is the meeting ground for southbound Arctic

outflow via Nares Strait and Jones Sound and northbound Baffin Bay water, both of which persist at depths up to 500 m (Ingram and Prinsenberg, 1998). Referring to the T-S plot of Figure 4-36, the Baffin Bay Water is warmer at depth (>2°C), whereas the Arctic outflow is significantly colder (<0°C); both water masses have similar salinities. The deep waters of both flows are of very similar density, allowing the two water masses to easily interleave and/or mix as they meet at depth, creating complex, but stable, thermal structures. These structures appear to persist as the flows join to become the southbound Baffin current, a portion of which intrudes west into Lancaster Sound as it travels south. As this deep flow has no western exit from Lancaster Sound (due to limiting sill depths in the central NWP), it eventually turns back and returns to Baffin Bay. Thus the variability observed in the southern North Water and eastern Lancaster Sound regions can likely be associated with the intermingling of the two aforementioned water masses with boundaries between inflowing and outflowing currents shifting as the flows react to topographic and bathymetric restrictions in the southern North Water region. This long period spatio-temporal variability could introduce significant sounding bias when using climatological average sound speed profiles.

Casts acquired in the northern North Water (Smith Sound) and western Lancaster Sound exhibited much less variability as compared to the other two regions. Topographic steering at depth limits the effects of the West Greenland Current (WGC) to the surface layer in the northern North Water; the casts from the northern section exhibit nearly invariant temperature and salinity characteristics below a depth of 300 m over the three years that it was sampled, suggesting that the deeper water mass has little inter-annual variability. Slight variability in the deep water of western Lancaster Sound suggests that

the troublesome currents and water masses found to the east occasionally intrude further west though an exact boundary is difficult to extract from the few observations (16 casts in the east, 17 in the west).

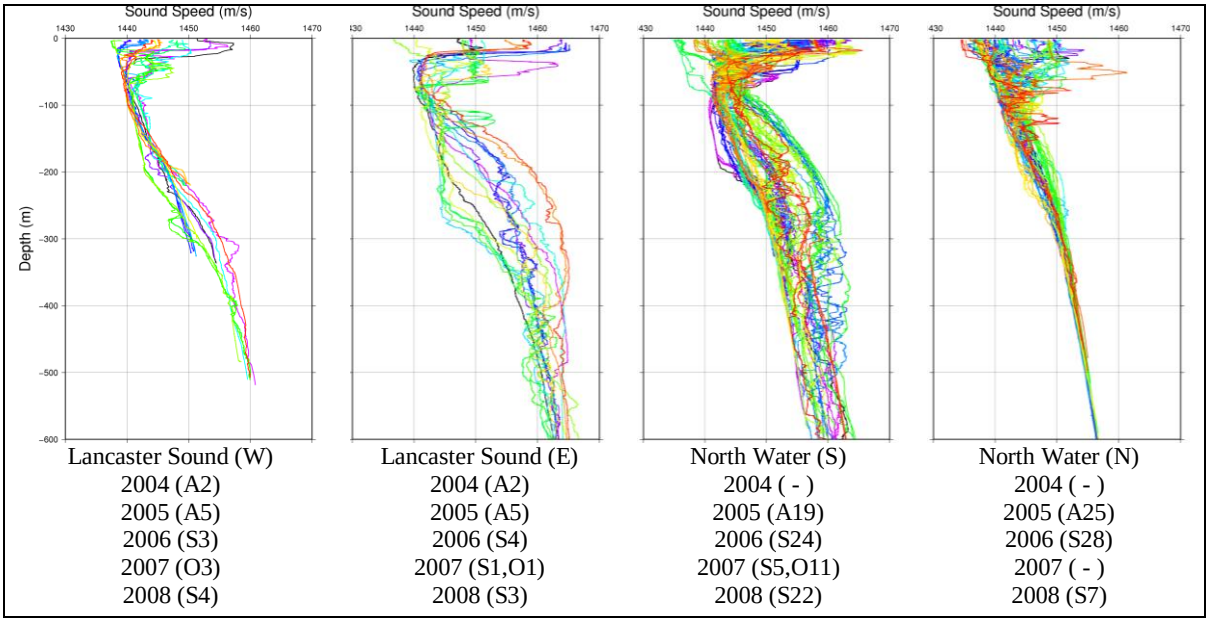

Figure 4-31. Eastern CAA sound speed profiles, grouped by regions of consistent variability. The years in which region was sampled is listed below each panel, followed by the number of casts acquired in each month of that year (A = August, S = September, O = October).

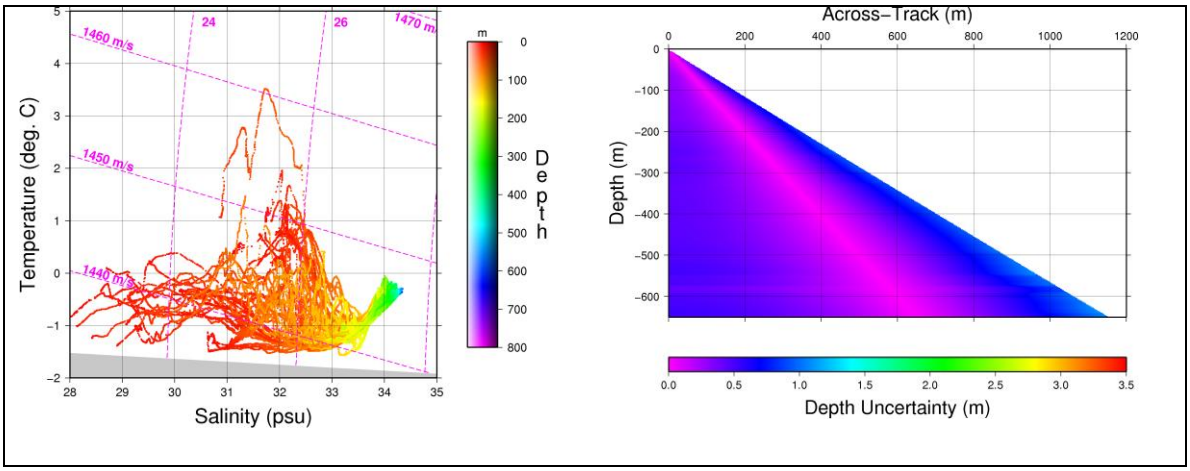

Figure 4-32. T-S diagram and v-wedge from northern sector of the North Water. Salinity variations at the surface are the dominant source of variability in the T-S diagram though a few casts exhibit warmer temperatures, hinting at northward surface flow of the WGC.

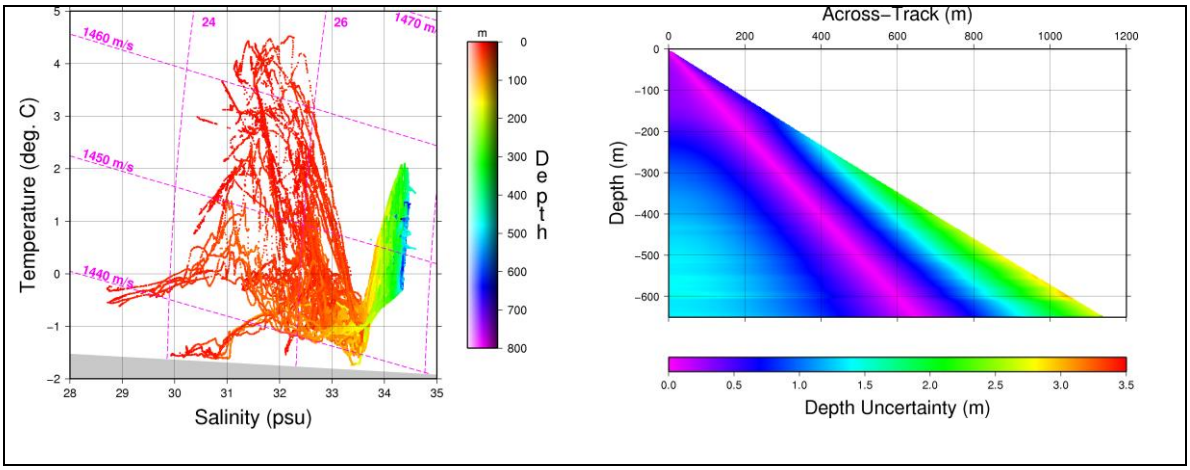

Figure 4-33. T-S diagram and v-wedge from southern sector of the North Water. Temperature variations are dominant in surface waters and at depth.

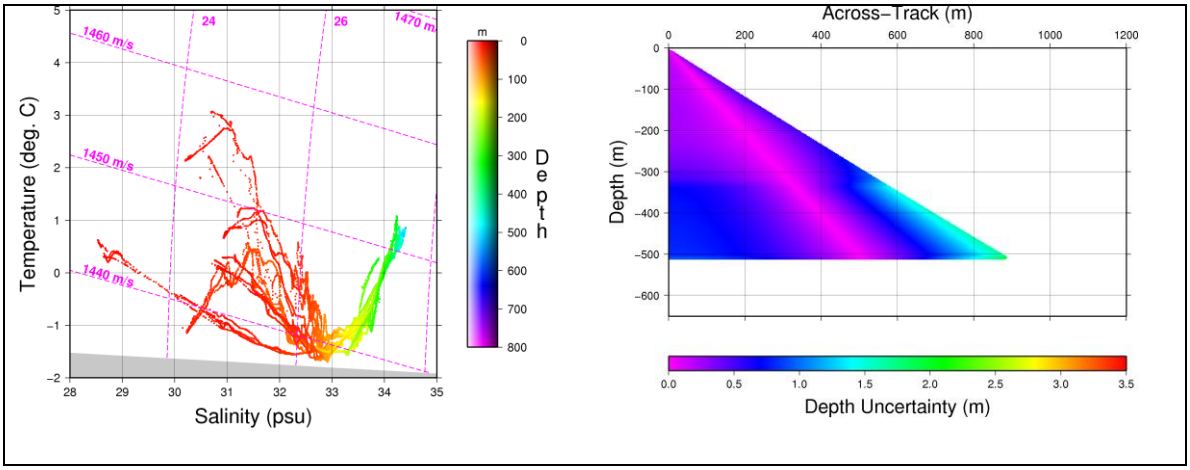

Figure 4-34. T-S diagram and v-wedge from western sector of Lancaster Sound.

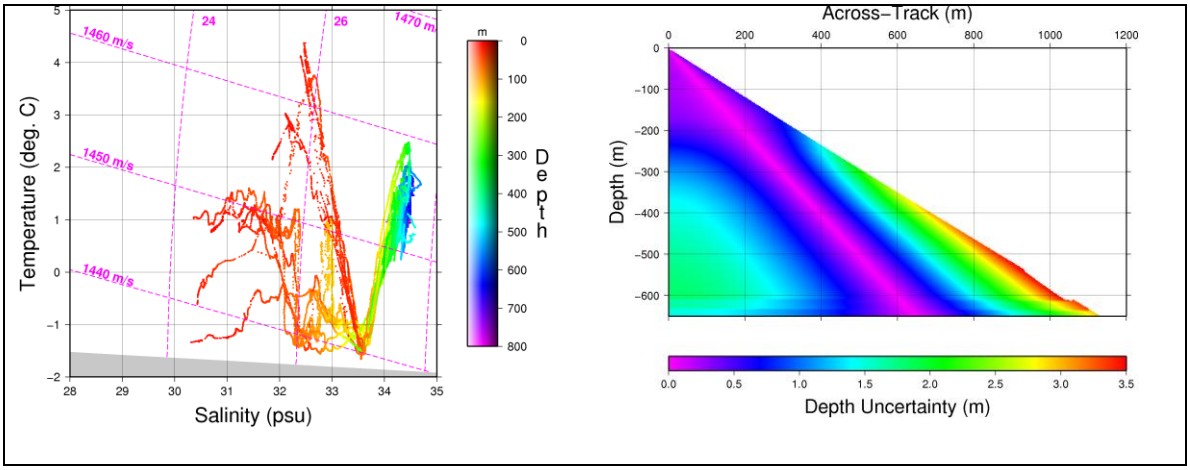

Figure 4-35. T-S diagram and v-wedge from eastern sector of Lancaster Sound.

The T-S diagrams and v-wedges suggest that eastern Lancaster Sound and the southern North Water sections are areas where climatologies could be of limited use. That is not to say that climatologies would perform well in the other regions. As witnessed with the MVP transect into Clark and Gibbs fjord, spatio-temporal variability that has negligible effect on sounding uncertainty does not shield the hydrographer from the effects of a potentially biased climatology or from significant departures of actual conditions from average conditions.

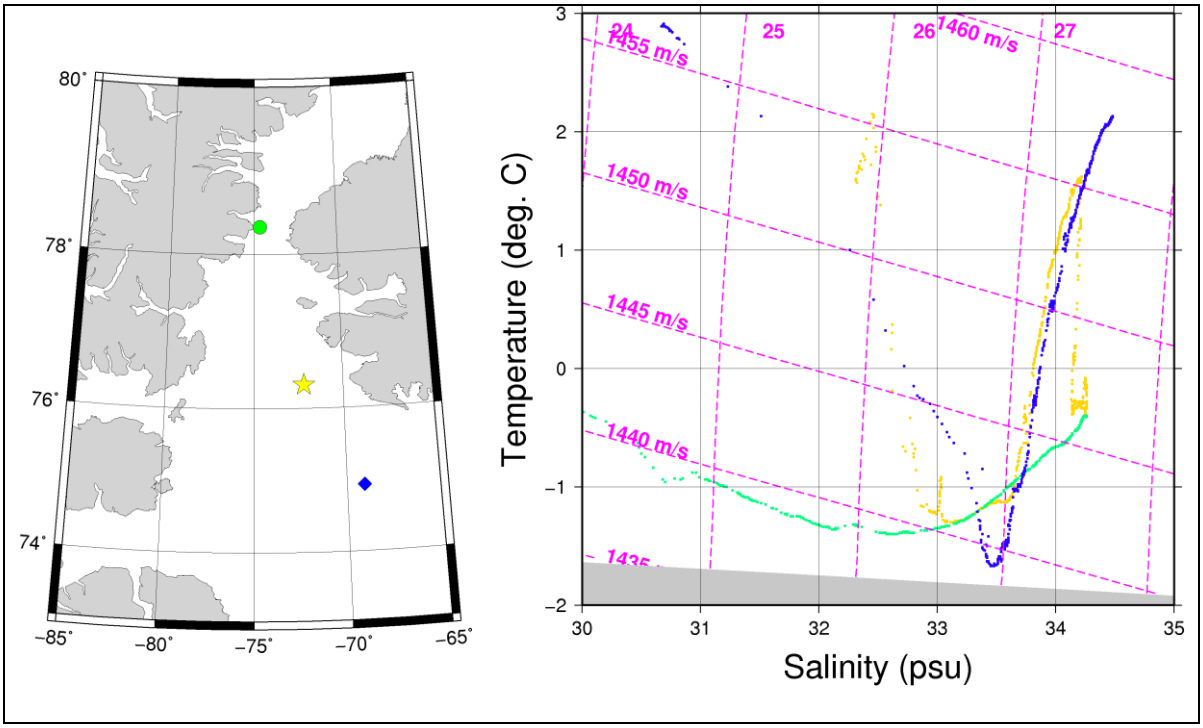

Figure 4-36. Map of three CTD casts in the North Water region (northern Baffin Bay: blue diamond, southern North Water: yellow star, Smith Sound: green circle). A T-S plot of the three casts is shown on the right with colour coding matching the map. Water masses below 300 m depth are to the right of the 34 psu line, with Baffin Bay water lying above 0°C and deeper Arctic outflow lying below 0°C. The cast from the southern North Water (yellow) demonstrates the potential for interleaving of the two deep water masses as the slight variations in temperature have little effect on the density relative to the effect of salinity.

A UA was performed for each of the three climatologies under investigation; the results are presented as uncertainty profiles for each climatology in Figures 4-37 through 4-40. The presentation format in these figures will be used consistently throughout the

remainder of this work, thus some preliminary explanation is warranted. Beginning with WOA01, a b-wedge is computed by comparing every CTD cast in a given set to the WOA01 cast derived for the same date and location. This procedure is repeated for all CTD casts in the set, generating a set of b-wedges. Bias profiles for the outermost beam in the Amundsen's 120° angular sector are plotted in the upper left panel of Figure 4-37. The WOA01 vs. CTD b-wedges are tallied to generate an m-wedge and s-wedge; a mean bias profile (from the m-wedge) is plotted in the lower left panel, with the uncertainty profile (from the s-wedge) bracketing the 95% confidence interval. This procedure is repeated for the GDEM and Kliem climatologies, with the results being plotted in the central and right panels, respectively.

The best performances are realized in the northern North Water region (Figure 4-37), with none of the climatologies suffering appreciable uncertainties. Characterized by seemingly invariant deeper water, the small variations in the upper layer introduces a few decimeters of uncertainty over the first 50 – 75 m of water after which the only remaining uncertainty appears to arise from the slightly different average conditions depicted by each of the climatologies. Whereas the Kliem climatology offers an unbiased solution over most of the water column, the WOA01 and GDEM climatologies suffered from slight negative bias at depth resulting from an overly warm prediction of the Arctic outflow temperature at depth (nearly 0.5°C warmer than the CTDs and the Kliem climatology at a depth of 100 m). The Kliem temperature profiles adequately represent the cooler Arctic halocline temperature signature, however it is nonexistent (or heavily dampened) in the WOA01 and GDEM climatologies.

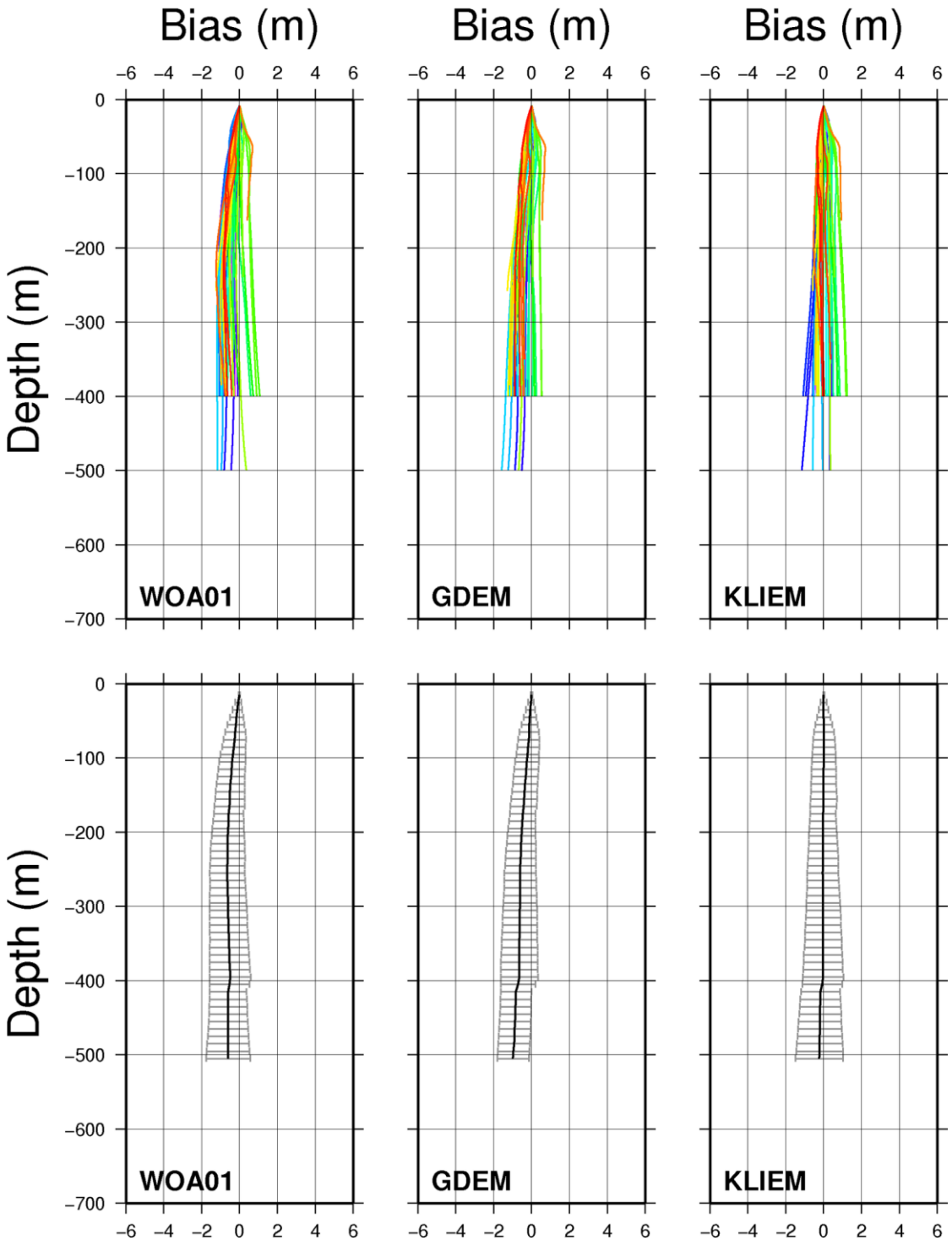

Figure 4-37. Uncertainty profiles for the northern North Water.

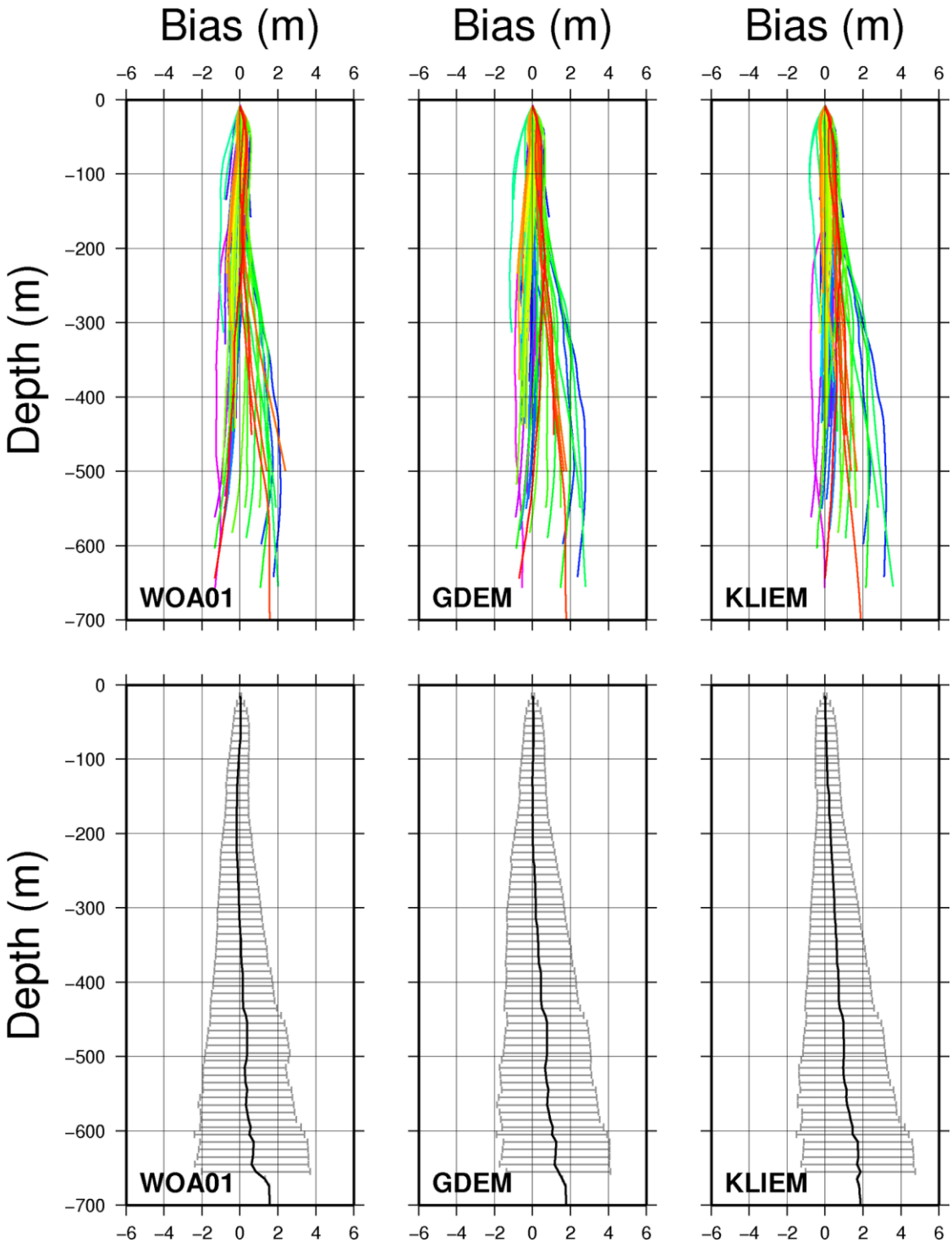

Figure 4-38. Uncertainty profiles for the southern North Water.

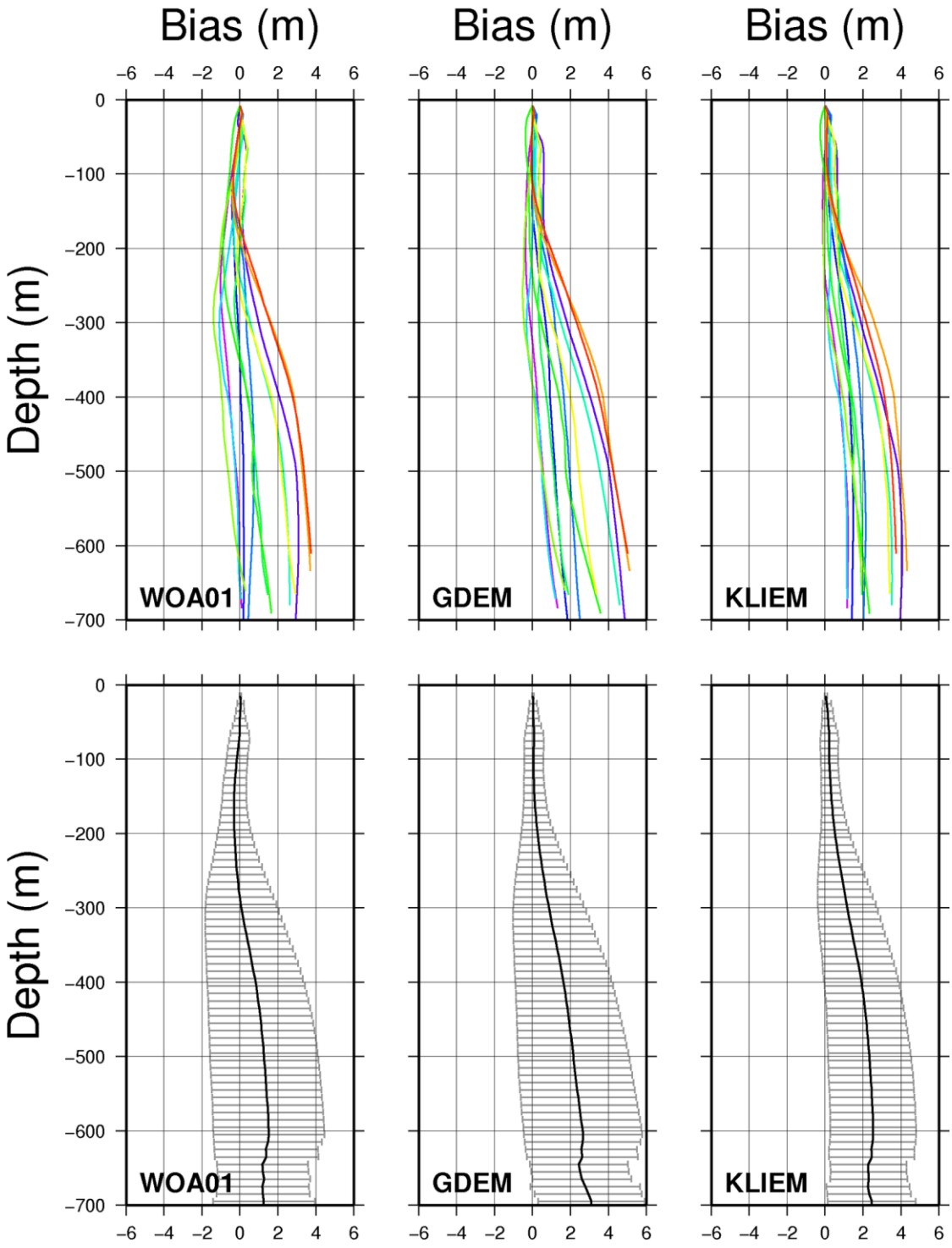

Figure 4-39. Uncertainty profiles for eastern Lancaster Sound.

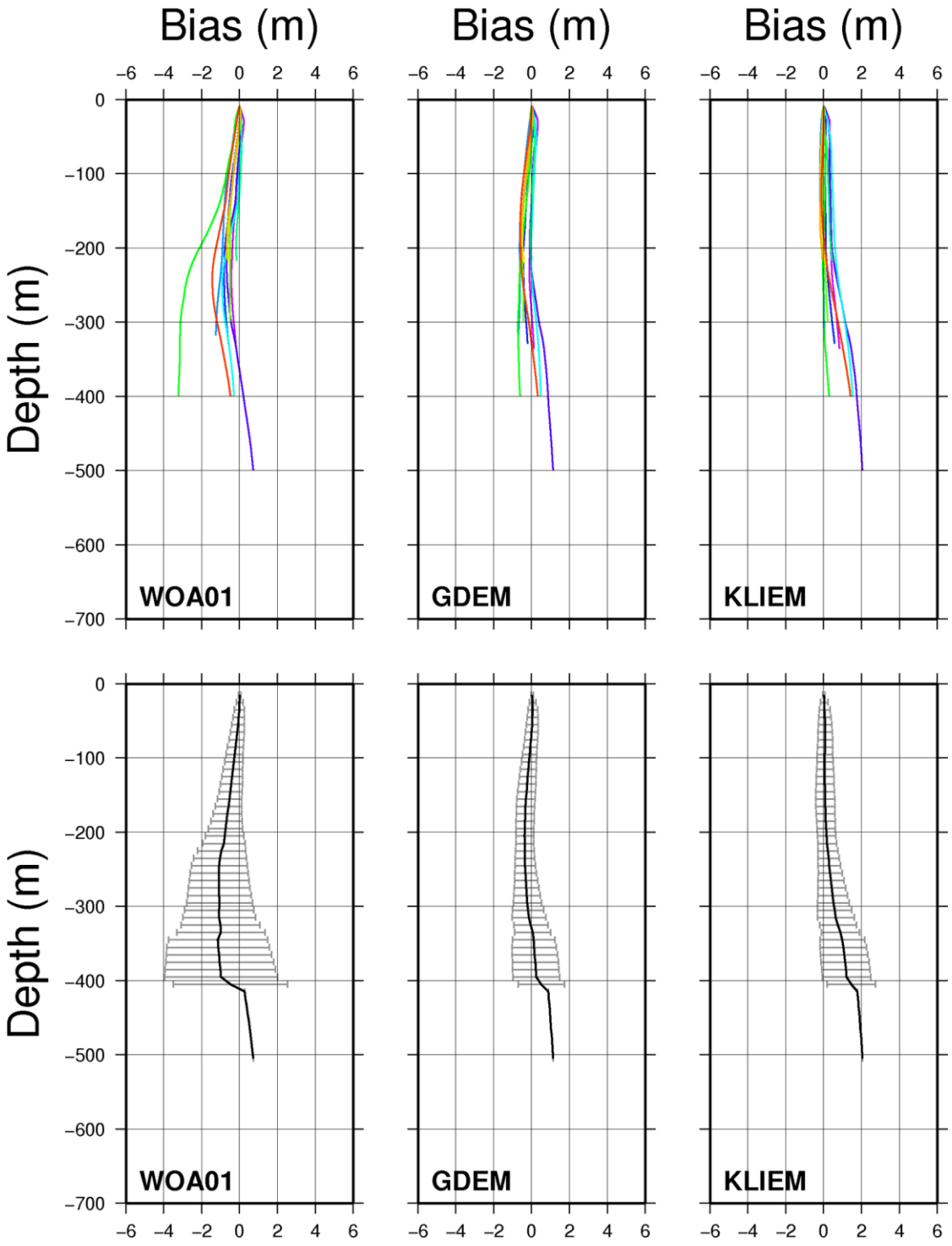

Figure 4-40. Uncertainty profiles for western Lancaster Sound.

Moving to the southern region of the North Water, the performance of the climatologies degrades significantly. Uncertainties of similar magnitude as the northern region are introduced due to surface variability in the upper 50 m of the water column. Uncertainty due to variability at depth begins to increase in the depth range of 150 – 200 m, this increases steadily to the maximum depth, reaching ~3 m at 650 m water depth (~0.5% w.d., for context) for all three climatologies. This is consistent with the potential uncertainty quantified in the v-wedge and it indicates that all three perform more or less equally poorly in matching the variable conditions.

All three climatologies are marked by a 1-2 m positive bias at depth, this being due either to (1) conditions being warmer or saltier than average, or (2) the climatologies being biased towards colder and/or fresher conditions. The WOA01 climatology presents the least biased solution over the majority of the water column with only a slight positive bias being introduced below a depth of 400 m whereas bias begins at depths of ~150 m for Kliem and ~240 m for GDEM. Though all of the climatologies predict an eastward warming of the lower layer in the southern North Water region, all of the three climatologies suffer from abnormally warm pulses of Baffin Bay water at depth, inducing a positive bias to the outermost soundings. The WOA01 climatology suffers the least as it over-predicts the temperature of the overlying Arctic halocline water (which helps to cancel out the positive bias associated with the deep water pulses of warm water) and it predicts warmer temperatures at depth compared to the other climatologies (Kliem predicts colder temperatures, GDEM lies between the two).

Moving to the mouth of Lancaster Sound (eastern sector), this basic pattern repeats itself though with less uncertainty due to surface variability but more uncertainty

at depth (Figure 4-39). Again, none of the climatologies perform well when faced with deep warm water masses such as those observed in the northern section of the MVP transect across the Sound. In this case, all three climatologies predict temperatures to reach up to 1°C below the halocline, however temperatures as high as 2.5°C are often observed in this location. Furthermore, the thermocline depth appears to be more variable than was observed in the North Water region and there is likely additional spatio-temporal variability due to the cold and fresh Arctic outflow from the west joining the water masses described in the last region.

Examining Figure 4-39, specifically the Kliem bias profiles at a depth of 600 m, the bias distribution appears bi-modal with modal means centered roughly on 1.75 m and 4 m (the same occurs with WOA01 and GDEM but is most easily observed in the Kliem bias profiles). The outermost mode (the larger of the two) is associated with a significantly shallower thermocline, perhaps due to upwelling or variations in the magnitude of Baffin Bay inflow at depth (refer to the orange and red sound speed casts in Figure 4-31). The innermost mode is likely associated with more quiescent conditions, however, all climatologies still exhibit a positive bias with WOA01 being the least affected overall due to negative biases in the upper water column cancelling out some of the effects of the positive bias associated with thermocline variability.

All three climatologies suffer similarly from surface variability, with all incurring ~0.25 m of uncertainty in the upper 70 m of the water column. The second introduction of uncertainty occurs through the variable thermocline layer (200 – 400 m). The GDEM and WOA01 bias curves diverge through this layer whereas the Kliem curves are more closely clustered together over the same depth range, thus the Kliem uncertainty has only

grown to +/-2 m at 400 m whereas the other two suffer +/-2.6 m at the same depth (both at the 95% confidence level).

The final location to examine is the western end of Lancaster Sound (Figure 4-40). Deep water variability has less of an impact as the depths shoal the further west one travels. The Kliem and GDEM climatologies performed similarly with very little bias introduced over the upper 200 m. Surface variability imparts 0.15 – 0.25 m of uncertainty within the upper 50 m with deeper variability introducing an additional ~0.25 m for the GDEM and Kliem climatologies.

The WOA01 climatology was characterized by a negative bias over most of the upper 100 m, much like previous areas. Below depths of 100 m, however, the WOA01 mean bias and uncertainty estimates are biased by an apparent outlier profile (green profile in Figure 4-40). This outlier profile is a valid assessment of how poorly the climatology represents mean conditions and thus cannot be discarded as is usually the case with outliers in statistical work. Figure 4-41 plots the CTD cast along with the three climatology casts for comparison. There is clearly a discrepancy at depth between the WOA01 cast and all other casts, the abnormally high sound speed is due to a temperature increase of ~2°C in the WOA01 profile at between depths of 150 – 250 m, relative to the other casts. Also shown in the figure are WOA01 temperature maps, at 200 m depth, for the Lancaster Sound region over 4 months (August to November). The positive sound speed anomaly at 200 m depth is associated with a positive temperature feature in the WOA01 October grid that is ~2°C warmer than surrounding waters. Interestingly, the feature also appears in the August, September and November grids as well, though the temperature maximum is smaller in these months.

The GDEM and Kliem grids exhibit no such anomaly, thus it is unique to the WOA01 grid. One possible explanation for the observed discrepancy is a lack of source data, indeed the month of October is one of the many months in which few observations exist in the CAA due to ice conditions hindering ship based observations (see Appendix B, specifically the section discussing the World Ocean Database). Such a lack of data can lead to artifacts in the WOA01 as the monthly climatologies will be biased towards the seasonal climatologies in areas without data for a given month. The lack of such a feature in the GDEM climatology in this region and in this month could be explained by GDEM's larger source data set, though this cannot be confirmed due to the classified nature of the underlying data set for GDEM. The Kliem grid exhibits no such feature as it is centered on September 1st and heavily weights data collected in September and August and there are ample data in both of these months in this region. It should be noted that the conditions depicted by the WOA01 profile are within the realm of possibility. Deep and warm thermal structures do occur in the eastern section of Lancaster Sound, it is simply a question of whether or not such structures can persist this far west into the Sound, and whether such transient type features would survive the spatial and temporal averaging associated with the creation of a climatology. Certainly, there exists no such feature in any ArcticNet CTD cast in the immediate vicinity. Referring to the temperature maps of Figure 4-41, the isolated nature of the feature and the fact that it persists on the north side of Devon Island (to the north of the Sound) points to a gridding artifact that could be explained by a single faulty measurement that biases estimates in that region due to sparse data.

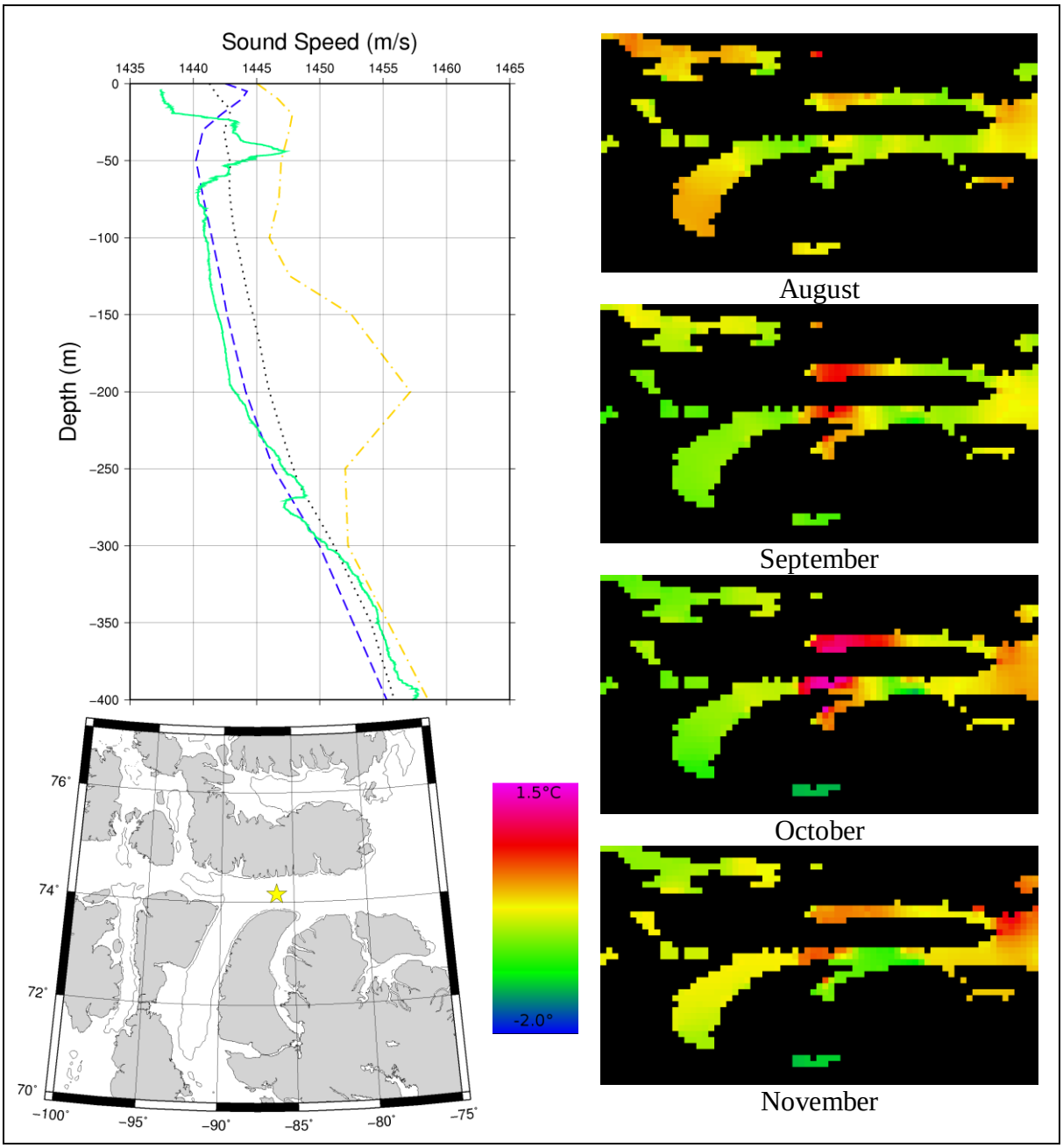

Figure 4-41. Sound speed casts associated with the anomalous WOA01 bias profile (CTD: solid green, WOA01: dashed-dotted yellow, GDEM: dotted black, Kliem: dashed blue). The CTD cast was collected in October at the location indicated by the star in the context map on the lower left (also shown is the 200 m isobath). Panels on the right are images of unprojected WOA01 temperature grids at 200 m depth from August to November, centered on the location of the CTD cast and spanning the same approximate area as that of the context map.

4.4.2 Central CAA

As discussed in Appendix A, deep water masses of the central CAA are distinct from the eastern CAA as they lie to the west of the central sills in Barrow Strait. Surface waters are also under much more direct influence of the Arctic ice pack. Floes of multiyear ice are often found clogging the waterways in this area, making it one of the more difficult sections of the NWP for surface based shipping. Surface waters are typically colder due to the near continual presence of sea ice. Figure 4-42 shows a location map of the 33 Amundsen CTD casts collected in the area, along with sound speed profiles derived from the casts.

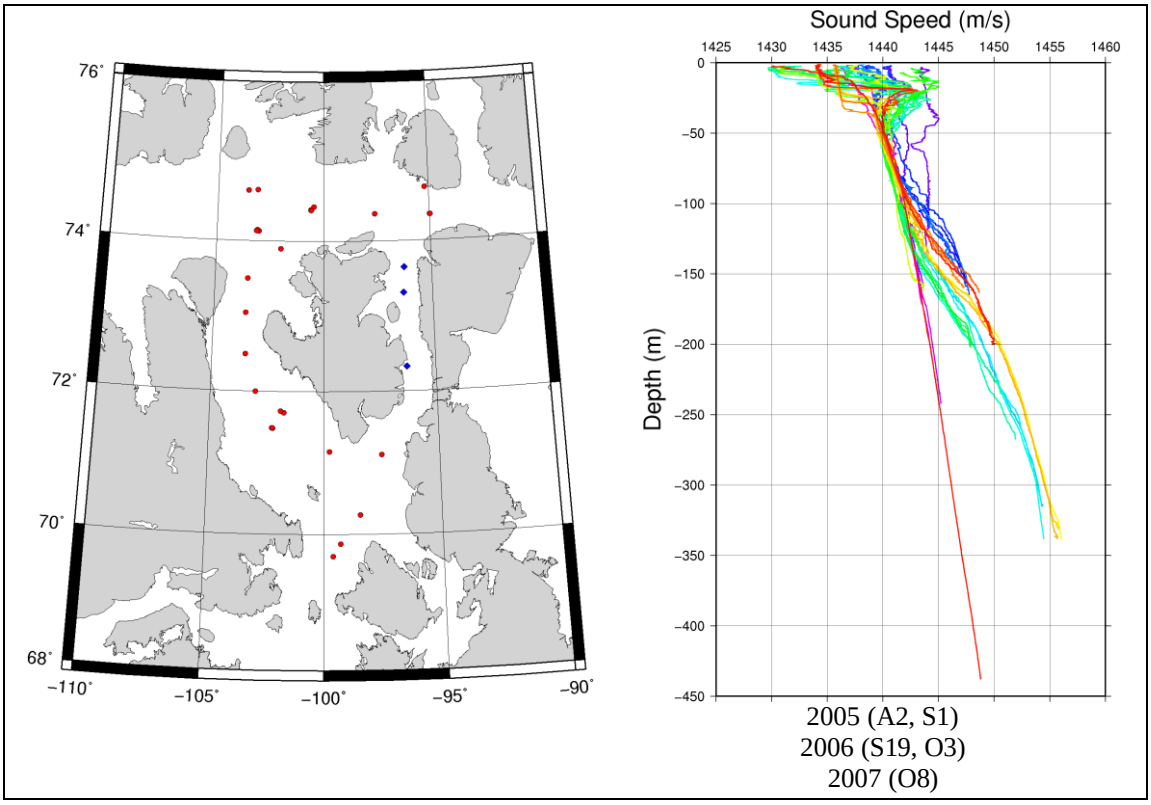

Figure 4-42. Sound speed casts from the central CAA. Casts in Peel Sound (blue casts in the location map) have distinct bottom water, leading to linear sound speed profiles below a depth of ~100 m (these casts were collected in 2005).

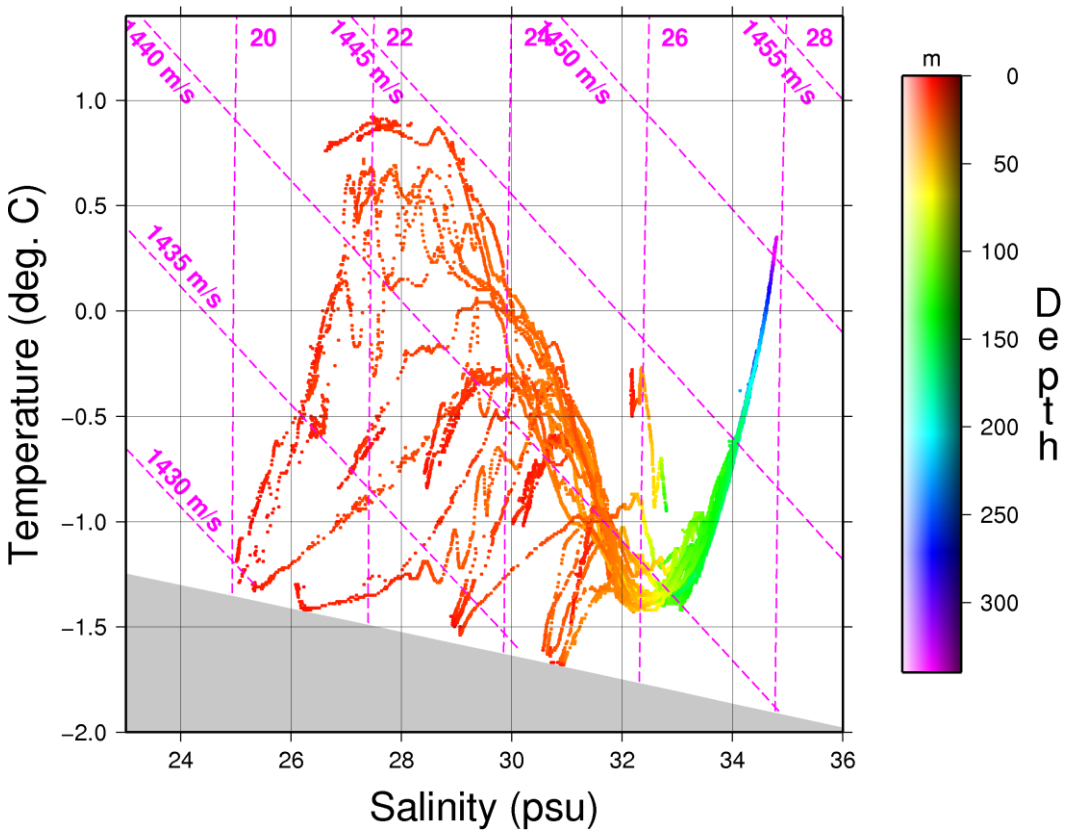

Figure 4-43. T-S plot for casts in the central CAA (excludes casts from Peel Sound).

Referring to the T-S plot of Figure 4-43, surface variability is less pronounced compared to the regions previously examined to the east; the maximum observed surface temperature falls just short of 1°C whereas the maximum observed temperature for eastern Lancaster Sound and the southern North Water regions reached ~4.4°C. Peel Sound, a deep and narrow sound running from 72°N – 74°N at a longitude of 96°W is distinguished by its unique bottom waters: sills at the northern and southern end limits replenishment of its deep waters, leading to nearly invariant temperature and salinity conditions below the sill depth. The WOD of 2005 contains 77 CTD casts in this location, these confirm the stability of water properties at depth: the mean temperature and salinity at 200 m depth does not vary by more than +/- 0.069° and +/-0.308 psu, both

at the 95% confidence level (observations were acquired in the months of March, April, August and September in years 1978, 1981-1984, 1995 and 1999). M'Clintock Channel runs in a similar north-south direction roughly 5° to the west. Deeper variability appears to be limited to variations in the depth of the thermocline and is much less pronounced than that observed in the regions to the east.

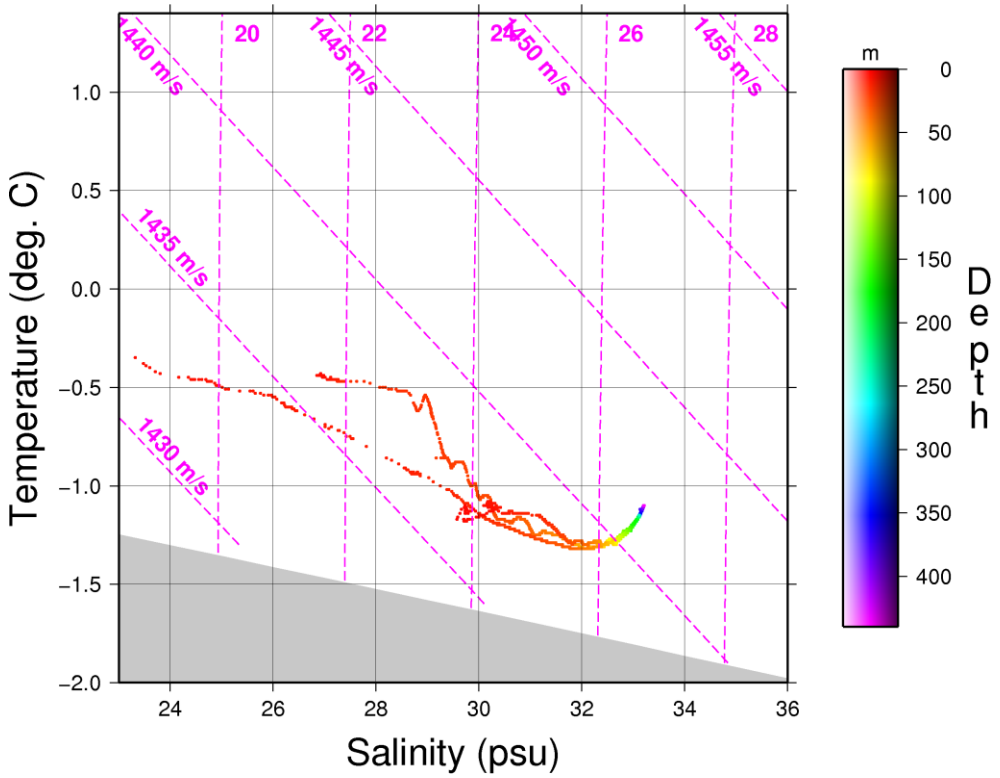

Figure 4-44. T-S plot for casts of Peel Sound. Note the distinct bottom water characteristics relative to M'Clintock channel (see Figure 4-42, scales are identical for ease of comparison, except for the depth scale).

A VA was performed on the set of ArcticNet casts, specifically excluding those of Peel Sound as the analysis would be overly pessimistic due to the significant differences between the deep water masses (Peel Sound was not examined on its own as only three casts were collected in the sound). The resulting v-wedge, shown in Figure 4-45, clearly demonstrates that the variability in this region has much less impact as compared to the

regions investigated thus far.

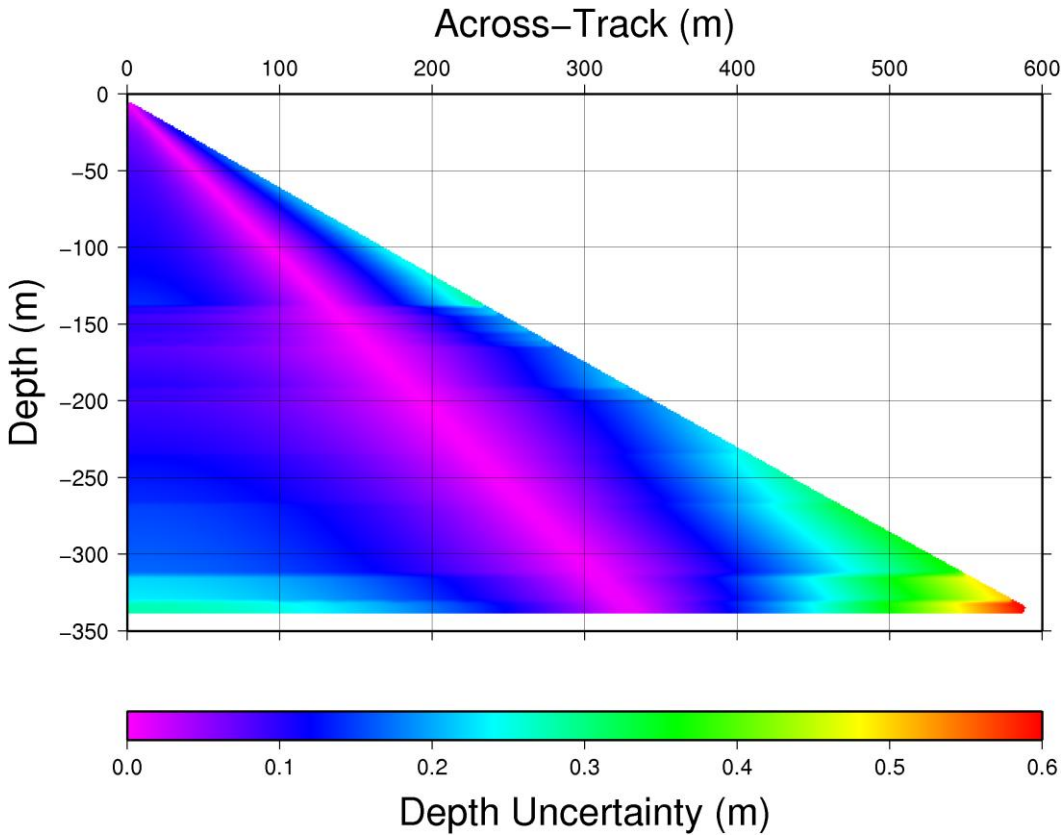

Figure 4-45. V-wedge for central CAA (excludes casts from Peel Sound).

Examining uncertainties at a depth of 300 m, variability in this region has approximately one quarter the effect of the variability in eastern Lancaster Sound and one half the effect of waters just east of the central sills in the western Lancaster Sound region. Discontinuities in the v-wedge occur due to inclusion of deep water and shallow water casts in the same VA. Casts from shallower (<150 m) areas in the region are marked by erosion of the thermocline due to tidal mixing at the seafloor; a v-wedge constructed from all casts exhibits increased uncertainty from this up to a depth of ~150 m. Beyond this depth, the only contribution to the VA is from deep water casts, which suffer no such tidal mixing effects (rather, tidal mixing near the seabed does not reach the thermocline). Remaining discontinuities are from the slight differences between the deep

temperatures observed in 2006 and 2007 (~0.25° of difference due to thermocline displacement) and the small number of casts contributing at this depth.

Climatological bias profiles from a UA are shown in Figure 4-46 (including casts from Peel Sound). All three climatologies suffer more or less equally from the surface variability but to a much lesser extent than in the regions to the east. At a depth of ~40 m, however, the performances of the climatologies diverge significantly; WOA01 and GDEM climatologies suffer non-negligible negative bias over the remainder of the water column though the biases observed with the former are significantly more pronounced than those of the latter. The negative biases are either due to conditions being colder/fresher than usual, or from a warmer/saltier bias in the two climatologies. Examination of the casts from WOA01 and GDEM revealed that the predictions from both are ~1.0°C warmer than observed over a depth range of 50 – 150 m with the WOA01 October grid exhibiting an additional 1.0°C spike feature at 50 m depth (for a total of 2°C). Of all the WOA01 bias profiles, those from the month of October yield the largest bias due to the temperature spike at 50 m; the September grid does not fare as poorly as it does not contain the same temperature spike at 50 m. The GDEM casts are similar in that they predict a much warmer upper water column, though none exhibit the additional 1.0°C spike at 50 m seen in the WOA01 casts. Essentially, both climatologies are lacking one of the characteristic water masses of the Arctic Ocean: the Arctic halocline. Given that little variability was observed (nor expected) in this region and that the high predicted temperature at depth is contrary to what is known about the oceanographic water masses and processes in the general vicinity (again, some of the worst ice conditions are known to exist in this area), the only conclusion can be that the

WOA01 and GDEM climatologies exhibit a temperature bias near the surface in this region for the months of September and October.

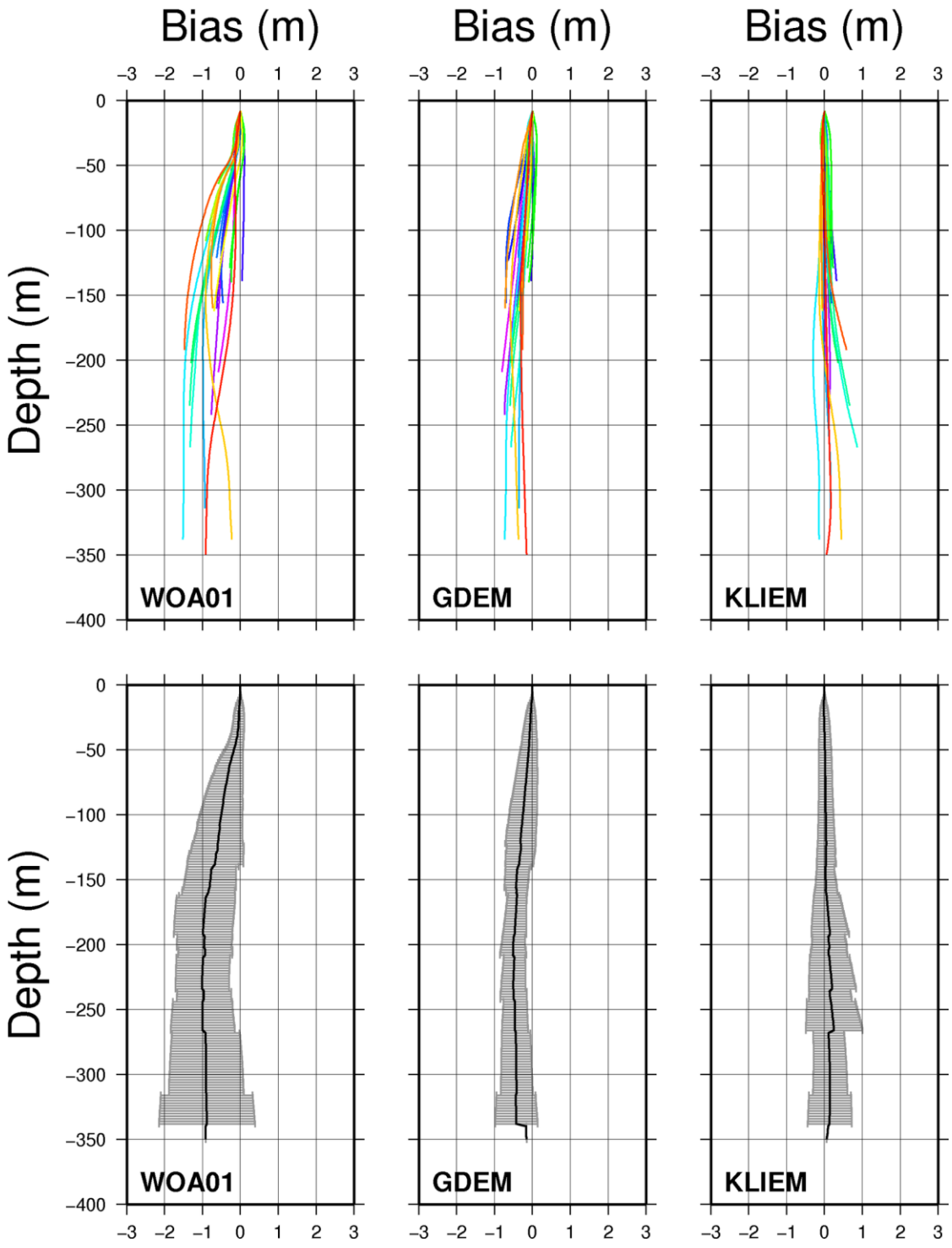

Figure 4-46. Climatological bias profiles for the central CAA. Note that the scale on the x-axis is half that used for the eastern CAA examinations.

This is further supported by the fact the the Kliem climatology suffers no such bias. Examining the WOD05 distribution maps in Appendix B, the M'Clintock Channel region has only been sampled in the Autumn months by mechanical bathythermographs (MBT). As the Kliem climatology specifically excludes data for which no concurrent salinity measurement is available, the MBT data would not have been used in the Kliem compilation and the interpolation in this area would have been based upon measurements in surrounding basins (and the few CTD casts in the months of March and April). As the Kliem climatology (1) accurately portrays the Arctic halocline and (2) agrees with the ArcticNet observations, it is highly probable that the MBT measurements that would have been used by the GDEM and WOA01 climatologies are positively biased.

Turning now to the Kliem bias profiles for the region, the Kliem climatology presents the least biased solution over the entire water column with mean bias never exceeding 0.25 m. Its bias profiles remain consistently small (almost negligible) until depths of 150 m are reached at which point the Kliem climatology predicts a constantly colder and fresher water mass at depth for the southern section of M'Clintock Channel, resulting in slight positive bias profiles which grow with depth (refer to the three worst positive bias profiles in Figure 4-46). As will be seen when examining the next region, depth invariant temperature and salinity at these depths is common in the southern regions of the Archipelago and it can perhaps be explained that the relative wealth of data in the gulfs to the south has biased estimates in southern M'Clintock Channel where few data exist otherwise.

It is interesting to note that the invariant properties of the Peel Sound deep water are best captured by the WOA01 and GDEM climatologies (though they still exhibit the

aforementioned positive temperature bias in the upper 150 m). The Kliem climatology's temperature and salinity match the expected values well up to depths of 200 m but are significantly biased beyond depths of 225 m. This occurs only when full Kliem profiles are used (extending to a depth of 3,500 m); if the profiles are clipped at the "depth" of the Kliem bathymetry model, the artifact does not exist, suggesting that no data were found at the deeper depths during the interpolation and that the profiles beyond that depth are contaminated by the different water properties of neighbouring basins.

4.4.3 Southern CAA

The southern CAA is characterized by shallow basins (< 300 m) with shallow sills limiting communication of water between adjacent deeper basins to depths of a few tens of metres. In contrast to the areas investigated thus far, these basins receive non-negligible continental river runoff via the Coppermine, Burnside, Back, Ellice and Hayes rivers. The water masses are distinguished from neighbouring basins by being relatively fresher on the whole with deeper water masses having nearly depth invariant temperature and salinity characteristics as was the case with Peel Sound but with minor spatial and inter-annual variability observed in the few casts collected in the region.

West of 107°W (see Figure 4-47), Coronation Gulf is characterized by many islands and submarine ridges; these separate a series of sub-basins with unique deep water characteristics and variability. For example, the temperature and salinity of the deepest basin (~300 m) in the southern Coronation Gulf varies by at most 0.25°C and 0.3 psu between 1999 and 2005 and is nearly depth invariant (based on ArcticNet and WOD05 casts).

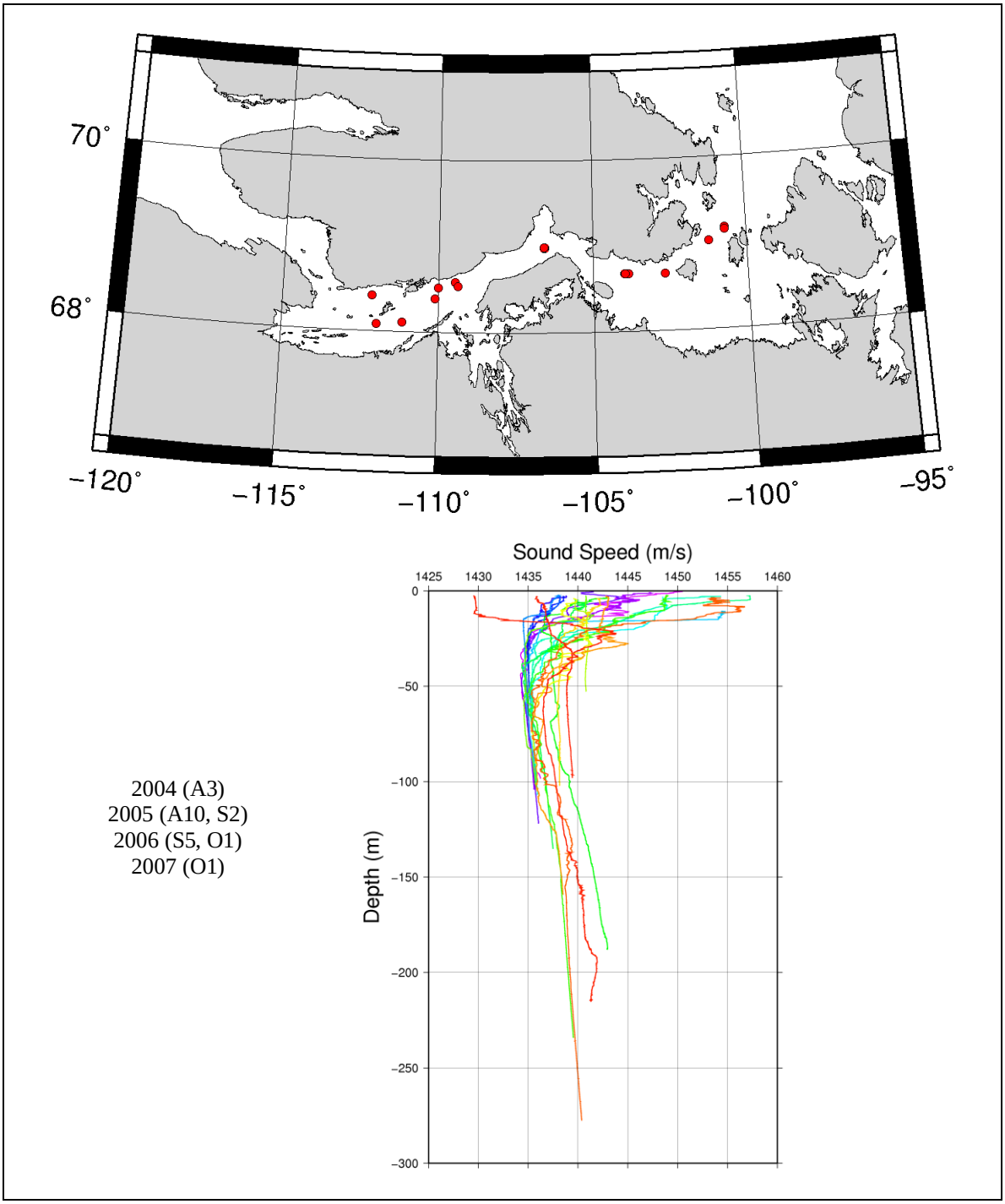

Figure 4-47. Location map and sound speed casts for Southern CAA.

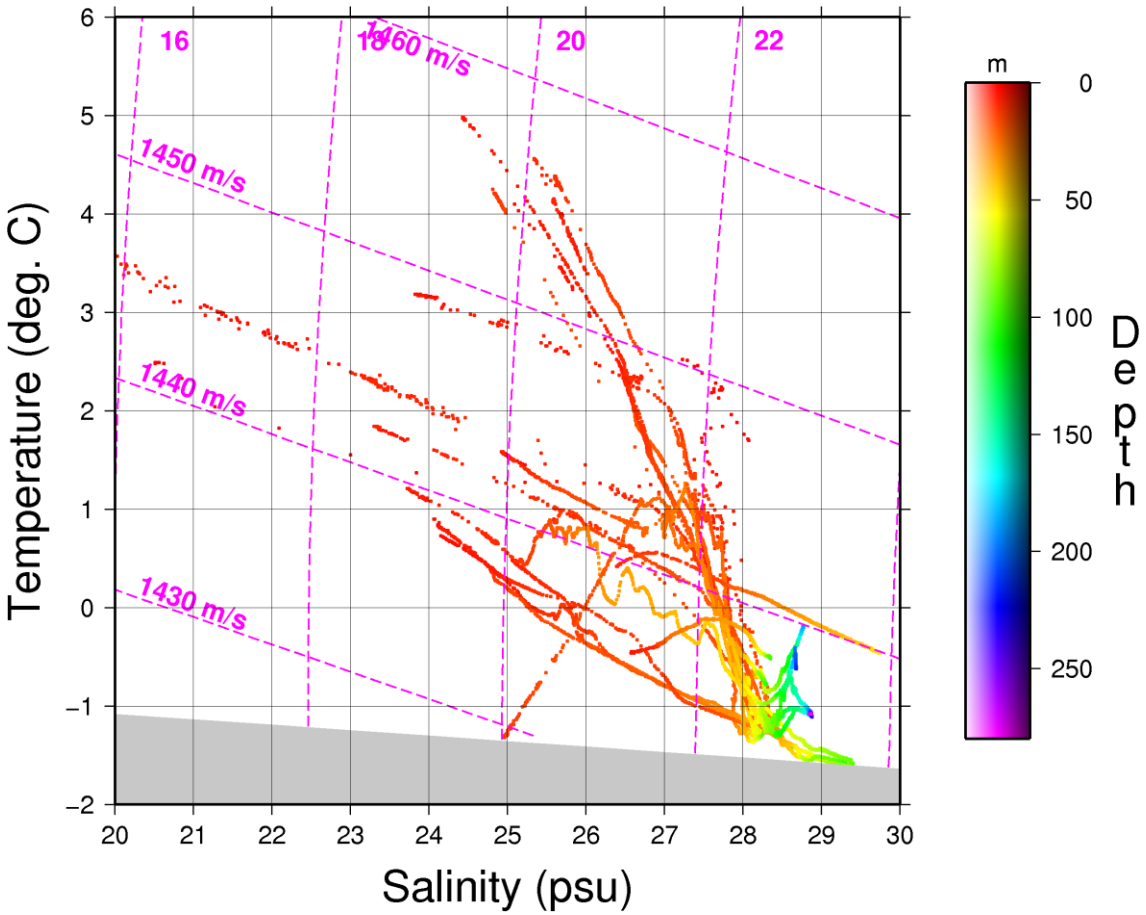

Figure 4-48. T-S plot for the Southern CAA. Note the differing properties of the deep water masses.

In contrast, the sub-basins to the north, which are separated from the former sub-basin by an island chain and ridge, reach depths of 200 – 250 m and have warm water at depths greater than 150 m, suggesting occasional replenishment of deep water of Atlantic origin (see Appendix A) from the Amundsen Gulf despite the shallow sill depth in Dolphin and Union Strait. The T-S plot in Figure 4-48 clearly shows the variations in deep water mass properties, also note the increase in the dynamic range of temperature and salinity as compared to the previous region (surface temperatures reach 5°C). East of 107°W, Queen Maud Gulf is much shallower with depths reaching a maximum of ~100 m. WOD and ArcticNet observations indicate constant temperature below ~60 m, salinity is also constant at depth but with inter-annual variations on the order of 0.5 psu.

Salinities in these two gulfs are significantly fresher than neighbouring basins, about 29 psu at depth, compared to 33 – 35 psu in the Amundsen Gulf and M'Clintock Channel. These deep waters are amongst the freshest of the CAA, suggesting that river inflow plays a significant role in formation and maintenance of the deep waters.

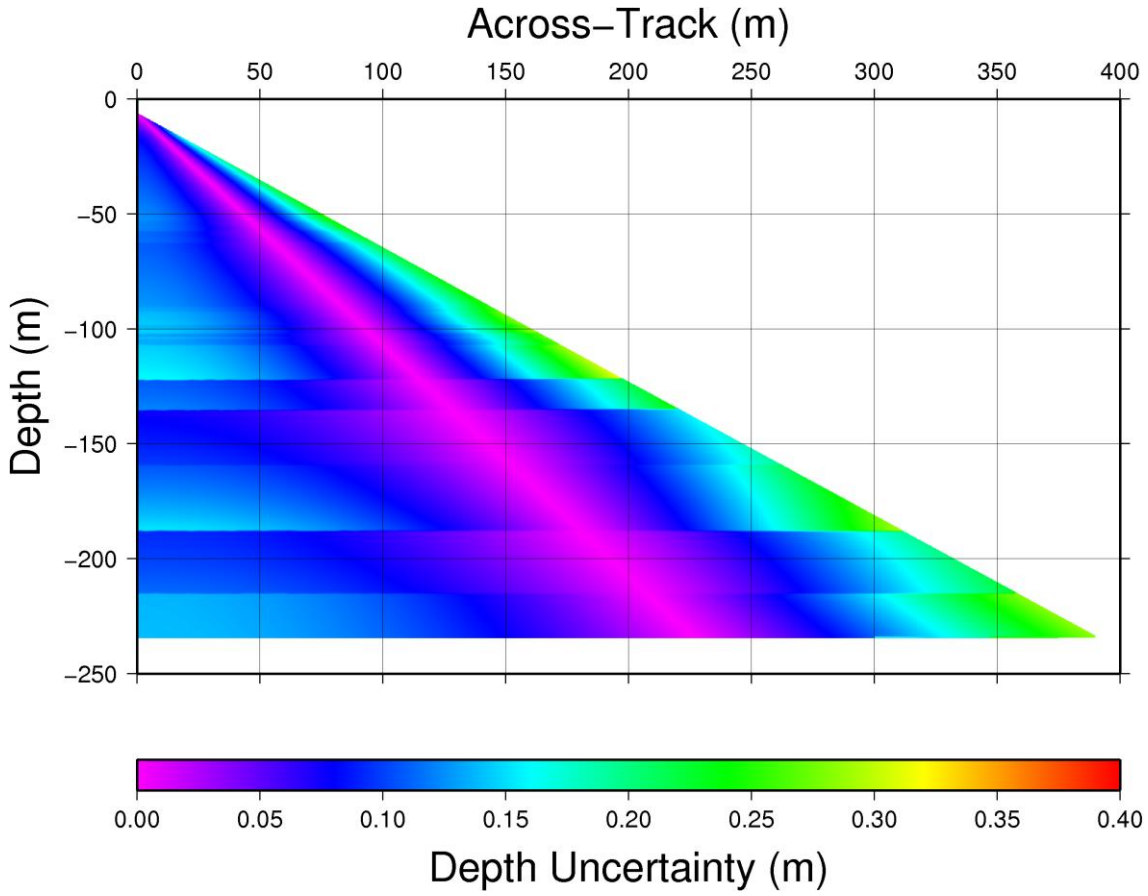

Figure 4-49. V-wedge for the Southern CAA casts.

As expected, sound speed variability is mostly concentrated in the upper 50 m of the water column, with the typically depth invariant temperature and salinity below this leading to little variation in sound speed at depth. Given the small number of total casts, the wide range of sampling depths and the differing bottom characteristics of the various sub-basins, the v-wedge suffers from many horizontal discontinuities (see Figure 4-49).

Limiting the examination to a depth of 50 m, the effect of surface variability is ~0.25 m for the outermost beam, which is 1.5x worse than that observed in M'Clintock Channel but smaller compared to the eastern regions of Lancaster Sound and the North Water. The effect of variability at depth is more difficult to gauge due to the few deep casts gathered in the area and the effect of the differing water mass characteristics at depth. It would be best to examine the sub-basins on an individual basis; however, there is insufficient data for this.

Turning to the climatologies, a UA was performed as with other areas, the uncertainty profiles are shown in Figure 4-50 (note the change in scale of the x-axis relative to the examination in the central CAA). Most surface based variability effects introduce bias over the upper 10 m in all three climatologies. All three demonstrate a slight negative bias, consistent with the prediction of warmer or saltier water over some depth range in the water column. The worst case bias profiles from the WOA01 and GDEM climatologies (orange in Figure 4-50) are associated with an overly warm and salty prediction for the deeper water in southern Coronation Gulf for the month of October. A comparison for a nearby cast collected in September has much more realistic deep temperature and salinity values for WOA01 and GDEM. This suggests that the October grids for both may be biased to warmer and saltier conditions from measurements in nearby basins due to lack of data for the month of October.

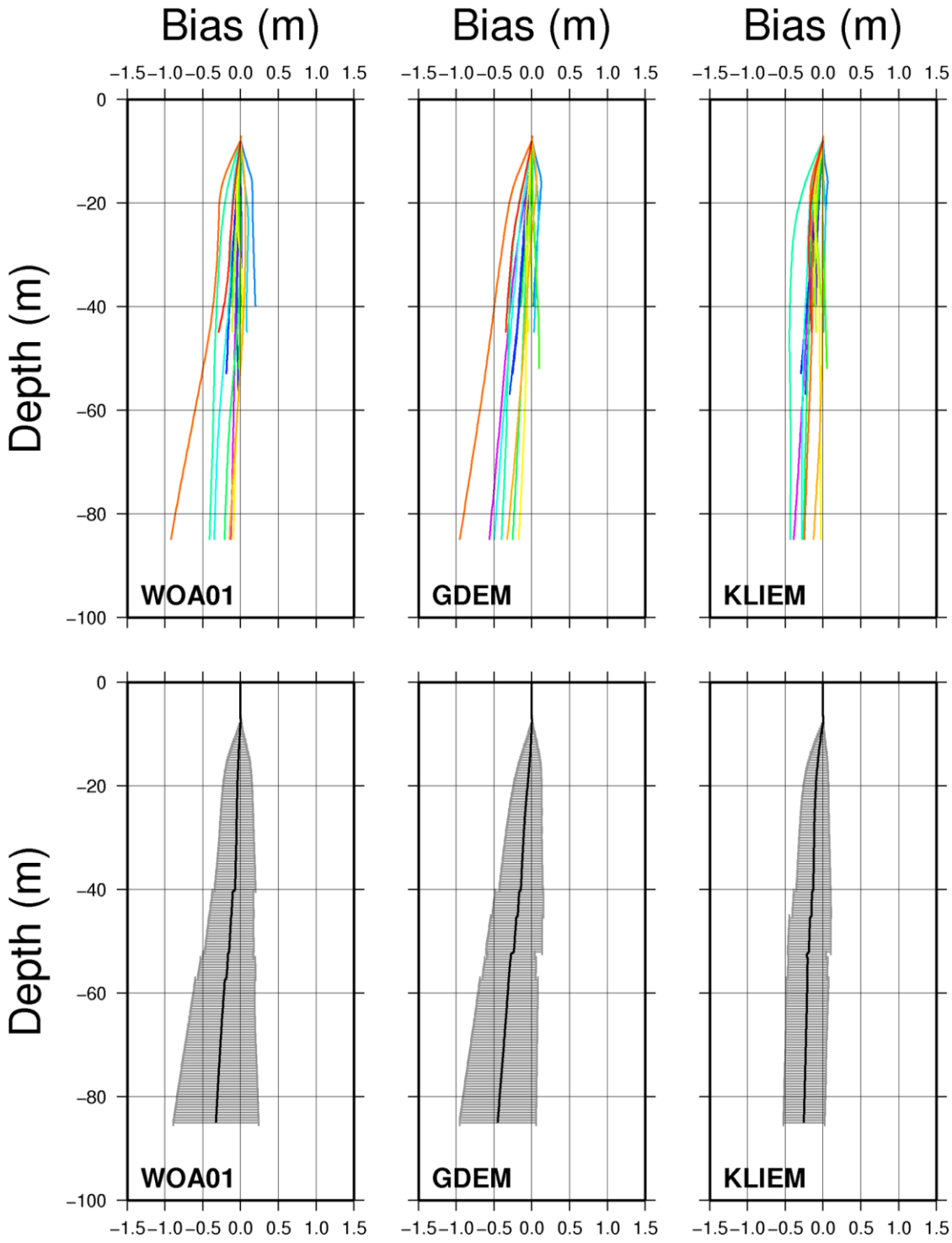

Figure 4-50. Climatological bias profiles for the Southern CAA.

The Kliem climatology suffers no such fate as it is based on summer measurements and there are sufficient observations in the area in this period to

adequately characterize the deep water masses. On the other hand, this same saving grace biases the upper portion of the water column to warmer and fresher summer time conditions, which hardly apply in October. The Kliem grid routinely over predicts the warmth of the surface layer, in fact it predicts a pronounced seasonal thermocline extending to a depth of 20 m; this introduces a mean negative bias in the upper 20 m of the water column. The WOA01 and GDEM climatologies provide estimates of surface temperatures that more closely match the observed conditions, thus they do not become negatively biased until the deeper layers are reached in which salinity and temperature are both higher than observed. As one would expect inter-annual variability in surface layer properties, it is difficult in this case to separate the cases of climatological bias from natural deviations from the true mean conditions; it simply may have been colder at the surface in the four years of ArcticNet observations. In either case, the Kliem climatology betters the performance of the other two by a factor of two, largely due to the WOA01 and GDEM grids being biased for the month of October. In this region, it appears to be preferable to carry on using a summer climatology in the month of October than to use the biased WOA01 and GDEM grids.

4.4.4 Western CAA

The western CAA has been more extensively sampled by the ArcticNet program, compared to other regions examined thus far. Figure 4-51 shows a location map of the 379 ArcticNet CTD casts collected in the area and the sound speed profiles derived from them. Observations have been made as early as June and as late as November, allowing

for examination of additional monthly climatological grids (other areas have only been sampled in the months of August, September and October).

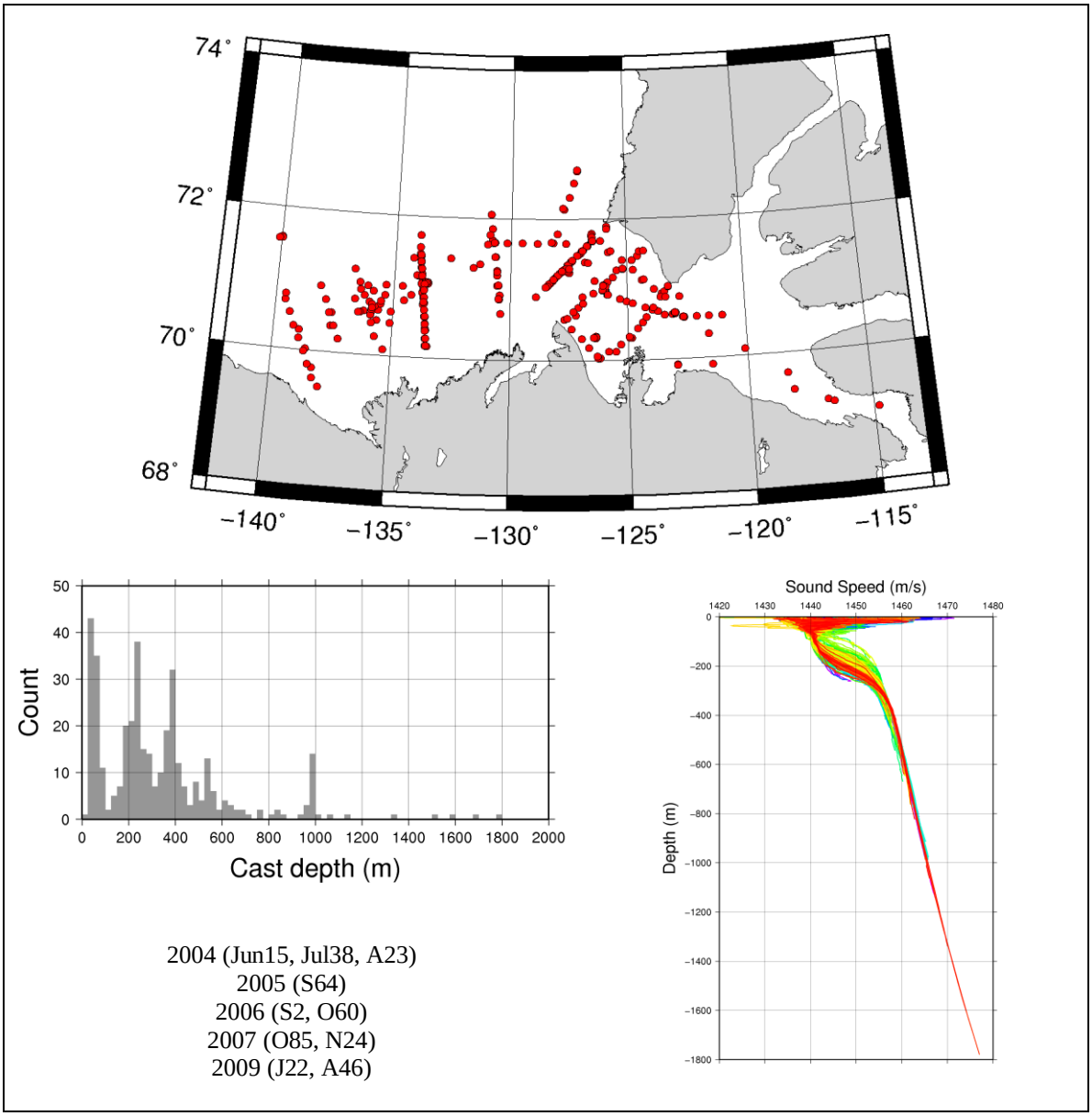

Figure 4-51. Location map and sound speed profiles for CTD casts of western CAA. The histogram indicates the wide range of sampling depths.

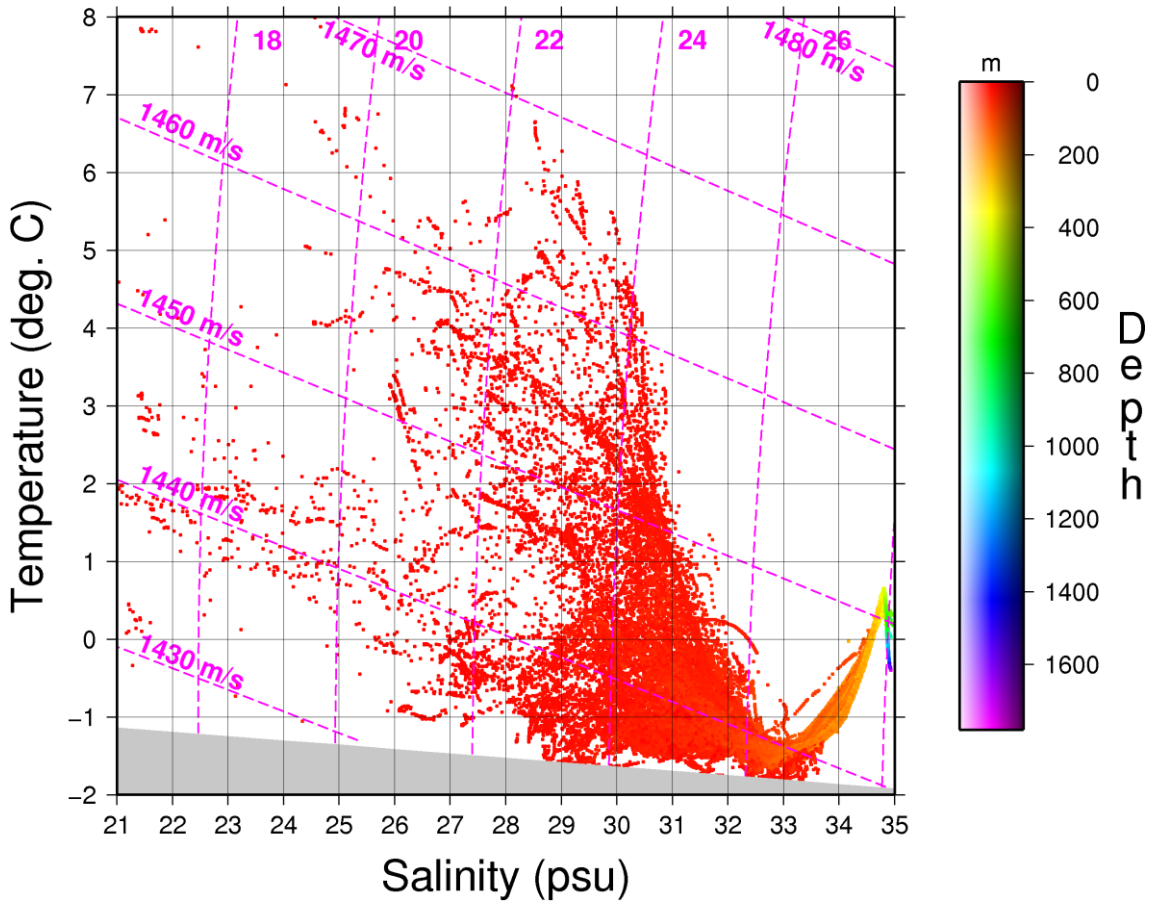

Figure 4-52. T-S plot for western CAA.

Important sources of surface variability include the absence/presence of the ice pack and the Mackenzie River plume, both of which have significant inter-annual and spatio-temporal variability (Carmack and MacDonald, 2002). The T-S plot of Figure 4-52 clearly distinguishes the high surface water temperatures and low salinities associated with the outflow of the Mackenzie River, along with the deep and nearly invariant Atlantic Water (temperature of ~0.6°C ,salinity of ~35 psu) and Arctic Surface Water (temperature of -1.5°C, salinity of 33). Offshore of the shelf, circulation patterns are controlled by the Beaufort Gyre, which brings about a clockwise circulation to the surface waters. The Beaufort Counter-Current runs deeper and in a counter-clockwise direction with maximum speed at about 100 m depth. In the absence of wind, Coriolis

effects force the Mackenzie River outflow to the east along the coast, however strong southeasterly winds can push the plume several hundred kilometers offshore (Carmack and MacDonald, 2002).

Table 4-2. Observations per month for shallow and deep water VA in western CAA.

Month	Shallow	Deep
June	5	2
July	16	9
August	17	13
September	8	7
October	39	14
November	5	2
Total	**90**	**47**

The wide range of CTD sampling depths precludes an all encompassing VA, thus the shallow (< 100 m) and deep (450 – 700 m) cases are examined separately. Table 4-2 summarizes the distribution of observations by month for each case, with v-wedges for both cases shown in figures 4-53 and 4-54, for the shallow and deep cases, respectively. Examining the shallow case first, surface variability introduces approximately 0.45 m of depth uncertainty in the outermost beam at a depth of 50 m (~1% of water depth), which is almost double that seen at the same depth in the southern Archipelago (it should be noted that the VA captures a wider range of variability as the casts were collected between June and November). It should be noted that 50 m is approximately the limit of surface variability effects in the ArcticNet CTD set. Turning to the deeper water case (Figure 4-53), surface variability has a reduced effect (~0.35 m) as expected; an additional ~0.20 m of uncertainty is introduced through variations in the thermocline depth between depths of 100 – 300 m, giving a total of approximately 0.60 m beyond depths of 300 m.

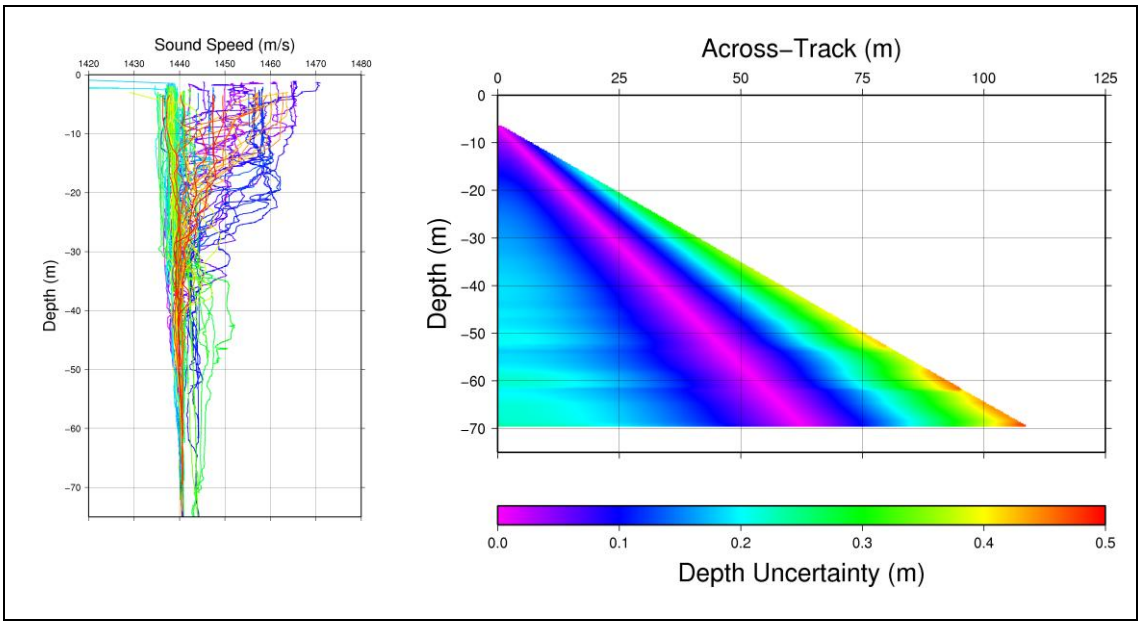

Figure 4-53. Sound speed profiles and v-wedge for casts between 20 - 100 m depth.

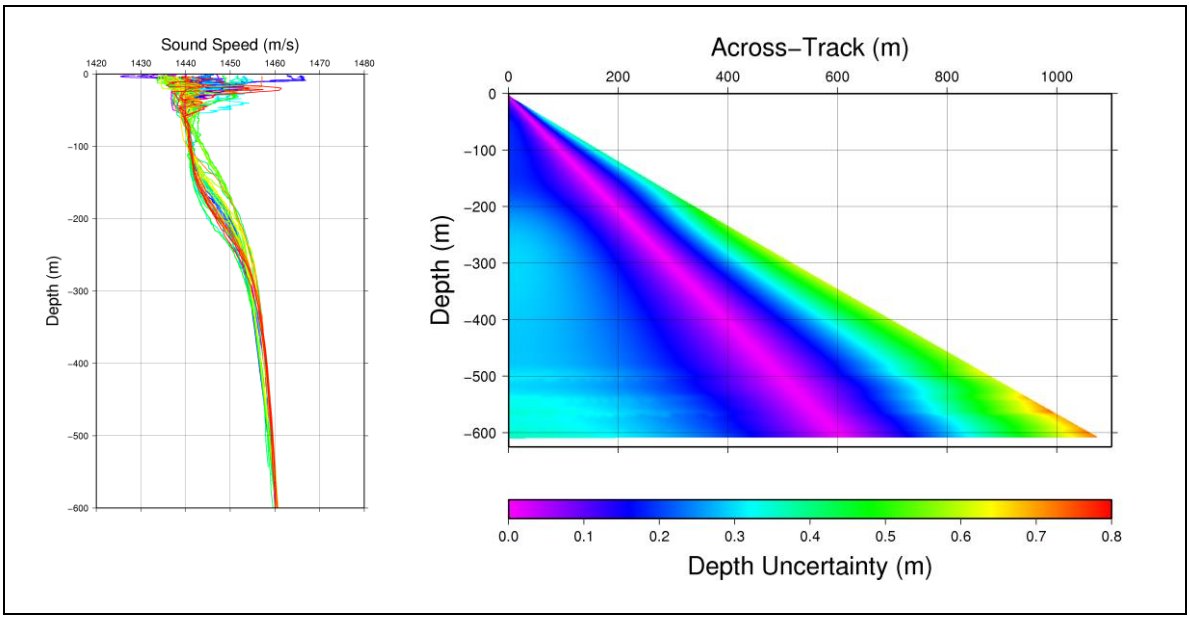

Figure 4-54. Sound speed profiles and v-wedge for casts between 450 - 700 m depth.

A UA was performed with casts grouped and examined by month of acquisition. Figure 4-55 plots the cast locations by month and figures 4-56 through 4-62 show the UA results for the each month of investigation. Though the western CAA is better sampled

than most of the previous regions, it should be noted that the sampling patterns rarely allow for a multi-year examination of the same general location, e.g. the Mackenzie Shelf for any given month.

Beginning with June, all of the climatologies perform nearly equally however the Kliem climatology shows a pronounced negative bias in the upper 50 m which is associated with predicting warmer or saltier water than what was observed. This is not surprising, as the Kliem grids are meant to represent conditions in late August and early September, a point in the season when surface waters are at the warmest and ice cover is at a minimum over most of the CAA (Kliem and Greenberg, 2003). It is interesting to note that an opposite bias at depth nearly cancels out the bias introduced in the upper 25 m, giving nearly zero mean bias beyond depths of 300 m, this is due to the Kliem grid predicting a deeper thermocline depth than was observed (~25 m deeper). The one cast for which WOA01 and GDEM are positively biased is associated with an observation off Cape Bathurst where the temperature and salinity of the upper 25 m was significantly warmer than other observations further to the west; in this case the Kliem climatology is the least biased. With only 15 casts collected in a single field season over a small subset of the entire region, there is little else that can be inferred for the month of June other than the fact that none of the climatologies introduced any bias greater than 0.50 m and that there was insignificant variability at depth. This is not to say there is never variability at depth in this region in June. As the WOD05 provides only a few hundred shallow CTD casts on the Mackenzie Shelf (with a sole cast extending below 100 m), more observations are required in this month before any conclusions can be made regarding the effects of water column variability on climatology performance.

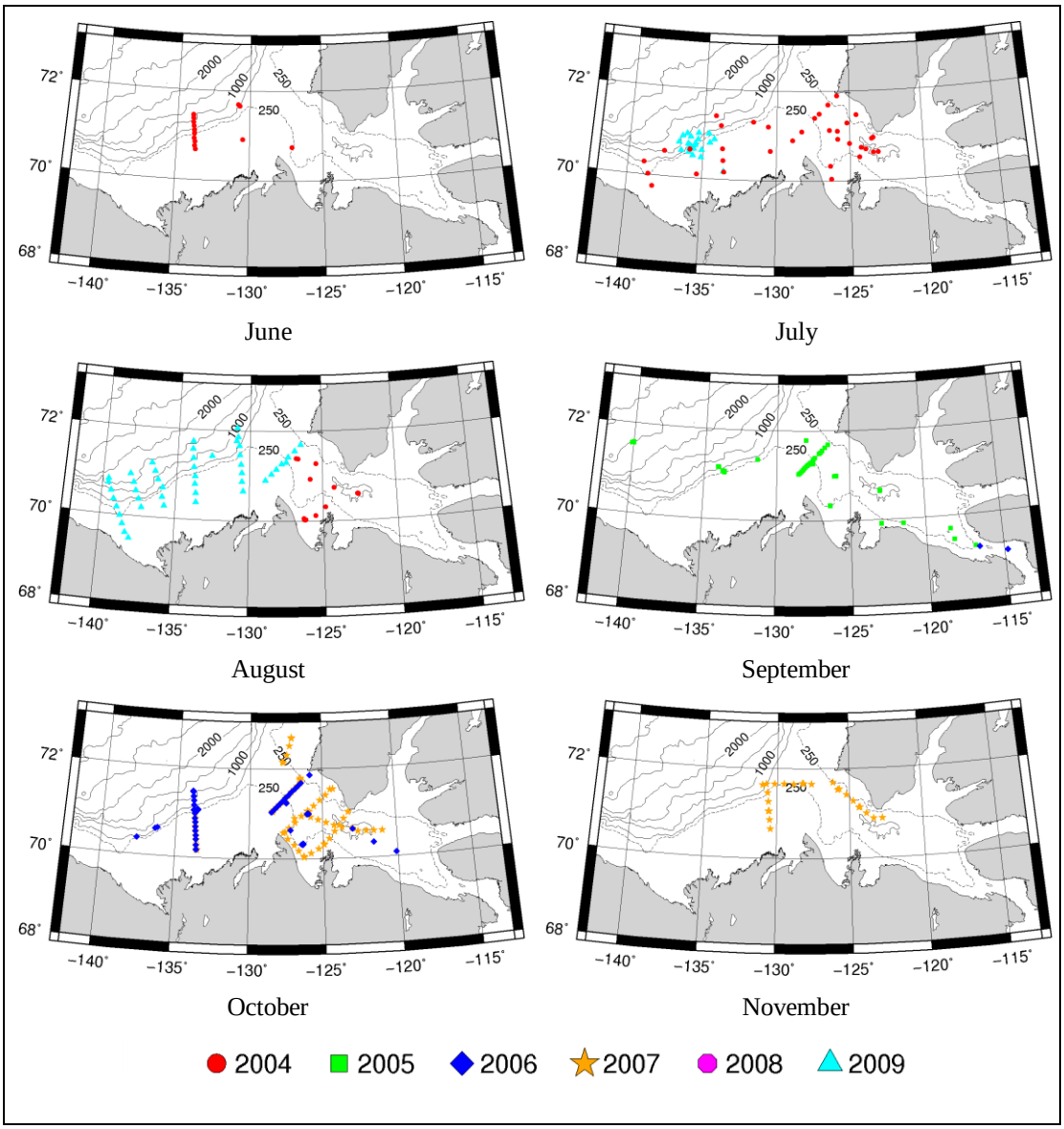

Figure 4-55. CTD locations in western CAA, by month.

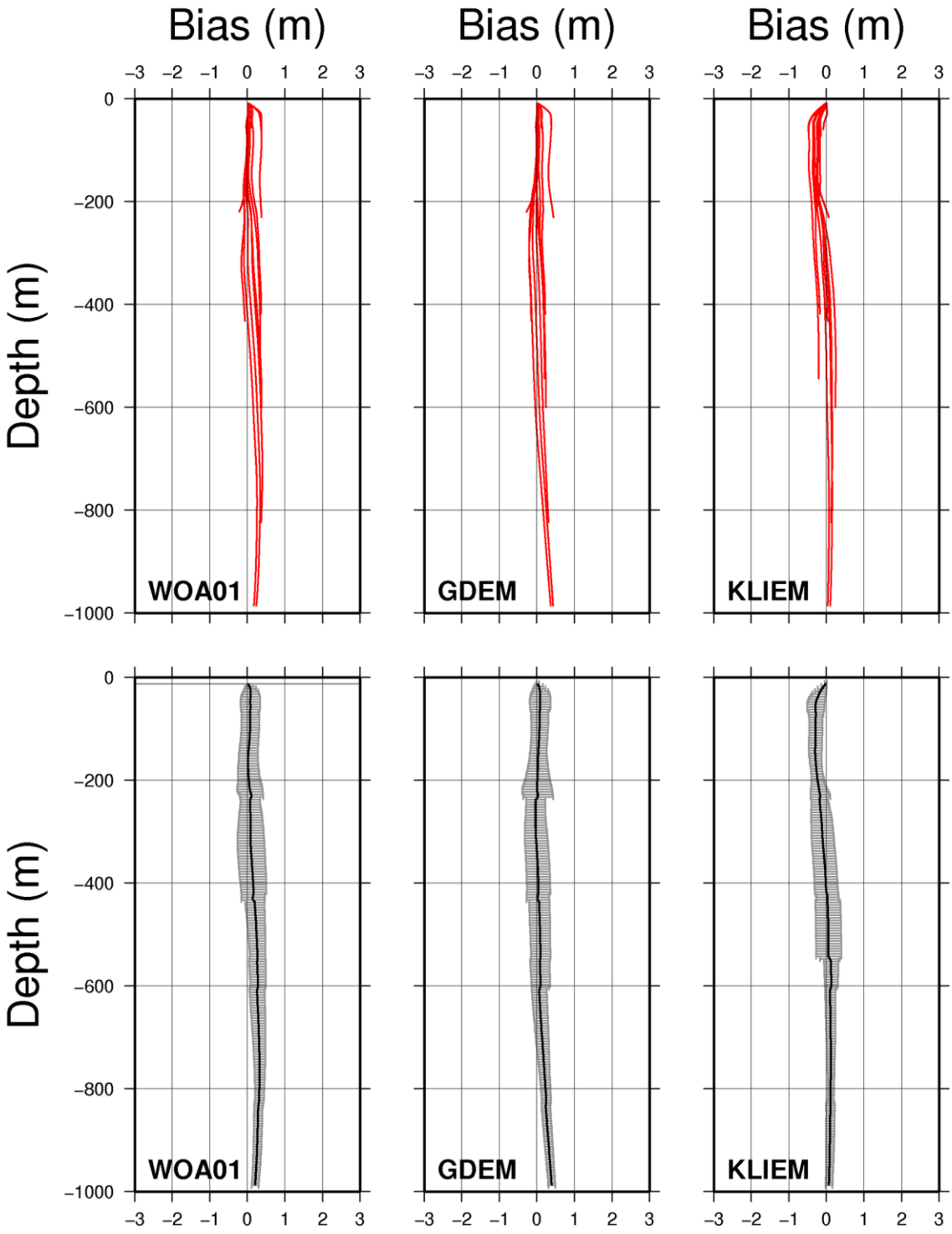

Figure 4-56. Uncertainty profiles for the western CAA, June 2004 (15 profiles).

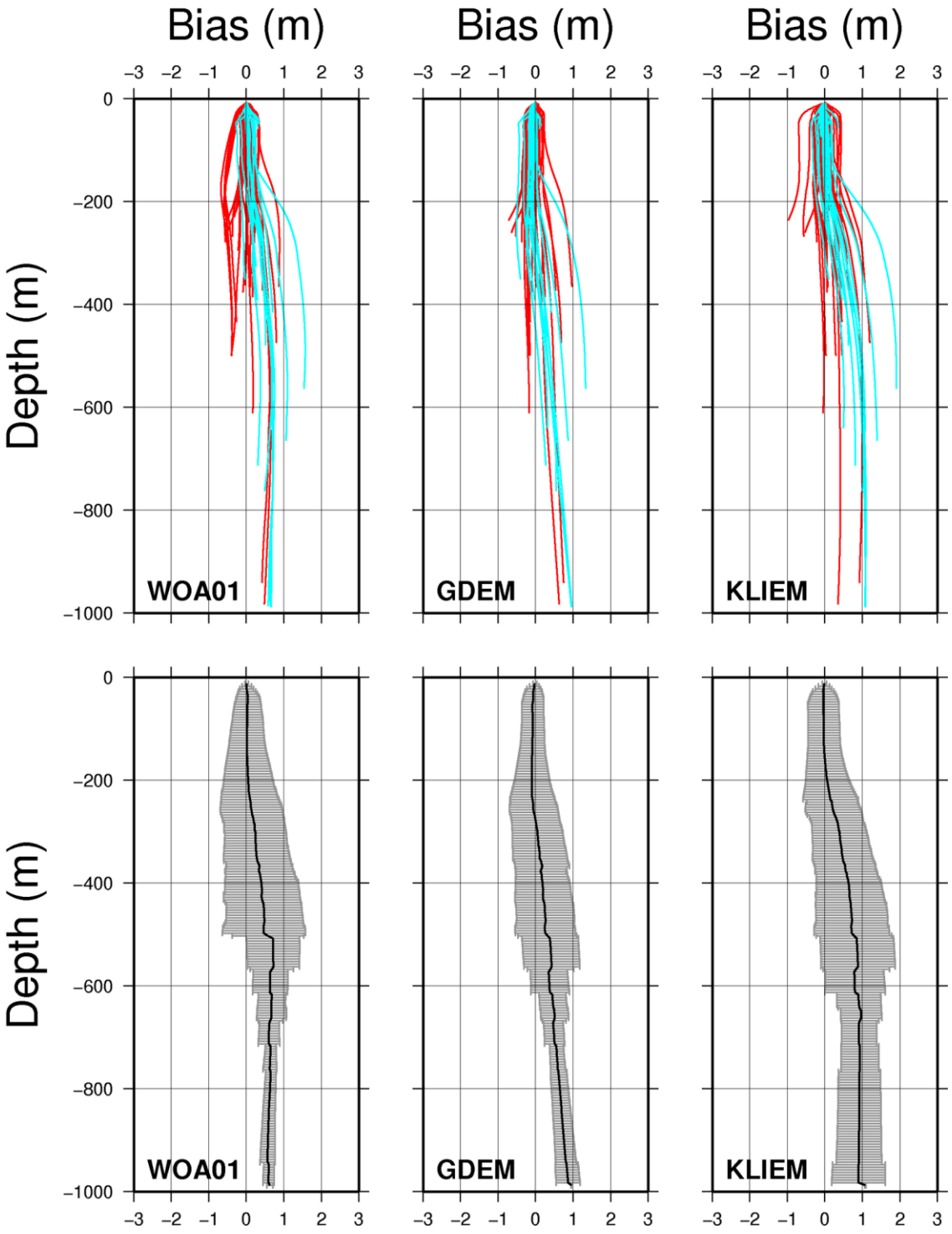

Figure 4-57. Uncertainty profiles for the western CAA, July (60 profiles). Colour coding matches that of the overview maps (red: 2004, cyan: 2009, see Figure 4-55).

Observations acquired in July spanned two field seasons with measurements gathered over most of the area in 2004 but concentrated in a small region on the Mackenzie Shelf break in 2009. Surface variability effects were more pronounced than in June, with the upper 50 m being warmer and fresher, which is consistent with the expected effects of increased ice melt in the region by this time of year (this warming and freshening trend continues into September). Variability at depth was observed with significant upward and downward displacements of the deep thermocline on the order of 60 m and 30 m, respectively. These displacements introduce significant bias relative to surface effects, with variations between the three climatologies being due to the slight differences in their predictions of the thermocline depth and temperature (which can vary by a few tens of meters and a few tenths of a degree, respectively).

The worst case WOA01 uncertainty profiles (negatively biased, reaching a maximum of -0.75 m at a depth of 175 m) are associated with over-prediction of the July temperature in the Arctic Halocline by 0.25 – 0.50°C over depths of 25 – 175 m, but *only* in the Amundsen Gulf. No other climatology and no other WOA01 profiles in July exhibit such a strong mid-water bias, suggesting a localized gridding artifact in the Amundsen Gulf. This is not surprising as there are only 4 WOD observations in this area for July. The worst-case negatively biased Kliem profile results from particularly cold and salty conditions. All three climatologies suffer the same negative bias due to over prediction of the surface layer temperature though Kliem fares worse as it is, again, a summer climatology and will almost always predict warmer temperatures when used in seasons that it was not intended for. On average though, the Kliem climatology provided

an unbiased estimate of the temperature and salinity in the upper 25 m compared to the month of June.

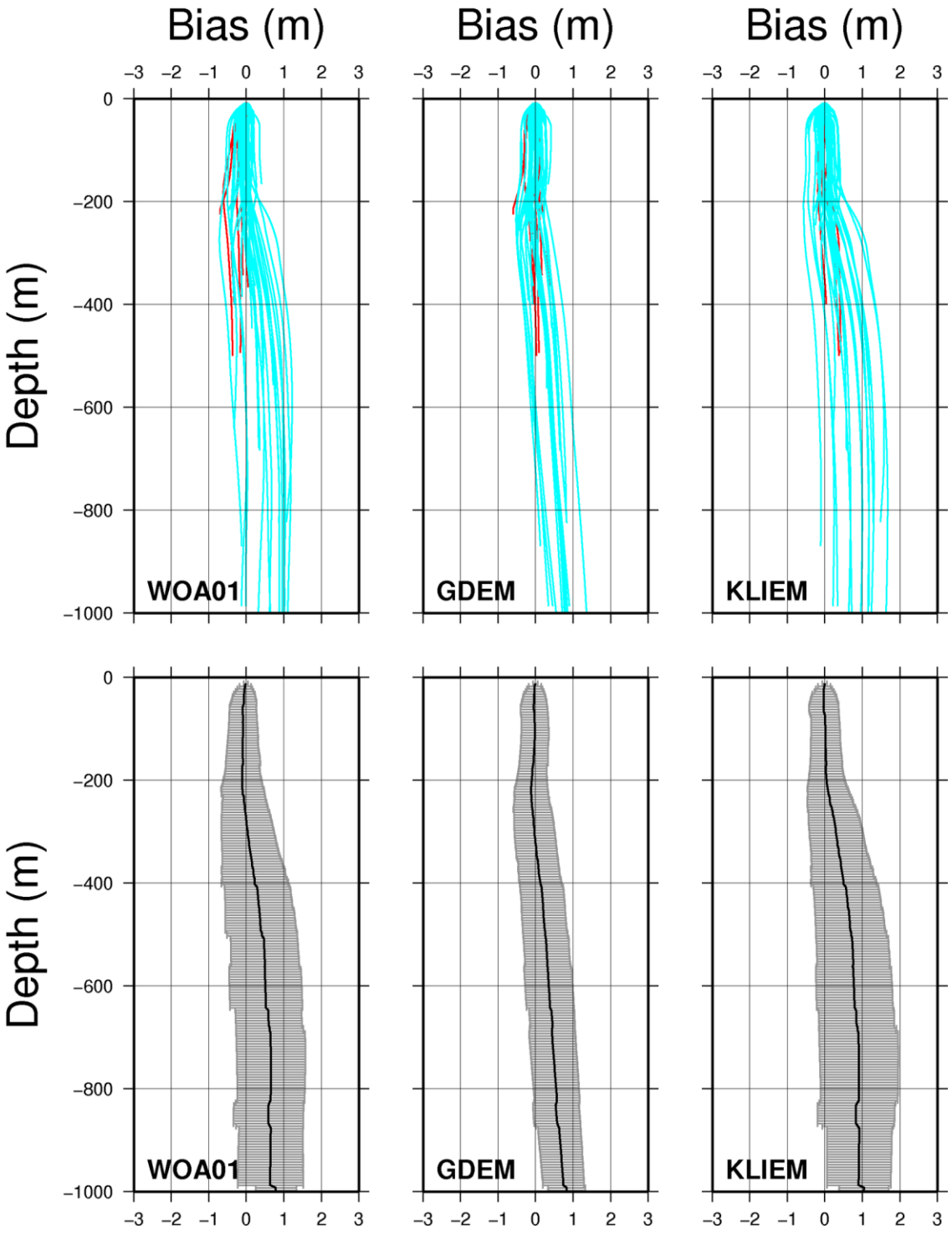

Figure 4-58. Uncertainty profiles for the western CAA, August (69 profiles). Colour coding matches that of the overview maps (red: 2004, cyan: 2009, see Figure 4-55).

The month of August was well sampled on the Mackenzie Shelf and shelf break in 2009, with operations focusing in the Amundsen Gulf and Franklin Bay in 2004. All three climatologies react more or less equally to surface variability and all offer an unbiased mean solution to depths of 200 m with similar uncertainties about the mean bias. Looking below 200 m depth, all three climatologies suffer a positive bias due to under prediction of the thermocline depth with slight differences associated with inconsistencies between the predictions from each (typically Kliem predicts the deepest and GDEM the shallowest). As the Mackenzie Shelf and Beaufort Sea areas are well sampled in the WOD for the month of August, this consistently positive bias for the 2009 field season is suggestive of long term variability between Arctic Water (AW) conditions in 2009 and conditions during the early 1950s, mid 1970s and late 1980s when the majority of WOD observations were acquired (see Figure 4-59). The casts of 2004 suffer no such positive bias at depth and react consistently to the local variability, which lends further support to this line of reasoning, though arguably they were collected in the Amundsen Gulf, which is not as well sampled. Looking back at the July results for 2009, the same pattern exists (persistent positive bias beyond depths of 200 m for the three climatologies). Examining the July casts in isolation, it is more difficult to argue for the case of inter-annual variability as the casts were collected over a very small area (approximately 50 km x 50 km) and over a small period of time (2 weeks). The August 2009 campaign, however, sampled a much larger area over a longer period of time (nearly 4 weeks). As the behaviour is persistent over two months and for all three climatologies, the evidence suggests that inter-annual variability is the cause of the positive bias.

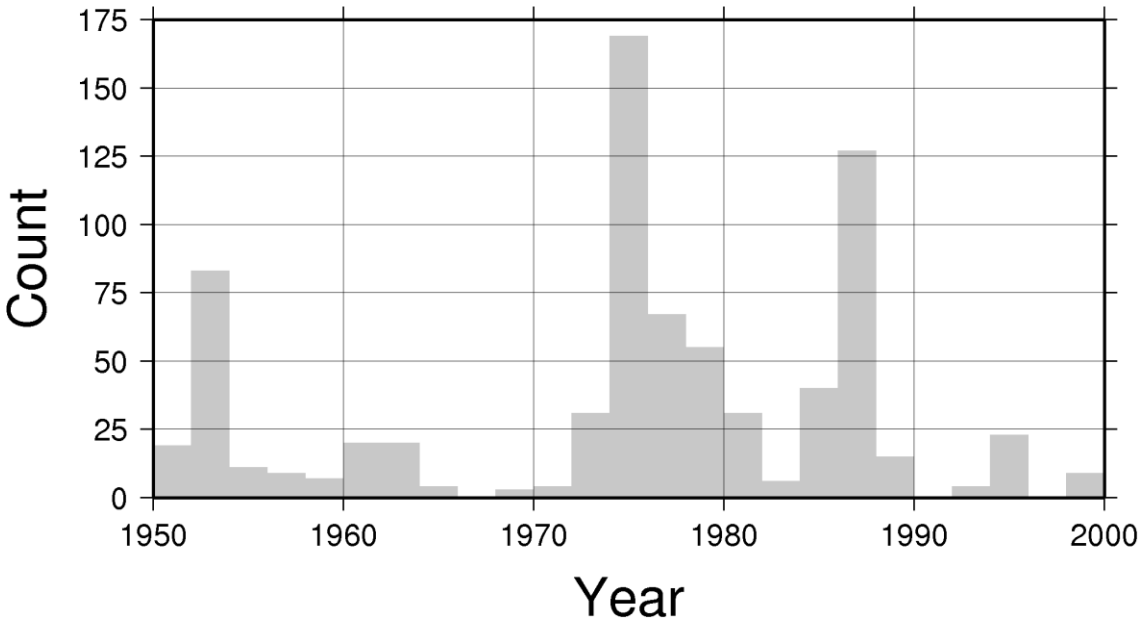

Figure 4-59. Histogram of acquisition year for WOD observations in the western CAA for the month of August.

The month of September saw extensive sampling in 2005 in the Amundsen Gulf with only a few samples acquired near the eastern reaches of the gulf in 2006. Uncertainty due to surface variability is similar to July and August, again without significant discrepancies between the three climatologies. In the 2005 season, the upper 15 m of the water column was bimodal in temperature distribution with the two means near freezing or several degrees above freezing, likely due to the presence or absence of sea ice. This explains the bi-modal distribution of bias in the upper 25 m, as most easily observed in the Kliem bias profiles of Figure 4-60. This suggests that the presence or absence of ice can introduce uncertainty on the order of +/-0.50 m, depending on which climatology's "mean" conditions most closely match the mid-point between ice-free and ice-covered waters. Only a few casts were gathered in deeper water, and all are suffer from a slight positive bias, however the small number of casts provide insufficient data

over a small time frame and a wide area to draw any conclusions as was done for the casts collected in August 2009.

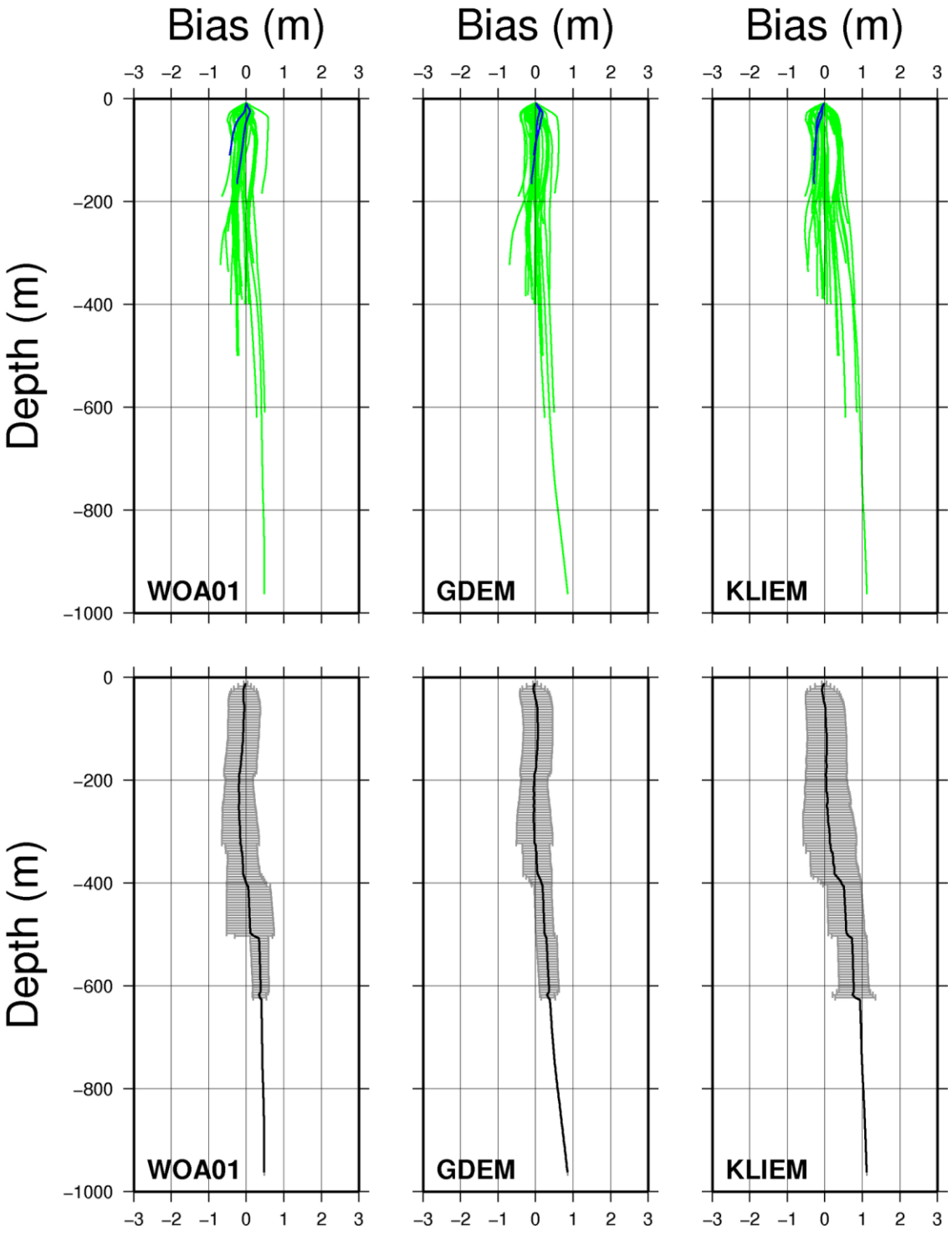

Figure 4-60. Uncertainty profiles for the western CAA, September (66 profiles). Colour coding matches that of the overview maps (green: 2005, blue: 2006, see Figure 4-55).

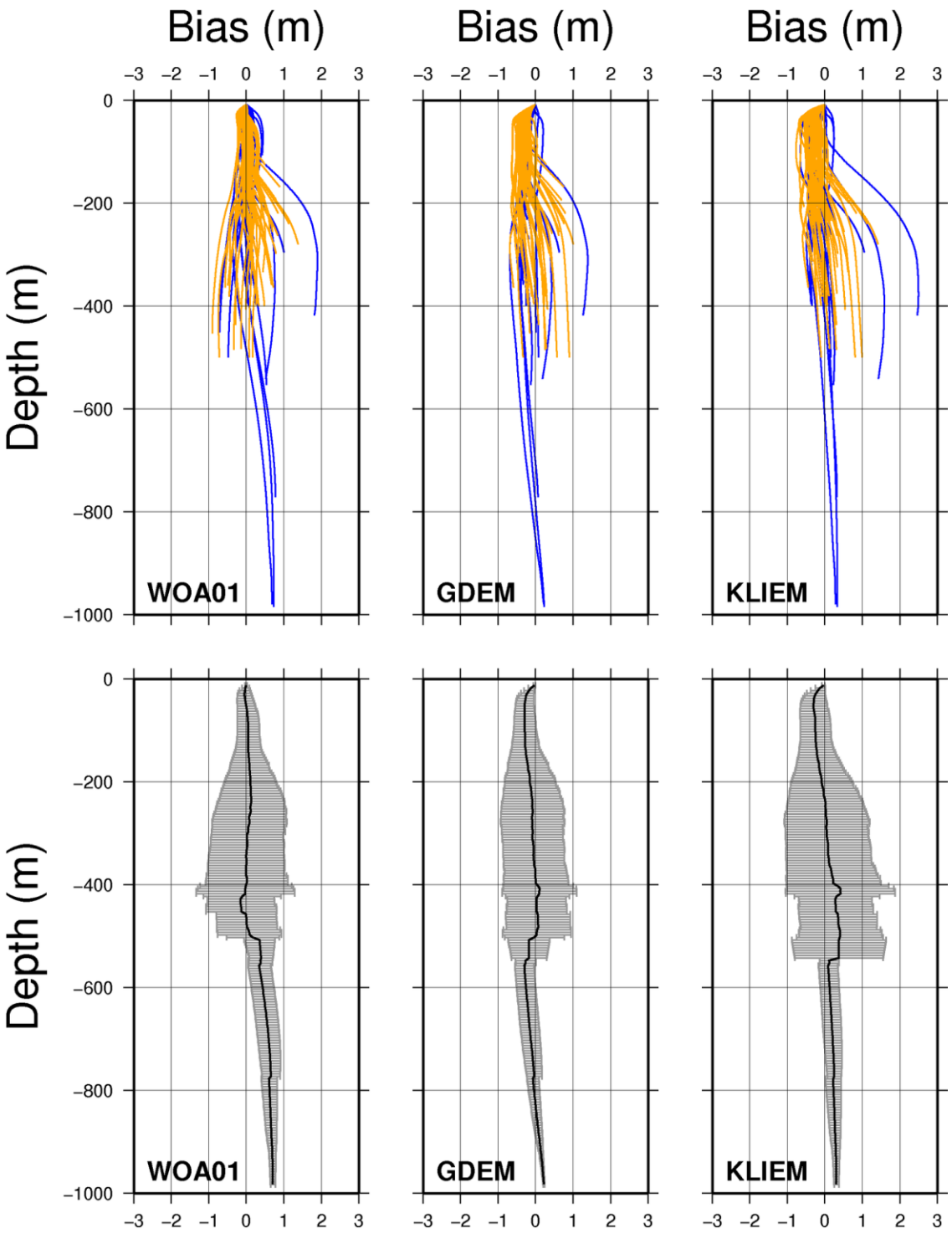

Figure 4-61. Uncertainty profiles for the western CAA, October (145 profiles). Colour coding matches that of the overview maps (orange: 2007, blue: 2006, see Figure 4-55).

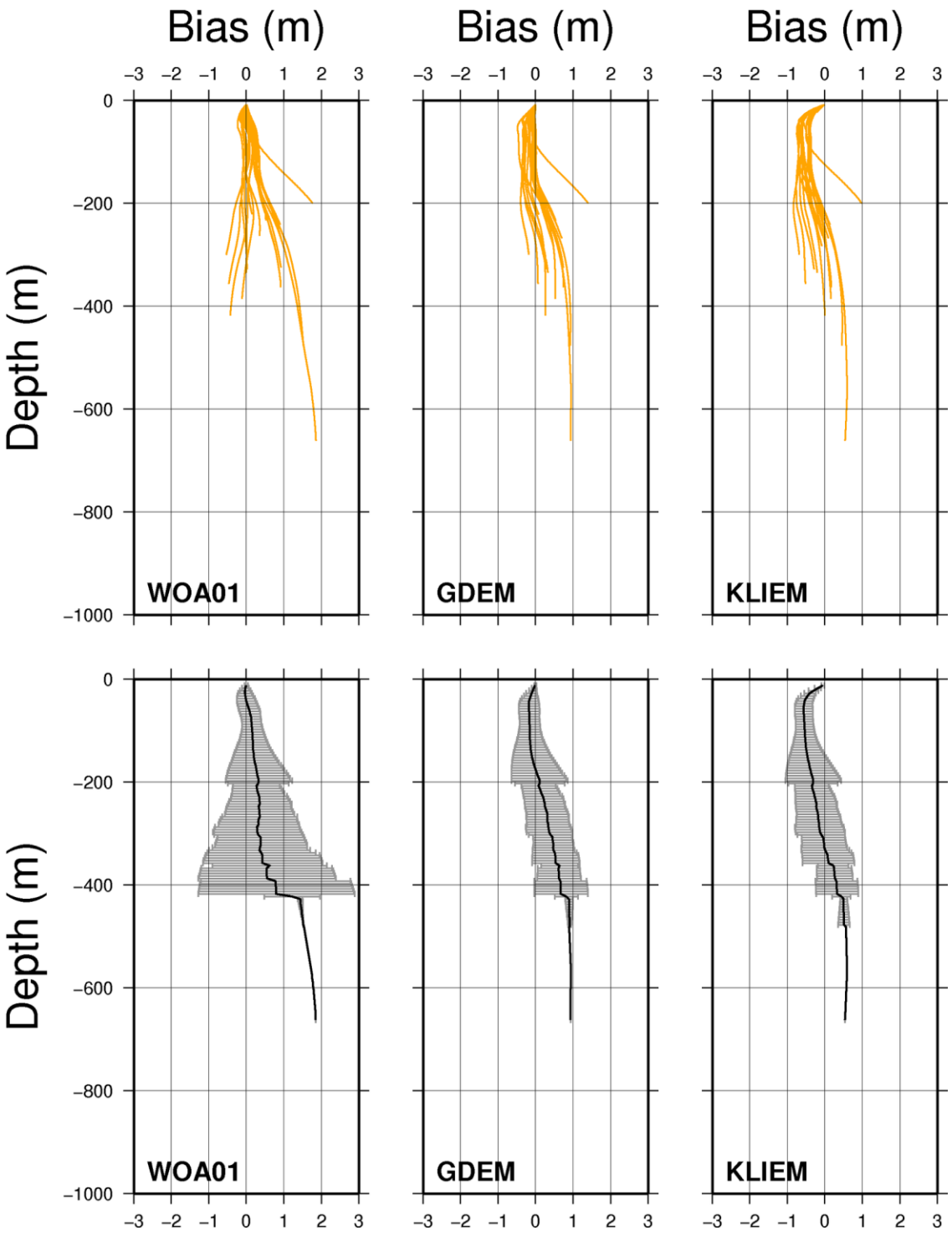

Figure 4-62. Uncertainty profiles for the western CAA, November 2007 (24 profiles).

The month of October differs from the previous months in two ways. Firstly, pronounced spatio-temporal variability in thermocline depth was observed in the two

field seasons over which observations were made (2006 and 2007). Secondly, there are very few observations in the WOD for October in the western CAA. This is an unfortunate pairing as the first leads to potentially significant spatio-temporal uncertainty and the second can lead to systematic bias.

Examining the uncertainty profiles, the Kliem grids provide a biased surface solution; again, the summer conditions of the climatology are no longer representative of the cooler and saltier surface waters. Curiously, GDEM suffers similarly and yields positively biased solutions within the upper 25 m, suggesting that it is biased towards summer conditions in the upper layers. Looking deeper into the water column, thermocline displacements occur often and are particularly large, on the order of 125 – 150 m. These events lead to large positive depth biases of 1 – 2.5 m, the largest seen thus far in this region. The uncertainty associated with surface variability is small in comparison though it is of similar magnitude to that seen in the previous seasons. Large (up to 400 m) thermocline displacements due to upwelling have been observed in the Mackenzie Trough region and are associated with strong northeasterly winds, which occur often in this season (Carmack and Kulikov, 1998). Cape Bathurst, at the eastern end of the Mackenzie Shelf, is another area of known upwelling (Williams and Carmack, 2008).

Though all climatologies suffer equally from these potential upwelling events, the WOA01 uncertainty profiles occasionally suffer from a negative bias at depth whereas the other two do not. This is due to the WOA01 October grid predicting a slightly shallower thermocline compared to the other two in the Amundsen Gulf. The September WOA01 grid shows no such bias in the Amundsen Gulf, suggesting it is yet another

gridding artifact due to sparse data in these two months. It should be noted that the Amundsen Gulf is poorly sampled as compared to the Mackenzie Shelf and shelf break. Indeed, no data whatsoever is available in the area for the months of October and November in the WOD (see Appendix B).

The ArcticNet data set for the month of November consists of only 24 casts, all collected in the same field season over a very small area. Little is different though from the findings of October as it is also affected by spatio-temporal variability in the thermocline depth due to Fall storm activity and bias due to sparse underlying data sets. The Kliem climatology is even more negatively biased in the colder and saltier surface conditions of November (and the GDEM is as well, as was found in October). WOA01 continues to provide an unbiased estimate of surface conditions, however, it also exhibits the same negative bias at depth for casts acquired in Amundsen Gulf as was the case for the October casts.

4.4.5 Discussion

It is useful at this point to compare the VA and UA results from the different regions. Beginning at the surface, the effect of surface variability has different impacts across the CAA, as summarized by Figure 4-63. As surface variability occurs on temporal and spatial scales beyond the resolving power of any of the climatologies investigated herein, they will all suffer the full effect of surface variability. Studying the results by region can provide some guidance for those that wish to rely on climatologies. The areas where variability has the most impact, at least as quantified through analysis of the occasionally limited ArcticNet data set, are the North Water, Lancaster Sound and the

western CAA. Areas with smaller surface variability effects were the central and southern CAA with the central area having the least worrisome surface variability. The sample size for each data set varied (and so did the sampling depths), thus some uncertainty in the uncertainty estimates must be expected. The North Water and the western CAA (shallow and deep) are likely the most robust estimates as these areas were extensively studied over several years and have a greater chance of having been exposed to more of the natural range of temperature and salinity variations. The estimates for all other areas are based on substantially smaller data sets and could be improved with more observations.

It is also useful to put these results in context of common survey orders. Referring again to Figure 4-63, it can be seen that most of the surface effects are negligible for an IHO Order 1A/B survey, which is likely the survey order that would be required for nautical charting in water depths greater than 50 m in these regions. In fact, most of the areas exhibit variability that would still permit a Special Order survey, though this order of accuracy is usually reserved for much shallower depths (though an uncertainty budget should make allowance for other sources of uncertainty, e.g. tides). This is not to say that climatologies could be used with little impact from surface variability in shallower waters. It must be remembered that, in sampling the waterways of the CAA, the ArcticNet CTD casts are biased toward deeper portions of channels, sounds and bays. The observed surface variability of these data sets is not representative of what would be expected in shallower water. Though the same stratification processes may be at work, there is much more potential for tidal mixing reaching into the stratified surface layer, which could alter the nature of the variability entirely. MVP transect B in

northeastern Hudson Bay provides a good example of the increased effects of tidal mixing and mixing due to turbulence as flows react to topography. These effects are simply not observed in the deeper Amundsen data sets and could lead to situations where uncertainty estimates derived from deeper water underestimate actual uncertainties associated with variability. On the other hand, overestimations may occur in areas where tidal mixing homogenizes the entire water column, e.g. in the vicinity of the central sills in Barrow Strait (Prinsenberg and Bennett, 1989a). Clearly more study is required for the shallow water case.

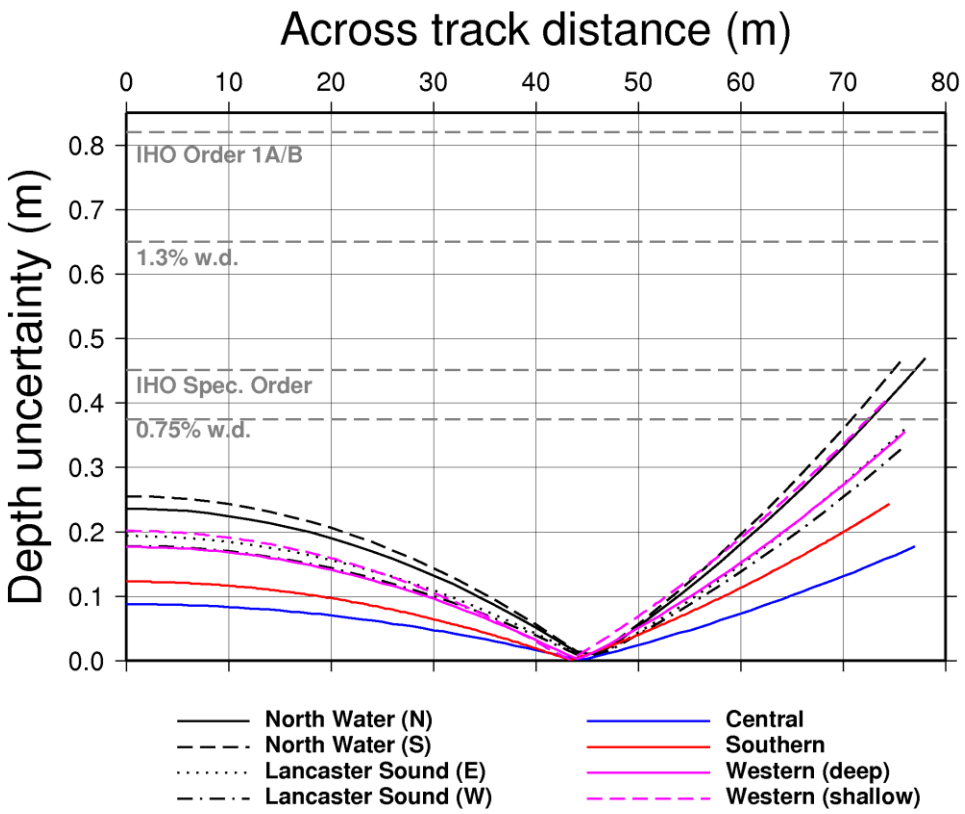

Figure 4-63. Comparison of surface variability effects across the CAA. Uncertainty sections at a depth of 50 m are extracted from the various v-wedges shown in previous examinations. Allowable vertical uncertainties for IHO Special Order and Order 1A/B are plotted as grey dashed lines for reference (both calculated for 50 m depth). The uncertaity minima at an across-track distance of approximately 45 m is consistent with the behaviour of water column variability in which the surface sound speed is used to augment the vertical sound speed profile (Capell, 1999).

If climatologies presented unbiased estimates of mean conditions in deep water and variability at depth was non-existent in the CAA, then this would be the end of the discussion. As has been shown earlier, this is not the case. Figure 4-64 shows uncertainty profiles for the outermost beam of the Amundsen's 120° angular sector, as derived from the regional VAs discussed in the previous regional examinations. The regions can be grouped into two categories based on which variability dominates the total observed uncertainty at the seabed. In the first category are those which are dominated by surface variability, this group includes the northern North Water region, and the central, southern and western CAA. In these regions, uncertainty on the order of 0.2 – 0.6 m is introduced in the upper 50 m of the water column, with little contribution from deeper variability beyond this depth. In the second category are those regions whose total predicted uncertainty are dominated by variability at depth, these include the southern North Water region and Lancaster Sound. In all of these regions the uncertainty associated with variability at depth easily matches and even exceeds that due to surface variability. Combined with high uncertainty due to surface variability (except perhaps western Lancaster Sound), these are the areas where any climatology would perform poorly as a substitute for in-situ measurement of sound speed. The term "poorly" is relative and somewhat subjective, however, and it is necessary to examine these findings in the context of common survey orders. As can be seen in Figure 4-64, even the worst of the regions would not present much difficulty to a hydrographer attempting an IHO Order 1 survey in water depths greater than 50 m. Though there are regions with apparently pronounced variability, the uncertainty that results from the variability is

negligible in terms of meeting IHO accuracy requirements (which many survey standards are based upon, if only loosely).

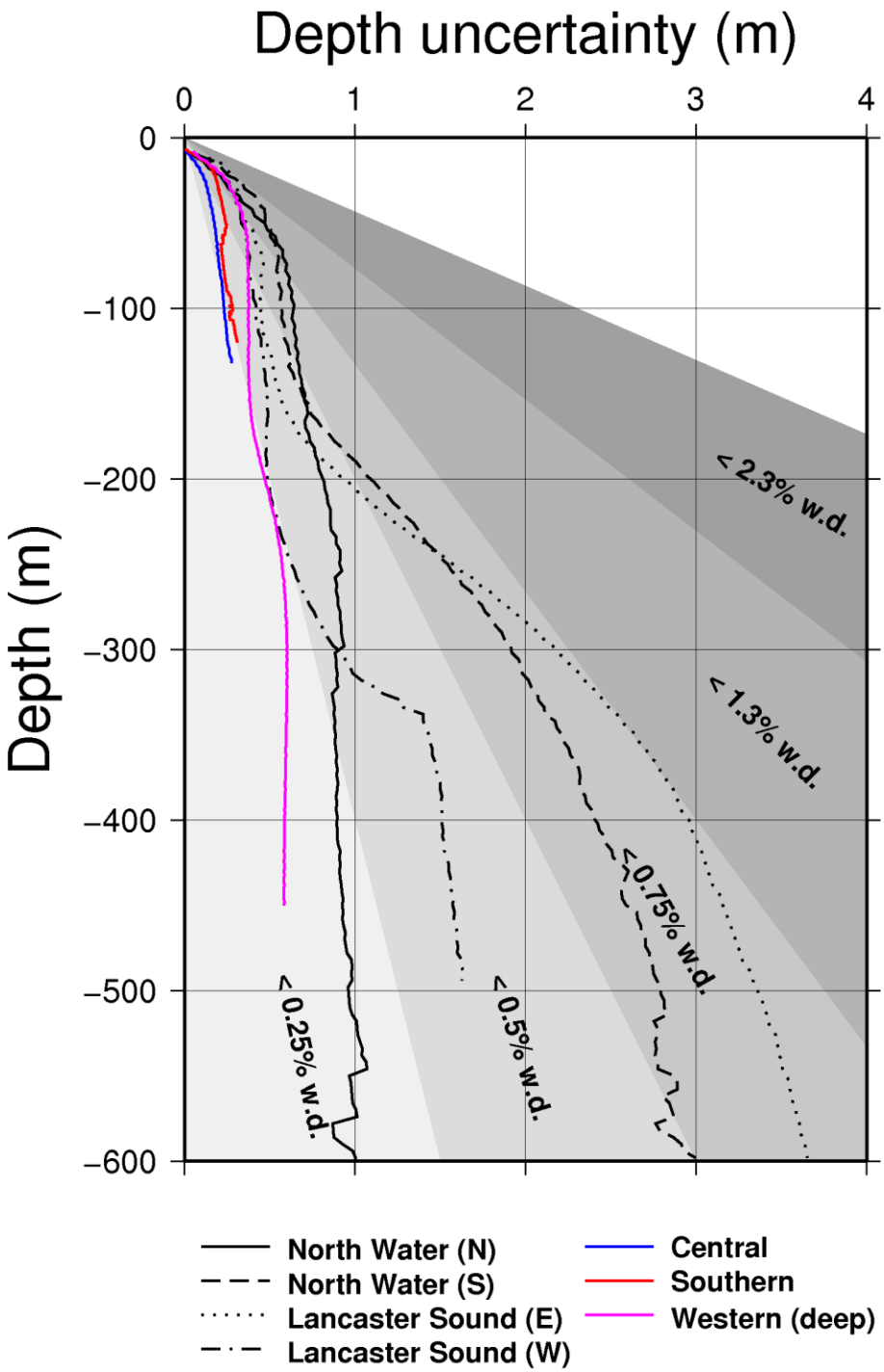

Figure 4-64. Comparison of uncertainty as a function of depth across the CAA. Uncertainty profiles are extracted from the various v-wedges shown in previous examinations.

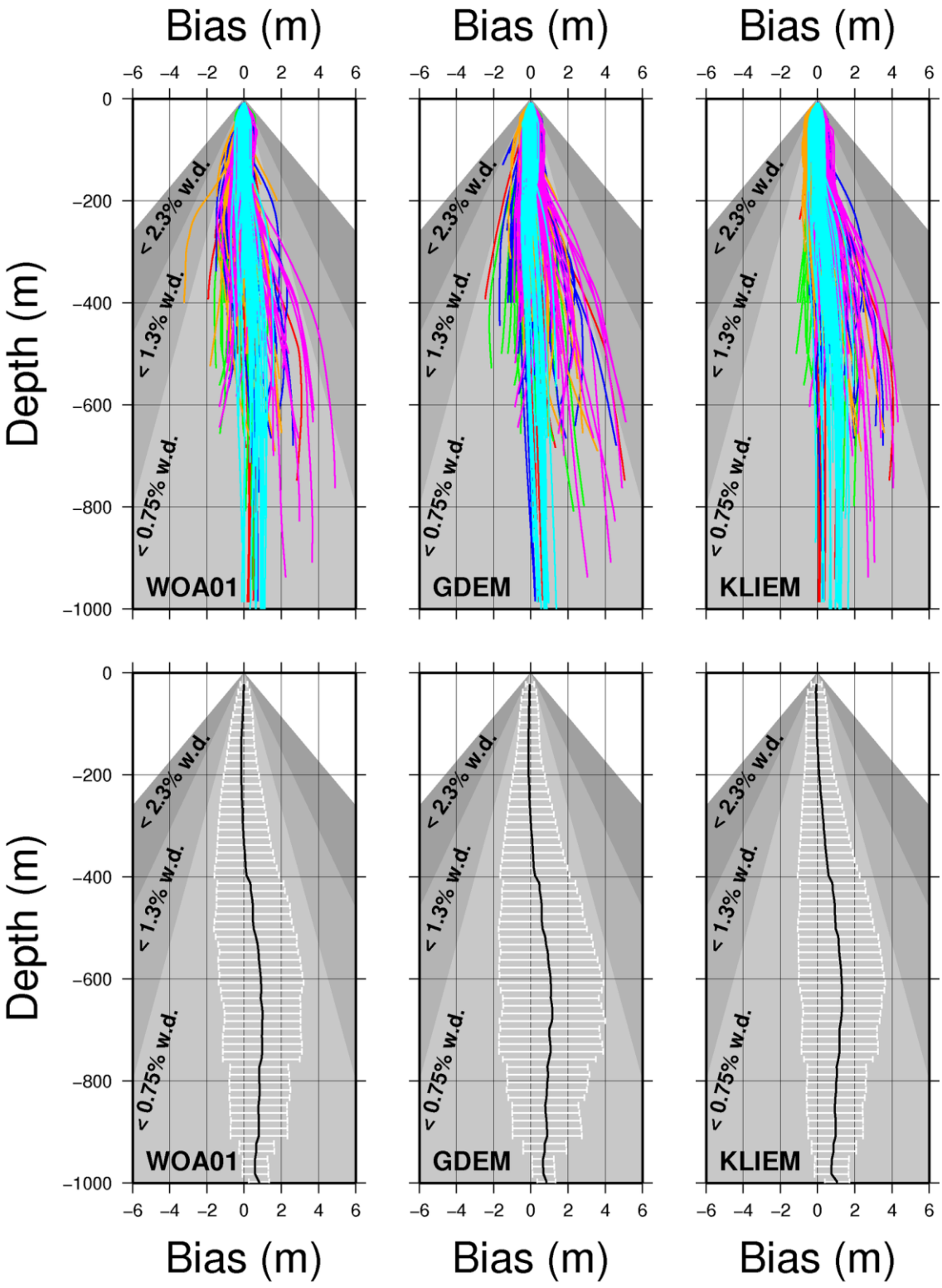

Figure 4-65. Summary of climatological uncertainty profiles for all regions investigated. Bias profiles are plotted in the upper row of panels, whereas the mean bias and standard deviation (scaled to 95% confidence level) are plotted in the lower panels.

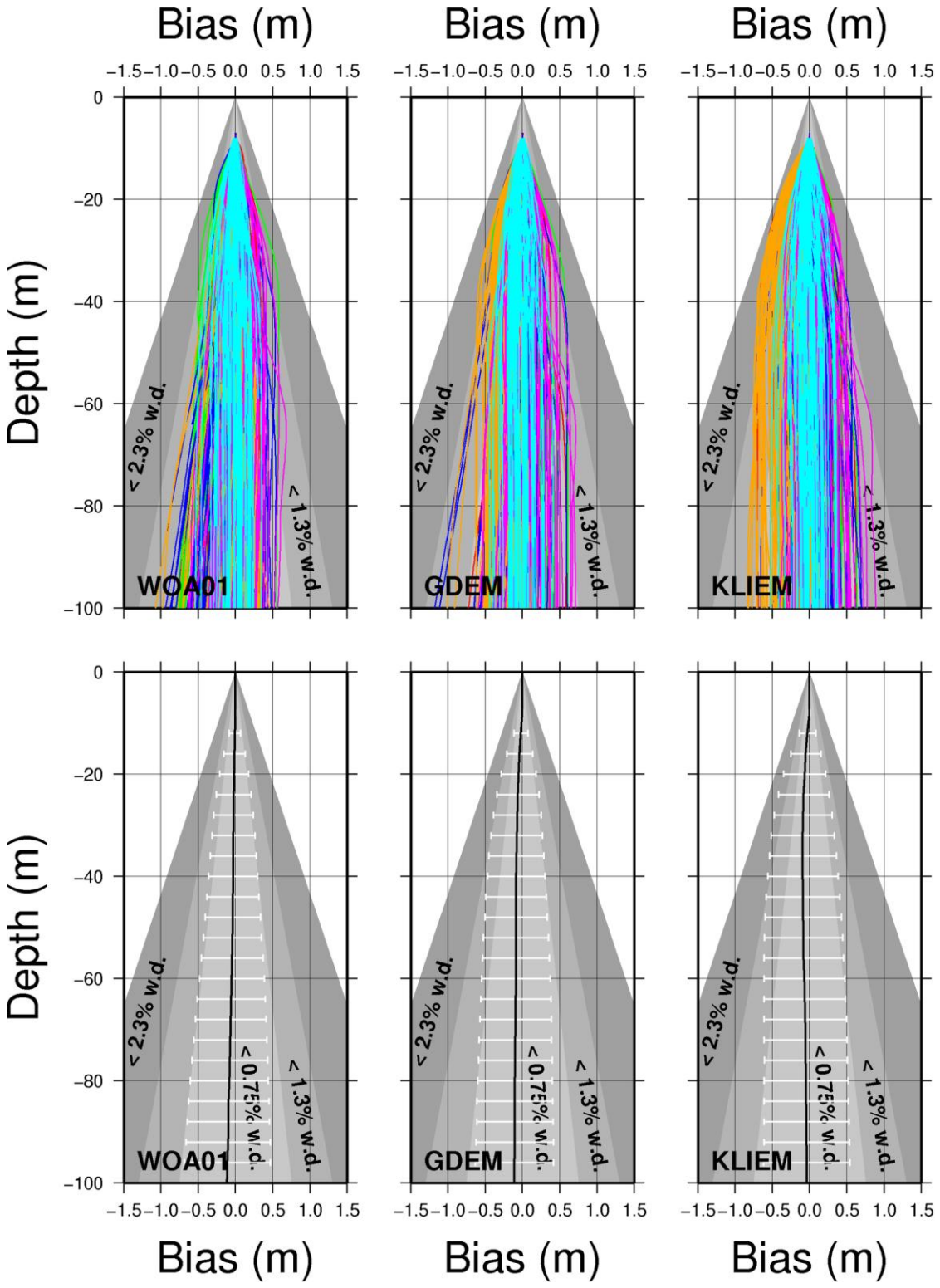

Figure 4-66. Summary climatological uncertainty profiles for the upper 100 m of all regions investigated. Bias profiles are plotted in the upper row of panels, whereas the mean bias and standard deviation (scaled to 95% confidence level) are plotted in the lower panels.

The results of all climatological investigations can similarly be summarized and examined in context of survey accuracy requirements. Figure 4-65 plots uncertainty profiles for all the regions investigated in a single graph, along with mean bias and the deviation about the mean bias (at the 95% confidence level). Despite the existence of clear biases in the climatologies (e.g. WOA01 October warm water artifact in Lancaster Sound) and inter-annual variability (e.g. 2009 thermocline depth bias in the western CAA), there are rarely circumstances where the resulting sounding biases exceed that allowed by an IHO Order 1 survey, especially if efforts were made to correct the clearly biased sections of some of the monthly climatologies. The largest concern is in water depths less than 100 m where most of the uncertainty budget can be consumed by sound speed uncertainties, leaving little room for non-depth scaling uncertainties such as tides (Figure 4-66).

On the whole, the climatologies provide adequate estimates of mean conditions. Of course, there are biases in some of the monthly grids. There appears to be significant inter-annual variability that alters water mass distributions over an entire region. There are cases of high spatio-temporal variability, both at the surface and at depth. These all introduce uncertainty when the climatologies are used for MBES sounding reduction. Given these limitations, how is it that results approaching those achieved by Calder et al (2004) are achieved (cf. Section 2.6), where much more sophisticated oceanographic models were used? The use of climatologies for ArcticNet mapping has four saving graces: (i) the surface sound speed is measured continuously, (ii) for the most part, the climatology profiles agree remarkably well with CTD profiles below the variable surface layer, (iii) the surface layer is usually small relative to the total depth as the Amundsen's

operations are usually limited to deeper waters, and (iv) the Amundsen's angular sector is limited to 120° due to the transducers being recessed in the hull for protection against ice (refer to Bartlett et al. (2004) for more details). As observed by Dinn et al (1995) and Cartwright and Hughes Clarke (2002), ray tracing algorithms tend to recover gracefully when faced with outdated sound speed profiles that converge at depth as long as one preserves the ray parameter (Snell's constant) through the measurement of the surface sound speed with a probe. By fixing the ray parameter at the surface, the true and computed ray paths will become parallel once the variable surface layer is passed. This is due to the fact that the ray parameter will maintain the correct departure angle at the deepest portion of the layer of surface variability regardless of the intervening sound speed structure in the water column. A bias in depth and across-track distance is introduced due to the poorly matching surface portion of climatological profiles, however, this bias is constant and becomes increasingly insignificant with depth, especially in the case where the thickness of the variable surface layer is small with respect to the entire water column (Cartwright and Hughes Clarke, 2002).

5 CONCLUSION

5.1 Summary

Intuitive analysis methods have been developed that allow for an in depth examination of the uncertainty impact associated with water mass variability and alternate water column representations. Variability Analysis techniques allow for the estimation of sounding uncertainty due to the effects of water column spatio-temporal variability and provide a significant improvement over existing models and methods. Uncertainty Analysis methods provide the means to address sophisticated sound speed analysis problems in a quantitative manner such that hydrographers can assess the uncertainty impact of water column sampling regimes, choice of instrumentation (e.g. XBT vs. XCTD), survey design, etc.

In the case study of the CAA, it was found that all of the climatologies provide a reasonable substitute for in-situ measurements for IHO Order 1 surveys in waters deeper than 100 – 200 hundred metres, despite potentially limiting biases in some of the temperature grids. Natural variability differed by region and was driven by the distribution and extent of the various water masses found in the Arctic. Though variability was pronounced in some regions, it did not preclude the use of climatologies as a source of sound speed for ArcticNet operations.

Though all of the findings regarding climatology biases, surface variability and inter-annual variability could have been done by examining temperature and salinity

profiles alone, the methods used in this analysis were able to arrive at the same conclusions but were also able to express the impact of these findings in terms that are meaningful to a hydrographic surveyor. By examining the depth evolution of potential sounding bias, the relative importance of the differing sources of variability were quantified, allowing for extraction of meaningful information from an extensive data set of water column measurements. This type of information can help the hydrographer tailor water column sampling strategies to mitigate the effects of spatio-temporal/inter-annual variability and climatological bias. Previous methods, which typically limit their investigation to the uncertainty at the seabed, would have been limited in their ability to identify and quantify the impacts of the differing sources of variability, be it at the surface, at depth, from climatological bias or from inter-annual variability.

Most other sources of uncertainty in MBES are well understood and relatively easily modeled compared to the effects of water column spatio-temporal variability (Hare, 2001). The analysis methods described herein provide a quantitative approach to one of the final pieces of the uncertainty puzzle and will enable hydrographers to be more certain about their uncertainty.

5.2 Limitations and Future Work

The results from the case study likely suffer from the underlying assumption that the natural range of variability has been sampled over the course of the six field seasons, especially in those regions that have been only sparsely sampled to date, e.g. the southern and central CAA. Future field programs should endeavour to gather more data in these

regions. Though the WOD has been purposely kept at arm's length during the case study, it might be prudent to use this resource in these areas to augment the fidelity of the Variability Analyses findings in these regions.

Variability Analysis and Uncertainty Analysis results rely heavily on having an extensively sampled water mass, something which is not always practical to collect. Future work will investigate the degradation of uncertainty estimates from UA and VA when given much smaller data sets of casts. These analysis tools also assume a normal distribution and could be improved to deal with cases when this assumption is false, for example, with skewed and multi-modal distributions. These cases should be identified and dealt with in a more robust fashion, as uncertainty scaling factors that apply to normal distributions will differ for other distributions and should be adjusted accordingly.

In many uncertainty models, uncertainty in the measurement of surface sound speed and uncertainty in the measurement of sound speed throughout the water column are treated separately (Hare, 2001). This is also the case for the analysis techniques proposed in this work. This work also limits itself to investigating the effect of an incorrect representation of the water column, however, it assumes zero uncertainty in the sound speed profiling instrumentation. The effect of sound speed instrumentation uncertainty should be included, whether it is measured continuously at the surface or through vertical profiling.

5.3 Recommendations

The fidelity of WOA climatologies, particularly in winter, is known to be low since the lack of observations biases the interpolation towards warmer summer conditions (Steele et al., 2001). This effect has been observed in this work as well, with October and November grids having significant warm biases at depth in several locations throughout the CAA. It is recommended that ArcticNet CTDs be submitted to the National Oceanographic Data Centre (NODC) such that they can be incorporated into future versions of the WOA and rectify these biases.

Until such updates to WOD and WOA are available, current climatological grids can be improved by removing some of the known artifacts. The biases discovered and patterns observed through the use of the ArcticNet data set can be used to help identify problem areas in regions that were not sampled by the Amundsen, for example, the Queen Elizabeth Islands to the north of Parry Channel. Though the Amundsen rarely ventures to these northerly latitudes, other Canadian Coast Guard vessels routinely do and examining the climatologies in these areas may provide guidance as to their use in the event that other Coast Guard vessels acquire sounding data while in transit.

Finally, several high-resolution MVP data sets collected in 2008 by the CSL Heron during coastal hydrographic surveys in the eastern CAA should be used to study the effect of variability in shallower waters. These data sets can help understand the degradation of uncertainty estimates resulting from applying uncertainty estimates from deep water sampling (as was done with the Amundsen) to the shallow coastal waterways of the CAA.

6 REFERENCES

Ambrose, J. T., and Geneva, A. (1995). "Wide swath bathymetric sonar error modeling for a hydrographic survey ship." *Oceans Conference Record (IEEE)*, IEEE, Piscataway, NJ, USA, San Diego, CA, USA, 339-346.

Andrews, J. (2002). "DoD Climate Programs: Brief to the CCSPO." US Office of Naval Research.

Angelari, R. (1978). "A Deterministic and Random Error Model for a Multibeam Hydrographic Sonar System." *Oceans Conference Record (IEEE)*, IEEE, Newark, DE, US, 48-53.

APL (2009). "AVHRR Imagery.", Applied Physics Laboratory, John Hopkins University, http://fermi.jhuapl.edu/avhrr, accessed Oct. 28, 2009.

Applanix Corporation (2004). "POS MV V4 Installation and Operation Guide." Applanix Corporation.

Barber, D. G., and Iacozza, J. (2004). "Historical Analysis of Sea Ice Conditions in M'Clintock Channel and the Gulf of Boothia, Nunavut: Implications for Ringed Seal and Polar Bear Habitat." *Arctic*, 57(1), 1.

Barnes, S. L. (1964). "A Technique for Maximizing Details in Numerical Weather Map Analysis." *Journal of Applied Meteorology*, 3(4), 396-409.

Barry, R. C., and Serreze, M. C. (2000). "Atmospheric components of the Arctic Ocean freshwater balance and their interannual variability." *The Freshwater Budget of the Arctic Ocean*, E. L. Lewis, E. P. Jones, P. Lemke, T. D. Prowse, and P. Wadhams, eds., Kluwer Academic Publishers, Dordrecht, The Netherlands.

Bartlett, J., Beaudoin, J., and Hughes Clarke, J. E. (2004). "CCGS Amundsen: A New Mapping Platform for Canada's North." *Lighthouse, Journal of the Canadian Hydrographic Association*,(65).

Beaudoin, J. (2008). "Real-time monitoring of uncertainty due to refraction in multibeam echosounding." *Proceedings of the 2008 Shallow Survey Conference*, Center for Coastal and Ocean Mapping/Joint Hydrographic Center, University of New Hampshire, Portsmouth, USA.

Beaudoin, J. (2009). "Field trials of the UNB refraction uncertainty monitoring toolkit." *Proceedings of FEMME 2009*, Kongsberg Maritime, Lisbon, Portugal, April 2009.

Beaudoin, J., Hiebert, J., Calder, B., and Imahori, G. (2009). "Uncertainty Wedge Analysis: Quantifying the Impact of Sparse Sound Speed Profiling Regimes on Sounding Uncertainty." *Proceedings of the US Hydrographic Conference*, The Hydrographic Society of America, Norfolk, USA.

Beaudoin, J., and Hughes Clarke, J. E. (2004). "Retracing (and re-raytracing) Amundsen's Journey through the Northwest Passage." *Proceedings of the 2004 Canadian Hydrographic Conference*, Ottawa, Canada.

Beaudoin, J., Hughes Clarke, J. E., and Bartlett, J. (2004). "Application of Surface Sound Speed Measurements in Post-Processing for Multi-Sector Multibeam Echosounders." *International Hydrographic Review*, 5(3), 26-31.

Beaudoin, J., Hughes Clarke, J. E., Bartlett, J., Blasco, S., and Bennett, R. (2008). "Mapping Canada's Arctic Seabed: Collaborative Survey, Processing and Distribution Strategies." *Proceedings of the 2008 Canadian Hydrographic Conference*, Victoria, Canada.

Birch, J. R., Fissel, D. B., Lemon, D. D., Cornford, A. B., Lake, R. A., Smiley, B. D., MacDonald, R. W., and Herlinveaux, R. H. (1983). "Northwest Passage: Physical oceanography - Temperature, salinity, currents and water levels." *Rep. No. 5*, Department of Fisheries and Oceans, Sidney, Canada.

Bourillet, J. F., Edy, C., Rambert, F., Satra, C., and Loubrieu, B. (1996). "Swath mapping system processing: Bathymetry and cartography." *Marine Geophysical Researches*, 18(2 - 4), 487-506.

Boyer, T., Stephens, C., Antonov, J., Conkright, M. E., Locarnini, R., O'Brien, T. D., and Garcia, H. E. (2002) World Ocean Atlas 2001, Volume 2: Salinity. NOAA Atlas NESDIS 50. U.S.Government Printing Office. Washington, D.C., USA.

Boyer, T. P., Antonov, J., Garcia, H. E., Johnson, D. R., Locarnini, R. A., Mishonov, A. V., Pitcher, M. T., Baranova, O. K., and Smolyar, I. V. (2006). "World Ocean Database 2005." *Rep. No. NOAA Atlas NESDIS 60*, U.S. Government Printing Office, Washington, D.C., USA.

Boyer, T., Levitus, S., Garcia, H., Locarnini, R. A., Stephens, C., and Antonov, J. (2005). "Objective analyses of annual, seasonal, and monthly temperature and salinity for the World Ocean on a 0.25 degree grid." *International Journal of Climatology*, 25(7), 931-945.

Brasseur, P., Beckers, J. M., Brankart, J. M., and Schoenauen, R. (1996). "Seasonal temperature and salinity fields in the Mediterranean Sea: Climatological analyses of a historical data set." *Deep Sea Research Part I: Oceanographic Research Papers*, 43(2), 159-192.

Capell, W.J. (1999). "Determination of sound velocity profile errors using multibeam data." Oceans '99 Conference Proceedings, Vol. 3, IEEE, 1143-1148.

C&C Technologies (2004). "C-Nav GPS System Operations Manual." C&C Technologies, Inc., Lafayette, USA.

Calder, B. (2003). "Automatic Statistical Processing of Multibeam Echosounder Data." *International Hydrographic Review*, 4(1).

Calder, B., Kraft, B., de Moustier, C., Lewis, J., and Stein, P. (2004). "Model-Based Refraction Correction in Intermediate Depth Multibeam Echosounder Survey." *European Conference on Underwater Acoustics*.

Caress, D. W., and Chayes, D. N. (2005). Mapping the seafloor: Software for the processing and display of swath sonar data. [5.0.6]. Columbia University. USA.

Carmack, E. C. (2000). "The Arctic Ocean's Freshwater Budget: Sources, Storage and Export." *The Freshwater Budget of the Arctic Ocean*, E. L. Lewis, E. P. Jones, P. Lemke, T. D. Prowse, and P. Wadhams, eds., Kluwer Academic Publishers, Dordrecht, The Netherlands, 91-126.

Carmack, E. C., and Kulikov, E. A. (1998). "Wind-forced upwelling and internal Kelvin wave generation in Mackenzie Canyon, Beaufort Sea." *Journal of Geophysical Research*, 103(C9), 18,447-18,458.

Carmack, E. C., and MacDonald, R. W. (2002). "Oceanography of the Canadian Shelf of the Beaufort Sea: A Setting for Marine Life." *Arctic*, 55(Supp. 1), 29-45.

Cartwright, D. S., and Hughes Clarke, J. E. (2002). "Multibeam surveys of the Fraser River Delta, coping with an extreme refraction environment." *Canadian Hydrographic Conference*, Ottawa, Canada.

Codispoti, L. A., and Owens, T. G. (1975). "Nutrient transport through Lancaster Sound in relation to the Arctic Oceans reactive silicate budget and the outflow of Bering Strait waters." *Limnology and Oceanography*, 20(1), 115-119.

Collin, A. E. (1962). "Oceanographic observations in the Canadian Arctic and the adjacent Arctic Ocean." *Arctic*, 15, 194-201.

Cousins, D. B., and Miller, J. H. (2000). "Model based system for simultaneously estimating bathymetry and sound speed characteristics - simulation results." *Oceans Conference Record (IEEE)*, IEEE, Providence, USA, 213-219.

Cousins, D. B., and Miller, J. H. (2002). "A model based system for simultaneously estimating bathymetry and sound speed profile characteristics - Non-isovelocity simulation results." *Oceans Conference Record (IEEE)*, IEEE, Mississippi, USA, 1098-1108.

Cressman, G. P. (1959). "An Operational Objective Analysis System." *Monthly Weather Review*, 87(10), 367-374.

de Lange Boom, B. R., Melling, H., and Lake, R. A. (1987). "Late winter hydrography of the Northwest Passage: 1982, 1983 and 1984." *Rep. No. 79*, Department of Fisheries and Oceans, Sidney, Canada.

Dinn, D. F., Loncarevic, B. D., and Costello, G. (1995). "Effect of sound velocity errors on multi-beam sonar depth accuracy." *Oceans Conference Record (IEEE)*, IEEE, Piscataway, NJ, USA, San Diego, CA, USA, 1001-1010.

Environment Canada (2003). "Canadian Climate Normals." http://www.msc.ec.gc.ca/climate/climate_normals_1990/.

Environment Canada (2007) "The Atlas of Canada.". http://atlas.nrcan.gc.ca.

Fissel, D. B., Birch, J. R., Melling, H., and Lake, R. A. (1988). "Non-Tidal Flows in the Northwest Passage." *Rep. No. 98*, Institute of Ocean Sciences, Sydney, Canada.

Fissel, D. B., Lemon, D. D., and Birch, J. R. (1980). "The Physical Oceanography of Western Baffin Bay and Lancaster Sound." *Rep. No. Environmental Studies No. 25*, Department of Indian and Northern Affairs, Ottawa, Canada.

Fofonoff, N. P., and Millard, R. C. (1983). "Algorithms for computation of fundamental properties of seawater." *Rep. No. 44*, Division of Marine Sciences, UNESCO, Place de Fontenoy, 75700, Paris.

Forrester, W. D. (1983). "Canadian Tidal Manual." Department of Fisheries and Oceans, Canadian Hydrographic Service, Ottawa, Canada.

Fortier, L., and Leblanc, R. J. (2003). The integrated natural/medical/social study of the changing coastal Canadian Arctic. ArcticNet National Centres of Excellence Proposal. Université de Laval, Quebec, Canada.

Furlong, A., Beanlands, B., and Chin-Yee, M. (1997). "Moving vessel profiler (MVP) real time near vertical data profiles at 12 knots." *Proceeding of the Oceans '97 Conference*, Halifax, Canada.

Geng, X., and Zielinski, A. (1998). "New methods for precise acoustic bathymetry." *Proceeding of the Canadian Hydrographic Conference 1998*, Victoria, Canada.

Geng, X., and Zielinski, A. (1999). "Precise Multibeam Acoustic Bathymetry." *Marine Geodesy*, 22(3), 157-167.

Godin, G., and Barber, F. G. (1980). "Variability of the Tide at Some Sites in the Canadian Arctic." *Arctic*, 33(1), 30-37.

Grabs, W. E., and Portmann, T. D. C. (2000). "Discharge observation networks in Arctic regions: Computation of the river runoff into the Arctic Ocean, its seasonability and variability." *The Freshwater Budget of the Arctic Ocean*, E. L. Lewis, E. P.

Jones, P. Lemke, T. D. Prowse, and P. Wadhams, eds., Kluwer Academic Publishers, Dordrecht, The Netherlands.

GRDC (2008). "Global Runoff Data Centre.". http://www.bafg.de/GRDC/EN/Home/homepage_node.html, Accessed Oct. 22, 2009.

Hare, R. (2001). "Error Budget Analysis for US Naval Oceanographic Office (NAVOCEANO) Hydrographic Survey Systems." University of Southern Mississippi, Hydrographic Science Research Center (HSRC), USA.

Hare, R., Godin, A., and Mayer, L. A. (1995). "Accuracy estimation of Canadian swath (multibeam) and sweep (multitransducer) sounding systems." Internal report, Canadian Hydrographic Service, Ottawa, Canada.

Head, M. E. M., Luong, P., Costolo, J. H., Countryman, K., and Szczechowski, C. (1997). "Applications of 3-D visualizations of oceanographic data bases." *Oceans Conference Record (IEEE)*, Halifax, Canada, 1210-1215.

Hughes Clarke, J. E. (1994). "Refraction Issues." *Multibeam Training Course*, Ocean Mapping Group, University of New Brunswick, Fredericton, Canada.

Hughes Clarke, J. E. (2003). "Dynamic Motion Residuals in Swath Sonar Data: Ironing out the Creases." *International Hydrographic Review*, 4(1), 6-23.

Hughes Clarke, J. E., Dare, P., Beaudoin, J., and Bartlett, J. (2005). "A stable vertical reference for bathymetric surveying and tidal analysis in the high Arctic." *United States Hydrographic Conference*, San Diego, USA.

Hughes Clarke, J. E., Lamplugh, M., and Kammerer, E. (2000). "Integration of near-continuous sound speed profile information." *Canadian Hydrographic Conference*, Montreal, Canada.

Hunkins, K. (1975). "The Oceanic Boundary Layer and Stress Beneath a Drifting Ice Floe." *Journal of Geophysical Research*, 80(24), 3425-3433.

IHO (2008). "IHO Standards for Hydrographic Surveys, Publication No. 44, 5th Ed." International Hydrographic Organization, Monaco.

Imahori, G., and Hiebert, J. (2008). "An Algorithm for Estimating the Sound Speed Component of Total Depth Uncertainty." *Proceedings of the 2008 Canadian Hydrographic Conference*, Victoria, Canada.

Ingram, R. G., and Prinsenberg, S. J. (1998). "Coastal Oceanography of Hudson Bay and Surrounding Eastern Canadian Arctic Waters Coastal Segment." *The Sea, Volume 11*, A. R. Robinson, and K. H. Brink, eds., J. Wiley, New York, 835-861.

ISO (1995). "Guide to the expression of uncertainty in measurements.", International Organization for Standardization, Geneva, Switzerland.

Jackett, D. F., and McDougall, T. J. (1995). "Minimal Adjustment of Hydrographic Profiles to Achieve Static Stability." *Journal of Atmospheric and Oceanic Technology*, 12, 381-389.

Johnson, D. R., Boyer, T. P., Garcia, H. E., Locarnini, R. A., Mishonov, A. V., Pitcher, M. T., Baranova, O. K., Antonov, J., and Smolyar, I. V. (2006). "World Ocean Database 2005 Documentation." *Rep. No. NODC Internal Report 18*, U.S. Government Printing Office, Washington, D.C., USA

Jones, E. P., and Coote, A. R. (1980). "Nutrient distributions in the Canadian Archipelago: indicators of summer water mass and flow characteristics." *Canadian Journal of Fisheries and Aquatic Sciences*, 37(4), 589-599.

Jones, E. P., Swift, J. H., Anderson, L. G., Lipizer, M., Civitarese, G., Falkner, K. K., Kattner, G., and McLaughlin, F. (2003). "Tracing Pacific water in the North Atlantic Ocean." *Journal of Geophysical Research*, 108(C4).

Kliem, N., and Greenberg, D. A. (2003). "Diagnostic Simulations of the Summer Circulation in the Canadian Arctic Archipelago." *Atmosphere-Ocean*, 41(4), 273-289.

Kongsberg (2001). "EM 1002 Hydrography multibeam echo sounder -- Operator manual." Kongsberg Simrad AS, Horten, Norway.

Kongsberg (2002). "EM 300 Multibeam echo sounder -- Operator Manual." Kongsberg Simrad AS, Horten, Norway.

Kongsberg (2006). "Operators Manual - EM Series Datagram Formats (20-01-06)." Kongsberg Maritime AS, Horten, Norway.

Kovacs, A., Weeks, W. F., Ackley, S., and Hibler, W. D. (1973). "Structure of a multi-year pressure ridge." *Arctic*, 26(1), 22-31.

Kuzyk, Z. A., MacDonald, R. W., Granskog, M. A., Scharien, R. K., Galley, R. J., Michel, C., Barber, D., and Stern, G. (2006). "Sea ice, hydrological, and biological processes in the Churchill River estuary region, Hudson Bay." *ArcticNet Annual Scientific Meeting 2006*, ArcticNet, Victoria, Canada.

Larouche, P. (1990). "Winter offshore/onshore wind differences in southeastern Hudson Bay, Canada." *Arctic*, 43(1), 55.

Leblond, P. H. (1980). "On the Surface Circulation in Some Channels of the Canadian Arctic Archipelago." *Arctic*, 33(1), 189-197.

Levitus, S. (1982). "Climatological Atlas of the World Ocean." *Rep. No. NOAA Professional Paper 13*, U.S. Government Printing Office, Washington, D.C., USA.

Lewis, J. K. (1997). "Three-dimensional ocean circulation model with wave effects." *Proceedings of the International Conference on Estuarine and Coastal Modeling*, Alexandria, USA, 584-600.

Lewis, J. K., Merrifield, M. A., and Eich, M. L. (2001). "Numerical simulations of internal tides around Oahu, Hawaii." *Estuarine and Coastal Modeling: Proceedings of the Seventh International Conference*, American Society of Civil Engineers, St. Petersburg, FL, United States, 185-203.

Loder, J. W., Han, G., Hannah, C. G., Greenberg, D. A., and Smith, P. C. (1997). "Hydrography and baroclinic circulation in the Scotian Shelf region: winter versus summer." *Canadian Journal of Fisheries and Aquatic Sciences*, 54, 40-56.

Lurton, X. (2002). "An Introduction to Underwater Acoustics: Principles and Applications." Springer-Praxis, London.

Lustig, H. E., Rossof, A. L., Frelich, P. D., and Farr, H. K. (1964) Radiation Mapping System. Patent 165173[3144631]. United States Patent Office.

MacDonald, R. W. (2000). "Arctic estuaries and ice: A positive-negative estuarine couple." *The Freshwater Budget of the Arctic Ocean*, E. L. LEWIS, E. P. Jones, P. Lemke, T. D. Prowse, and P. Wadhams, eds., Kluwer Academic Publishers, Dordrecht, The Netherlands.

MacDonald, R. W., and Carmack, E. C. (1991). "The role of large-scale under-ice topography in separating estuary and ocean on an arctic shelf." *Atmosphere-Ocean*, 29, 37-53.

Makinson, J., Schroder, M., and Østerhus, S. (2006). "Effect of critical latitude and seasonal stratification on tidal current profiles along Ronne Ice Front, Antarctica." *Journal of Geophysical Research*, 111(C03022).

Marsden, R. F., Paquet, R., and Ingram, R. G. (1994a). "Currents under land-fast ice in the Canadian Arctic Archipelago Part 1: Vertical velocities." *Journal of Marine Research*, 52, 1017-1036.

Marsden, R. F., Ingram, R. G., and Legendre, L. (1994b). "Currents under land-fast ice in the Canadian Arctic Archipelago Part 2: Vertical mixing." *Journal of Marine Research*, 52, 1037-1049.

Maxwell, J. B. (1981). "Climatic Regions of the Canadian Arctic Islands." *Arctic*, 34(3), 225-240.

McLaren, A. S., Wadhams, P., and Weintraub, R. (1984). "The Sea Ice Topography of M'Clure Strait in Winter and Summer of 1960 from Submarine Profiles." *Arctic*, 37(2), 110-120.

McLaughlin, F. A., Carmack, E. C., Ingram, R. G., and Williams, W. J. (2005). "Oceanography of the Northwest Passage." *The Sea, Volume 14*, A. R. Robinson, and K. H. Brink, eds., President and Fellows of Harvard College, 1213-1244.

McNutt, M., and Caress, D. W. (1996). "EW9602 Cruise Report: Origin of Lineated MidPlate Volcanism in the Southern Austral Islands." Massachusetts Institute of Technology, Cambridge, USA.

Medwin, H., and Clay, C. S. (1997). "Fundamentals of Acoustical Oceanography." Academic Press Limited, London.

Melling, H. (1997). "Flow from the Arctic Ocean through the Channels of the Canadian Arctic Archipelago." *Proceedings of Polar Processes and Climate*, Arctic Climate System Study, Orcas Island, Washington, 164-166.

Melling, H. (2000). "Exchanges of Freshwater Through the Shallow Straits of the North American Arctic." *The Freshwater Budget of the Arctic Ocean*, E. L. LEWIS, E. P. Jones, P. Lemke, T. D. Prowse, and P. Wadhams, eds., Kluwer Academic Publishers, Dordrecht, The Netherlands, 479-502.

Melling, H. (2002). "Sea Ice of the Northern Canadian Arctic Archipelago." *Journal of Geophysical Research*, 107(C11).

Melling, H., Lake, R. A., Topham, D. R., and Fissel, D. B. (1984). "Oceanic thermal structure in the western Canadian Arctic." *Continental Shelf Research*, 3(3), 233-258.

Muench, R. D. (1971). "The Physical Oceanography of the Northern Baffin Bay Region." *Rep. No. The Baffin Bay-North Water Project Scientific Report.no. 1*, Arctic Institute of North America, Washington DC, USA.

NOAA Office of Coast Survey (2001). "Sound Velocity Program.", Computer program, NOAA Office of Coast Survey, Maryland, USA.

NPL (2000). "Underwater Acoustics: Technical Guides - Speed of Sound in Sea-Water." National Physical Laboratory, Teddington, Middlesex, UK.

Peyton, D., Furlong, A., Smyth, S., Beaudoin, J., and Lamplugh, M. (2009). "Optimizing sound speed profiling to meet TPU requirements using a CAST gauge." *Proceedings of the US Hydrographic Conference, 2009*, The Hydrographic Society of America, Norfolk, USA.

Pickard, G. L. (1963). "Descriptive Physical Oceanography." Pergamon Press Ltd., London.

Prinsenberg, S. J. (1988). "Damping and Phase Advance of the Tide in Western Hudson Bay by the Annual Ice Cover." *Journal of Physical Oceanography*, 18(11), 1744-1751.

Prinsenberg, S. J., and Bennett, E. B. (1989a). "Transport between peel sound and barrow strait in the Canadian Arctic." *Continental Shelf Research*, 9(5), 427-444.

Prinsenberg, S. J., and Bennett, E. B. (1989b). "Vertical Variations of Tidal Currents in Shallow Land Fast Ice-Covered Regions." *Journal of Physical Oceanography*, 19(9), 1268-1278.

Prinsenberg, S. J., and Hamilton, J. (2005). "Monitoring the volume, freshwater and heat fluxes passing through Lancaster Sound in the Canadian Arctic Archipelago." *Atmosphere-Ocean*, 43(1), 1-22.

Rabiner, L., Sambur, M., and Schmidt, C. (1975). "Applications of a nonlinear smoothing algorithm to speech processing." *J. Acoust. Soc. Am., 57, S2*.

Rattray, M. (1962). "Interpolation errors and oceanographic sampling." *Deep Sea Research and Oceanographic Abstracts*, 9(1-2), 25-37.

Reiniger, R. F., and Ross, C. K. (1968). "A method of interpolation with application to oceanographic data." *Deep Sea Research and Oceanographic Abstracts*, 15(2), 185-193.

Shuman, F. G. (1957). "Numerical Methods in Weather Prediction: II. Smoothing and Filtering." *Monthly Weather Review*, 85(11), 357-361.

Steele, M., Morley, R., and Ermold, W. (2001). "PHC: A Global Ocean Hydrography with a High-Quality Arctic Ocean." *Journal of Climate*, 14(9), 2079-2087.

Stephens, C., Antonov, J., Boyer, T., Conkright, M. E., Locarnini, R., O'Brien, T. D., and Garcia, H. E. (2002). World Ocean Atlas 2001, Volume 1: Temperature. NOAA Atlas NESDIS 49. U.S.Government Printing Office . Washington, D.C., USA

Tan, F. C., and Strain, P. M. (1980). "The Distritubion of Sea Ice Meltwater in the Eastern Canadian Arctic." *Journal of Geophysical Research*, 85(C4), 1925-1932.

Teague, W. J., Carron, M. J., and Hogan, P. J. (1990). "A Comparison Between the Generalized Digital Environmental Model and Levitus Climatologies." *Journal of Geophysical Research*, 95(C5), 7167-7183.

Tomczak, M., and Godfrey, J. S. (2002). "Regional Oceanography: An Introduction." Pergamon (1994)/Flinder University of South Australia (2002).

Turner, J. S. (1973). "Buoyancy effects in fluids." University Press, Cambridge.

US Naval Oceanographic Office (2002). "GDEMV 3.0 Documentation." US Naval Oceanographic Office, USA.

Vuglinsky, V. S. (1997). "River inflow to the Arctic Ocean: Conditions of formation, time variability and forecasts." *Proceedings of Polar Processes and Climate*, Arctic Climate System Study, Orcas Island, Washington, 277-278.

Walker, E. R. (1977). "Aspects of the oceanography in the Archipelago." Institute of Ocean Sciences, Sydney, Canada.

Williams, W. J., and Carmack, E. C. (2008). "Combined effect of wind-forcing and isobath divergence on upwelling at Cape Bathurst, Beaufort Sea." *Journal of Marine Research*, 66(5).

APPENDIX A – PHYSICAL OCEANOGRAPHY OF THE CAA

A.1 Introduction

Oceanographic conditions in polar regions can differ significantly from conditions at lower latitudes due to the effects of decreased temperature and salinity. As polar water temperatures are close to the freezing point, salinity has a pronounced effect on the density structure of the water column and drives much of the thermohaline circulation in these regions. The presence and/or absence of sea ice can further modify mixing, stratification and circulation processes in polar waters. Given the important role of sea ice, it is investigated first in this section. This is followed by a brief review of the physical oceanography of the Arctic Ocean and other basins surrounding the CAA to provide context for the processes occurring in the CAA. Lastly, the processes affecting the physical oceanography of the CAA are investigated, namely the meteorological, hydrological, sea ice and tidal regimes. The section is concluded with a summary of general circulation patterns and water mass characteristics.

A.2 Sea ice

Ice occurs in three forms in the ocean: icebergs, pack ice and land fast ice. Icebergs derive from glaciers and are composed of freshwater. Most icebergs found on the east coast of North America originate from the west coast of Greenland and the east

coast of Ellesmere Island. They break off, or calve, from tide water glaciers and are carried south by the Baffin Current and Labrador Current with some occasionally drifting into Lancaster Sound and Hudson Strait. Sea ice is derived from sea water, it is initially slightly salty but loses salt over its lifetime, eventually becoming nearly fresh over the course of a few years. There is a distinction between first year sea ice and multi-year sea ice. Multi-year ice is harder, thicker and fresher (due to snow cover melting into freshwater pools during the warm season, and then freezing into fresh water ice the next year). Sea ice and icebergs also differ in the vertical extent, with icebergs being several tens of meters thick whereas sea-ice normally can only attain a few meters of thickness (though underwater ridges that form when ice sheets collide can reach thicknesses of 10-20m). Land fast ice is a sheet of sea ice that is rigidly attached to a land mass. Pack ice, on the other hand, is mobile and free to drift with wind and current action. Much of the Arctic Ocean consists of loose pack ice whereas the NWP has much more land fast ice with stable ice arches forming over many of the channels during winter.

Ice has a strong modifying effect on stratification processes. It severely limits the transfer of thermal energy from the atmosphere to the sea as it acts as an insulating cap and impedes many of the processes that exchange heat between the atmosphere and the ocean. Absorption of short wave radiation drops dramatically with the appearance of sea ice: 85-90% is absorbed in open water whereas only 30-50% is absorbed with ice cover (Pickard, 1963). The long-wave radiation term of sea water, Q_{LW}, is relatively unaffected by the transition from liquid to solid form, i.e. sea ice loses just as much energy through long wave back radiation as open water, thus once ice forms it tends to be maintained. The opposite feedback loop can also occur in which melting ice will expose more open

water which has a smaller albedo, leading to more warming and accelerated ice melt. The presence of ice also limits the seasonal range of temperatures in the upper portion of the water column. In winter, the ice keeps the surface layer near freezing. By contrast, the large latent heat of melting ice absorbs much of the heat that is introduced at the surface in summer time, leaving very little energy to warm the water column (Pickard, 1963).

In terms of stratification due to fresh water input, ice can act as a sink or a source depending on whether it is forming or melting. Brine is ejected from ice in the early stages of formation. This process continues as the sea ice thickens throughout winter and can also continue in subsequent winters such that multi-year ice is fresher than first year ice as a result. As the ejected brine is heavier than the underlying water, a brine-driven convection can occur underneath the ice. When sea ice melts, freshwater is returned to the system. As ice can isolate the upper layer of the water column from direct wind mixing, the freshwater input can lead to a stable, stratified environment underneath the ice with a cold, fresh surface layer lying overtop a warmer and saltier layer. After sea ice clears, the fresh water can be mixed to depth; one study found sea ice melt down to depths of 140 m in Lancaster Sound and 50 m in Baffin Bay, based on an analysis of oxygen isotopes that allowed for the separation of sea ice meltwater and meteoric water (precipitation, river runoff, glacial melt) (Tan and Strain, 1980).

Though ice prevents the wind from directly mixing the sea surface, indirect mixing can result as loose ice sheets (and their sizeable keels) are moved through wind action. In one experiment, Ekman spirals were observed to develop underneath storm driven pack ice, with surface currents being induced down to depths of 15 to 25 m, with

the growth of the Ekman spiral being limited by a strong pycnocline at 35 m (Hunkins, 1975). A further effect of ice on wind is the increased drag coefficient of ice relative to open water, the former being approximately twice the magnitude of the latter (Larouche, 1990). This leads to reduced wind speeds over ice and a calming effect of ice on nearby water in the presence of winds which can further promote stratification in areas of heavy ice congestion.

Ice can also impact the distribution of freshwater input from river outflow. The underside of sea ice can be quite rugged with pressure ridges forming when wind and current driven ice sheets collide. In extreme cases, the ridges have keels that can extend several tens of meters below the water surface (McLaren et al., 1984; Kovacs et al., 1973). Pressure ridges are prominent along the boundary between land fast ice and pack ice on the continental shelves; these ridges can form underwater barriers to the flow of surface waters in much the same way as topographic sills do to bottom waters. If the ridge is near a river mouth, the river runoff can be effectively trapped behind the barrier (Carmack, 2000). This effect is found on the Beaufort Shelf near the mouth of the Mackenzie River and leads to unique convection regimes on either side of the barrier with the landward side being dominated by freshwater input. On the other hand, the seaward side of the pressure ridge is characterized by frequent reopening due to offshore ice movement with brine formation ensuing as new ice forms over the opening (MacDonald and Carmack ,1991). Similar processes have been observed in Hudson Bay, which drains a large portion of the Canadian land mass and features several sizeable estuaries (Kuzyk et al., 2006).

Sea ice presents an additional frictional boundary layer with which the currents can interact leading to an additional region of tidal mixing at the surface. Whereas land fast ice acts as a rigid lid, loose pack ice can drift with the current or in any arbitrary direction depending on prevailing winds, thus the apparent current speed is diminished (which reduces the effectiveness of mixing). In shallow water, where the frictional boundary layers at the seabed and surface occupy the majority (or entirety) of the water column, the rotation direction and amplitudes of semi-diurnal tidal currents have been observed to be dependent on the latitude and the frequency of tidal component. In work done near Barrow Strait and in north western Hudson Bay, the semi-diurnal tidal current ellipses were observed to change rotation direction at mid-depth, i.e. the surface and bottom current ellipses may exhibit a counter-clockwise rotation throughout the tidal cycle whereas the mid-depth ellipse rotates clockwise. Further to this, the semi-diurnal tidal amplitude had a maximum at mid-depth, with minima at the surface and seabed. The diurnal component was found to have a different behaviour altogether with a constant rotation direction and amplitude throughout the water column. This observed behaviour was markedly different from the open water case where the semi-diurnal tidal current amplitude decreased in magnitude as it approached the boundary layer at the seabed and the rotation sense changed direction only once throughout the water column (Prinsenberg and Bennett, 1989b; Marsden et al., 1994a).

Ice has a secondary effect on tidal mixing in that it can modify the amplitude and phase of the tide, as has been observed in the White Sea, the Beaufort Sea and Hudson Bay. In the case of western Hudson Bay, the amplitudes of the semi-diurnal tides were observed to be reduced by 10% and the arrival of high and low tide was advanced by as

much as 20 minutes as compared to ice free conditions (Prinsenberg, 1988). A study of several stations throughout the CAA indicated that stations in Hudson Bay and the Amundsen Gulf are most influenced by ice cover due to the dampening of basin scale resonances whereas those in the NWP experience little change in amplitude and phase of the tide (Godin and Barber, 1980). Tidal amplitudes in Barrow Strait were observed to vary by a few centimeters between ice-covered and ice-free seasons in Barrow Strait (Prinsenberg and Hamilton, 2005).

A final noteworthy effect of sea ice is its ability to trigger internal waves from tidal flows over pressure ridges between ice floes. Internal wave generation has been inferred from Acoustic Doppler Current Profiler (ADCP) backscatter and vertical velocity measurements near Barrow Strait, with internal waves being observed roughly 15 km from a pressure ridge (Marsden et al., 1994a). Calculations of the Richardson number from the ADCP current profiles and CTD density profiles indicated that the passing internal waves provide a significant source of mixing between the pycnocline and the sea ice (Marsden et al., 1994b).

A.3 Oceanography of the Arctic Ocean

Before discussing the physical oceanographic characteristics of the CAA, it is important to first touch on the oceanography of the neighbouring basins as they strongly influence what is observed in the Archipelago. An overview of the physical oceanography of the Arctic Ocean is provided by Tomczak (Tomczak and Godfrey, 2002), the entirety of this section of text is a synopsis of the major points of discussion in

his work. The Arctic Ocean can be regarded as a mediterranean sea as it is a basin whose exchange with the surrounding oceans is limited by sills on its periphery. The flow characteristics of Mediterranean seas are dominated by thermohaline forcing compared to other oceans where wind is the largest driving force on currents and thermohaline effects play a smaller role. As fresh water input to the system exceeds evaporation (sea ice blocks direct evaporation), the Arctic Ocean is a dilution basin with inflow/outflow mimicking estuarine circulation: water of low salinity flows out at the surface and is replaced by saltier water flowing in at depth.

Referring to Figure A-1, the majority of this exchange occurs through the straits that separate Greenland, Iceland, the Faroe Islands and Scotland. Sill depths range from 400 to 800 meters through these straits and their width is large enough that Coriolis strongly modifies the flow characteristics. Thus, inward flow tends to be directed to the east (flowing through the Norwegian Sea along the coast of Norway) whereas outward flow is directed along the east coast of Greenland, exiting via the Greenland Sea. It should be noted that outflow is not restricted to the surface layer as in the classic model of a dilution basin: the cold water found at the bottom of the Arctic Ocean occasionally escapes over the sills through the straits separating Greenland and Scotland. These outflows occur during upwelling events associated with strong storms and they play an important role in the formation of North Atlantic Deep Water (NADW).

The other two connections between the Arctic, Pacific and Atlantic Oceans are the Bering Strait and the CAA. The shallow sill depth and narrowness of Bering Strait (approximately 45 meters deep and 85 km wide) limits exchange with the Pacific Ocean. Inflow does occur through Bering Strait, though it is small relative to the amount of water

entering from the Atlantic via the Norwegian Sea (approximately an order of magnitude less). The CAA provides an alternate exchange pathway from the Arctic to the Atlantic Ocean; however, it is limited by the shallow sills and narrow straits between the islands, the details of which are left for the discussion of CAA oceanography in the next section.

The Arctic Ocean consists of three layers of water, each having very distinct temperature and salinity properties. In order of increasing depth, they are (1) Arctic Surface Water, (2) Atlantic Water, and (3) Arctic Bottom Water. The Arctic Bottom Water (ABW) is formed from two sources: (1) the Greenland Sea Deep Water (GSDW) and (2) water from the shallow seas on the continental shelves surrounding the Arctic Ocean. The GSDW forms in winter through storm event related ice formation. Ice formation ejects salt into the underlying water, increasing its density to the point that it can penetrate the Atlantic Water (which is warmer but saltier than the relatively fresh surface water). With the sinking of the newly formed GSDW comes an upwelling of warm water which melts the newly formed ice and halts the formation of cold, dense water. The GSDW formation is thus limited in time to several days after storm events and is typically limited in spatial extent to areas only a few kilometers across. In the case of the second source, the shelf water is fresher due to river inflow and ice forms more readily than in the Greenland Sea. Again, during ice formation, salt is ejected into the underlying water which increases its density to the point that it sinks and contributes to the ABW.

The Atlantic Water (AW) is an inflow associated with the West Spitsbergen Current. Unlike typical mediterranean inflows, the density of inflowing AW is not high enough to permit it to sink to the bottom of the Arctic Ocean as it is warm relative to the

ABW (though it has similar salinity). Instead, it forms a layer at depths between 150 and 900 m and separates the ABW and the surface water. It is distinguished by a temperature maximum that is most pronounced at the source of inflow, becoming less pronounced across the basin due to mixing.

The Arctic Surface Water (ASW) is characterized by cold and relatively fresh water and extends from the surface down to approximately 150 – 200 m. The temperatures are very cold, typically near freezing, but are nearly uniform over the depth range. Large variations in salinity are often present, these being the product of ice melt or formation. Such variations are most pronounced near the upper portion of the ASW leading to distinct surface layer, 25 to 50 meters thick. Similar to the shelf water that feeds the ABW, strong mixing of incoming Atlantic Water on the Siberian shelf increases its density but not to the point that it can penetrate the AW layer; this forms the source of the sub-surface layer in the ASW. Inflow from Bering Strait also contributes to the ASW. Similar to how the AW enters the Arctic Ocean, this flow spreads at depth due to its high salinity relative to the ASW (even though, as in the case of the AW, it is warmer). The depth at which it pools into the basin fluctuates seasonally due to temperature variations of the incoming water: in summer it spreads at depths between 50 and 100 m, while in winter it sinks to approximately 150 m depth as its temperature is quite similar to the ASW but its higher salinity drives it down.

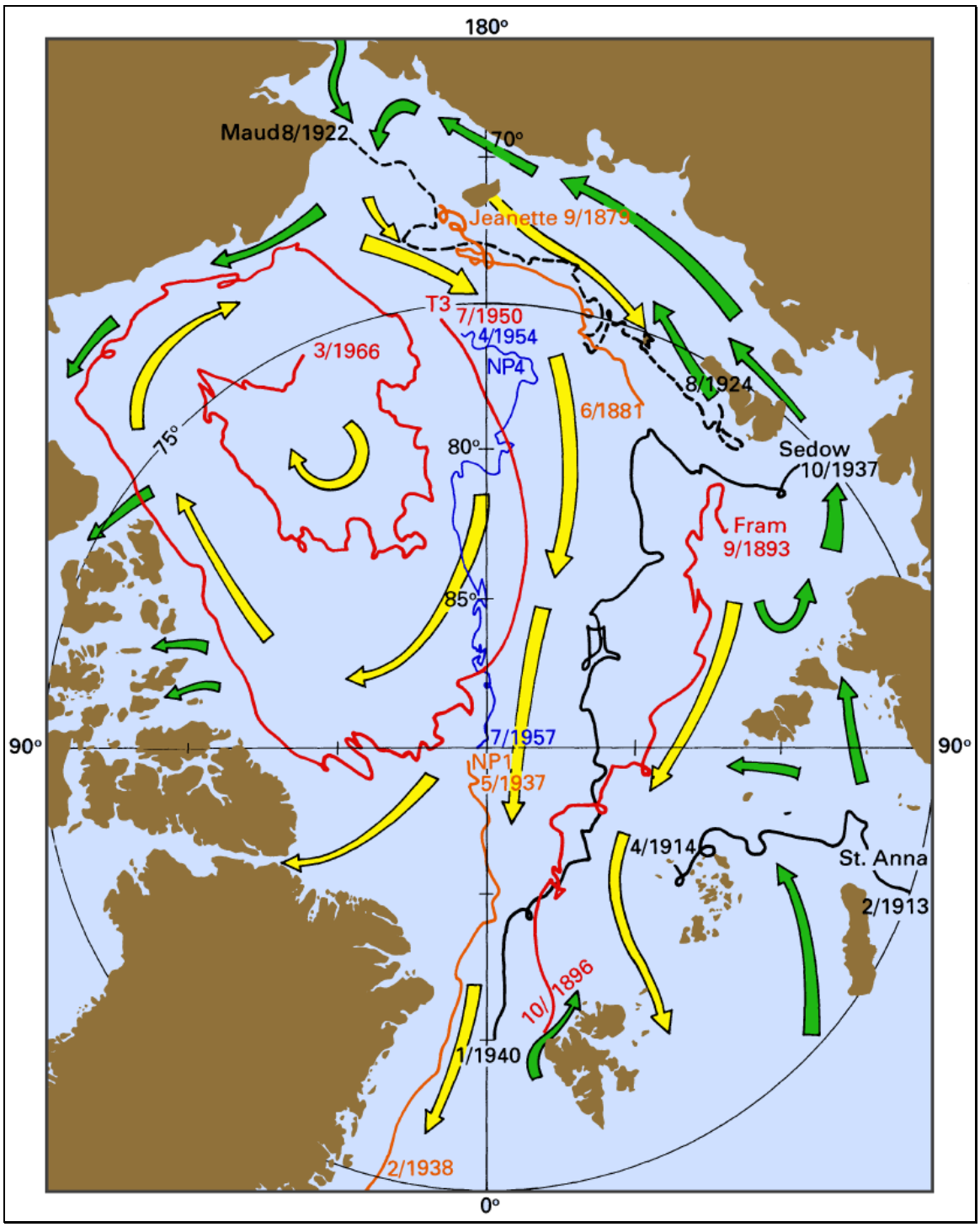

Figure A-1. Arctic ocean surface currents and vessel/ice station drift tracks, after Tomczak and Godfrey (2002), p. 89.

A.4 Oceanography of surrounding basins

As mentioned above, the CAA provides an alternate pathway for waters to travel from the Arctic Ocean to the Atlantic Ocean via the Labrador Sea (see Figure A-2). Whereas it is important to understand the source of water in the CAA (that being primarily the Arctic Ocean), understanding the fate of the water after it passes through the CAA to the Atlantic Ocean is not germane to this work. This discussion is therefore limited to oceanic waters immediately adjacent to the CAA, namely Foxe Basin, Hudson Bay and Baffin Bay.

Baffin Bay is a deep and large bay separating Greenland from the CAA with maximum depths reaching 2300 m. It is bordered primarily by large, glacier capped islands: Greenland, Ellesmere Island, Devon Island and Baffin Island. The islands are characterized by fjords and calving glaciers and are the major source of icebergs in the transatlantic shipping lanes to the south. At its northernmost extremity, it can exchange water directly with the Arctic Ocean through Nares Strait, the small strait separating Greenland from Ellesmere Island. The sill depth via this path is 200 m, and the strait is very narrow, thus exchange is quite limited in this area. A second exchange path exists through the channels, islands and straits of the CAA proper. The largest and most obvious pathway from the Arctic Ocean to Baffin Bay is Parry Channel, a wide channel that cuts across the CAA roughly between the 74^{th} and 75^{th} parallels (occasionally referred to as the *direct* NWP in literature). Details of Parry Channel are left to the following section; at this point it is only relevant to mention that the sill depth at the centre of Parry Channel is 130 m. Other pathways exist through the islands north and

south of Parry Channel, their sill depths are less than 100 m and are all shallower than the limiting sill depth of 130 m in Parry Channel (McLaughlin et al., 2005).

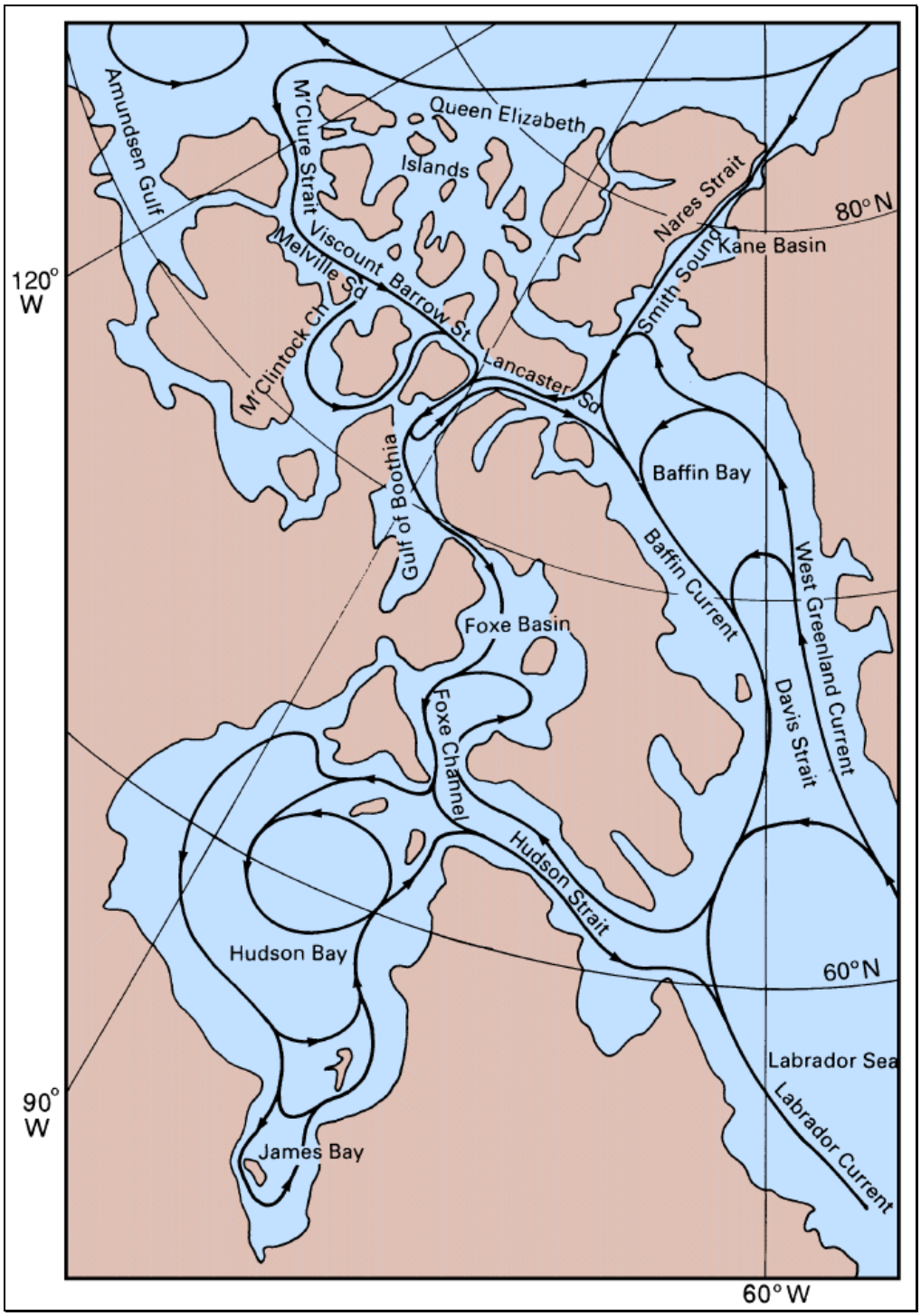

Figure A-2. Geography and circulation of currents in the vicinity of the CAA, after Tomczak and Godfrey (2002), p. 272.

Recalling that the ASW extends to nearly 150 to 200 m, direct exchange from the Arctic to the Atlantic via the CAA is limited to the ASW. The sill depth in Nares Strait allows AW to communicate from the Arctic Ocean to Baffin Bay via this route and may form a source of renewal of the deep water in the bay much in the same way it does for the Arctic Ocean on the Siberian shelf. Davis Strait connects Baffin Bay to the Labrador Sea with a sill depth of 600 m. Given that it receives primarily fresh ASW inflow, Baffin Bay acts as a dilution basin.

The other major incoming flow is the West Greenland Current (WGC), running along the west coast of Greenland, bringing warm and salty Atlantic water north. Flow from the CAA and through Smith Sound combines with the West Greenland Current on the western edge of Baffin Bay to form the Baffin Current, which travels south to later join outflow from Hudson Strait to become the Labrador Current, making forays into Lancaster Sound and Hudson Strait along the way. In these areas, the currents form westward counter-currents running along the northern edges of the aforementioned passages whereas the predominant eastward outflow currents run along the southern edges. These intrusive currents are more variable in time than the outflow currents; however, they are of similar magnitude (Tomczak and Godfrey, 2002). The outflow from the CAA and inflow from the West Greenland Current drive a cyclonic circulation in Baffin Bay; there is evidence for strong cyclonic circulation at depths below the sill depth in Davis Strait (Ingram and Prinsenberg, 1998).

The vertical distribution of water masses in Baffin Bay is similar to that found in the Arctic Ocean: (1) a thin layer (<50 m), originating from the ASW whose temperature and salinity vary seasonally, (2) a cold sub-surface layer extending over depths of 50 to

200 m, again originating from the ASW (though saltier than its arctic counterpart due to injection of brine during its travel), (3) an intermediate layer of warmer and saltier water originating from the south via the East Greenland Current, and finally (4) the Bottom Water of Baffin Bay, distinguished as cold, salty and with low oxygen content (Tomczak and Godfrey, 2002).

The oceanic source waters of Hudson Bay derive from the Arctic Ocean (Jones et al., 2003). With an area greater than 1 million km^2, it is often referred to an inland sea. Its maximum depth is approximately 250 m and it connects to the Labrador Sea via Hudson Strait without any sill limiting communication of waters between the two. Given the large hydrological basin that drains into Hudson Bay, it is very estuarine like with its temperature and salinity exhibiting strong horizontal gradients and seasonal variability (Tomczak and Godfrey, 2002). Circulation in the bay is cyclonic and driven by wind forcing and buoyancy input in addition to the inflow and outflow through the channels at its northern end; topographic steering plays a significant role in directing the circulation (Ingram and Prinsenberg, 1998).

Hudson Bay differs from the CAA in that it is nearly entirely ice free during the summer though sea ice is often found in the narrow channels between Southampton Island and the mainland, however, this technically falls within Foxe Basin. Further to this, average ice thicknesses are smaller than in the CAA due to the lower latitude. A final difference is the considerable fresh water input to the system via river inflow (which is nearly negligible in the CAA, as will be discussed later). This inflow drives an estuarine circulation with a freshwater surface outflow into Hudson Strait being balanced by a saltier inflow at depth (Ingram and Prinsenberg, 1998).

Moving to the north of Hudson Bay, the much shallower Foxe Basin is typically ice covered for longer portions of the year than Hudson Bay. During ice formation, it acts like a negative estuary and ejects cold salty water at depth and takes in fresher water at the surface. At its northwestern extremity, Foxe Basin is connected to the CAA via Fury and Hecla Strait though which it receives 0.04 Sv and 0.10 Sv of wintertime and summertime transport, respectively. The inflow from Fury and Hecla Strait is vertically homogeneous due to intense tidal mixing in the narrow and shallow channel (Ingram and Prinsenberg, 1998).

A.5 Oceanography of CAA

A.5.1 Regional description

The CAA occupies the majority of the northern continental shelf of North America and is characterized by a maze of islands and channels which, combined with ever present sea ice, frustrated early exploration attempts. Hypsometric curves for the CAA show that ~70% of the waterways are shallower than 500 m (McLaughlin et al., 2005). The *direct* NWP runs roughly along the 74th parallel and connects, from east to west, Lancaster Sound, Barrow Strait, Viscount Melville Sound and M'Clure Strait. Together, these sounds and straits form Parry Channel, the largest channel in the CAA through which waters may freely communicate between the Arctic and Atlantic oceans, though this exchange is limited by a sill of 130 meters in Barrow Strait. As mentioned in the section discussing Atlantic oceanography, a deeper sill depth in Nares Strait between

Greenland and Ellesmere Island provide an alternate and more direct path (but much narrower) between the Arctic and Atlantic ocean, effectively bypassing the CAA. It should be noted that Parry Channel is the least navigable route through the CAA as sea ice concentration is typically quite high in the western portion due to a near continuous inflow of sea ice from the Beaufort Sea into M'Clure Strait. The *practical* NWP, i.e. the route which is most often navigable by vessels without ice reinforcement, diverts to the south in Barrow Strait, passing through Peel Sound and taking the southerly route through Queen Maud Gulf, Coronation Gulf and the Amundsen Gulf.

To the north of Parry Channel lie the Queen Elizabeth Islands through which several channels provide connections to the Arctic Ocean. The myriad channels provide a third route from the Arctic to the Atlantic Ocean through Cardigan Strait/Hell Gate, which separates Devon and Ellesmere islands with a sill depth of 85 m. Alternate and much shallower pathways exist to the south of Parry Channel. In the western CAA, Dolphin and Union Strait separates the mainland from Victoria Island, however it presents a sill depth of 15 meters (Melling, 2000). Bellot Strait separates Somerset Island from Boothia Peninsula, the northernmost extremity of the North American landmass and provides an alternate eastern entrance to the practical NWP though it is characterized by strong tidal currents and is quite narrow and shallow with a sill depth of 25 m (Melling, 2000).

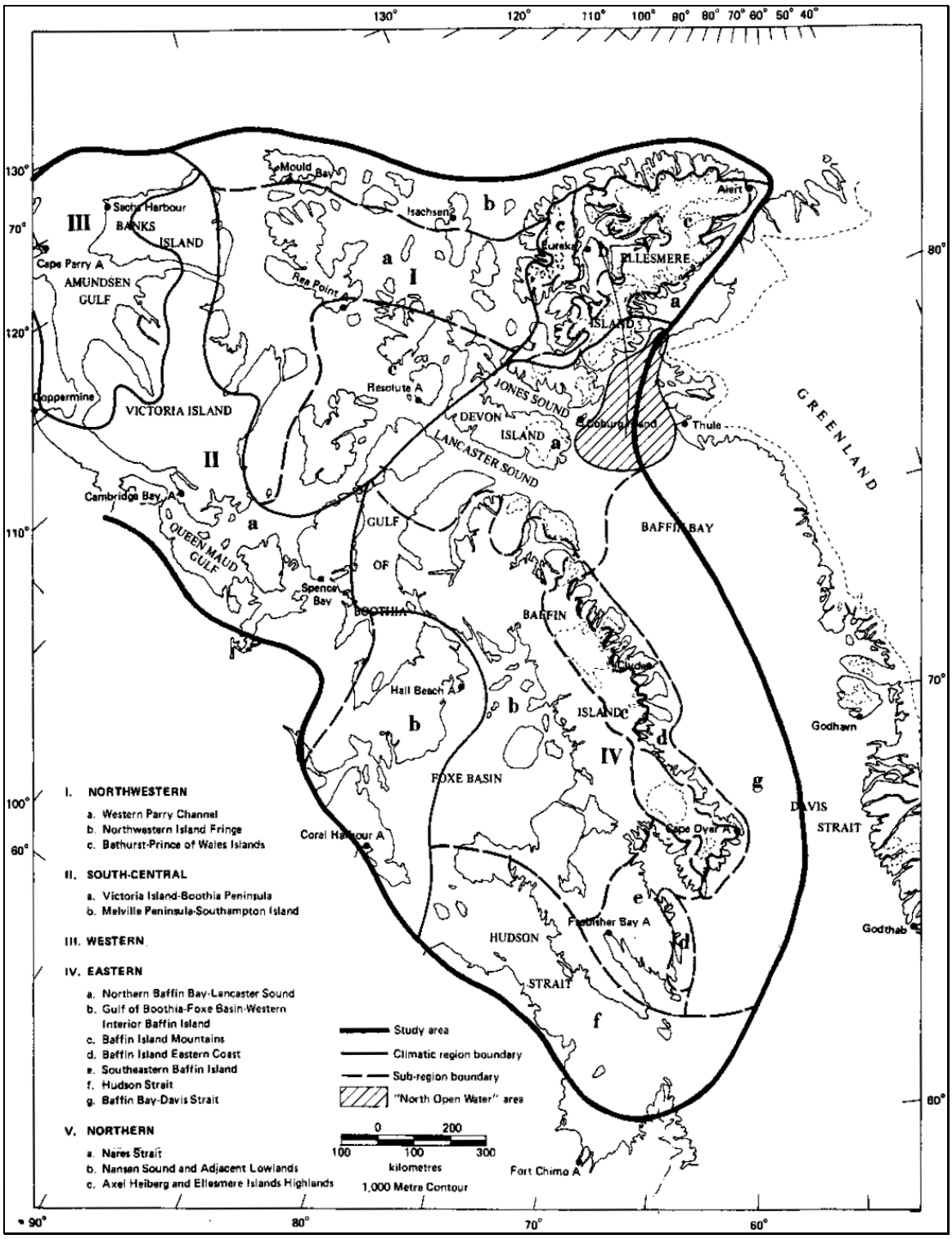

Figure A-3. Climatic regions of the CAA (after Maxwell (1981), Figure 7, p. 229)

A.5.2 Meteorology

Several climatic regions are distinguishable in the CAA with regions categorized on the basis of (1) cyclonic activity, (2) sea ice-water regime, (3) broad-scale physiographic features, and (4) net radiation. Five separate climatic regions are identified based on these four parameters (refer to Figure A-3 and Table A-1), with sub-regional classification based on major local variations of parameters such as local topography, aviation weather, maritime influences, temperature, precipitation, snow cover and wind (Maxwell, 1981).

Table A-1. Regional climatic characteristics of the CAA (Maxwell, 1981).

Region	Characteristics
I	• High anticyclonic activity • Eastern boundary based on maximum westward extent of cyclonic activity of region IV (Davis Strait/Baffin Bay/Baffin Island) • Western boundary based on maximum eastward extent of cyclonic activity of region III (Beaufort Sea/Amundsen Gulf) • Low relief • Shares climatic characteristics of Arctic Ocean to the north • Southern boundary region is area of gradual change to conditions of region II • Low net radiation due to coastal fog and stratus/stratocumulus clouds that result from sources of moisture in Arctic Ocean (incomplete ice coverage, existing ice covered with melt ponds/puddles) • Multi-year ice is persistent throughout the year, reduces maritime effect leading to large temperature range over the year (38-40°C) • Mix of multi-year and first year ice as one progresses towards central sills region
II	• High anticyclonic activity • Eastern boundary based on maximum westward extent of cyclonic activity of region IV (Davis Strait/Baffin Bay/Baffin Island) • Western boundary based on maximum eastward extent of cyclonic activity of region III (Beaufort Sea/Amundsen Gulf) • Low relief • Shares climatic characteristics of mainland to the south • Northern boundary region is area of gradual change to conditions of region I

Region	Characteristics
	• High ratio of land area to sea area relative to other areas of CAA, also shallow and narrow waterways between islands: maritime effect is not as strong, resulting in large temperature range (42-45°C) • Low cloud and fog during ice break up season maintain cooler temperatures than nearby inland areas • Low precipitation amounts over southern Victoria Island/King William Island area (< 100 mm/year) • Melville Peninsula/Southampton Island are transition from continental to maritime conditions • Committee Bay distinguished by multi-year ice, ice fog is common on western Melville Peninsula; sea ice in centre of Foxe Basin is too far to have any effect on coastal conditions in eastern Melville Peninsula • Autumn cloudiness near Foxe Basin due to occasional stagnant low pressure zones centred over the basin • Precipitation is higher in Melville Peninsula/Southampton Island area compared to west (200 – 300 mm/year)
III	• Alternation of cyclonic/anticyclonic activity (only occurrence in CAA, other areas are dominated by one or the other) • High net radiation relative to regions I and II • Maritime air masses originating from the west heavily influence local conditions; pronounced maritime effect leads to smaller temperature range (36°C) • Higher precipitation and cloudiness relative to Victoria Island/Boothia Peninsula • Sea ice clears early
IV	• High degree of cyclonic activity • First-year ice is dominant • Net radiation is similar to that of region I • Mountainous terrain influences precipitation; has highest precipitation of all regions due to storm activity and abrupt uplift of onshore winds onto rugged coastline • Lancaster Sound is area where cyclonic activity from Davis Strait/Baffin Bay dies out • Maritime character to climate of northern region due to maritime air masses that enter the region and presence of open water (notably the North Water polynya), thus temperature range is 33-36°C and can be as low as 22°C over the North Water polynya • Western interior of Baffin Island is fair-weather in general with maritime effects over Foxe Basin that do not reach far inland; occasional cyclonic storms enter Foxe Basin, but most stagnate; precipitation ranges from 150 mm (near Pond Inlet and Arctic Bay) up to 300 mm over central Baffin Island • Baffin Island mountains can have less extreme temperature range as

Region	Characteristics
	their altitude excludes them from the temperature inversions that are common throughout the archipelago; the temperature range is <33°C; conditions for glacial formation exist due to proximal sources of moist air, temperature regime and terrain; precipitation is > 300 mm • East coast of Baffin Island characterized by fjords with heavy maritime influence on temperature range (26-30°, growing with latitude); cyclonic activity maintains warmer temperatures and strong winds in winter and year round cloudiness; southward moving Baffin current maintains cooler temperatures in summer and transports sea ice into the area; fog and low clouds are the norm in summer; mean precipitation is 400 mm • Southern tip of Baffin Island is much less mountainous and experiences more cyclonic activity; precipitation is higher (300-400 mm in lowland, > 500 mm at higher altitudes); maritime effect is pronounced leading to small temperature range (22°C at Resolution Island); fog is common along coast due to confluence of ice in Hudson Strait and cold Baffin Current water in addition to warm moist air associated with cyclonic activity • Baffin Bay/Davis Strait has waters of Arctic and Atlantic origin; first-year ice is the norm; heavily dominated by cyclonic activity with frequent storm activity; temperature range is 25-30°C due to maritime influence
V	• Rugged, mountainous terrain • Transition zone between region I and IV • Southern boundary marks limit of cyclonic activity originating in region IV (Baffin Bay/Davis Strait) • Nares Strait/Hall Basin/Kane Basin area has mixture of first year and multi-year ice; formation of an ice plug in Smith Sound hinders clearing of ice in summer; storm activity from Baffin Bay occasionally travels into area resulting in late ice formation relative to other smaller channels in the CAA; temperature range is 38°C; precipitation is < 200 mm; continual presence of sea ice and open water lead to foggy and low cloud conditions in coast regions • Nansen Sound and adjacent lowlands surrounded by mountains resulting in a strong rain-shadow effect and little precipitation (lowest in Canada); this area has the largest temperature range in the CAA (43°C); insolation is high relative to other areas of the CAA where fog and low cloud cover attenuate insolation • Axel Heiberg and Ellesmere Island highlands are mountainous and dominated by glacial activity; precipitation is 200 mm at highest altitudes; mean temperature range is lower than surrounding lowlands

The largest drivers of climatic conditions in the CAA are the large seasonal variability in insolation and air temperature. It is important to note that the entire archipelago is north of the Arctic Circle with the exception of the most southerly third of Baffin Island and the islands of northern Hudson Bay. It is thus subject to periods of 24 hour darkness in the winter and 24 hours of daylight in the summer. The additional insolation during the summer time has little effect due to the low incidence angle and the high albedo of ice and snow. Insolation is also attenuated by foggy conditions associated with areas of partial ice coverage in the summer. Temperatures range, on average, from -30°C in winter to 4°C in the summer.

Winds are typically from the north and northwest with stronger winds in winter; these are associated with a semi permanent high pressure system over the Beaufort sea (Tomczak and Godfrey, 2002). Summer winds directions are more variable due to weaker atmospheric pressure systems (Birch et al., 1983). The western portion of the CAA is heavily influenced by the meteorology of the neighbouring Beaufort Sea whereas topography plays a strong modifying role on the local meteorology and wind regime in the central and eastern CAA. The mountainous terrain of Baffin, Devon and Ellesmere Islands protects the central CAA from storms that are common in Baffin Bay (McLaughlin et al., 2005). Relative to the open ocean, the effect of wind is diminished within the CAA as there is much less fetch due to the islands and ice, thus the wind cannot set up a fully developed sea (notable exceptions include Hudson Bay, Baffin Bay and the Beaufort Sea in late summer when ice cover is absent, or at a minimum). From a physical oceanography viewpoint, this reduces the amount of energy available for surface mixing. This effect is compounded by the presence of sea ice as ice severely dampens

direct wind mixing. It should be noted, however, that the keels of wind driven ice ridges can stir the upper layers of the water column.

The CAA experiences relatively little rainfall or snowfall compared to more southerly latitudes (refer to Figure A-4). For example, near the centre of the NW Passage, Resolute Bay and Cambridge Bay receive their maximum rainfall in July: 18.3 mm and 22.1 mm, respectively. This pales in comparison to mid-latitudes, for example, Fredericton receives 84.5 mm of rain in July on average. Snowfall follows the same trend. Resolute Bay and Cambridge Bay receive their maximum snowfall in the month of September: 18.6 mm and 15.8 mm of snow, respectively. As a comparison, Fredericton receives it maximum amount of snowfall in December: 70.8 mm (Environment Canada, 2003).

Barry and Sereze (2000) have collated the work of several studies of precipitation/evaporation rates over the Arctic Ocean and surrounding landmasses. Their work indicates that the mean annual precipitation over the CAA ranges from 250 mm in the southern CAA to 150 mm in the Queen Elizabeth Islands. Evaporation rates over land were estimated at 150 mm in the southern CAA, dropping to 100 mm north of Parry Channel. The annual evaporation over the waterways of the CAA was significantly less: 50 mm to 80 mm, with no significant spatial trends. The underlying data sets used to derive these values are sparse and often biased (particularly the precipitation component, which is almost always underestimated). Uncertainties for the net precipitation minus evaporation term (P-E) were estimated to be 27 mm. The P-E is approximately 200 mm in the southern CAA, falling to ~130 mm in Parry Channel. The only location where

evaporation equaled or exceeded precipitation was in the vicinity of the North Water polynya in Smith Sound (Barry and Serreze, 2000).

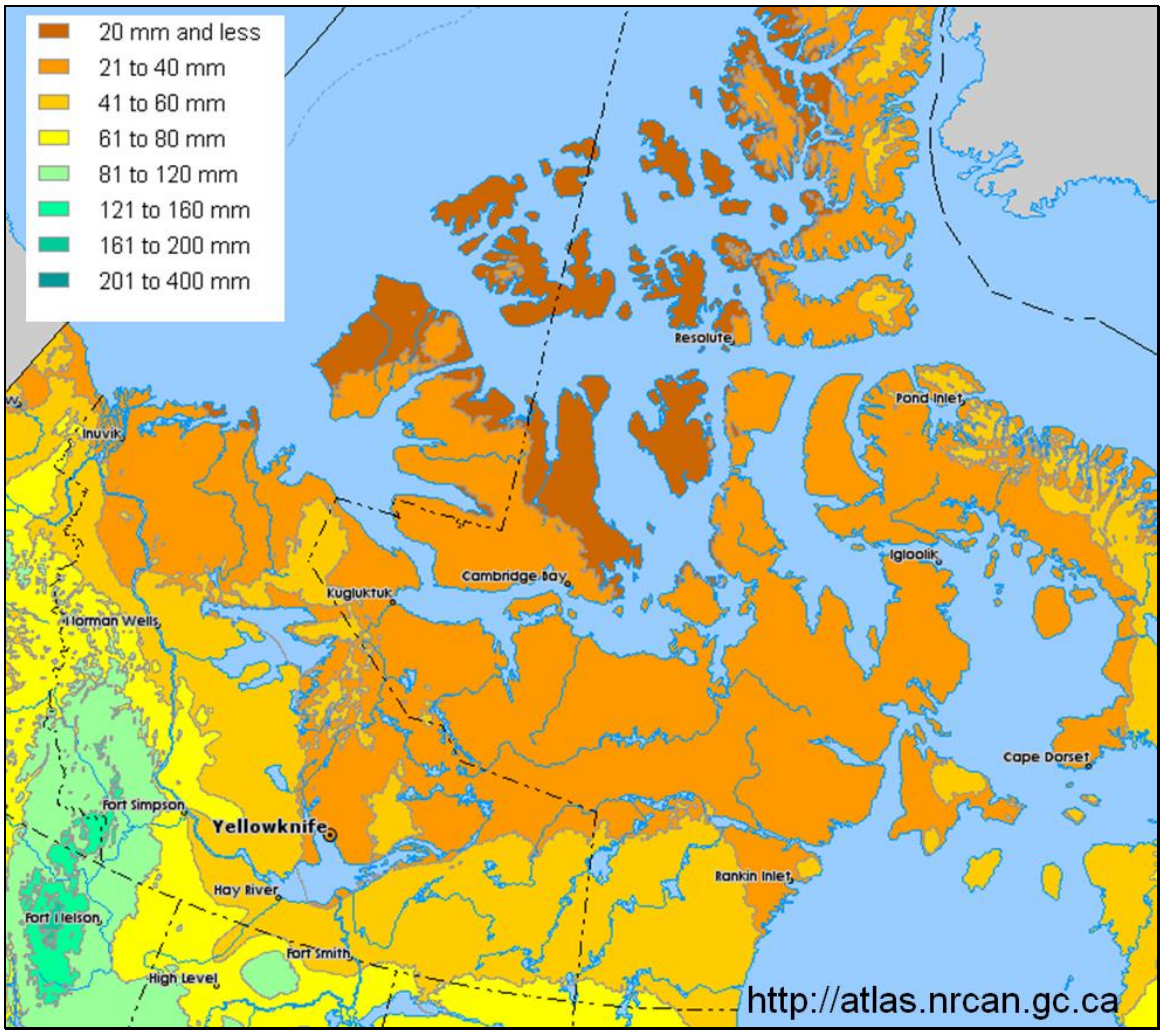

Figure A-4. July mean total precipitation, after (Environment Canada, 2007).

A.5.3 Hydrology

Freshwater input from rivers in the CAA exhibits a large seasonal variation, with maximum river output occurring during the spring/summer runoff periods (usually June/July). The watershed that empties into the Arctic Ocean is quite large and is

dominated by the drainage basin of the Mackenzie River, with an estimated yearly outflow of 340 km^3. The Mackenzie River drains directly into the Beaufort Sea over an extensive shallow shelf, several hundred kilometers west of the CAA. The quantity of freshwater delivered to the CAA from the Mackenzie is potentially very important yet its impact on the oceanographic conditions of the CAA is poorly understood (McLaughlin et al., 2005). In winter, the Mackenzie river plume is trapped behind an ice pressure ridge at the edge of the land fast ice (roughly along the 20 m isobath), forming an under ice freshwater lake with a volume of about 70 km^3. In summer, the plume of the river can extend eastward along the coast under the influence of Coriolis. However, it is sensitive to wind directions with easterly winds driving the plume seaward onto the shelf, sometimes reaching the shelf edge (Carmack and MacDonald, 2002).

Eastward from the Mackenzie along the mainland coast, notable sources include the Coppermine, the Burnside and the Back rivers, of which the Back is longest (refer to Figure A-5). The Burnside and Back rivers drain into extensive shallow and protected inlets (Bathurst and Chantrey Inlets, respectively; note that portions of the Back river were missing from the mapping software database used to generate Figure A-5, the location of final section and outlet is indicated by a red line). Of the three, the Coppermine is the only one that could be considered a point source of freshwater at the coast as its flow discharges directly into the westernmost point of Coronation Gulf. These three rivers (along with the Mackenzie) are also characterized by head water lakes; this has the effect of maintaining a base amount of flow throughout the year provided that the head water lakes are sufficiently large. On the other hand, nivel (meltwater) rivers have different discharge patterns than rivers with head water lakes: nivel rivers have

considerable discharge events during the summer but little or no flow in the winter with those in the high arctic being frozen for most of the year. Nivel rivers are predominant among the islands of the CAA and provide pulses of freshwater during the runoff season, typically in June and July. As an example, Freshwater Creek flows into Cambridge Bay on Victoria Island and has an average yearly peak flow of 30 m^3 s^{-1} in late June with considerable interannual variability (reaching 80 m^3 s^{-1} at least once in the past thirty years). By contrast, the Burnside River has an earlier average peak flow (mid-June) of approximately 750 m^3 s^{-1}, with one year recording a peak flow of 3000 m^3 s^{-1} (McLaughlin et al., 2005).

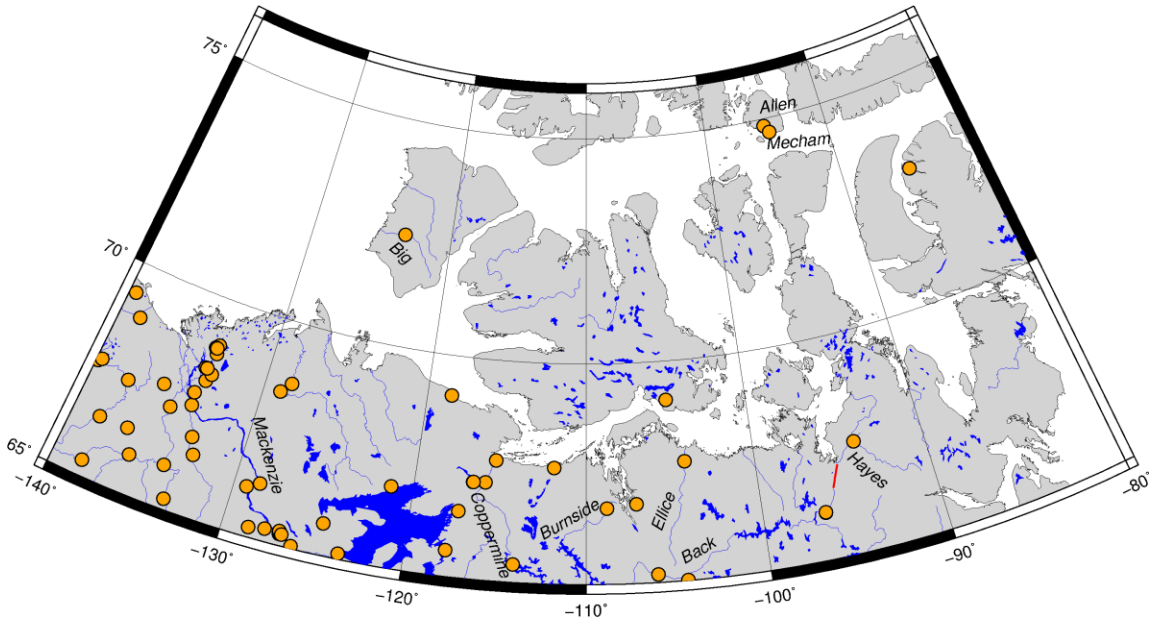

Figure A-5. Rivers and ARDB gauge stations in the CAA.

Many of the river systems in the CAA are not gauged, thus it is difficult to approximate the total contribution of freshwater input to the CAA. Databases containing discharge data do exist, for example, the Arctic Runoff Database (ARDB) which has been compiled by the Global Runoff Data Centre (GRDC) (GRDC, 2008). Figure A-5

indicates the locations of gauges recorded in the ARDB; Table A-2 lists the yearly volume output of selected rivers in the CAA, as recorded in the ARDB. The Back and Coppermine rivers deliver the most water by far. The Allen and Mecham rivers are likely representative of smaller rivers throughout the Archipelago. All of these sources pale in comparison to the Mackenzie which delivers 340 km^3 yearly to the Arctic Ocean. For comparison, the Saint John River delivers 25.482 km^3/year (gauged below the Mactaquac dam).

Table A-2. Mean yearly volume output of selected rivers in the CAA (Source: ARDB).

River	Record span (years)	Mean yearly volume (km^3)	Percentage of missing values in monthly time-series
Coppermine	1983-1993	9.051	0.00
Burnside	1976-1996	4.204	3.28
Ellice	1971-1996	2.717	0.00
Back	1965-1996	15.161	0.00
Hayes	1971-1992	4.040	9.34
Allen	1971-1984	0.098	57.41
Mecham	1971-1979	0.032	56.86
Big	1975-1988	0.203	16.05

Though these databases are very useful for studies in the Arctic, they often provide an incomplete picture of the total discharge. For example, the installation and maintenance of many of the stations is directly linked to economic interests, thus several areas are not gauged at all. There are numerous logistical restraints to gauging Arctic rivers as they are remote, difficult and costly to access, covered in ice for the majority of the year, and dangerous to work on during periods of high runoff. Further complicating the situation is the fact that many gauges are installed along rivers, but not necessarily at the mouth (again, station locations follow economic interests). Focusing only on the

river runoff into the Arctic Ocean, approximately 30% of the catchment area is ungauged (Grabs and Portmann, 2000). One study estimates the total ungauged discharge from North American Arctic islands to be 603 km^3 yr^{-1}, which is of a comparable magnitude to the estimated mainland discharge of 582 km^3 yr^{-1} (sum of gauged and approximated ungauged discharges) (Vuglinsky, 1997). McLaughlin cites an earlier study which estimated the total fresh water discharge to the CAA at 219 km^3 yr^{-1}, excluding Foxe Basin and Hudson Strait (Walker, 1977). Clearly there is considerable variation in the estimates of river discharge found in the literature.

In general, river input to the CAA can be considered as estuarine-like only during the short ice free season in the late summer and early autumn. During the early open-water season, the situation is similar to that found in more southerly latitudes with the exception of an additional broadly-based source of freshwater from sea ice melt. During the winter, a "frozen estuary" model is more applicable as the standard categorizations do not apply (i.e. salt wedge, partially-mixed, and well-mixed) (MacDonald, 2000).

A.5.4 Sea ice

New ice formation usually begins in the CAA in late September with the eastern channels typically being the last to freeze over. In the restricted channels to the south, pack ice is often immobilized as land-fast ice; in some areas stable ice arches form across channels as wide as 100 km (Melling, 2002). On the contrary, some of the larger channels such as Lancaster Sound and M'Clure Strait can experience large movements in the ice field throughout the winter. The times and locations of ice breakup in the spring and summer can vary markedly as they depend much on air temperature, solar heating,

wind and currents. Areas such as the Coronation Gulf are typically fully ice free for a short time in the summer whereas other areas remain congested year round, e.g. M'Clure Strait (Birch et al., 1983). The presence of sea ice is highly variable from year to year, thus probabilities are often used to characterize the sea ice regime for different areas of the CAA. In general, there is a 50%-100% chance of encountering ice in the western sections of the NWP. The probability of encountering sea ice drops to less than 50% in the eastern half of the NWP (McLaughlin et al., 2005). Historically, the most problematic sections for navigation are western Parry Channel and the channels to the east of Victoria Island as they are clogged with thick, multiyear pack ice of Arctic Ocean origin. Multiyear ice floes are typically thicker, ranging from 3 m to 5 m, whereas the thickness of first-year ice ranges from 2 m to 2.5 m in the CAA, depending on latitude (Melling, 2002).

As mentioned above, sea ice is highly variable from year to year in its presence, date of break-up and date of formation. The Gulf of Boothia and M'Clintock Channel, both located in the central CAA, provide an example of the variability. The two waterways form elongated north-south oriented bodies of water of comparable size that span the same range of latitude; they are separated in the east-west direction by the Boothia Peninsula, Somerset Island and Prince of Wales Island. One would expect similar ice conditions in both areas; however a 21 year analysis of sea ice conditions found otherwise, as summarized in Table A-3 below.

Table A-3. Comparison of "Ice Scapes" between M'Clintock Channel and Gulf of Boothia, 1980-2000 (Barber and Iacozza, 2004).

	M'Clintock Channel	**Gulf of Boothia**
Sea Ice Breakup	Begins in southern region, progresses northward; breakup begins early in season; relatively small areas left ice covered at end of season	Begins in northern region, progresses southward; significant amounts of breakup still occurring in late summer/early autumn; large areas left ice covered at end of season
Sea Ice Consolidation	Consolidation begins in northern region and progresses south; consolidation progresses slow relative to Gulf of Boothia	Consolidation begins in southern region and progresses southward; consolidation progresses quickly relative to M'Clintock Channel
External influences on sea ice regime	Dominated by input of ice from Beaufort Sea via M'Clure Strait and Viscount Melville Sound, thus is coupled with processes linked to Beaufort gyre	Direct connection to Lancaster Sound polynya links ice regime to Lancaster Sound/Baffin Bay ice conditions

A.5.5 Tidal regime

Tidal ranges are less than 2 m for most of the CAA, with the smallest amplitudes observed in the south and the west. Though the tidal heights are small in amplitude, tidal currents of appreciable magnitude can occur due to the narrow, constricted nature of many of the channels. For example Barrow Strait routinely has currents as high as 0.5 to 1.5 m/s (McLaughlin et al., 2005). The tidal character for several historic tidal stations throughout the CAA is shown in Figure A-6, these classifications are based on the ratio of the diurnal O1 and K1 components over the sum of the semi-diurnal M2 and S2

components, as suggested in the Canadian Tidal Manual (Forrester, 1983). The majority of stations have semi-diurnal tides with diurnal inequalities.

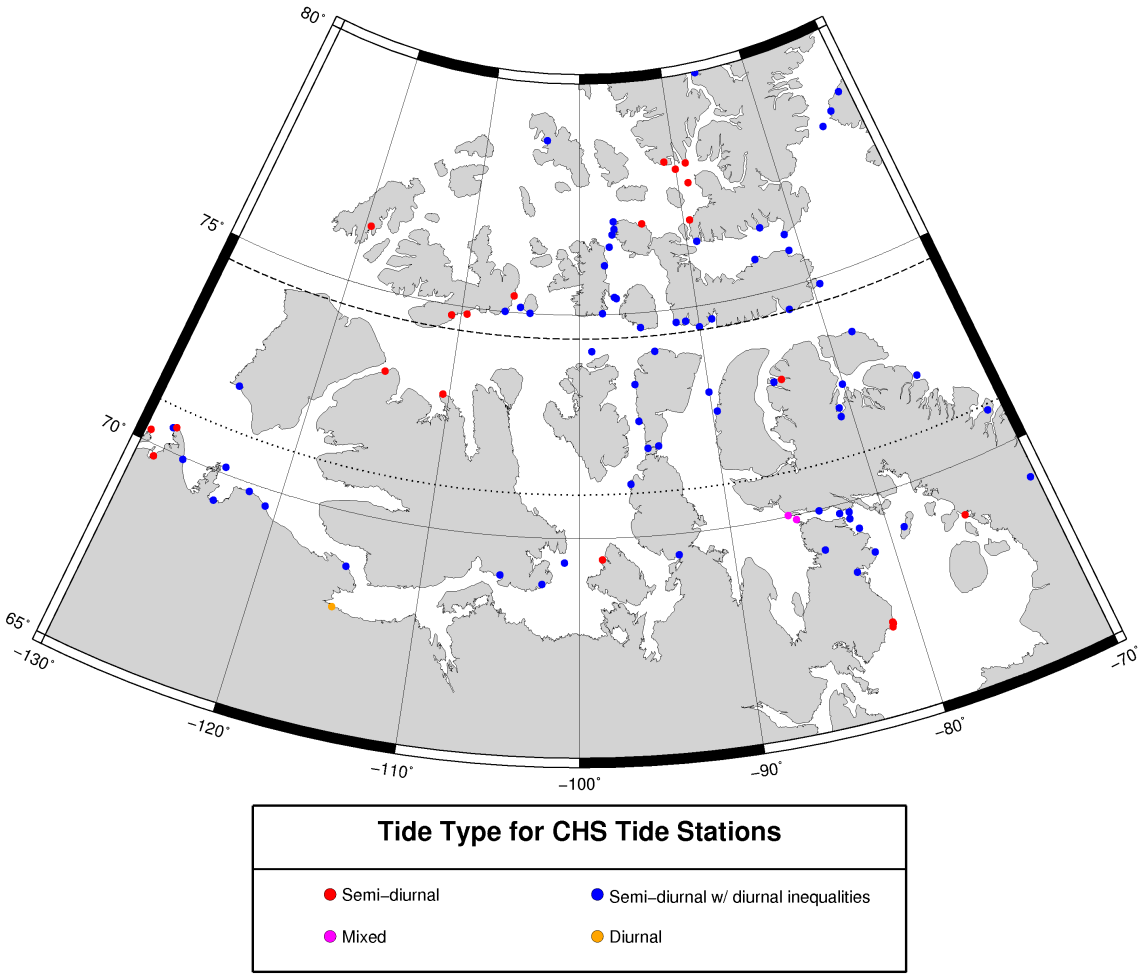

Figure A-6. Classification of tides in the CAA. Critical latitudes for the M2 and N2 tide are indicated by the dashed and dotted lines, respectively.

The parameter U^3/h, where U is the current speed and h is the water depth, is often used to quantify the potential for tidal mixing. Using this parameter, McLaughlin identifies several regions in the CAA that have the potential for energetic tidal mixing: Barrow Strait, Gulf of Boothia, Queen Maud Gulf, Dolphin and Union Strait, Hell Gate and Cardigan Strait (McLaughlin et al., 2005).

The existence of inertial, or critical, latitudes for the N_2, M_2, and S_2 tidal components further enhance tidal mixing at these latitudes through the establishment of a thicker boundary layer since the semi-diurnal tidal constituents resonate with inertial waves (Melling, 2000). Critical latitudes are found where the Coriolis frequency is equal to the tidal frequency, i.e.

$$\omega = |f| = 2\Omega \sin \varphi_c \tag{A.1}$$

where ω is the tidal frequency, f is the Coriolis parameter, Ω is the Earth's angular velocity and φ_c is the critical latitude. Solving for the critical latitude yields the following expression.

$$\varphi_c = \sin^{-1}\left(\frac{\omega}{2\Omega}\right) \tag{A.2}$$

At critical latitudes, tidal velocities throughout the water column are depth dependant and can be strongly modified by stratification and by the presence of ice cover (Prinsenberg and Bennett, 1989b; Makinson et al., 2006). Critical latitudes for the four principal semi-diurnal tidal constituents are listed in Table A-4. Note that the M_2 critical latitude coincides with the direct NWP through Parry Channel. The critical latitude for the N2 constituent cuts across two north-south oriented sections of the CAA, namely M'Clintock Channel/Larsen Sound and the Gulf of Boothia. The critical latitudes for the M2 and N2 components are indicated in Figure A-6 by a dashed and dotted line, respectively.

Table A-4. Critical latitudes of semi-diurnal tidal constituents.

Constituent	Period (hours)	Frequency (rad/s)	Critical latitude (deg)
M2	12.4206	1.4052×10^{-4}	74.4718
S2	12.0000	1.4544×10^{-4}	85.7651
N2	12.6584	1.3788×10^{-4}	70.9789
K2	11.9673	1.4584×10^{-4}	89.8127

A.5.6 Circulation

The Pacific Ocean has a higher steric sea-level relative to the Atlantic due to its fresher and lighter waters. This difference in steric sea-level drives flow from the Arctic Ocean through the CAA to the Atlantic, thus the CAA is a transition zone between the Arctic and the Atlantic oceans (McLaughlin et al., 2005). Observed and calculated mean surface flows are generally to the south and east through the archipelago with generally weak flows. Exceptional cases have been observed in Penny Strait and Lancaster Sound (15 cm/s and 20 cm/s, respectively) (de Lange Boom et al., 1987). The circulation is much more complex than that of a simple channel between the Arctic and Atlantic oceans. The CAA forms a series of inter-connected sub-basin circulations in which buoyancy-boundary currents carry the fresh water through flow in narrow and thin surface flows (order 10 km and 10 m, respectively) along the right hand side of channels. The CAA has several sub-basins with circulation patterns of their own that re-circulate through flow instead of providing a direct path. The westerly and southerly sub-basins have sills at their periphery that severely limit the renewal of deeper water in the

individual sub-basins thought that is not to say that renewal does not occur (Carmack, 2000; Melling et al., 1984).

In general, deep and wide channels have weak and disorganized flow in the central portions of the channels with narrow and strong buoyancy boundary currents. Good examples are M'Clure Strait, Viscount Melville Sound and M'Clintock Channel. Shallower and narrower straits such as Byam Martin Channel, Penny Strait, Wellington Channel and Barrow Strait have stronger and more consistent flow patterns. Flow speeds are tied to the season, increasing by up to a factor of two in summertime. The few observations collected to date point to stronger summertime flows on the southern and western edge of straits (these flows being associated with right hand bounded outflow from the Arctic Ocean); the northern and eastern sides of straits experience a weakening of summertime flow (Melling, 1997). Aside from the Baffin Current which crosses the eastern entrance to Lancaster Sound, the strongest non-tidal currents are found in the vicinity of the central sills and are 20-30 cm s^{-1}, on average (Melling, 2000).

Several attempts have been made to estimate the flow through the CAA, some using direct current measurements and some using dynamical methods. Early work using geostrophic calculations suggested transports of 0.7 to 1.7 Sv through Lancaster, Jones and Smith Sounds (Collin, 1962), and 2.1 Sv into northern Baffin Bay (Muench, 1971). Direct current measurements from many observation campaigns were compiled by Fissel to compute a net transport of 1.7 Sv through the CAA (Fissel et al., 1988). Diagnostic simulations using gridded temperature and salinity fields synthesized from a number of sources resulted in an estimated summer flow of 0.9 Sv from the Arctic to the Atlantic

Ocean (including Nares Strait between Ellesmere Island and Greenland) (Kliem and Greenberg, 2003).

Though net surface transport is to the south and east in the CAA, many channels have been observed to have surface counter flows on the opposite bank. This is explained by the small internal Rossby radius in the CAA. The internal Rossby radius is a measure of the distance a buoyancy flow can travel without being significantly affected by the Coriolis force, it is given by:

$$R_i = \frac{\sqrt{g'H}}{f} \tag{A.3}$$

where *g'* is reduced gravity, *H* is the thickness of the upper layer above the pycnocline, and *f* is the Coriolis parameter. Reduced gravity is:

$$g' = g\frac{\Delta\rho}{\rho} \tag{A.4}$$

where g is gravity, $\Delta\rho$ is the density difference between the two layers and ρ is the density of the lower layer. If the radius of curvature of shoreline topography is greater than the internal Rossby radius, then a buoyancy boundary current will be trapped along the shoreline. Thus, in the absence of wind forcing, buoyancy driven flows through the Archipelago follow the shoreline topography provided that the radius of curvature of the shoreline is larger than the internal Rossby radius. Many of the channels in the CAA are much wider than the internal Rossby radius of deformation, allowing for counter-flowing currents to exist on opposite sides of a channel without interfering with each other (Leblond, 1980). Leblond observes that the situation of counter-flowing currents is somewhat unique to the CAA, due to the increased effect of Coriolis at high latitudes. He contrasts the CAA to the East Indian Archipelago, where similar channel geometries and

density structures exist (albeit thermal density structures) and concludes that the much smaller effect of Coriolis at low latitudes leads to a much larger internal Rossby radius (one order of magnitude), thus counter-flowing surface currents are less likely to occur in the East Indian case (though counterflows can occur at depth).

Small and medium scale eddies and meanders have been observed in many studies throughout the CAA (e.g. Fissel et al. (1980)). McLaughlin et al. (2005) notes that the buoyancy boundary currents observed in the CAA can generate eddies through two mechanisms. Firstly, if the radius of curvature of a sharp bend in the coastline is smaller than the internal Rossby radius, topographically spawned eddies can be formed which can carry the buoyant water across the strait. Secondly, sub-critical flows can also generate and shed eddies; these are characterized by a densimetric, or internal, Froude number less than unity:

$$F_d = \frac{U}{\sqrt{g'H}} \tag{A.5}$$

where U is the current speed in m/s, g' is the reduced gravity and H is the depth of the upper layer (in a two layer model of the ocean). The dimensionless Froude number represents a ratio of inertial and gravitational forces. When it is less than unity, the flow is referred to as sub-critical and disturbances to the flow can propagate against the direction of the flow (the shallow wave speed is greater than the flow speed). A super-critical flow with a Froude number greater than unity, on the other hand, will always propagate disturbances in the direction of the flow (Turner, 1973). In cases where buoyancy boundary currents have sub-critical flows, instabilities in the flow can generate eddies.

A.5.7 Water mass characteristics

Arctic waters enter the CAA via Amundsen Gulf, M'Clure Strait and through the western Queen Elizabeth Islands to the north of Parry Channel. Nares Strait provides a more direct route from the Arctic Ocean to the Atlantic Ocean that bypasses the CAA. The upper 200 m of the Canadian Basin of the Arctic Ocean are composed primarily of Pacific water, which is fresh relative to the underlying water of Atlantic origin. The sill depth of 125 meters in Barrow Strait limits the communication of waters to the surface layer only, i.e. the ASW described earlier, but with a large component deriving from the Pacific Ocean via Bering Strait. Ultimately, the AW of the Arctic Ocean cannot communicate with the eastern portions of the NWP, resulting in distinct water masses below sill depth to the east and west of the central sills. Therefore, the deep waters of M'Clure Strait and Viscount Melville Sound will have different characteristics than the deep water of Lancaster Sound.

Whereas underlying AW is blocked by the central sills, the surface layer is free to flow throughout the CAA. An early study based on silicate and phosphate measurements estimated that 60% of the outflow of Lancaster Sound is of Pacific Origin (Codispoti and Owens, 1975). A later study, based on nitrate-phosphate relationships, found that the entire Lancaster Sound surface outflow was of Pacific Origin based on measurements taken east of the central sills in Barrow Strait (Jones et al., 2003). A little to the north, the same study found that flow through Cardigan Strait into Jones Sound was almost entirely of Pacific water. The upper 100 m of the water column in Jones Sound is of Pacific origin, with the underlying water mass containing water of Atlantic origin that has passed through the Arctic Ocean via Nares Strait rather than having travelled north

through Baffin Bay. The upper 50 m of water in Smith Sound is largely of Pacific origin; the percentage of Pacific water remains high at depth with 20% of water at 570 m depth being of Pacific origin. Moving south through Baffin Bay, the same study traces Pacific water in the upper layers as far south as the Grand Banks (composing about 50% of the waters in the main boundary current). Water flowing south from Barrow Strait into the Gulf of Boothia eventually passes through Fury and Hecla Strait to arrive in Hudson Bay. This flow, along with the deviation of the Baffin Current into Hudson Strait, brings ASW of Pacific origin into Hudson Bay. Excluding river runoff, Pacific water forms a potentially important source of water for Hudson Bay, though there are only a few noisy measurements to support this (Jones et al., 2003).

The aforementioned study does not address the origin of surface waters in the southern portions of the Archipelago, specifically Coronation Gulf and Queen Maud Gulf each with approximate maximum depths of 310 m and 120 m, respectively. Little is mentioned of either gulf in the literature; presumably the surface waters are of Pacific origin via inflow from Amundsen Gulf and M'Clintock Channel. In general, waters of Atlantic origin can be found throughout the CAA when depths are greater than 135 m. They are identified by an increase in temperature with depth and a change in the slope of salinity with depth (McLaughlin et al., 2005). However, this is not likely the case in the southern CAA. At the western entrance to Coronation Gulf, the shallow sill (15 m) in Dolphin and Union Strait precludes the direct transmission of AW from Amundsen Gulf. Likewise to the east, shallow depths bar the entry of any AW from M'Clintock Channel with a sill depth of approximately 35 m in Victoria Strait. Figure A-7 shows plots of temperature and salinity profiles collected by the CCGS Amundsen within the area. The

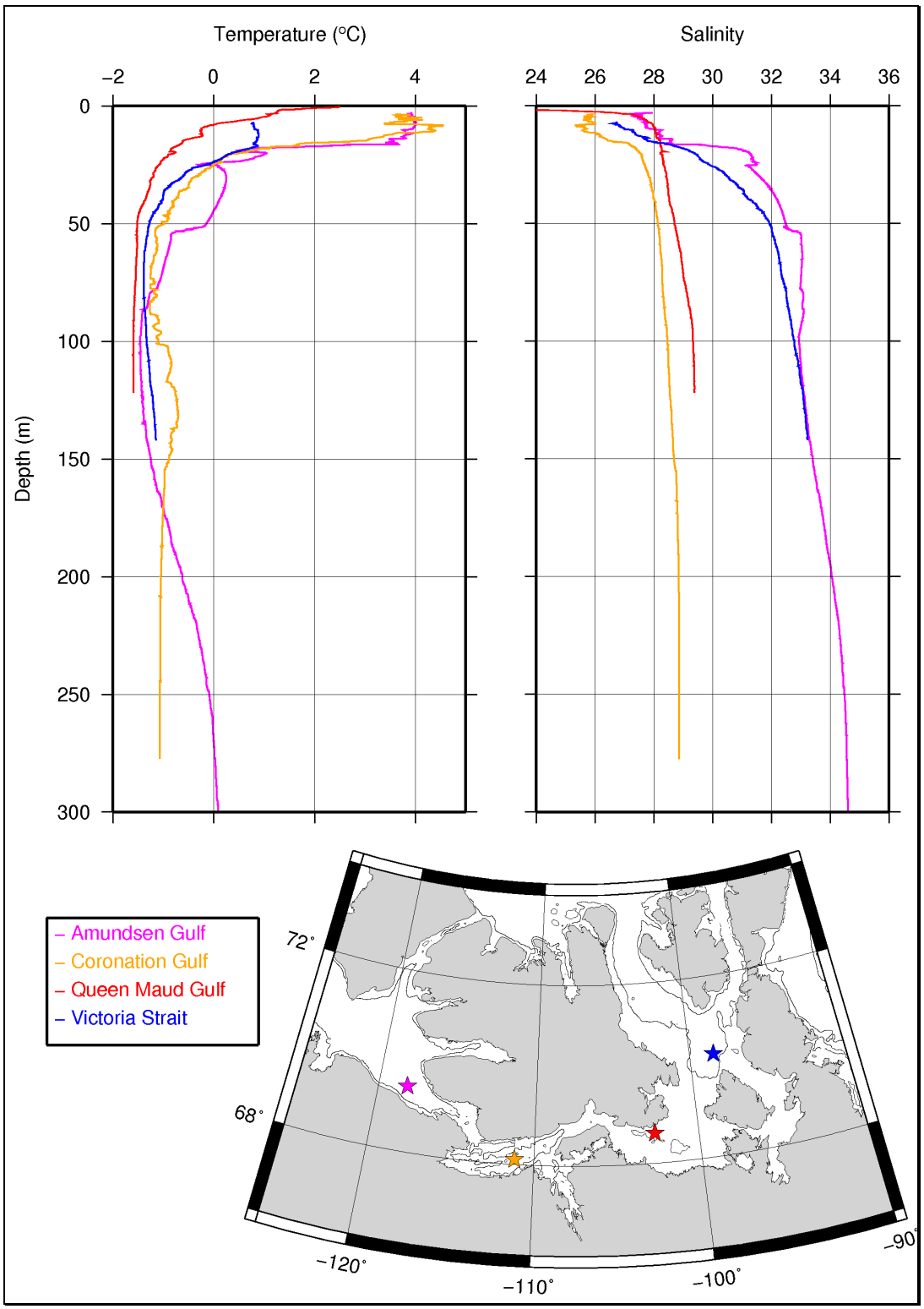

Figure A-7. Temperature and salinity profiles in the southern CAA. The 50 m isobath is drawn in the inset map.

sub-basins of both Coronation Gulf and Queen Maud Gulf have fresh deep water relative to the water at the same depths of the neighbouring deeper water masses in Amundsen Gulf and Victoria Strait. It should be noted that both of these sub-basins receive the outflow of the Coppermine, Burnside and Back rivers, thus they have higher fresh water input relative to other areas of the CAA.

M'Clure Strait and Viscount Melville Sound form deep sub-basins (475 m and 600 m, respectively) which are cut off from the Canada Basin by a 375 m sill at the western edge of M'Clure Strait. A potential mechanism for deep water renewal in these sub-basins is the ejection of high salinity surface water during ice formation. The depth of penetration of high salinity density flows into the water column is strongly dependent on several factors (Melling et al., 1984): (1) divergent ice cover due to wind forcing; this allows for a continuous supply of brine as new ice forms over open water, (2) a large shelf like area with depths comparable to depths of surface mixing, and (3) a mechanism to trap shelf water near the freezing interface; either bathymetric features at the periphery of the shallow area, or a prevention of direct flow to deeper areas due to Coriolis. These conditions are met on the large continental shelves on the Eurasian side of the Arctic Ocean; this allows for the renewal of Arctic Deep Water, as discussed earlier. These conditions are not met in M'Clure Strait and Viscount Melville Sound, thus this mechanism does not likely play a significant role in the formation of deep waters in these two regions. The temperature and salinity properties of the deep water in western Parry Channel are similar to those found opposite the sill in the Arctic Ocean (Melling et al., 1984), however, decreasing oxygen content with depth and an absence of CFC-113 in

both sub-basins indicate that these waters are not renewed on a regular basis (McLaughlin et al., 2005).

Returning to the discussion of surface waters in the CAA, the ASW is modified during its eastward transit through the passage, marking a transition of the surface waters of the Arctic Ocean to the surface waters of Baffin Bay. Upward diffusive heating increases the halocline temperature by as much as 0.25°C, with the amount of heating increasing towards the central sills. The absence of conditions for mid and deep water renewal, as discussed above, specifically allow for the diffusive upward warming of the halocline in M'Clure Strait and Viscount Melville Sound (on the contrary, the presence of such conditions prevents upward diffusive flux of heat in the Arctic Ocean as the pycnocline is cooled by lateral intrusions of cold, salty shelf waters). Strong mixing in the area of the central sills increases the surface temperature to the point that it retards sea ice formation and growth. In these areas, the resulting maximum sea ice thickness attains only half that of other areas in the CAA (1 m thickness compared to 2 m). In the shallower sections of these areas (depth < 100 m), there is sufficient heat brought to the surface to allow for the formation and maintenance of polynyas over the sills of Penny Strait, Hell's Gate and Byam Austin Channel (Melling et al., 1984). The seasonal mixed layer also becomes shallower between the Arctic Ocean and the central sills (McLaughlin et al., 2005).

Moving to the eastern CAA, Lancaster Sound is a meeting point for waters deriving from several origins: Atlantic Water from the south via the west Greenland Current, Canadian Basin ASW from the west via Parry Channel, and Lincoln Sea ASW from the north via Nares Strait. A field campaign undertaken by Jones and Coote (1980)

took observations along three oceanographic sections across Lancaster Sound, two sections across Jones Sound, one section across Smith Sound and a longitudinal section along the center of Lancaster Sound extending across Baffin Bay to Greenland. Nutrient relationships were used to identify water masses from the three aforementioned sources. ASW was seen to flow south through Nares Strait and Fram Sound (at the western end of Jones Sound) into Baffin Bay. ASW from Baffin Bay was traced into Lancaster Sound, with an intrusive surface current flowing westward along the north shore of Lancaster Sound. An eastward flowing current carries ASW of Canadian Basin origin along the south shore. A subsurface flow of Baffin Bay water of Atlantic origin was detected just west of Prince Leopold Island (at the western edge of the mouth of Prince Regent Inlet) (Jones and Coote, 1980).

Earlier work with surface drifters found a gyre circulation in Lancaster Sound to the north of Bylot Island (Muench, 1971). A two year field campaign (1978-1979) in the western Baffin Bay and Lancaster Sound region found similar patterns and shed more light on general circulation patterns in the surrounding area (Fissel et al., 1980). The study identified two modes of cross-channel transport of the westward intrusive ASW current along Lancaster Sound's north shore with the main difference between the two modes being the location of the southern terminus of the cross-channel current (either Borden Peninsula or Bylot Island). The cyclonic cross-channel flow was observed to be narrow (10-30 km) with areas of weak and disorganized flow found immediately to the east and west of the flow. In addition to this, the study identified several transient yet repeatedly occurring eddies east of Bylot Island where the Baffin Current separates from the coastline (eddies were also observed seaward of the current). Transient mid-sound

gyres and eddies were also observed in Lancaster Sound between Borden and Brodeur Peninsula (Fissel et al., 1980).

APPENDIX B – OCEANOGRAPHIC CLIMATOLOGIES

B.1 Introduction

An oceanographic climatology provides a continuous representation of a scalar value, at some prescribed depth level or over a series of depth levels, over a specified region from non-synoptic observations and is meant to serve as a model representing the mean conditions for the epoch for which the climatology is constructed. Temperature and salinity fields are those most often constructed. Other fields often encountered include, for example, dissolved oxygen, phosphate, silicate, and nitrate. Climatologies vary in several aspects: source data, coverage, resolution, construction techniques, etc, all of which can greatly influence the fidelity of the climatological mean fields. There are three such climatologies under investigation in this work:

1. ¼° World Ocean Atlas 2001 (WOA01)
2. Generalized Digital Environmental Model, Variable resolution, v3.0 (GDEM)
3. Kliem and Greenberg climatology of the CAA (Kliem and Greenberg, 2003)

As each of these is examined in detail in later sections, comments in this section are only introductory in nature.

The WOA01 climatology is a standard data product of the U.S. National Oceanographic Data Centre (NODC), it has its roots in the first global oceanographic climatology, i.e. that constructed by Levitus in the early 1980s (Levitus, 1982). It is built solely from the World Ocean Database (WOD, also from the NODC, see next section)

and is available with horizontal resolutions of 5°, 1° and ¼°. Grids of monthly means are available, as well as three month seasonal means and an annual mean. The yearly and seasonal grids extend from the ocean's surface to 5,500 m whereas the monthly grids extend only to 1,500 m.

The GDEM climatology is a product of the US Navy's Naval Oceanographic Office (NAVOCEANO) and was initially developed in 1975. Though it was developed prior to the 1982 Levitus climatology, it was not worldwide in coverage (Teague et al., 1990). Early versions had horizontal resolutions of ½° and were limited to areas with depths greater than 100 m. Later versions increased the horizontal resolution in some areas to 1/6° and extended geographic coverage to the coast instead of limiting the coverage to areas deeper than 100 m as was done previously (Head et al., 1997). The current version, GDEM-V 3.0, is worldwide in coverage, has a horizontal resolution of ¼° and also extends to the coast (US Naval Oceanographic Office, 2002).

The Kliem and Greenberg climatology was developed to study summer circulation in the CAA and is limited in coverage to the archipelago. It is constructed only for the summer season, being centered on September 1st, which loosely corresponds to the time of surface ice minima throughout most of the CAA (Kliem and Greenberg, 2003).

The WOA01 and GDEM climatologies are similar in coverage, horizontal and temporal resolutions: both are global in coverage, share a fixed horizontal grid size and provide monthly averages. The Kliem and Greenberg climatology differs in all three aspects: the coverage is limited to the CAA, an irregular grid is used and the analysis is limited to a seasonal average centred on September 1st. Turning to the topic of vertical

resolution, all three share a relatively coarse vertical resolution, with the resolution varying throughout the water column and coarsening with depth. Table B-1 lists the standard depth levels used in each of the three climatologies, with the WOA01 and Kliem and Greenberg climatologies being vertically spaced to roughly line up with the GDEM standard levels, which are of a higher resolution than the other two.

All three climatologies assume no inter-annual variations, i.e. data from different years are treated as if collected in the same year. Kliem and Greenberg (2003) note that inter-decadal and inter-annual variations in the Arctic Oscillation (AO) and North Atlantic Oscillation (NAO) could generate significant changes in the exchange of water between the Arctic and Atlantic oceans which presumably could affect the throughflow and overall oceanographic characteristics in the CAA. If, as Kliem and Greenberg suggest, the spatial distributions of temperature and salinity oscillate between two (or more) modes, then the average conditions depicted by the climatologies could be biased toward one or the other modes depending on when the most significant number of observations were collected in relation to the respective phases of the inter-decadal and inter-annual phenomena.

Table B-1. Climatology vertical resolutions.

WOA01	GDEM-V 3.0	Kliem & Greenberg	WOA01	GDEM-V 3.0	Kliem & Greenberg
Depth < 1,000 m			**Depth ≥ 1,000 m**		
0	0	0	1000	1000	1000
	2		1100	1100	
	4		1200	1200	
	6	5	1300	1300	1250
	8		1400	1400	
10	10	10	1500	1500	1500
	15			1600	
20	20	20	1750	1800	1750
	25		2000	2000	2000
30	30	30		2200	
	35			2400	
	40		2500	2600	2500
	45			2800	
50	50	50	3000	3000	3000
	55			3200	
	60			3400	
	65		3500	3600	3500
	70			3800	
75	75	75	4000	4000	
	80			4200	
	85			4400	
	90		4500	4600	
	95			4800	
100	100	100	5000	5000	
	110			5200	
	120			5400	
125	130	125	5500	5600	
	140			5800	
150	150	150		6000	
	160			6200	
	170			6400	
	180			6600	
	190				
200	200	200			
	220				
	240				
250	260				
	280				
300	300	300			
	350				
400	400	400			
500	500	500			
600	600	600			
700	700				
800	800	750			
900	900				

The three climatologies under investigation in this work differ in several aspects, some of which are important in understanding the results of the experiments outlined in this work. Errors in the source data temperature and salinity profile measurements are likely well within tolerance for sound speed estimation, however, the differing interpolation processes used to generate the three climatologies may introduce biases if the temporal and spatial resolution of the source data does not justify a high-resolution interpolation. It is important to explore the construction techniques used to create each climatology in order to identify how each construction method treats data sparse sectors, especially given the general lack of observations in the CAA.

The remainder of this appendix will provide an overview of the pre-processing and construction methods used for each of the three climatologies. The World Ocean Database is discussed first as it is the largest contributor of source data for all three climatologies.

B.2 World Ocean Database

The WOD is a worldwide database of oceanographic measurements maintained by the NODC. Though the WOD is maintained by the US government, the NODC accepts source data from all countries. Oceanographic data are maintained in a standard format that preserves metadata associated with the cast, instrumentation, cruise, quality control procedures, etc.

The most recent edition was released in 2005 along with extensive documentation regarding supported instrumentation and data validation procedures. Table B-2 lists the

instrument types supported in the current version of the database (2005). The 2005 database contains a total of 7,900,349 profiles (compared to 7,037,213 in the 2001 edition) and supports a new glider data type. Of the instruments listed in Table B-2, only OSD, CTD, XBT and MBT observations have been collected in the CAA.

Table B-2. WOD Dataset types (Boyer et al., 2006).

Dataset	Source
OSD	Bottle, low-resolution Conductivity-Temperature-Depth (CTD), low-resolution XCTD data, and plankton data
CTD	High-resolution Conductivity-Temperature-Depth (CTD) data and high-resolution XCTD data
MBT	Mechanical Bathythermograph (MBT) data, micro-BT
XBT	Expendable Bathythermograph (XBT) data
SUR	Surface only data (bucket, thermosalinograph)
APB	Autonomous Pinniped Bathythermograph – Time-Temperature-Depth recorders attached to elephant seals
MRB	Moored buoy data
PFL	Profiling float data
DRB	Drifting buoy data from surface drifting buoys with thermistor chains
UOR	Undulating Oceanographic Recorder data from a Conductivity/Temperature/Depth probe mounted on a towed undulating vehicle
GLD	Glider data

Documentation regarding quality control procedures is described by Johnson (Johnson et al., 2006). All data are preserved throughout the process with questionable values being flagged to indicate a failure to meet certain statistical criteria. Procedures include:

- Position, date and time check
- Speed check (time elapsed and distance travelled between successive stations)
- Duplicate check
- Depth inversion and depth duplication check
- Range check

- Excessive gradient check
- Observed level density check

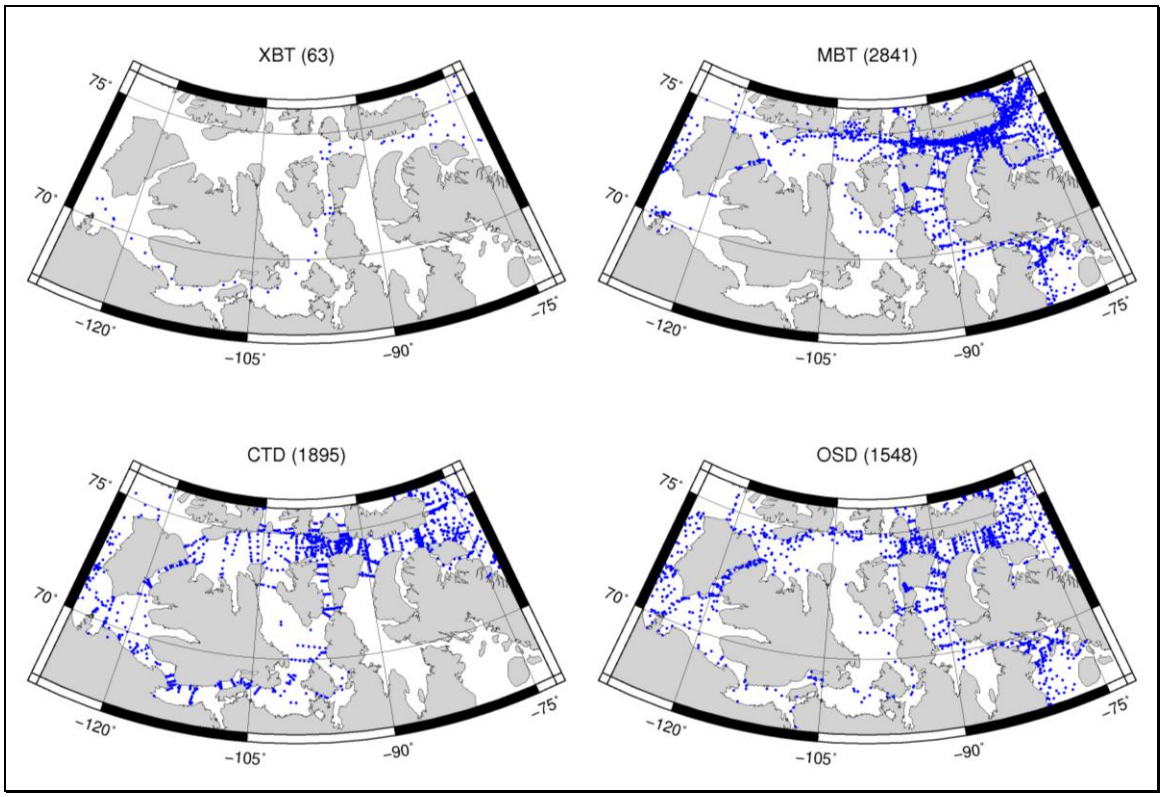

Figure B-1. WOD observations in the CAA, by instrument. Numbers in parentheses indicate the number of observations for each instrument type for all months of the year.

WOD data coverage is sparse in some sections of the CAA. Referring to figures B-1 and B-2, there is a notable lack of data in the south central portions of the CAA (M'Clintock Channel, Queen Maud Gulf and Coronation Gulf). Data in Figure B-1 are plotted separately by instrument to point out the amount of data that is *not* included in the Kliem and Greenberg climatologies, namely the XBT and MBT data as they contain no concurrent salinity observation.

Figure B-2 shows that most oceanographic observations in the CAA are collected in the relatively ice free summer months (July through September) with a second peak in March/April when conditions are favourable for through-ice observations.

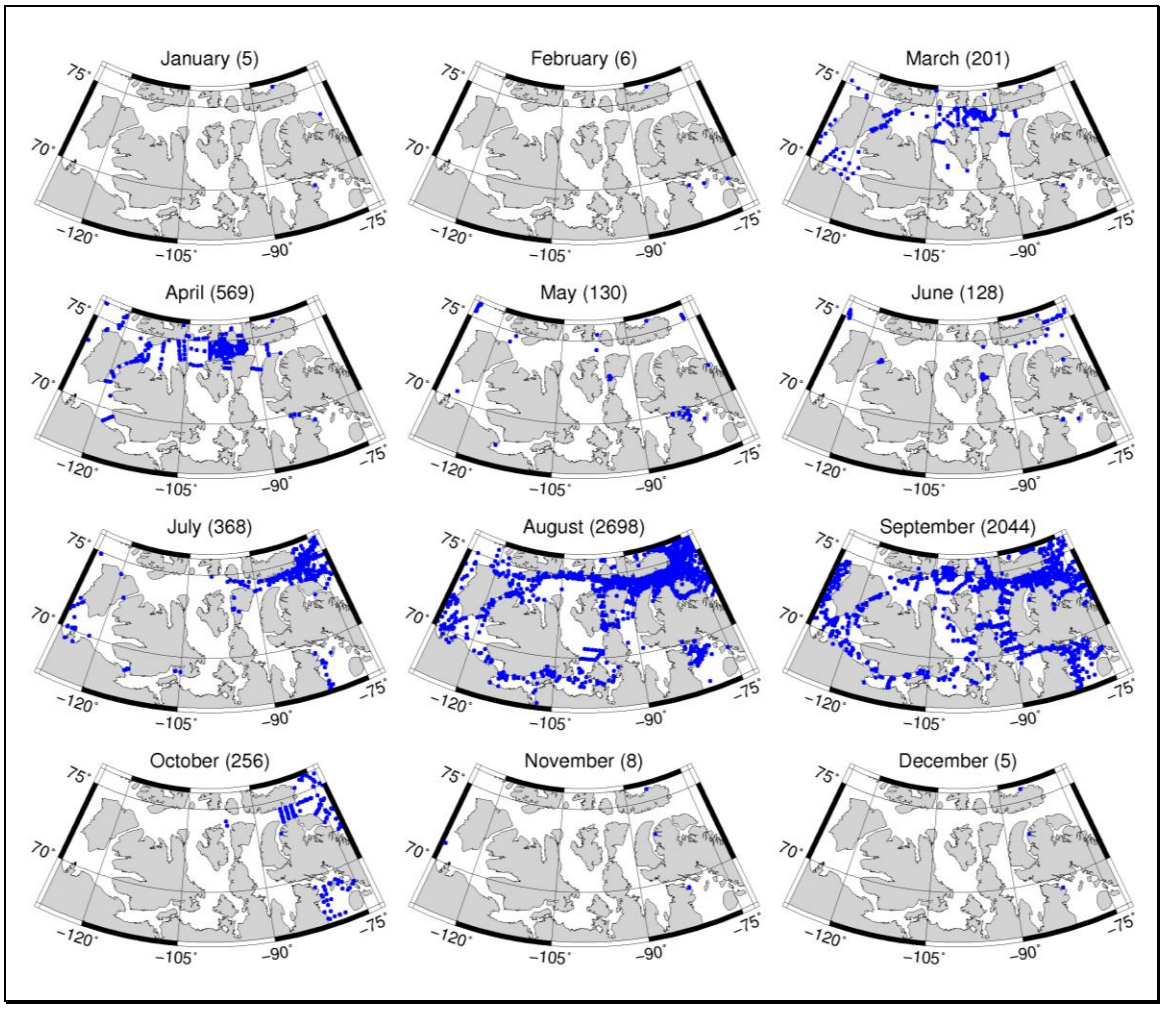

Figure B-2. WOD observations in the CAA, by month. Numbers in parentheses indicate the number of observations in each month for all instruments.

B.3 WOA01

B.3.1 Source Data and Pre-processing

The WOD01 source data are extensively filtered to remove erroneous and non-representative data, and in rare instances, suspicious data from entire oceanographic cruises (the last is a subjective procedure). The pre-processing procedure is thorough and very well documented; the reader is directed to the documentation accompanying the WOA01 climatologies for more detail (Stephens et al., 2002; Boyer et al., 2002; Boyer et al., 2005). A summary of the steps involved is presented below.

1. Removal of duplicate casts: entire casts are flagged for exclusion if they are an exact (or near exact) match to another cast.
2. Check on valid ranges and gradients: temperature and salinity observations are compared against expected ranges of validity and are flagged if out of range (ranges of validity vary by region and with depth); samples that cause excessive gradients are flagged as well.
3. Statistical check for removal of outliers: means of each value being analyzed are computed for 5° bins at each depth level. Samples are flagged as outliers if they fall more than a specified number of standard deviations from the mean. The number of standard deviations used for a cutoff varies with depth and proximity to land with a larger standard deviation criterion used in shallow areas in 5° grid boxes containing land.
4. Static stability checks (OSD and CTD casts only): a local static stability check flags observations that cause excessive inversions (density should increase

monotonically with depth). An entire cast is excluded if more than two inversions are detected within the cast.

5. In the case of XBT profiles, an additional drop-rate error correction is applied to correct the depths of the temperature observations if necessary.

A final step to pre-processing includes vertical interpolation of the observed level data to standard levels, i.e. resampling the observed data to the standard depth levels used in the WOA01 climatology. For each standard level, the four observed samples (two shallower and two deeper) are used to interpolate the value at the required standard level following the procedure outlined in the Joint Panel on Oceanographic Tables and Standards (JPOTS) 1991 publication "Processing of Oceanographic Station Data", which is largely based on the paired parabola procedure developed by Rattray (Rattray, 1962) which was later refined Reiniger and Ross (Reiniger and Ross, 1968).

B.3.2 Construction methods

The WOA01 temperature and salinity grids are available in 5°, 1°, and ¼° horizontal resolution. The construction of the ¼° grid relies on the 1° degree grid and is potentially biased towards the 1° grid in areas of sparse data coverage. Thus, it is necessary to investigate the construction methods used in the latter before examining those used for the former, though they are very similar.

A brief description of the construction technique, objective analysis, is warranted prior to exploring the details of the procedure. An objective analysis aims to provide a continuous representation of a variable over a surface from observations that are scattered in space and time; the product is typically a regularly gridded dataset derived from

irregularly spaced observation points (Cressman, 1959). The technique, which was developed by the meteorological community in the 1950s, hinges on a first-guess field and is based upon the idea that "the difference between a first-guess value and an analyzed value at a gridpoint is the same as the difference between an observation and a first-guess value at a nearby observation station" (Levitus, 1982). This principle is used to construct a correction to a first-guess value at a given grid point value based on a weighted mean of the differences between observations and their associated first-guess values within a specified radius of influence. In other words, the first-guess value is corrected based on a weighted mean of the observed interpolation errors at surrounding observation points to produce an analyzed value, i.e. the final result of the analysis at a given gridpoint:

$$G_{i,j} = F_{i,j} + C_{i,j} \tag{B.1}$$

where

(i,j) = location of the gridpoint in a north oriented cartesian grid

$G_{i,j}$ = analyzed value at gridpoint i,j

$F_{i,j}$ = first-guess value at gridpoint i,j

$C_{i,j}$ = correction applied at gridpoint i,j

The correction factor, $C_{i,j}$, is given by

$$C_{i,j} = \frac{\sum_{s=1}^{n} W_s Q_s}{\sum_{s=1}^{n} W_s} \tag{B.2}$$

Where

n = number of observations falling within the specified radius of influence with respect to the grid point i,j

Q_s = difference between the observed value and the first-guess at the s^{th} point in the influence area

The weight function, W_s, is an inverse distance weighting (Barnes, 1964):

$$W_s = \exp(-Er^2R^{-2}) \text{ for } r \leq R \quad \text{(B.3)}$$

$$W_s = 0 \text{ for } r > R \quad \text{(B.4)}$$

where

r = distance of the observation from the gridpoint

R = influence radius

E = 4

Applying this in an iterative fashion with the radius of influence diminishing at each pass, the analyzed value will converge to a value representative of a local set of observations in the case of high density of observations. On the other hand, data sparse areas will eventually reach a point in the iteration where no further data exists within the diminishing radius of influence and the analyzed value is no longer corrected from this point onwards in the iterative process. In the extreme case where the first iteration finds no data within the radius of influence, the final analyzed value is equal to the first-guess value at the gridpoint and remains so through the entire set of iterations and is only modified by the smoothing that occurs with each iteration (see below for discussion of smoothing). The 1° grids employ three iterations with the radius of influence diminishing from 888 km, 666 km, to 444 km (Stephens et al., 2002). The ¼° grids undergo three iterations as well during construction, however, the radius of influence

used for each iteration is significantly smaller: 321 km, 267 km, and 214 km (Boyer et al., 2005).

Smoothing is performed after each iteration to remove discontinuities that occur between regions of low and high data density. The 1° grids undergo a gradient preserving median smoother (Rabiner et al., 1975) and a five point Shuman smoother (Shuman, 1957) whereas the ¼° grids only use the median smoother. In the case of the 1° grids, the median smoother uses data from the north, east, south and west grid points, including the value at the grid point itself. The ¼° grids use data from the neighbouring five gridpoints in the aforementioned directions (Boyer et al., 2005).

At the core of the objective analysis technique is the idea that a first-guess field is populated with initial estimates of the variable to be analyzed, providing a launching point for the iterative correction process. The output of the grid is heavily dependant on the first-guess estimate in data sparse regions, thus it is important to have a reasonable initial estimate. The first-guess fields are different for the 1° and ¼° grids, thus they are treated separately below, beginning with the 1° grids.

The first-guess field for the annual 1° grid is computed at each standard level and is done separately for 56 subareas that comprise the world's oceans (e.g Hudson Bay is identified as a subarea). This separation into subareas is done in an effort to preclude observations from one area influencing the first-guess estimates in an adjacent basin in case the adjacent basin suffers from sparse observations. The first-guess field is computed as a zonal average of observations within a 1° latitudinal band, that is, all grid values along a latitudinal band within a subarea share the same first guess value: the mean of all the observations within the 1° latitudinal band. This procedure is repeated for

all depth levels for both temperature and salinity. The annual grid is used as a first-guess field for the seasonal grids; the seasonal grids are in turn used as first-guess fields for the monthly grids. These form a preliminary set of climatological yearly, seasonal and monthly means; they are then used to produce an updated annual first-guess field which is then used to generate new seasonal and monthly fields in the following manner:

1. The upper 1500 m of the preliminary monthly fields are averaged over the twelve months to produce an annual mean. The lower 1500 m of the first-round seasonal fields are averaged to produce the deeper portion of the annual mean field. This produces the final annual mean field for both temperature and salinity.
2. The final annual mean field generated in (1) is used as a first-guess field to produce a second round of seasonal mean fields. The resulting fields are the final seasonal mean fields.
3. The fields produced in (2) are used as first-guess fields for second round monthly mean fields.

Turning to the ¼° grids, the overall procedure is similar but with a few key differences (Boyer et al., 2005). Firstly, each of the WOA01 1° grids is used as a first-guess field for the corresponding ¼° grid, e.g. the 1° annual mean grid is used as the first-guess field for the 1/4° annual mean grid. Three iterations of the objective analysis are performed for all of the fields, but with smaller radii of influence and slightly different smoothing, as previously noted. The monthly mean fields are smoothed temporally via Fourier analysis: the time-series at each grid point in the monthly grids is Fourier

analyzed (at each depth level) and then used to reconstruct new monthly fields based on the annual mean at that grid point and the first three harmonics from the Fourier analysis. The temporally smoothed monthly fields are then averaged to produce new annual and seasonal fields from the surface down to 1500 m. Below 1500 m, the seasonal fields are averaged to produce the final version of the deeper portion of the annual mean field. A final processing step is applied at each gridpoint for each field and consists of minimal adjustment of the temperature and salinity profiles to ensure a vertically stable density structure (Jackett and McDougall, 1995).

B.2 GDEM

B.2.1 Source Data and Pre-processing

Source data for the GDEM climatology comes from the US Naval Oceanographic Office's (NAVOCEANO) Master Oceanographic Observation Data Set (MOODS), which contains oceanographic data dating back to 1870 (Head et al., 1997; Andrews, 2002). As of 2002, MOODS held ~8 million temperature profiles and ~2 million salinity profiles. Roughly 75% of MOODS is derived from the WOD, the remaining 25% consists of restricted data (Andrews, 2002).

Pre-processing steps are not as well documented as those used in the creation of WOA01. The profiles are subjected to a range and static stability check, date and positions of the profiles are checked for consistency and duplicates are removed (Teague, et al. 1990). Profiles are manually examined in groups covering small geographic

regions and over short time periods (monthly to seasonal) in order to eradicate anomalous profiles (US Naval Oceanographic Office, 2002).

B.2.2 Construction Methods

The construction of the GDEM climatology follows an entirely different method than that of the WOA01 climatologies and is succinctly summarized by Head (1997):

> *"GDEM is created by fitting curves to each profile from MOODS. All equivalent coefficients within a grid cell are averaged. Boxes without any observations are filled by spatial interpolation. A profile can then be constructed at each grid point using the coefficients".*

The underlying philosophy behind the design of GDEM is the belief that averages of coefficients yield more realistic profiles than profiles derived from coefficients of averaged profiles. Teague et al. (1990) provides more details on construction methods used for the GDEM 2.5 climatology, this is more or less the procedure used in the construction of GDEM 3.0, which is the version used in this work. The GDEM approach models the world's oceans as a set of three overlapping sub-model depth layers with the curve fitting process being done separately for each of the layers. Once curves are fit in each sub-model, the sub-models are merged in such a manner to remove discontinuities in the vertical gradients of temperature and salinity at the interface between sub-models. The characteristics of each sub-model are summarized in Table B-3 (Teague et al., 1990).

Table B-3. GDEM sub-model characteristics.

Sub-model	Depth range	Temperature Functions	Salinity Functions
Shallow Top	0 m – 400 m	Squared amplitude response for a Butterworth filter with exponential tail	Five degree orthogonal polynomial
Middepth	200 m – 2450 m	Seven degree orthogonal polynomial	Five degree orthogonal polynomial
Deep	2000 m – bottom	Quadratic	Quadratic

The details involved with each sub-model are examined in turn below, closely following the description provided by Teague et al. (1990). Beginning with temperature in the Shallow Top sub-model, the Butterworth filter amplitude response function is chosen for two reasons: (1) its ability to generate smooth curves with only two coefficients, and (2) it can be made as steep as necessary without introducing overshooting sidelobes. It is given as

$$R(Z) = \frac{1}{1 + (Z / A)^{2B}} \tag{B.5}$$

Where

Z is the depth in meters,

A and B control the middle depth and sharpness of the thermocline, respectively.

This function is used from the surface to the bottom of the seasonal thermocline, z_1, which is defined as the depth of zero vertical gradient in temperature below the surface mixed layer. In the case where the base of the seasonal thermocline occurs at a depth shallower than 400 m, an exponential tail function is used to extend the curve down to 400 m:

$$E(Z) = x^{ax+b} \tag{B.6}$$

$$x = (Z - z_1)/(z_2 - z_1) \tag{B.7}$$

Where

a and *b* are the coefficients that control the shape of the exponential function

z_2 is 400m, the bottom depth of the Surface Top sub-model

The two functions are combined to give the mean temperature as a function of depth

$$\hat{T}(Z) = \frac{(T_0 - T_{z_1})[1 + (z_1 / A)^{2B}]}{[1 + (Z / A)^{2B}](z_1 / A)^{2B}} + T_{z_1} - \frac{(T_0 - T_{z_1})}{(z_1 / A)^{2B}} \qquad 0 \le Z \le z_1 \qquad \text{(B.8)}$$

and

$$\hat{T}(Z) = (T_{z_2} - T_{z_1}) x^{ax+b} + T_{z_1} \qquad z_1 \le Z \le z_2 \qquad \text{(B.9)}$$

The values T_0, T_{z1}, T_{z2} and z_1 are directly determined from each observed cast; the remaining unknown coefficients (*A*, *B*, *a*, *b*) are solved via a least-squares adjustment.

An orthogonal Gram polynomial is used as the functional form for the Shallow Top salinity layer and the Middepth temperature and salinity layers. The degree of the polynomials were chosen to be the lowest order possible that maintained an acceptable RMS fit to profiles with high vertical variability (0.1‰ and 0.05‰ for the top and middle salinity sub-models and 0.25° for the middle temperature sub-model). Orthogonal Gram polynomials were chosen for the reason that higher order coefficients can be recomputed without the need to recomputed lower order coefficients. They are given as

$$P_{NM}(D) = \sum_{K=0}^{M} (-1)^K \binom{M}{K} \binom{M+K}{K} \frac{D^K}{N^K} \qquad \text{(B.10)}$$

for degree $M = 0, 1, 2, \ldots, N$. The functional form is then given by

$$\hat{G}(D) = a_0 P_{N0}(D) + a_1 P_{N1}(D) + \ldots + a_m P_{NM}(D) \qquad \text{(B.11)}$$

Where *G* represents either temperature or salinity as a function of depth, *D*. As with the top sub-model, the coefficients of the polynomials were determined through a least-squares adjustment.

$$a_K = \frac{\sum_{D=0}^{N} G(D) P_{NK}(D)}{\sum_{D=0}^{N} P_{NK}^2(D)} \tag{B.12}$$

for K = 0, 1, 2, …, *N*.

Turning to the deep sub-model, this last sub-model uses a quadratic polynomial of the form

$$F(Z) = c_1 + c_2 Z + c_c Z^2, \qquad 2000 \le Z \le \text{bottom depth} \tag{B.13}$$

Once the coefficients are computed for each sub-model, the coefficients are averaged for each grid cell for which there exist observations. Grid cells without data are spatially interpolated in the horizontal for each of the depth layers. The two-dimensional interpolation is done with a multistage, minimum-curvature least squares spline which was explicitly designed to (1) minimize spatial aliasing, and (2) preserve the continuity of gradients in all three spatial dimensions. The regularly spaced, interpolated coefficients are then used to generate temperature and salinity values at each grid node for each depth level in each sub-model.

The sub-models are then joined together, taking care to smooth the transition between sub-models. In the case of the upper two models, the difference in temperature is computed at the 400 m depth level, this serves as a source of correction to either one or both sub-models, depending on the magnitude of the correction. Corrections less than 0.25° are applied to the middle sub-model only, corrections greater than this but less than

1° are split evenly between the middle and upper model. In the case of corrections greater than 1°, the lower sub-model absorbs only 0.5° of the correction with the remainder being applied to the upper sub-model. In each sub-model, the correction is then propagated vertically away from the 400 m layer and is allowed to decay with vertical distance using the following scheme, which computes a new temperature for any given depth, Z

$$T_{new} = T_Z + \alpha \Delta T (0.835)^{\delta |Z - d_{merge}|} \tag{B.14}$$

Where

T_{new} = merged temperature

T_Z = model temperature at depth Z

ΔT = difference in temperature at merge depth 400 m,

$T_{top} - T_{mid}$ for the top sub-model and $T_{mid} - T_{top}$ for the middle sub-model

α = percent of ΔT assigned to each sub-model

δ = scaling factor, 0.01 and 0.05 for middle and top model, respectively

d_{merge} = merge depth between models

The merged values for 400 m and 500 m are removed and replaced with those generated from a cubic spline which is fitted from the surface to the bottom of the middle model, ensuring continuity in the first and second derivatives at the merged depth. The merge process is similar for the middle and bottom sub-models, occurring at a depth of 2000 m. The major difference is that the correction scaling factor δ is 0.02 and, more significantly, the bottom model is not corrected at all, i.e. the middle model absorbs the entire

correction (α = 1). The merge between the middle and bottom sub-models is carried out prior to the upper merge.

A few notable omissions of the construction procedure described by Teague et al. (1990) should be mentioned. Firstly, it is noted that all observed profiles are resampled to regularly spaced depth intervals prior to the curve fitting procedure, however, no mention is made of the method employed (it should also be noted that the depth intervals vary with sub-model as well: 20 m, 50 m, and 500 m – 1000 m for the shallow, middle and bottom sub-models, respectively). Secondly, there is no indication of how the merge correction process is applied to salinity values. Presumably it is the same procedure, however, the absence of the salinity correction sharing scheme between the top and middle sub-models is a significant oversight (α in the above equation, which dictates each sub-model's share of the correction). It is also assumed that the corrective procedure is carried out at all depth levels until negligible. Lastly, there is no mention of how the merged model is resampled to the standard depth levels used in the final model, which varies from 10 m intervals near the surface, and drops to 1000 m intervals at depths greater than 3000 m.

GDEM 3.0 is the version that is used in this work; it includes MOODS profiles up to 1995 and has monthly grids computed at a fixed ¼° horizontal resolution. The documentation delivered with the GDEM 3.0 used in this work points out refinements in the latest version of the GDEM climatology and its construction techniques (US Naval Oceanographic Office, 2002). Construction methods, though not spelled out as clearly as by Teague et al. (1990), vary slightly. Notable differences are listed below.

1. There is an increase in number of vertical levels in the climatology (from 35 to 78), also, the deepest level represented has increased from 5500 m to 6800 m.
2. The horizontal interpolation of grid cells without observations follows a slightly different methodology as the methods used in earlier versions had the potential to introduce large erroneous oscillations in data sparse areas. Oscillations are reduced through the inclusion of a tension term which minimizes the squared first derivative of gridded values (Brasseur et al., 1996).
3. Zero-gradient boundary conditions were included to inhibit gridding across land boundaries, with the land boundary being uniquely defined for each depth level.
4. Static stability is verified for each grid node using the same method as used in the preparation of WOA01 (Jackett and McDougall, 1995).

Most importantly, it appears that the underlying design philosophy, i.e. that of computing averages of profile coefficients, has been abandoned. The new documentation is woefully inadequate in explaining what methods replace the old procedures:

> *"The function fitting approach leads to several other problems, and was therefore not used in the construction of GDEM-V 3.0. Instead, the vertical gradient of each vertical profile in the final gridded climatology was corrected by an objective least-squares technique which forces the*

vertical gradient of each profile toward the gradient estimated from the data while simultaneously minimizing the difference between the original and modified profile." (US Naval Oceanographic Office, 2002)

The document also hints at "gridding observations" whereas Teague et al. (1990) was very meticulous about describing operations performed on observations versus those performed on coefficients derived from the function fitting procedure. On the other hand, a briefing prepared by the Office of Naval Research clearly states that GDEM-V 3.0 is not "profile averaging", which implies that the original method is still used (Andrews, 2002). Further adding to the confusion, it is unclear whether the sub-models overlap or not. There is mention made of "different, but overlapping" depth ranges, however the depth ranges listed later in the document imply that the sub-models abut instead (the depth ranges are top: 0 m– 200 m, middle: 200 m – 1000 m, bottom: 1000 m – seafloor). Unfortunately, there is little information in the literature to clear up the confusion regarding this latest version of GDEM.

B.3 Kliem and Greenberg

B.3.1 Source Data and Pre-processing

The Kliem and Greenberg climatology is unique compared to WOA01 and GDEM in that it was designed and constructed for a single purpose: calculation of the mean summer flow field within the CAA through the use of a diagnostic numerical ocean

model (Kliem and Greenberg, 2003). Its geographic coverage is limited to the CAA, extending only slightly into the adjacent ocean basins (Arctic Ocean, Hudson Bay and Baffin Bay). The climatology is also limited in temporal scope in that only the summer season is represented (the analysis is centered on September 1st).

As with WOA01 and GDEM, the Kliem and Greenberg climatology indirectly relies on the World Ocean Database (pre-2001). Other sources of data include (1) the Marine Environmental Data Service (MEDS), (2) the Bedford Institute of Oceanography (BIO) Ocean Sciences hydrographic database, and (3) the National Snow and Ice Data Center in Boulder, Colorado which provided additional data for the south-western and central part of the CAA. It should be noted that Kliem and Greenberg limited their input data set to observations that contained concurrent observations of temperature and salinity, thus all XBT and MBT casts were discarded from the source data sets prior to construction of the climatology.

Source data were investigated in 10°x10° spatial bins to check for outliers and duplicates and all in situ temperature measurements were converted to potential temperature for use in the numerical model. The profiles were then sub-sampled to a set of standard depths similar to those chosen for the final climatology; this was done simply by extracting the observation closest to the desired depth without any averaging or interpolation.

B.3.2 Construction Methods

A four dimensional optimal linear interpolation, following Loder (Loder et al., 1997), is used to generate the temperature and salinity fields for each depth level in the

climatology. A major difference between this climatology and the previous two is that there is an attempt to account for anisotropic correlation of the observations; in this case, the correlation is expected to be greatest in the along-channel direction and weakest in the across-channel direction. Each grid node is populated by the inverse-distance weighted mean of surrounding observations that fall within a four-dimensional ellipsoid centered upon the grid point. The four dimensional distance is computed for each observation as

$$r = \sqrt{\left(\frac{a_d}{S_a}\right)^2 + \left(\frac{b_d}{S_b}\right)^2 + \left(\frac{z_d - z_g}{S_z}\right)^2 + \left(\frac{t_d - t_g}{S_t}\right)^2} \tag{B.15}$$

where z is the vertical coordinate, t is the time (day of year) and indices d and g refer to data and grid points, respectively. The correlation scales S_a, S_b, vary with geographic location whereas S_z grows with the depth of the gridpoint (5 m at the surface, increasing to 200 m for depths greater than 1200 m). The temporal scale, S_t, is fixed at 90 days, thus the grid can be regarded as a seasonal average as opposed to a monthly average. The horizontal distances, a_d and b_d, are calculated as

$$a_d = (x_d - x_g)\cos\varphi + (y_d - y_g)\sin\varphi \tag{B.16}$$

$$b_d = (y_d - y_g)\cos\varphi + (x_d - x_g)\sin\varphi \tag{B.17}$$

Where x and y are the coordinates in a Lambert azimuthal projection and φ is the orientation of the search ellipsoid. The weighting used for each observation point is

$$w = e^{-\left(r + r^2 + \frac{r^3}{3}\right)} \tag{B.18}$$

For gridpoints shallower than 800 m, the initial size of the horizontal axes of the search ellipsoid are based on tidal velocity ellipses deduced from a barotropic simulation of the M2 tide:

$$S_a = S_0 \frac{c_a}{\sqrt{c_a^2 = c_b^2}} \tag{B.19}$$

$$S_b = S_0 \frac{c_b}{\sqrt{c_a^2 = c_b^2}} \tag{B.20}$$

where c_a and c_b are the relative sizes of the axes of the tidal velocity ellipse. The same tidal velocity ellipses presumably set the orientation angle of the search ellipsoid as well though this is not explicitly stated in the documentation (though it is mentioned that the orientation of the search ellipses remains fixed with each iteration). A slightly different approach is taken for gridpoints with depths greater than 800 m at which depth flow is expected to be steered by topography. In this case, the bottom slope *s* is used to estimate the relative sizes of c_a and c_b through the following relationship

$$\frac{c_b}{c_a} = 1 - 200s \tag{B.21}$$

To allow for some degree of cross-flow mixing in both the shallow and deep cases above, the magnitude of c_b is not allowed to fall below a value such that $c_b/c_a \geq 3/20$.

As source data availability is highly variable throughout the CAA, an iterative approach is taken which allows for the growth (or reduction) of search ellipsoids until a specified number of data points are found to within an ellipsoid defined by r = 1 (at least 10 and no more than 70). This is done by varying the isotropic correlation scale with each iteration. The isotropic correlation scale, S_0, is initially set to 80 km for depths from 0 to 300 m and is increased linearly up to a value of 800 km at a depth of 800 m, remaining constant for all depths greater than 800 m. This iterative procedure is repeated for each depth level in the climatology, thus the final horizontal correlation scales may

vary with depth. A final smoothing procedure is performed on each horizontal level by taking the mean of surrounding elements over 20 iterations.

B.4 Important Differences

There are several important differences between all three climatologies that can potentially affect their relative performances for the purposes described in this work. The discussion below is limited to those differences that are most likely to impact on the analysis performed in this work.

B.4.1 Source data

In general, WOA01 has by far the most openly available and easily acquired underlying data set as it is available in its entirety from a single source point on the NODC website. The underlying Kliem and Greenberg source data sets are all available for download, however from several different locations. Roughly 25% of GDEM source data locations are restricted and there is no way to find out if additional data are available in the CAA such that one could say that the GDEM climatology has better data density than the other two. Technically, GDEM could only have ***more*** source data than the other two due to the inclusion of restricted profiles; as such, this is not really a limitation to its potential performance. On the other hand, in the case that GDEM does indeed perform better than the other two climatologies, it will be difficult to assess whether it is due to (1)

additional, but unknown, source data, (2) differences in construction methods, or (3) a combination of (1) and (2).

Turning to the types of source data used (by instrument), WOA01 and GDEM include temperature measurements from XBT and MBT instruments, whereas the Kliem and Greenberg climatology does not. This could have a significant impact on the fidelity of the temperature field in the Kliem and Greenberg climatology as XBT and MBT measurements represent roughly half of all the available measurements in the CAA (2904 out of 6347 profiles, as shown in Figure B-1). Arguably, the poor accuracy of the MBT measurements (+/- 0.3°C (Johnson et al., 2006), presumably 1σ) would argue for their exclusion as this is a large uncertainty relative to the dynamic range of temperatures below the variable surface layer in the CAA.

B.4.2 Horizontal, vertical and temporal resolutions

WOA01 and GDEM are regularly spaced grids whereas the Kliem and Greenberg climatology is an irregular mesh with grid point density controlled by the water depth (varies from 2 km to 80 km). The horizontal correlation scales used during the construction of the Kliem and Greenberg climatology are independent of the final grid point spacing. It is therefore unlikely that the higher grid resolution in some areas is an advantage, especially once one considers the scarcity of observations and the degree of smoothing that is applied to achieve the final product.

Turning to the vertical dimension, each layer of the WOA01 and GDEM grids are independent of observations in other layers although the adjustment of the grid profiles for static stability introduces some measure of ensuring that adjacent depth levels are

physically consistent. The Kliem and Greenberg climatology allows for vertical interpolation during the grid construction, however, a stability check on the final profiles is not performed (Greenberg, pers. comm.).

Lastly, temporal resolution is examined. The monthly, seasonal and yearly WOA01 grids are tightly coupled in time due to the use of the first-guess fields and iterative procedure that is used to construct the final version of each grid. This can have significant effects in data sparse regions as these areas can be heavily influenced by the first-guess background field:

> *Most of the arctic data used in creating the WOA98 were taken in the summer. This influences the annual means that are used to define the background field, with a resulting bias towards fresh and warm conditions in the data-poor seasons of autumn, winter, and spring.* (Steele et al., 2001)

This has the potential to impact on the months of October and November as there are very few observations at all throughout the CAA for these months (refer to Figure B-2). This has a potential impact on this work as the ArcticNet field season almost always extends into October and sometimes into November.

Kliem and Greenberg explicitly allow for weighted averaging in time with the time weighting factor decaying away from September 1st. As the climatology is a seasonal mean and includes data within +/- 45 days of September 1st, it has the potential to be biased in data poor areas. Fortunately September and August are the months with the most observations throughout the CAA (see Figure B-2) and the seasonal mean is thus heavily weighted towards the observations from these two months.

The GDEM-V 3.0 documentation is unclear about temporal averaging though it is mentioned that all the monthly mid-depth layers are derived from three month averages (recall that the mid depth layer extends from 200 m to 1000 m). Data below 1000 m are averaged together in GDEM regardless of the month of acquisition, forming a yearly average below this depth with the underlying assumption that seasonal variability does not extend below this depth. For comparison, WOA01 monthly profiles extend to a depth of 1500 m. This is not likely to pose any noticeable problems in the CAA as water depths are typically much less than 200 m, with a maximum depth of 700 – 800 m in the eastern entrance to Lancaster Sound.

B.4.3 Topographic and bathymetric restrictions

WOA01 limits interpolating over land by enumerating all significant oceanographic basins and specifying the maximum depth of communication between neighbouring basins. Unfortunately, the CAA is regarded as an extension to the Arctic Ocean thus the physical limitations imposed by the sills and islands within the CAA are disregarded. GDEM applies a zero gradient restriction on land boundaries that precludes gridding over land though it is unclear if the land boundary evolves with depth such that oceanographic sills are treated as a land boundary below the sill depth. The Kliem and Greenberg climatology does not explicitly deal with this problem, hoping instead that the small across-channel correlation scales will minimize the effect of gridding over land and sills.

APPENDIX C – REFERENCE MAP

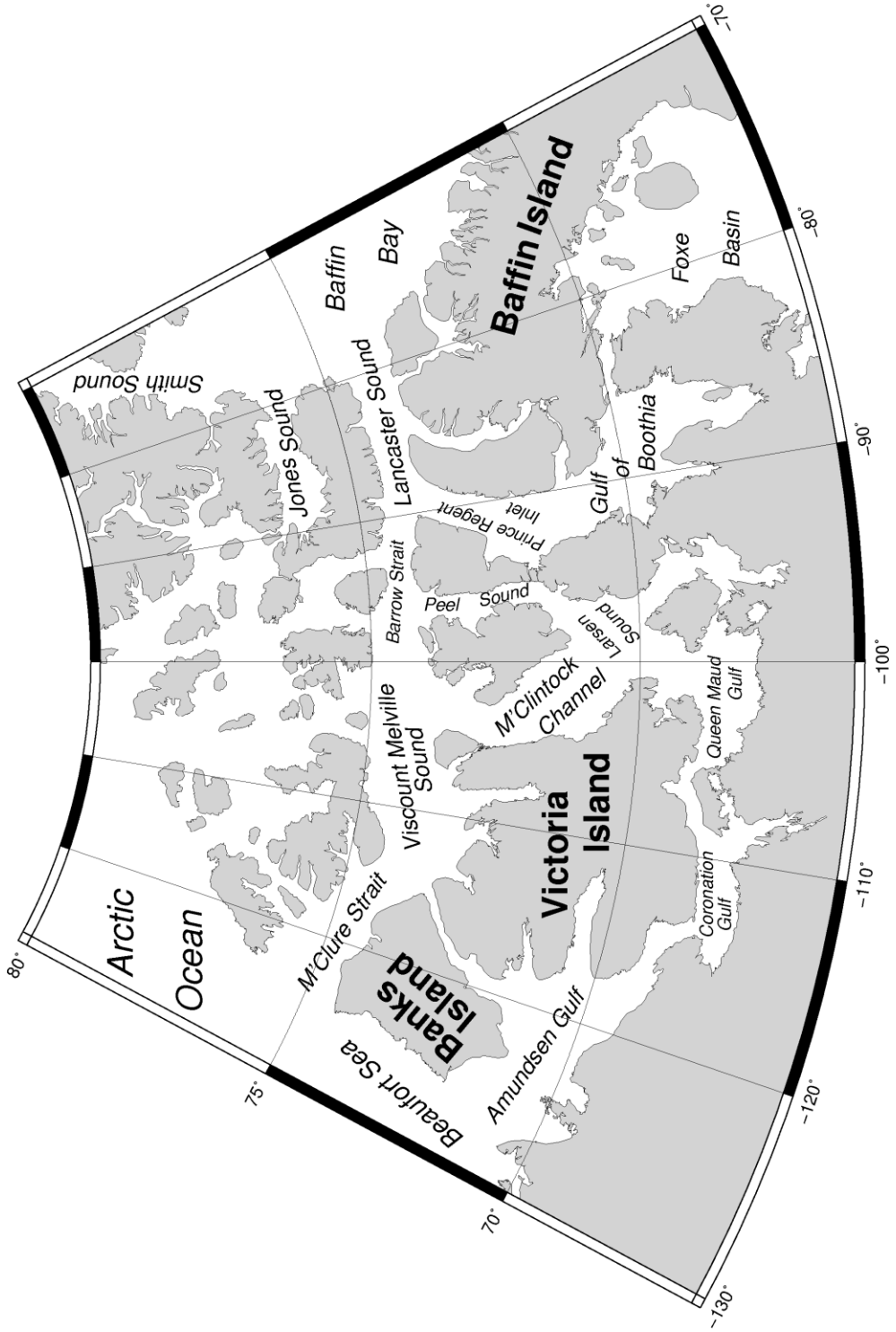

CURRICULUM VITAE

Candidate's Name: Jonathan Daniel Beaudoin

Universities attended: University of New Brunswick
Fredericton, Canada
September 1995 – December 2002
B.C.S. & B.Sc.Eng. (Geomatics)

Refereed Publications:

Beaudoin, J., Calder, B., Hiebert, J. and G. Imahori, 2009, Estimation of Sounding Uncertainty from Measurements of Water Mass Variability, International Hydrographic Review, No. 2., November 2009, pp. 20-38.

Beaudoin, J., Hughes Clarke, J., and Bartlett, J., 2004. Application of Surface Sound Speed Measurements in Post-Processing for Multi-Sector Multibeam Echosounders : International Hydrographic Review, v.5, no.3, p.26-31.

Magazine Articles:

Beaudoin, J., Hughes Clarke, J.E. and Bartlett, J., 2006, Usage of Oceanographic Databases in Support of Multibeam Mapping Operations Onboard the CCGS AMUNDSEN: Lighthouse, Journal of the Canadian Hydrographic Association; Edition No. 68

Conference Papers:

Beaudoin, J., Hiebert, J., Calder, B. and G. Imahori, 2009, Uncertainty Wedge Analysis: Quantifying the Impact of Sparse Sound Speed Profiling Regimes on Sounding Uncertainty , US Hydro 2009, May 11th-14th, Norfolk, Virginia

Beaudoin, J., Hughes Clarke, J.E., Bartlett, J., Blasco, S. and Bennett, R., 2008, Mapping Canada's Arctic Seabed: Collaborative Survey Processing and Distribution Strategies Paper 9-4, Proceedings of the Canadian Hydrographic Conference and National Surveyors Conference, Victoria, BC

Beaudoin, J., Hughes Clarke, J.E. and Bartlett, J., Usage of oceanographic climatologies and databases in support of multibeam mapping operations onboard the CCGS Amundsen. ArcticNet Annual Scientific Meeting, poster presentation, December 2005, Banff, Canada.

Beaudoin, J. and Hughes Clarke, J.E., 2004, Retracing (and re-raytracing) Amundsen's Journey through the Northwest Passage: proceedings of the Canadian Hydrographic Conference 2004, Ottawa, CDROM

Beaudoin, J., Hughes Clarke, J.E. and Bartlett, J. A Sound Speed Decision Support System for Multibeam Sonar Operations in the Canadian Arctic. ArcticNet Annual Scientific Meeting, poster presentation, December 2004, Quebec, Canada.

Conference Presentations:

Beaudoin, J., 2009, Field Trials of the UNB Refraction Uncertainty Monitoring Toolkit , Paper 26, FEMME 2009, Lisbon, Portugal

Beaudoin, J., 2008, Real-time Monitoring of Uncertainty due to Refraction in Multibeam Echosounding , Paper 10, Shallow Survey 2008, Portsmouth, NH